Study of Two-Dimensional Materials with Honeycomb Geometry

Universiteit Utrecht

Cover: Artist's impression of an AFM measurement of the edge of a graphene flake. The measured data in the image stems from Figure 2.11(a).
Cover design: Mark Boneschanscher

Printed by: Proefschriftmaken.nl || Printyourthesis.com
Published by: Uitgeverij BOXPress, 's Hertogenbosch

ISBN 978-90-8891-877-3

Study of Two-Dimensional Materials with Honeycomb Geometry

Studie van Tweedimensionale Materialen met Honingraat-Geometrie

(met een samenvatting in het Nederlands)

Proefschrift

ter verkrijging van de graad van doctor aan de
Universiteit Utrecht op gezag van de rector magnificus,
prof. dr. G.J. van der Zwaan, ingevolge het besluit van het
college voor promoties in het openbaar te verdedigen
op 4 juni 2014 des middags te 12.45 uur

door

Mark Pieter Boneschanscher

geboren op 28 november 1985 te Amersfoort

Promotor:	Prof. dr. D. A. M. Vanmaekelbergh
Co-promotoren:	Prof. dr. P. Liljeroth
	Dr. I. Swart

The research described in this thesis was financed by the Foundation for Fundamental Research on Matter (FOM).

Gracious words are a honeycomb, sweet to the soul and healing to the bones. — Proverbs 16:24

Contents

1 Introduction

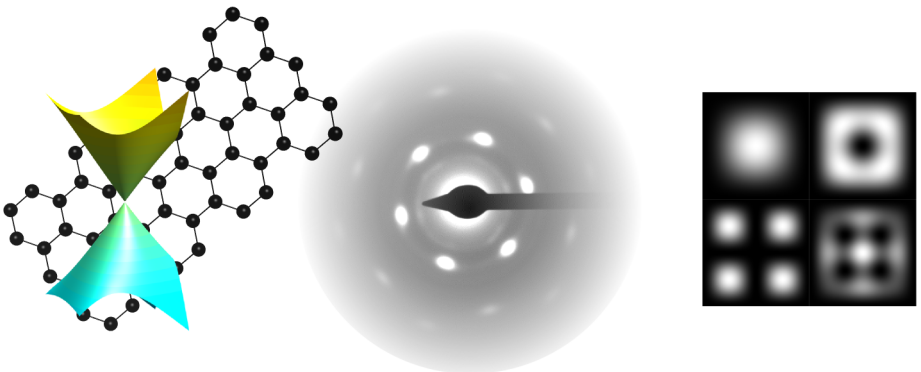

This thesis describes the study of thin, layered structures, with a particular focus on structures with a honeycomb geometry. The systems studied range from rather simple structures, *e.g.*, graphene, a single plane of carbon atoms bound to each other in a honeycomb pattern, to much more complicated structures consisting of multiple types of nanocrystals. What all these structures have in common is that the electronic properties are strongly dependent on the geometric structure. This chapter will introduce the systems studied in this thesis. It will also provide an introduction into the methods used to study their geometric and electronic structure.

1.1. Scope and outline of this thesis

This thesis can be divided into two parts. The first part is concerned with graphene, a single layer of carbon atoms forming a honeycomb pattern. In this research, we have used epitaxial graphene grown on the (1 1 1) surface of an iridium crystal as a model system. The interaction between the Ir(1 1 1) surface and the graphene layer results in buckling of the graphene and the emergence of a moiré pattern. It is expected that this perturbation of the graphene lattice could in turn lead to a perturbation of the electronic properties. The results of probing the atomic structure of the graphene layer by atomic force microscopy (AFM) are presented in Chapter 2. In this chapter, it is also shown how the image contrast in the AFM images depends on the chemical reactivity of the AFM tip and the tip-sample distance. Finally, the chapter describes how the use of chemically inert tips can improve image contrast on the edges of graphene islands on the iridium substrate. In Chapter 3 the moiré pattern itself is studied in more detail using a combination of low-energy electron diffraction (LEED) and AFM with chemically inert tips. Chapter 4 describes how one needs to take care with the use of carbon monoxide (CO) modified tips for AFM imaging, since bending of the CO molecule at the tip apex can distort the obtained images. In this chapter the moiré pattern of graphene on Ir(1 1 1) is used as a model system to show the effect of sample corrugation on the CO bending. Chapter 5 presents electronic properties of nanometer-sized graphene islands measured by scanning tunneling microscopy (STM). The results show that quantum confinement strongly influences the electronic properties. A comparison of the results to both atomistic theory and a wave-equation model makes clear that the peculiar nature of the charge carriers is preserved.

The second part of this thesis is concerned with structures obtained by self-assembly and oriented attachment of colloidal quantum dots. These quantum dots are nanometer sized crystals of semiconductor materials, *e.g.*, PbSe and CdSe. In these quantum dot solids the quantum dots are brought into close proximity. This should permit quantum coupling between the quantum dots, giving rise to new material properties such as the emergence of band-like transport. The exact material properties are expected to strongly depend on the geometry of the superlattice. Chapter 6 describes how electron tomography can be used to fully resolve the 3-D position of quantum dots in self-assembled superlattices. This allows for a full crystallographic description of the superlattices and for the study of defects.

The chapter also presents a completely new crystal structure formed by the self-assembly of PbSe and CdSe quantum dots. Chapter 7 shows how the spontaneous release of the ligands from certain facets can lead to the formation of 2-D superlattices of covalently bound quantum dots. We present a structural characterization of the superlattices formed in this way, showing the nanometer-scale geometry and long-range atomic coherence.

Finally, Chapter 8 provides an outlook on the research described in this thesis. It will show both prospects of the research techniques used, in particular the use of computer-aided image analysis, as well as possible applications of the materials studied.

1.2. Graphene

The history of graphene is quite a peculiar one. Graphene was first studied as a model system to understand graphite, since graphite consists of a stack of graphene layers. Already in 1947 the band structure of graphene was calculated using a tight-binding method [1]. This was mainly meant as a first onset for the calculation of the band structure of graphite. For another four decades, understanding the properties of graphite would remain the only reason why people where interested in graphene. In this time much progress was made on the theoretical understanding of graphite. For example McClure applied the Dirac equation to the states close to the Fermi level in order to get a theoretical description of the diamagnetism of graphite [2]. This approach got more attention when DiVincenzo and Mele used it to study electron dynamics in the vicinity of impurities in graphite intercalation compounds [3].

The emergence of the massless Dirac equation to describe the electronic properties of graphite and graphite intercalation compounds widened the theoretical work on what is now known as graphene, and propelled it into the field of quantum electrodynamics. For example, later in the same year that the paper by DiVincenzo and Mele was published, Semenoff showed that a magnetic field caused the emergence of an electronic Landau level precisely at the Dirac point [4]. It is this Landau level that is responsible for the anomalous integer quantum Hall effect. While the theoretical work on the electronic properties of graphene was growing, it was still believed that graphene as a free-standing material — or any purely two-dimensional crystal — would be thermodynamically unstable and could not exist [5]. Therefore the theoretical work on graphene remained exactly that, theoretical.

Although the theoretical work on graphene could be applied in research on fullerenes [6], the real breakthrough came in 2004, when Novoselov *et al.* reported the first experimental work on actual monolayer graphene, and showed it exhibited a remarkably high carrier mobility at room-temperature [7]. Soon after, more experimental reports on monolayer graphene where published, confirming the massless Dirac fermion character of the charge carriers as well as the quantum Hall effect [8, 9]. Even though substantial progress on the experimental side has been made since, the theoretical work still surpasses the experimental.

1.2.1. Geometric and electronic structure. The geometric structure of graphene is a honeycomb lattice. This can be rationalized as follows: the 2s orbitals of the carbon atoms mix with two of the three 2p orbitals, resulting in an sp^2 hybridized system. The carbon atoms form σ bonds to each other by overlapping their sp^2 orbitals. This results in a planar structure with a typical 'chicken wire' or 'honeycomb' pattern formed by the 120° bond angle between the carbon atoms (Figure 1.1). The remaining p_z orbital contributes one π electron for each carbon atom, resulting in a delocalized π system forming a half-filled π band.

The interesting physics of this delocalized π system is a direct result of the honeycomb geometry of the graphene lattice. This is readily shown when following the tight-binding method proposed by Reich *et al.* [10]. The unit cell of graphene consists of two carbon atoms, labeled A and B in Figure 1.1. An infinite graphene sheet can be constructed by repeated translations of the unit cell according to $\boldsymbol{R} = n_1\boldsymbol{a}_1 + n_2\boldsymbol{a}_2$, using as base vectors

$$\boldsymbol{a}_1 = \frac{a}{2}(3, \sqrt{3}), \quad \text{and} \quad \boldsymbol{a}_2 = \frac{a}{2}(3, -\sqrt{3}), \tag{1.1}$$

where $a \approx 1.42$ Å is the carbon-carbon bond distance. The plane wave describing the free p_z electrons can be combined with the atomic orbitals in the diatomic graphene unit cell. This results in the following Bloch wave describing the behavior of the p_z electrons in graphene

$$\begin{aligned} \psi_{\boldsymbol{k}}(\boldsymbol{r}) &= \sum_{\boldsymbol{R}} e^{i\boldsymbol{k}\cdot\boldsymbol{R}} \left[a_{\boldsymbol{k}} \varphi^{\mathrm{A}}_{\boldsymbol{k}} (\boldsymbol{r} + \boldsymbol{\delta}_{\mathrm{A}} - \boldsymbol{R}) + b_{\boldsymbol{k}} \varphi^{\mathrm{B}}_{\boldsymbol{k}} (\boldsymbol{r} + \boldsymbol{\delta}_{\mathrm{B}} - \boldsymbol{R}) \right] \\ &= a_{\boldsymbol{k}} \psi^{\mathrm{A}}_{\boldsymbol{k}} + b_{\boldsymbol{k}} \psi^{\mathrm{B}}_{\boldsymbol{k}}. \end{aligned} \tag{1.2}$$

Here, $\boldsymbol{\delta}_{\mathrm{A}}$ and $\boldsymbol{\delta}_{\mathrm{B}}$ are the vectors from the Bravais lattice point to atom A and B respectively. Having rewritten the Bloch function to a weighted linear combination of the electron wave functions on the two different sublattices ($\psi^{\mathrm{A}}_{\boldsymbol{k}}$ and $\psi^{\mathrm{B}}_{\boldsymbol{k}}$), we

can set up the Schrödinger equation

$$H\left(a_{\boldsymbol{k}}\psi^{\mathrm{A}}_{\boldsymbol{k}} + b_{\boldsymbol{k}}\psi^{\mathrm{B}}_{\boldsymbol{k}}\right) = E\left(a_{\boldsymbol{k}}\psi^{\mathrm{A}}_{\boldsymbol{k}} + b_{\boldsymbol{k}}\psi^{\mathrm{B}}_{\boldsymbol{k}}\right). \tag{1.3}$$

Using the same convention as Reich *et al.*, we define

$$E_0 = H_{\mathrm{AA}}S_{\mathrm{AA}}, \qquad E_1 = S_{\mathrm{AB}}H^*_{\mathrm{AB}} + H_{\mathrm{AB}}S^*_{\mathrm{AB}},$$
$$E_2 = H^2_{\mathrm{AA}} - H_{\mathrm{AB}}H^*_{\mathrm{AB}}, \qquad E_3 = S^2_{\mathrm{AA}} - S_{\mathrm{AB}}S^*_{\mathrm{AB}}.$$

Then, using the equivalence of the A and B atoms of the graphene, we write the equation in matrix form

$$\begin{vmatrix} H_{\mathrm{AA}} - E(\boldsymbol{k})S_{\mathrm{AA}} & H_{\mathrm{AB}} - E(\boldsymbol{k})S_{\mathrm{AB}} \\ H^*_{\mathrm{AB}} - E(\boldsymbol{k})S^*_{\mathrm{AB}} & H_{\mathrm{AA}} - E(\boldsymbol{k})S_{\mathrm{AA}} \end{vmatrix} = 0, \tag{1.4}$$

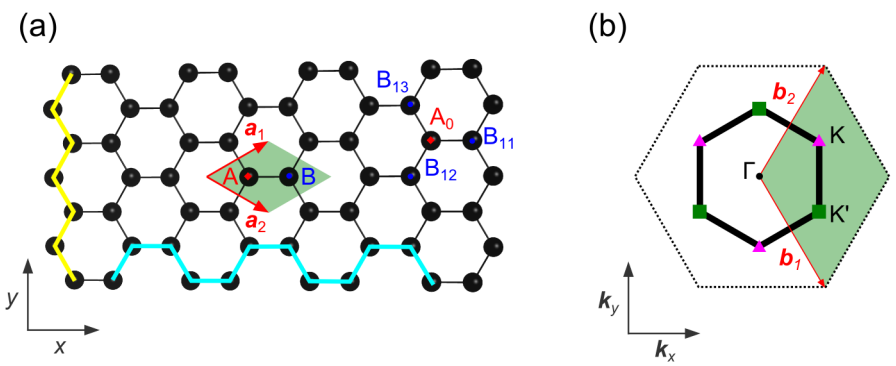

FIGURE 1.1. Structure of graphene. (a) The honeycomb structure of graphene. Two base vectors $\boldsymbol{a}_1$ and $\boldsymbol{a}_2$ span the unit cell, which comprises the two inequivalent carbon atoms 'A' and 'B'. The graphene slab can be terminated in two kinds of edges: the 'zigzag' edge (yellow) and the 'armchair' edge (cyan). (b) The reciprocal lattice. Two reciprocal lattice vectors $\boldsymbol{b}_1$ and $\boldsymbol{b}_2$ span the reciprocal unit cell, which comprises two inequivalent K points (K and K'). The first Brillouin zone is indicated with a thick black line. The trigonal symmetry dictates that it contains three K and three K' points, also known as Dirac points.

where $E(\boldsymbol{k})$ are the electronic eigenvalues of the energy. This is a quadratic equation in the energy and can be solved analytically to find that

$$E_{\pm}(\boldsymbol{k}) = \frac{-\left(-2E_0 + E_1\right) \pm \sqrt{\left(-2E_0 + E_1\right)^2 - 4E_2E_3}}{2E_3}. \tag{1.5}$$

The problem can greatly be simplified by only taking nearest-neighbor interactions into account. As the nearest-neighbor of an atom A can only be an atom B, H_{AA} reduces to the 2p atomic orbital energy $\epsilon_{2\mathrm{p}}$. The overlap integral $S_{\mathrm{AA}} = 1$, as the atomic wave functions are assumed to be normalized. To find the interaction energy H_{AB}, we can simply sum over the three nearest neighbors, as they are all of type B:

$$H_{\mathrm{AB}} = \gamma_0 \left(e^{i\boldsymbol{k}\cdot\boldsymbol{R}_{11}} + e^{i\boldsymbol{k}\cdot\boldsymbol{R}_{12}} + e^{i\boldsymbol{k}\cdot\boldsymbol{R}_{13}}\right),$$

with

$$\gamma_0 = \langle \varphi_{\mathrm{A}}(\boldsymbol{r} - \boldsymbol{R}_{\mathrm{A}}) \left|H\right| \varphi_{\mathrm{B}}(\boldsymbol{r} - \boldsymbol{R}_{\mathrm{A}} - \boldsymbol{R}_{1i})\rangle \qquad (i = 1, 2, 3).$$

The same reasoning holds for the overlap integral

$$S_{\mathrm{AB}} = s_0 \left(e^{i\boldsymbol{k}\cdot\boldsymbol{R}_{11}} + e^{i\boldsymbol{k}\cdot\boldsymbol{R}_{12}} + e^{i\boldsymbol{k}\cdot\boldsymbol{R}_{13}}\right),$$

with

$$s_0 = \langle \varphi_{\mathrm{A}}(\boldsymbol{r} - \boldsymbol{R}_{\mathrm{A}}) | \varphi_{\mathrm{B}}(\boldsymbol{r} - \boldsymbol{R}_{\mathrm{A}} - \boldsymbol{R}_{1i})\rangle \qquad (i = 1, 2, 3).$$

Here, $\boldsymbol{R}_{1i}$ is the vector pointing from atom A_0 to the nearest neighbors B_{1i} in Figure 1.1. Implementing the nearest neighbor simplifications in the general result of Equation 1.5 yields the well-known formula [6, 10]

$$E_{\pm}(\boldsymbol{k}) = \frac{\epsilon_{2\mathrm{p}} \mp \gamma_0 \sqrt{f(\boldsymbol{k})}}{1 \mp s_0 \sqrt{f(\boldsymbol{k})}}. \tag{1.6}$$

Here,

$$\begin{aligned} f(\boldsymbol{k}) &= 3 + u(\boldsymbol{k}) \\ &= 3 + 2\cos \boldsymbol{k}\cdot\boldsymbol{a}_1 + 2\cos \boldsymbol{k}\cdot\boldsymbol{a}_2 + 2\cos \boldsymbol{k}\cdot(\boldsymbol{a}_1 - \boldsymbol{a}_2). \end{aligned}$$

The three parameters $\epsilon_{2\mathrm{p}}$, γ_0 and s_0 are usually obtained by fitting experimental or first-principles data. Fitting the tight-binding dispersion to a correct description of the π bands at the K point results in a Fermi level $\epsilon_{2\mathrm{p}} = 0$ eV (since the band is half filled), a nearest-neighbor hopping energy γ_0 between -2.5 and -3 eV, and a nearest-neighbor overlap integral s_0 below 0.1 — often allowing the latter to be neglected [10]. The band structure obtained in this way is presented in Figure 1.2. It shows that graphene is a semimetal, *i.e.*, the edges of conduction and valence band touch. In graphene this happens at the six corners of the first Brillouin zone,

where both the conduction and the valence band have a conical shape. The Fermi level of graphene is exactly in between the conduction and valence band, at the position where the two bands touch.

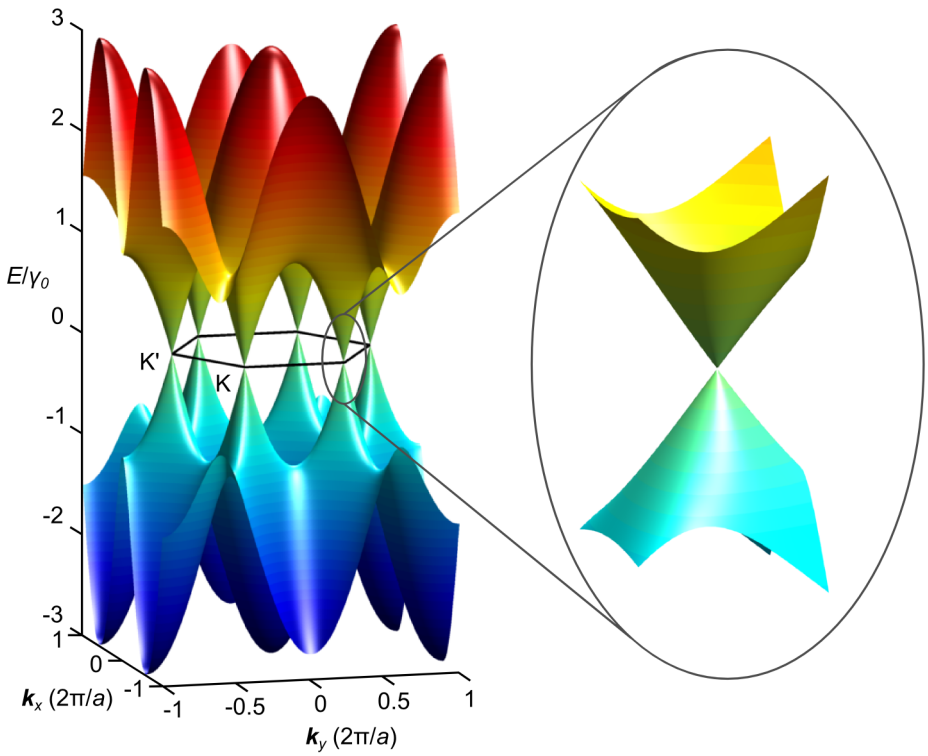

FIGURE 1.2. The π band structure of graphene calculated with the nearest-neighbor tight-binding model assuming ϵ_{2p} and s_0 to be zero. The first Brillouin zone is indicated at the Fermi level. Zooming in on one of the corners of the Brillouin zone shows the linear dispersion.

1.2.2. Linear dispersion, pseudo-spin and all that. One of the most intriguing aspects of the electronic structure of graphene is the linear dispersion (*i.e.*, the energy of the electronic states is a linear function of electron momentum) close to the Fermi level. From Figure 1.2 the energy dispersion is approximated to be linear for $|\boldsymbol{k} - \boldsymbol{K}| \equiv \boldsymbol{\kappa} \lesssim 0.1\,(2\pi/a)$. This results in a linear regime of

roughly one γ_0, or ≈ 2.8 eV — approximately 100 times the thermal energy $k_B T$ at room temperature. This implies that for all reasonable applications the full band structure (Equation 1.6) can be expanded close to the K (or K') point to [11]:

$$E_{\pm}(\boldsymbol{\kappa}) \approx \pm\hbar\,\nu_F|\boldsymbol{\kappa}|, \tag{1.7}$$

where ν_F is the Fermi velocity $\nu_F = \sqrt{3}\,\gamma_0\,a/2\hbar \approx 10^6$ m/s. This result is very different from the usual case of quadratic dispersion, where $E(\boldsymbol{k}) = (\hbar\boldsymbol{k})^2/2m^*$ with m^* being the effective mass of the electrons. The major difference is that in the case of linear dispersion the Fermi velocity is independent of energy and momentum, whereas in the case of quadratic dispersion $\nu = k/m^* = (2E/m^*\hbar^2)^{0.5}$. This means that, within the window of linear dispersion, the charge carriers in graphene can be thought of as relativistic particles. Since these are best described by the Dirac equation, they are referred to as massless Dirac fermions — and the corners of the Brillouin zone as Dirac points.

The implications of using the Dirac equation to describe the electronic structure of graphene are best understood when following the review of Beenakker [12]. First the Dirac equation is set up for the honeycomb lattice of graphene [2]:

$$-i\hbar\,\nu_F \begin{pmatrix} 0 & \frac{\partial}{\partial_x} - i\frac{\partial}{\partial_y} \\ \frac{\partial}{\partial_x} + i\frac{\partial}{\partial_y} & 0 \end{pmatrix} \begin{pmatrix} \psi_{\boldsymbol{k}}^{\mathrm{A}} \\ \psi_{\boldsymbol{k}}^{\mathrm{B}} \end{pmatrix} = E \begin{pmatrix} \psi_{\boldsymbol{k}}^{\mathrm{A}} \\ \psi_{\boldsymbol{k}}^{\mathrm{B}} \end{pmatrix}. \tag{1.8}$$

Here, only nearest neighbor hopping is taken into account. This is reflected in the differential operator that only couples $\psi_{\boldsymbol{k}}^{\mathrm{A}}$ to $\psi_{\boldsymbol{k}}^{\mathrm{B}}$ but not to itself. Using the momentum operator in the x-y plane $\boldsymbol{p} = -i\hbar(\partial/\partial x, \partial/\partial y)$ and letting $\boldsymbol{\sigma}$ be the vector of Pauli matrices $\boldsymbol{\sigma} = (\sigma_x, \sigma_y, \sigma_z)$ acting on the spinor $\psi = (\psi_{\boldsymbol{k}}^{\mathrm{A}}, \psi_{\boldsymbol{k}}^{\mathrm{B}})$, Equation 1.8 can be rewritten to:

$$\nu_F \boldsymbol{p}\cdot\boldsymbol{\sigma}\psi = E\psi. \tag{1.9}$$

This is a two-dimensional Dirac equation describing the states with wave vector $\boldsymbol{k}$ in the valley at the K point. The valley at the opposite corner (a K' point) produces an independent set of states $\psi_{\boldsymbol{k}}^{\mathrm{A}\prime}$ and $\psi_{\boldsymbol{k}}^{\mathrm{B}\prime}$ with equally large, but opposite, amplitude to $\psi_{\boldsymbol{k}}^{\mathrm{A}}$ and $\psi_{\boldsymbol{k}}^{\mathrm{B}}$. The two components $\psi_{\boldsymbol{k}}^{\mathrm{A}\prime}$, $\psi_{\boldsymbol{k}}^{\mathrm{B}\prime}$ satisfy the same Dirac equation (Equation 1.9) but with $p_x \to -p_x$. Combining both valleys into one spinor $\Psi = (\psi_{\boldsymbol{k}}^{\mathrm{A}}, \psi_{\boldsymbol{k}}^{\mathrm{B}}, -\psi_{\boldsymbol{k}}^{\mathrm{B}\prime}, \psi_{\boldsymbol{k}}^{\mathrm{A}\prime})$ therefore results in the four-dimensional Dirac equation:

$$\begin{pmatrix} \nu_F\boldsymbol{p}\cdot\boldsymbol{\sigma} & 0 \\ 0 & \nu_F\boldsymbol{p}\cdot\boldsymbol{\sigma} \end{pmatrix} \Psi = E\Psi. \tag{1.10}$$

The spin degree of freedom described by the Pauli matrices $\boldsymbol{\sigma}$ has nothing to do with the electron spin. In fact, electron spin is ignored in this discussion altogether (since the energy levels of the p_z electrons with different spin are assumed to be degenerate). However, the spin degree of freedom described here is called pseudo-spin, and it distinguishes the electrons belonging to the different sublattices of graphene.

The pseudo-spin of the electrons is directly proportional to the current operator

$$\boldsymbol{j} = \nu_F \boldsymbol{\sigma} \otimes \boldsymbol{\tau}_0. \tag{1.11}$$

Here, $\boldsymbol{\tau}_0$ is the 2×2 unit matrix, acting on the valley degree of freedom (while $\boldsymbol{\sigma}$ acts on the sublattice degree of freedom). The proportionality between pseudo-spin and current implies that the direction of motion of the charge carriers in graphene is directly tied to the direction of pseudo-spin, so that an electron moving in the x or y direction has a pseudo-spin pointing in the x or y direction. For this reason the electrons in graphene are called 'chiral'. This chirality of the electrons in graphene has some peculiar consequences, of which Klein tunneling is perhaps the most fascinating. In short, Klein tunneling allows an electron to continue to move in the same direction even as its momentum along the field lines of an electric field goes through zero and changes sign. This is achieved by making the transition from electron-like to hole-like dynamics. Since the chirality imposes the preservation of the group velocity upon this transition the tunneling probability is found to be 100%, resulting in zero backscattering [12].

1.2.3. Preparation. Research on freestanding graphene dates back to the work on mechanical exfoliated graphene by Novoselov *et al.* [7]. However, already before 2004 there was extensive research on intercalated graphite [13], graphene obtained by thermal decomposition of SiC [14, 15] as well as epitaxial graphene grown by chemical vapor deposition of hydrocarbons on metal substrates [16, 17]. Since the latter is the method used for graphene growth throughout this thesis research, it will be briefly reviewed here.

The advantage of growing graphene by chemical vapor deposition on a metal substrate is that the whole process can be done in an ultra-high vacuum (UHV) system. The metal substrate can thus be prepared prior to graphene growth to be atomically flat and completely clean. Since the metal substrate works as a catalyst for the graphene growth, the process is for most metals self-terminating, resulting in a flat, clean monolayer of graphene. The substrate that we use for growth is the iridium(1 1 1) surface, since it only weakly interacts with the graphene layer [18].

We use the temperature controlled growth method, adapted from the group of Michely [19, 20]. This allows us to tune the coverage of the substrate as well as the size of the graphene islands.

A clear trademark of graphene grown on metal surfaces is the formation of a moiré pattern. This is caused by the mismatch of the graphene periodicity (2.46 Å) with the periodicity of the underlying metal crystal (*e.g.* 2.73 Å for iridium). It is energetically favorable for the graphene to be, as much as possible, in registry with the underlying metal crystal. Therefore the graphene forms a buckled superstructure resulting in a moiré pattern with the underlying metal atoms [21]. Depending on the growth temperature the graphene can also grow in an angle with respect to the metal substrate, resulting in a change in the moiré periodicity due to an orientational mismatch [19]. Although the moiré pattern can be observed in the STM using current feedback [19] we found that it was often more pronounced in the simultaneously obtained frequency shift (Figure 1.3). As can be observed in Figure 1.3(b) the orientation of the moiré pattern is different for islands with a different orientation of the atomic lattice with respect to the underlying Ir lattice. For islands where the graphene lattice is perfectly aligned with the underlying Ir lattice, the moiré pattern will also be aligned with the graphene lattice and will have a periodicity of 2.5 nm [19]. The alignment of the islands on the iridium(1 1 1) lattice is tuned by the growth temperature. A higher growth temperature will result in larger islands with a smaller orientational distribution around perfect alignment. However, we also found that a higher growth temperature often leads to more defects. This is presumably caused by the growth of larger islands via attachment of smaller islands, while the grain boundaries are not completely annealed out.

1.3. Quantum confinement: from 3-D to 0-D

As already shown in the previous paragraph for the case of graphene, the position of the atoms inside a crystal has a large influence on the electronic properties of that crystal. This is caused by the wave character of quantum objects as expressed in the Bloch wave $e^{i\boldsymbol{k}\cdot\boldsymbol{r}}u_{\boldsymbol{k}}(\boldsymbol{r})$. Herein the electron state is expressed as a combination of a plane wave envelope function (describing the free electron) with a function that has the periodicity of the lattice. The advantage of using a Bloch wave is most readily understood if we consider the simple case of a 1-D crystal with lattice constant a (Figure 1.4). Suppose that every atom at position $x = na$

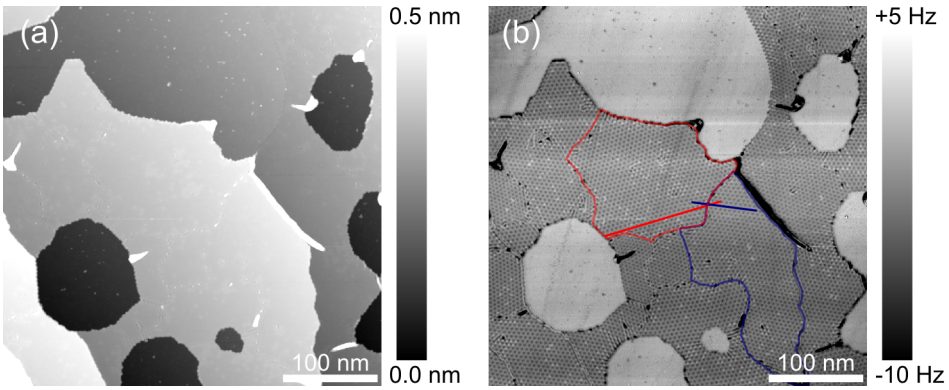

FIGURE 1.3. Graphene grown on iridium(1 1 1). (a) Constant current STM image of several graphene islands that are interconnected or growing out of a step edge in the iridium. The height profile clearly reveals the different terraces. (b) Simultaneously obtained frequency shift image, revealing a difference in tip-sample interaction over the moiré unit cell. This allows for easy identification of grain boundaries and differently oriented graphene islands (*e.g.*, for the grains marked blue and red the difference in orientation is indicated with lines parallel to the moiré pattern). Feedback parameters: 500 pA at 5 mV.

with $n = 0, \pm 1, \pm 2, ...$ contributes one electron. Ignoring the potential energy induced by the positive atomic cores, the energy dispersion $E(k)$ for a one electron state is given by $E = \hbar^2 k^2/(2m)$, *i.e.*, a parabola in k-space. The periodicity due to the crystal lattice in real space translates to a set of parabolas in k-space, separated by the reciprocal lattice vector $2\pi/a$. The unit cell in k-space centered around the $k = 0$ (Γ) point is called the first Brillouin zone. At the edges of the Brillouin zones, *i.e.*, at $k = n\pi/a$ with $n = \pm 1, \pm 3, \pm 5, ...$ the parabolas intersect, resulting in a degeneracy of the eigenvalues. This requires that the solution to the Schrödinger equation at the intersection is a superposition of both particular solutions (the individual parabolas). Ignoring potential variations, we can write the corresponding plane waves as

$$e^{i\pi x/a}, \quad \text{and} \quad e^{i[(\pi/a)-(2\pi/a)]x} = e^{-i\pi x/a}. \tag{1.12}$$

This results in a general solution at π/a consisting of the two linear superpositions

$$\begin{aligned} \psi_+ &\propto \left(e^{i\pi x/a} + e^{-i\pi x/a}\right) \propto \cos(\pi x/a)\,, \\ \psi_- &\propto \left(e^{i\pi x/a} - e^{-i\pi x/a}\right) \propto \sin(\pi x/a)\,. \end{aligned} \tag{1.13}$$

When visualizing the probability density of the two superpositions, we find that $\psi_+^*\psi_+$ corresponds to an increase of electron density on the positive atomic cores [minimum of the electrostatic potential $V(x)$] and thus to a lowering of the total energy, whereas $\psi_-^*\psi_-$ corresponds to an increase of electron density in between the atomic cores and thus to an increase in electron energy. The originally degenerate states at the edge of the Brillouin zone therefore split, creating a so-called band gap (E_g) in the energy dispersion (Figure 1.4).

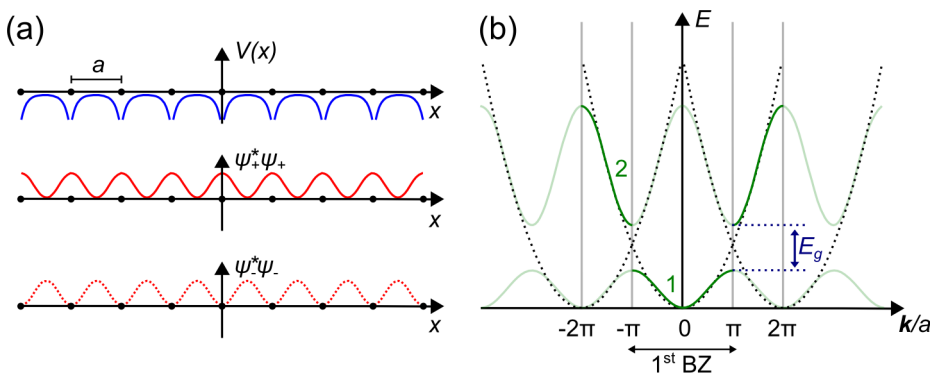

FIGURE 1.4. Band structure of a 1-D crystal. (a) A chain of atoms with potential $V(x)$. Bragg reflection at the atoms results in standing waves. The wave ψ_+ (top of band 1 in panel b) results in electron accumulation on top of the atoms. The next wave with wave vector $k = \pm\pi/a$ is ψ_-, corresponding to the bottom of band 2 in panel b. This wave results in electron accumulation in between the atoms. (b) Energy dispersion for the chain of atoms. The quadratic energy dispersion for a chain of free electrons is plotted with dashed lines. At the intersection of the free electron parabolas the degeneracy of the particular solutions is lifted by the effect of the atomic potentials on the superposition states. This results in a bending away from the intersection and the opening of a band gap E_g. Adapted from Reference [22].

Extending this concept to multiple dimensions is relatively easy, but the complexity of the shape of the Brillouin zones quickly increases with increasing complexity of the 3-D crystal structure. Therefore plots of the energy dispersion, or band structure plots, are often depicted along high symmetry directions in the Brillouin zone. These plots are insightful tools to show where certain energy states originate from, and to explain for example results from optical spectroscopy. For comparison with STM results however, a more useful way of representing the energy levels is a plot of the density of states (DOS). This quantity is inversely proportional to the gradient of the energy dispersion, resulting for the chain of atoms in a high DOS at the edges of the Brillouin zone. The DOS is given in units of Energy^{-1}Dimension^{-1} where Dimension = Volume, Area or Length for the 3-D, 2-D, and 1-D case, respectively. This dependency of the DOS on the dimensionality of the crystal brings us to the effect of quantum confinement.

Until now we considered crystals with infinite size. However, when we introduce crystal boundaries in one or more dimensions, the electron wave is confined between these boundaries. This results in an increase of the kinetic energy of the electron and a change from band-like energy dispersion to a more discrete spectrum. This effect is called quantum confinement.

One can think of quantum confinement as the additional kinetic energy that is needed to squeeze the electron wave function in the finite crystal. An estimate for the length scale at which quantum confinement becomes relevant can be obtained by comparing the energy of a free electron at room temperature, $E = k_bT = 25$ meV, to the energy for a particle confined in a 1-D box: $E = n^2h^2/8mL^2$. This gives us a confinement length of $L = (n^2h^2/8\ m\ E)^{0.5}$, or $\sim$ 4 nm for the ground state. For an electron in a crystal more complicated factors play a role, such as the effective mass of the electron. However, the length scale at which quantum confinement effects become essential is indeed $\sim$ 10 nm.

As stated above, the DOS depends on the dimensionality of the crystal. Quantum confinement in 1, 2, or 3 directions therefore results in very different shapes of the DOS. As an example in Figure 1.5 the general shape of the DOS for a macroscopic 3-D object (bulk material) is compared to that for a 2-D object (quantum well), a 1-D object (quantum wire) and a 0-D object (quantum dot). For a full derivation see [22].

In this thesis both discrete quantum dots as well as quantum dot ensembles will be discussed. Using the STM allows not only to measure the DOS of these objects of interest, but also to look how the energy states are spatially distributed

over the object. These measurements of the local density of states (LDOS) allow for a deeper understanding of the origin of electronic transitions or the reactivity of molecules. Confinement of the electron waves in quantum objects results in shapes similar to the atomic orbitals. Therefore these energy levels are often labeled S, P, D, etc.

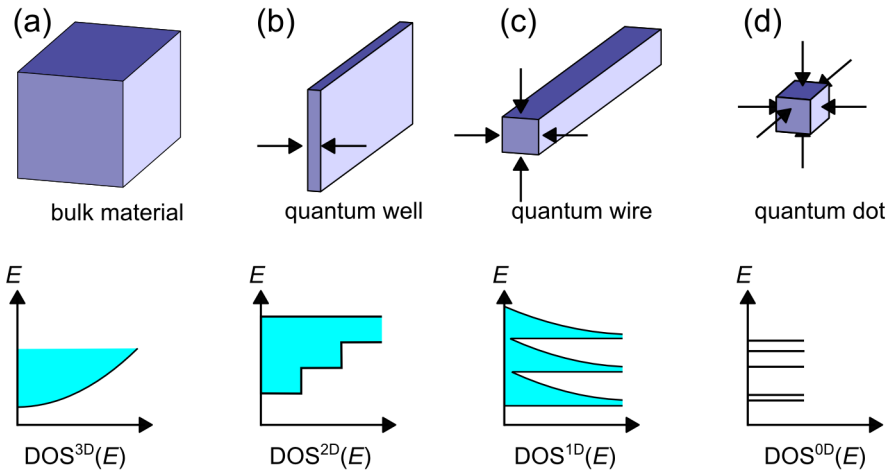

FIGURE 1.5. Effect of quantum confinement on the DOS. (a) In bulk materials the DOS depends on the square root of the energy, leading to smooth, continuous bands. (b) Characteristic for a 2-D quantum object such as a quantum well is a step-like DOS. (c) In quantum wires the bands already start to look like a set of discrete levels. (d) In quantum dots the DOS shows a set of discrete levels like the discrete spectrum of an atom. Adapted from Reference [22].

1.4. An introduction to scanning probe microscopy

The field of scanning probe microscopy (SPM) saw its birth with the first working scanning tunneling microscope, developed by Binnig and Rohrer at the IBM Research Laboratories in Zürich, Switzerland [23]. Soon, this invention was followed by that of the atomic force microscope (AFM) [24]. In addition to these two there is nowadays a broad family of SPM techniques, *e.g.*, Kelvin probe force microscopy, magnetic force microscopy, scanning near-field optical microscopy, and many others. All these techniques share some general features:

- An (atomically) sharp probe, or tip. The sharpness of the tip has a large impact on the image resolution.
- A surface of interest. The tip is brought in close contact (near field regime) to this surface of interest.
- An interaction between tip and sample that depends strongly on the tip-sample distance, *e.g.*, for STM the tunneling current and for AFM the forces between tip and sample. In combination with the sharpness of the tip, the slope of the tip-sample interaction determines the image resolution.
- An actuator with a high resolution. Typically, piezoelectric elements are used for this. The tip is then raster scanned over the surface. This is done either in constant height or using a feedback loop scheme to actuate the tip height in order to maintain a constant tip-sample distance. In the first case the tip-sample interaction is plotted to generate an image, whereas in the second the tip height is plotted to generate an image.
- Vibration isolation. When a tip is scanned over a sample at a distance of typically 1 nm with subatomic spatial resolution, the damping of external vibrations becomes very important. In the first working STM this was achieved by floating the entire stage using the Meissner effect [23]. At present more elegant solutions are used to consume less liquid helium (*e.g.*, a combination of springs, eddy current damping, etc.).

In the following two sections the two SPM techniques used throughout this thesis research are presented.

1.5. Scanning tunneling microscopy and spectroscopy

The STM operates on the principle of electron (hole) tunneling from one conductor to another. This immediately shows the largest drawback of STM: it is limited to (semi)conducting tips and substrates. However, the tunneling effect is exponentially dependent on the tip-sample distance, allowing for high image resolution. Also the dependence of the tunneling current on the applied bias can be used to infer the LDOS of the material, allowing for orbital imaging of molecules etc. In order to see where these features come from, let us consider a simple tunneling junction consisting of two metals separated by an energy barrier V that is larger than the kinetic energy of the electrons in the metals (Figure 1.6). In the metals the electron wave functions are described by a plane wave moving in the $\pm z$ direction, whereas in the barrier the wave function decays exponentially as the distance

to the nearest metal increases:

$$\begin{aligned}\psi_I(z) &= Ae^{ik_1 z} + A'e^{-ik_1 z},\\ \psi_{II}(z) &= Be^{k_2 z} + B'e^{-k_2 z},\\ \psi_{III}(z) &= Ce^{ik_3 z} + C'e^{-ik_3 z}.\end{aligned} \tag{1.14}$$

Since energy must be conserved during the tunneling event, the wave vectors for the two metals are the same: $k^2 \equiv k_1^2 = k_3^2 = 2mE/\hbar^2$. For the wave vector in the barrier we find $\kappa^2 \equiv k_2^2 = 2m(V-E)/\hbar^2$, showing that the higher the barrier V is with respect to the kinetic energy of the electron, the smaller the penetration depth of the exponential tail in the barrier, resulting in a smaller tunneling probability. This wave vector is from here on denoted as κ to show that it is a decay constant.

To get a measure for the tunneling probability we will consider the probability current $\boldsymbol{j} = 1/(2m)[\psi^* \boldsymbol{p}\psi - \psi \boldsymbol{p}\psi^*]$ with $\boldsymbol{p} = -i\hbar(\partial/\partial z)$ of the wave function in the regions I and III:

$$\begin{aligned}j_I &= \frac{\hbar k}{m}\left(A^2 - A'^2\right),\\ j_{III} &= \frac{\hbar k}{m}\left(C^2 - C'^2\right).\end{aligned} \tag{1.15}$$

Thus the probability current is logically determined by the difference in probability for traveling in the positive z direction $\left(A^2, C^2\right)$ and traveling in the negative

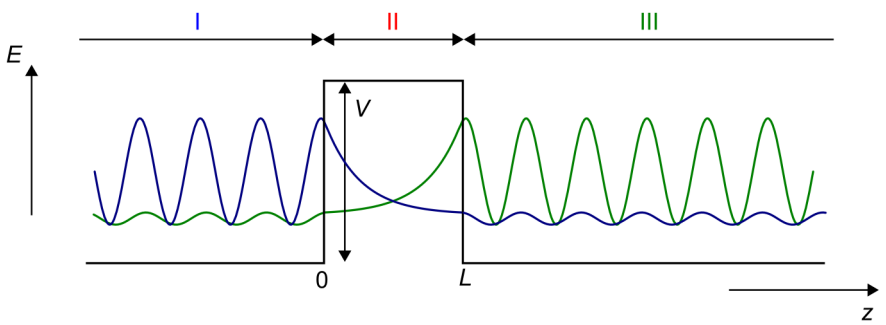

FIGURE 1.6. Electron (hole) tunneling. The wave function of electrons in the metal 'leak' with an exponentially decaying function outside the metals. Overlap of the exponential decaying tail with the metal across the gap results in a nonzero probability of tunneling, *i.e.*, the electron moving from left to right (blue) or *vice versa* (green). The tunneling probability is reflected in the ratio of the amplitudes before and after the tunneling event.

z direction $\left(A'^2, C'^2\right)$. We can express the transmission coefficient as the ratio between these two, considering either the positive or negative direction,

$$T = \frac{|C|^2}{|A|^2} = \frac{|C'|^2}{|A'|^2}. \tag{1.16}$$

This represents the probability of an electron tunneling from left to right or from right to left. Since there is no bias applied between the two metals the tunneling probability is equally large in both directions. The transmission coefficient can be solved exactly considering that both the wave functions and their gradients are continuous at the boundaries. The boundary conditions then allow to solve for A and C (or A' and C'), and thus for T:

$$T = \frac{1}{1 + \left(k^2 + \kappa^2\right)^2 / \left(4k^2\kappa^2\right) \sinh^2\left(\kappa L\right)}. \tag{1.17}$$

This solution is exact. However, if we consider a strongly attenuating barrier ($\kappa L \gg 1$) we can simplify to

$$T \approx \frac{16k^2\kappa^2}{\left(k^2 + \kappa^2\right)^2} \cdot e^{-2\kappa L}, \tag{1.18}$$

with the decay rate

$$\kappa = [2m(V - E)]^{\frac{1}{2}}/\hbar.$$

The strong exponential dependence of T on the barrier width L and the square root of the effective barrier height $(V - E)^{\frac{1}{2}}$ is typical for the tunneling process and independent of the exact shape of the barrier [25]. It is also the reason why the STM has an extremely high spatial resolution. If we take some reasonable experimental parameters and assume an effective barrier height of about 5 eV (*e.g.*, the work function for Cu or Au) and a typical tip-sample distance of 1 nm we find a value of 10^{-10} for the exponential part of T. Changing the tip-sample distance by 1 Å then results in a change of T by an order of magnitude, *i.e.*, bringing the tip closer over the diameter of an atom (± 3 Å) results in a thousandfold increase in the transmission coefficient. Therefore $> 99\%$ of the tunneling current will flow through the outermost atom of the tip. When studying (nearly) atomically flat surfaces, this implies that tip sharpness (beyond the frontier atoms) is not very important in STM.

Since the transmission T is quite small, another useful way of describing the tunneling phenomenon is to use perturbation theory. Bardeen [26] proposed to do this using two complete orthonormal systems of wave functions, each residing on one of the metals (the green and blue wave functions in Figure 1.6). The overlap

of these two wave functions can then be treated as a small perturbation using a transfer Hamiltonian H_T which describes electron tunneling from the initial state to the final state [27]. This can be expressed in the form of a tunneling matrix element

$$M_{i\to f} = \int \psi_i^* H_T \psi_f \, \mathrm{d}z. \tag{1.19}$$

Using Fermi's golden rule we can then calculate the tunneling current. This depends on the transmission coefficient (which we find back in the form of the tunneling matrix element), but also on the density of states of both the metals. Considering a fixed number of initial states and a constant transmission coefficient, the tunneling current can intuitively be understood to scale linearly with the number of degenerate final states. *Vice versa*, considering a fixed number of final states the tunneling current can be understood to scale linearly with the number of degenerate initial states. Besides changing the degeneracy, we can also change the number of accessible states by applying a bias V between the two metals. Assuming that the DOS of the two metals does not vary considerably near the Fermi level within the range of the applied bias voltage, the tunneling current is then given by (for a more thorough derivation see [28])

$$I = \frac{2\pi e^2}{\hbar} \left|M_{i\to f}\right|^2 \rho_f(E_{F,final})\rho_i(E_{F,initial})V. \tag{1.20}$$

The first important observation to make here is that the tunneling current in principle behaves Ohmic, *i.e.*, the current depends linearly on the applied bias. The second is that the tunneling current depends on the DOS of both metals. This means that in STM, one in principle measures the convolution of the DOS of both sample and tip. Since it is difficult to know the tip states, Tersoff and Hamann presented a widely applied model to take these out of the problem [29, 30]. The model represents the tip as a locally spherical potential well, allowing to describe it as a geometrical point at the center of curvature of the tip ($\boldsymbol{r}_0$). This allows to describe the tunneling matrix element $M_{i\to f}$ as the sum of all sample wave functions (*i.e.*, the sample DOS) at $\boldsymbol{r}_0$. This means that, except for the s-wave tip wave function, all other tip wave functions can be neglected. The s-wave-only assumption is estimated to hold for feature sizes $\gtrsim$ 0.3 nm [28].

The Tersoff–Hamann model has proven extremely useful in the interpretation of STM images, since it shows that the STM measures the electronic states of the surface, rather than the atomic corrugation directly. Tersoff and Hamann showed that their model can also be extended to the case of finite bias voltages, assuming that in the energy range of interest:

- the tip state is spherically symmetric, as discussed above;
- the tunneling matrix element does not depend on energy level;
- the tip DOS can be treated as a constant;
- the sample DOS does not change significantly with respect to kT.

First we describe the tunneling current from the tip (initial state) to the sample (final state) at a bias voltage V by summing over all relevant states. Assuming that the electrons in both metals follow the Fermi distribution and approaching that Fermi distribution with a step function, we can write Equation 1.20 as [28]

$$I = \frac{4\pi e}{\hbar} \int_0^{eV} |M_{t\to s}|^2 \, \rho_s(E_{F,sample} + \epsilon)\rho_t(E_{F,tip} - eV + \epsilon)d\epsilon. \tag{1.21}$$

Using the assumptions above and the Tersoff–Hamann definition for the tunneling matrix element we can take both ρ_t and $|M_{i\to f}|$ out of the integral. When realizing that we now probe the local density of states of the sample at the center of curvature of the tip ($\boldsymbol{r}_0$), we are left with

$$I \propto \int_0^{eV} \rho_s(E_{F,sample} + \epsilon, \boldsymbol{r}_0)d\epsilon. \tag{1.22}$$

When differentiating with respect to V, we find the dynamic tunneling conductance at bias voltage V to be

$$\frac{dI(V)}{dV} \propto \rho_s(E_F + eV, \boldsymbol{r}_0). \tag{1.23}$$

This shows that STM is capable of measuring the LDOS of the sample via the tunneling conductance. In order for the above assumptions to be true in the experiment, the tip DOS is preferably as flat as possible. This is tested by measuring well-known features, *e.g.*, metal surface states. If the tip DOS is not perfectly flat, it is often sufficient to perform a simple background subtraction using spectra recorded on the substrate, away from the object of interest [31].

Having established the theoretical origin of the high resolution and LDOS imaging capability of the STM, we can look at a *Gedankenexperiment* where this can be used, *e.g.*, the well-known particle in a 2-D box problem. We assume a square box with sides a confining an electron. The walls are defined by a step potential going from 0 to ∞. The electron obeys the time-independent Schrödinger equation

$$-\frac{\hbar^2}{2m}\left(\frac{\partial^2}{\partial x^2} + \frac{\partial^2}{\partial y^2}\right)\psi = E\psi. \tag{1.24}$$

This partial differential equation can be solved using the *ansatz*

$$\psi = A\sin(k_x x)\ \sin(k_y y).$$

Boundary conditions demand that $k_{x,y} = n_{x,y}\pi/a$. This results in an energy spectrum of

$$E(n_x, n_y) = \frac{h^2}{8ma^2}\left(n_x^2 + n_y^2\right). \tag{1.25}$$

The energy spectrum and probability density plots for the first four energy levels are presented in Figure 1.7.

Now the full capability of the STM can be presented. First of all, the STM is in principle able to resolve the object that confines the electron (the 2-D box). Secondly, the STM can be used to probe the energy spectrum by means of measuring the tunneling current, or the conductance as a function of bias voltage. In addition, since STM is a local technique, it also allows to resolve the energy spectrum spatially. We could, for example, measure the conductance at an energy (bias) of $E = 5\,h^2/8ma^2$ at different positions in the box, and find that there would be hardly any conductance in the center of the box.

The conductance is not measured by simply applying a bias V. Doing so would result in a current composed of the integrated conductance over all states between $E = 0$ and $E = eV$, rather then a measurement of the conductance at $E = eV$.

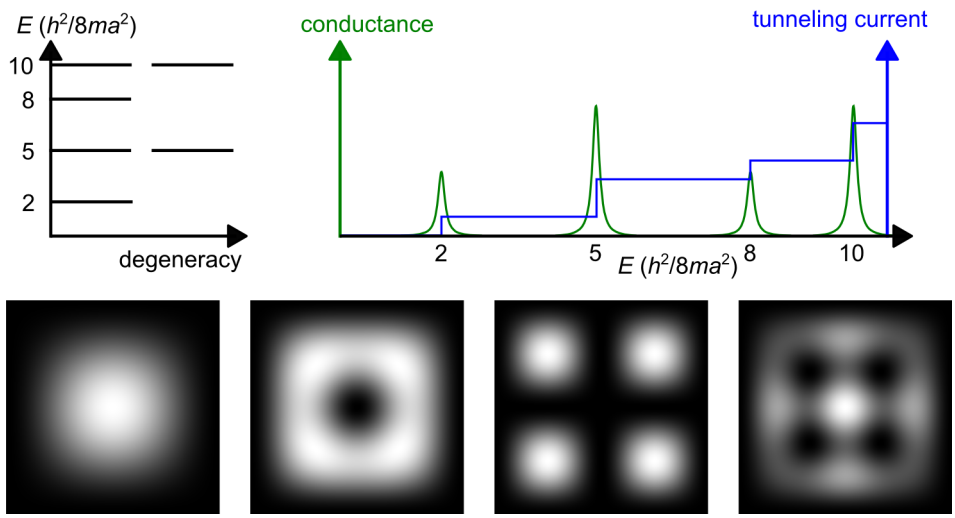

FIGURE 1.7. Energy spectrum for a particle in a square box. The degeneracy of the energy levels dictates the height of the step like increase in the tunneling current and the peaks in the conductance. The bottom row shows the probability density function for the first four energy levels.

Instead, conductance measurements are done using a lock-in technique. The bias is modulated around V, and the resulting modulation of the tunneling current I is measured. This modulation is directly proportional to the conductance dI/dV at that bias V. Furthermore, since $dI/dV \propto$ DOS (Equation 1.23), we can map the spatial distribution of the probability function, *i.e.*, the LDOS, for the different energy levels.

1.6. Atomic force microscopy and chemical force spectroscopy

In the same year that Binnig and Rohrer received the Nobel prize for their invention of the STM, Binnig, Quate, and Gerber presented the first AFM [24]. The choice for force as a feedback parameter between tip and sample broadens the scope enormously with respect to STM. Not only is this technique applicable for non-conducting samples and tips, but also force itself is a much more universal concept in nature. The AFM is therefore applied in a wide variety of force measurements, *e.g.*, frictional forces [32], electrostatic forces [33], chemical forces [34], magnetic forces [35], etc. For this reason the technique has been widely received and adapted for use in various sample environments, ranging from in vivo biological applications [36] to harsh reactor conditions [37]. The first and foremost application however remains the measurement of interatomic forces.

Looking at atomic scale interactions the most important forces are the van der Waals forces, Pauli (or hard-core) repulsion, ionic bond formation, and covalent bond formation. Here, we will shortly address these forces:

- The van der Waals forces can be subdivided into the forces between permanent dipoles (Keesom), a permanent dipole and a corresponding induced dipole (Debye), and two instantaneously induced dipoles (London dispersion). Since atoms rarely carry a permanent dipole, the first two forces typically only play a role on the molecular scale, *e.g.*, for hydrogen bonding. In contrast, the London dispersion force is relevant at the atomic scale. It accounts for the correlated movement of electrons of interacting atoms. Quantum mechanically this can be described as a second-order perturbation effect on the Hamiltonian of the total system. This then results in a weak attractive force proportional to r^{-6} where r is the distance between the interacting atoms. The London dispersion effect can be pictured as an instantaneous rearrangement of the electron density of one atom in response to fluctuations in the electron density of another atom close by. It does not require wave function overlap and can therefore be considered as long-range. Although quite weak, the London dispersion force is additive. Therefore it gives

a strong contribution to the total interaction energy in condensed matter. For example, when modeling an AFM tip with local radius of curvature r_c above a flat surface, a volume integral over the London dispersion interaction results in [38]

$$U = -\frac{Hr_c}{6r}, \tag{1.26}$$

with r the tip-sample distance and the Hamaker constant for metals $H \cong 2$–3 eV. Considering that in a typical experiment both the tip-sample distance and the tip curvature are of the order of a nanometer, the resulting interaction is a few hundreds of meV.

- The Pauli repulsion is a repulsive force arising from the Pauli exclusion principle. It acts on atomic distances, when the electron cloud of two atoms starts to overlap. It stems from the fact that no pair of fermions (*e.g.*, electrons) can have an identical set of quantum numbers, *i.e.*, there are not more than two isoenergetic electrons (both with different spin) that can occupy the same space at the same time. This purely quantum mechanical problem cannot be solved analytically, and therefore lacks a general mathematical expression. However, it is described by a number of empirical potential functions. Chemists usually use the repulsive part of the Lennard–Jones potential

$$U = U_0 \left(\frac{r_e}{r}\right)^{12}, \tag{1.27}$$

where r_e and U_0 are the equilibrium distance and associated energy minimum of the full Lennard–Jones potential. Physicists usually prefer the repulsive part of the Morse potential

$$U = U_0 e^{-2\beta(r-r_e)}, \tag{1.28}$$

where β is a decay constant determining the slope of the repulsive potential. In both cases it is a short range, repulsive force that depends strongly on small changes in distance.

- Ionic bond formation takes place between ions with opposite charge, and is therefore an electrostatic effect. Although not as strong as a covalent bond, ionic bond formation is much stronger than the van der Waals interactions. Since electrostatic interactions are long range, ionic bond formation in crystals is usually described in terms of empirical parameters depending on the crystal's structure. As ionic bond formation is not relevant for the work in this thesis, the interested reader is referred to the standard condensed matter textbooks, *e.g.*, [39].

- A covalent bond is the strongest bond between atoms. The bond arises from shared electron pairs, and it is labeled by its symmetry in a similar way as

the atomic orbitals *e.g.*, a σ bond has zero nodal planes, a π bond has one nodal plane, etc. Quantum mechanically the nature of the covalent bond can be thought of as the arising of resonant states by coupling of the two separate wave functions of the individual atoms. This would result in a resonant state with lower energy (bonding) than the energy of the separate wave functions, and a resonant state with higher energy (antibonding) than the energy of the separate wave functions. Depending on the electron occupation, the energy can then be lowered with respect to the energy of the individual wave functions, resulting in bond formation. In quantum chemistry this concept is usually known as the 'linear combination of atomic orbitals' theory. Covalent bonding requires wave functions to overlap, and therefore is in the distance regime between van der Waals attraction and Pauli repulsion (see also Figure 1.8). When looking deeper into covalent bond formation, a surprising fact turns up: the resonance energy between the bonding atoms can in fact be described with a tunneling matrix element. This implies a correspondence between covalent bond formation and the Bardeen theory of tunneling, and thus STM and AFM. For a more in depth analysis of this correspondence see [28, 40–42].

The different forces and their distance dependence are compared in Figure 1.8 for the case of the hydrogen molecule (H_2). The resonance interaction (covalent bond formation) is calculated using the LCAO method with the hydrogen atom 1s wave functions as input and including configuration interaction, following reference [43]. This results in a reasonable agreement with the experimental data — the energy minimum is underestimated by ~ 1.5 eV, and the bond length is slightly overestimated [44]. The van der Waals interaction energy between two hydrogen atoms is calculated (according to [45]) for comparison. It shows a significant contribution to the total interaction in the long-distance regime, but does not give an accurate description anymore when the wave functions start to overlap. Here, the potential is better described by the resonance interaction between the two atomic H wave functions. This results in bond formation if the wave functions are in resonance ($^1\Sigma_g^+$). However, if we would excite the electrons from the ground state to the triplet state $^3\Sigma_u^+$, the molecule would break apart — showing that the van der Waals description breaks down at these short distances. Finally when bringing the atoms closer than 0.1 nm the Pauli repulsion starts to contribute, and quickly takes over when the atoms are compressed beyond their bond length (~ 0.8 Å). The two empirical approximations to the Pauli repulsion as discussed above are plotted. For the repulsive part of the Lennard–Jones potential the U_0 and r_e from the bonding orbital obtained by the LCAO method were used as input. For the

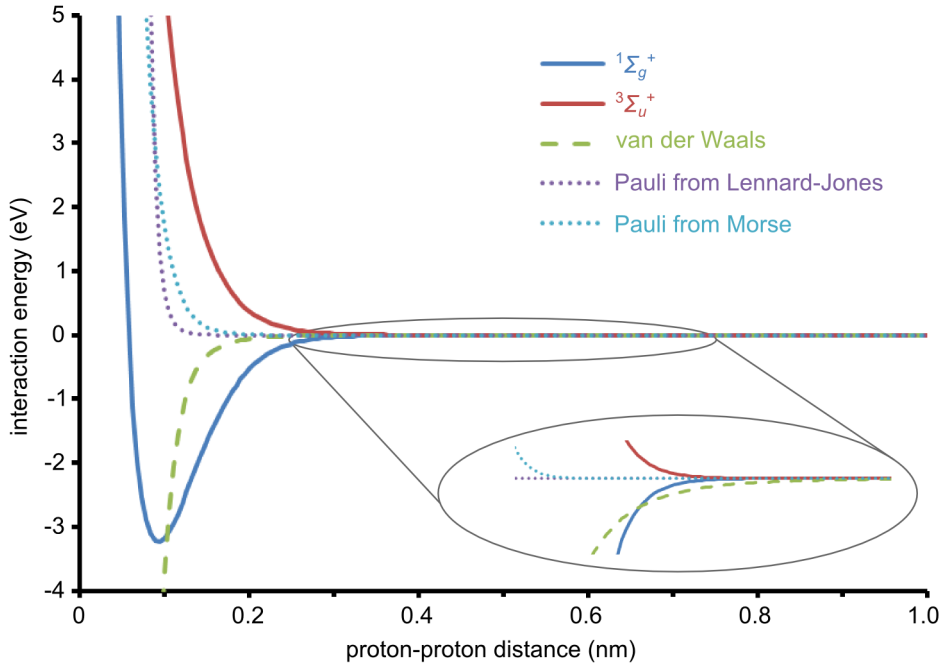

FIGURE 1.8. Interaction energy for the hydrogen molecule (H_2). A LCAO treatment results in a reasonable approximation for the lowest bonding ($^1\Sigma_g^+$) and antibonding ($^3\Sigma_u^+$) molecular orbitals [43]. The van der Waals (London) interaction dominates in the long-range regime ($r > 0.5$ nm). In the range $0.1 < r < 0.5$ nm, the resonance interaction (covalent bond formation) dominates. For distances $r < 0.1$ nm, the Pauli repulsion starts to contribute.

repulsive part of the Morse potential the decay constant was obtained by fitting the full Morse potential to the bonding orbital obtained by the LCAO method. This resulted in an overestimation of the spring constant for H_2 by a factor of two.

Knowing the forces relevant in AFM, we can consider the principle of operation. The AFM has all the general SPM features as described in Section 1.4. However, in an AFM the tip itself is mounted on a cantilever, allowing for it to be actuated. The actuation of the cantilever carries the signal of the interaction between the tip and sample. This signal can be recorded by different means. In the original AFM an STM tip was placed on top of the cantilever, and the change

in tunneling was recorded [24]. Nowadays the actuation of the cantilever is mostly measured by means of laser deflection. However, in the QPlus setup that is mainly used throughout this thesis, the signal is recorded using the piezoelectric response of a quartz cantilever.

The AFM can be operated in a static and a dynamic mode. In the static mode the tip basically acts as a profiler. The tip is dragged over the surface and the forces acting on the tip result in a deflection of the cantilever. In dynamic mode the cantilever is excited at or near its resonant frequency. When the oscillating tip is brought in close contact with the surface, the interaction between tip and sample will affect the oscillation. This can be monitored either in terms of the change in amplitude (amplitude-modulated, or tapping mode AFM), or in terms of the change in frequency (frequency-modulated, or non-contact AFM). Generally speaking, tapping mode AFM gives better results in ambient conditions, whereas non-contact AFM excels in UHV conditions. For a more detailed comparison see [46]. Here, we will only present results obtained by non-contact AFM, using QPlus sensors with a typical resonance frequency f_0 of ~ 25 kHz and quality factor Q of the order of $10\text{–}15\times10^3$.

The non-contact mode of operation of the AFM can be understood when picturing the force between tip and sample (F_{ts}) in terms of Hooke's law. A change in force then results in a change in the associated spring constant k_{ts}. Following the reasoning of Giessibl [46], we can then describe the motion of the cantilever $z'(t)$ (see also Figure 1.9) by a weakly perturbed harmonic oscillator with the Hamiltonian

$$H = \frac{p^2}{2m^*} + \frac{kz'^2}{2} + V_{ts}(z), \tag{1.29}$$

where z' is the deviation of the cantilever from its rest position, k is the force constant of the cantilever with effective mass m^*, and V_{ts} is the tip-sample interaction energy. The unperturbed motion of the cantilever is

$$z'(t) = A\cos(2\pi f_0 t), \tag{1.30}$$

with amplitude A and resonance frequency

$$f_0 = \frac{1}{2\pi}\sqrt{\frac{k}{m^*}}. \tag{1.31}$$

A quadratic potential V_{ts} (or constant k_{ts}, since $k_{ts} = -\partial F_{ts}/\partial z = \partial^2 V_{ts}/\partial z^2$) results in a constant frequency shift

$$\Delta f = f_0 \frac{k_{ts}}{2k}. \tag{1.32}$$

However, k_{ts} can vary considerably over one oscillation amplitude (*e.g.*, compare with Figure 1.8). Therefore Giessibl [47] used first-order perturbation theory to show that

$$\Delta f = -\frac{f_0}{kA^2} \langle F_{ts} z' \rangle \,, \tag{1.33}$$

where the brackets indicate an average over one oscillation cycle. The first-order perturbation theory is valid as long as the energy of the oscillating cantilever is larger than V_{ts}, which usually is the case [46].

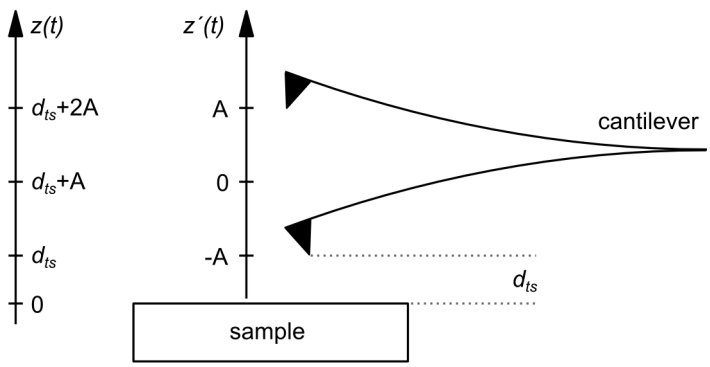

FIGURE 1.9. Scheme of an oscillating cantilever with amplitude A in coordinates relative to the sample $z(t)$ and relative to the equilibrium position of the tip $z'(t)$. Adapted from Reference [47].

Using integration by parts, Equation 1.33 can be rewritten to express the change in frequency as a function of tip sample distance [48]:

$$\Delta f(z) = \Delta f = f_0 \frac{\langle k_{ts}(z) \rangle}{2k}. \tag{1.34}$$

This function closely resembles Equation 1.32, however it includes a weighted average over k_{ts} in the form of semicircle with amplitude A as radius

$$\langle k_{ts}(z) \rangle = \frac{2}{\pi A^2} \int_{-A}^{+A} k_{ts}(z - z') \sqrt{A^2 - z'^2} \, \mathrm{d}z'. \tag{1.35}$$

This implies that amplitude determines what forces (length scales) you are sensitive to. This can intuitively be understood, considering that the gradient of the forces relevant in AFM is much stronger at close distance (Figure 1.8). Therefore the contribution of forces from different atoms in the sample are easier to distinguish at small tip-sample distance than at large tip-sample distance. When using

small oscillation amplitudes we mainly probe forces at small tip-sample distances, and thus have a better sensitivity to short-range forces, *e.g.*, chemical forces.

In the experiments described in this thesis, oscillation amplitudes of the order of 0.5–1 Å (single peak) were used. These can be reached due to the high stiffness of the quartz cantilevers used. Typical frequency shifts measured are of the order of 1–100 Hz. For constant force measurements the frequency shift Δf is used as input for a feedback loop. However, since the interaction between tip and sample is not monotonic (see Figure 1.10) a constant force measurement can only be performed in certain tip-sample distance regimes, and only on samples where the tip-sample interaction does not change drastically as a function of lateral position. For samples where the reactivity does change significantly with position, or for measurements at tip-sample distances where the gradient of the $\Delta f(z)$ curve changes sign, a feedback loop mechanism will be unable to regulate the tip height. An attempt to do so anyway often results in either the tip totally retracting itself from the sample, or crashing itself into the sample. Therefore, experiments on such samples or at such tip-sample distances are usually performed in constant height mode. In this mode the feedback loop is disconnected and the Δf itself is mapped as a function of lateral position to generate the image.

Positioning the tip above a specific feature on the sample, the frequency shift can also be measured as a function of tip-sample distance. This allows for force spectroscopy: after a long range $\Delta f(z)$ curve is recorded, it can be integrated using Equation 1.34 to obtain a force-distance curve, or after double integration the corresponding potential curve. As an example of how such a spectrum would look, Figure 1.10 shows a theoretical $\Delta f(z)$ curve. The H_2 potential (Figure 1.8) was used as input. The tip is represented by one of the hydrogen atoms, and the sample by the other hydrogen atom. The tip-sample distance is then in fact the binding axis of the H_2 molecule. Assuming an infinitesimally small oscillation amplitude and a tip with resonant frequency $f_0 = 25$ kHz and spring constant $k = 2000$ N/m, the $\Delta f(z)$ curve is readily obtained via Equation 1.32. The combination of the quite deep H_2 potential and the assumption of an infinitesimally small oscillation amplitude results in a $\Delta f(z)$ that is about an order of magnitude deeper than measured in experiments. What is also not taken into account in Figure 1.10 is the contribution of the van der Waals forces. This usually results in an even slower rise of the tail of the $\Delta f(z)$ curve, only reaching zero after a couple of nanometers. However, the shape of the curve in the covalent bond formation regime provides a realistic model for measurements with a reactive tip. Since the depth of the

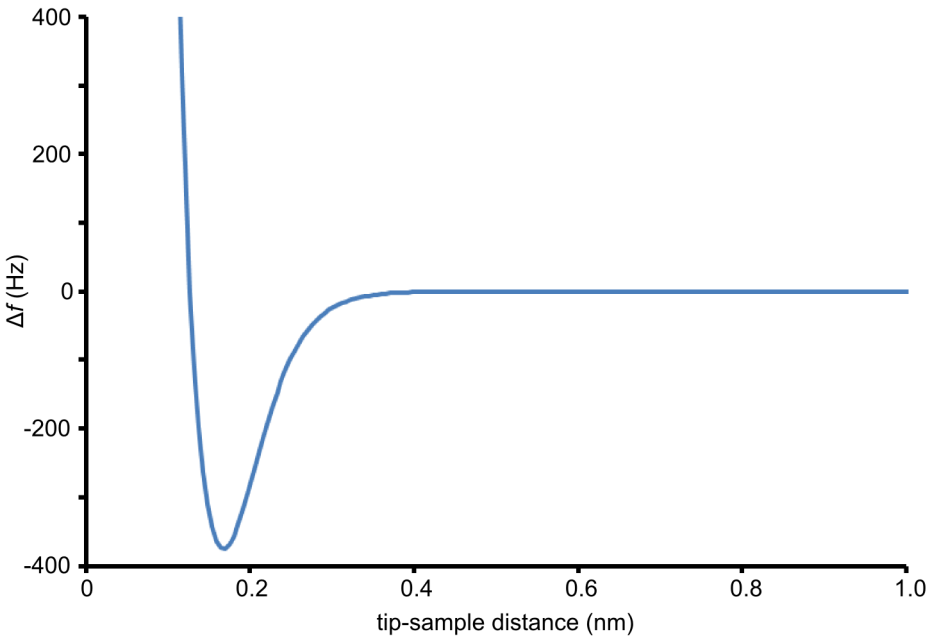

FIGURE 1.10. Simulated frequency shift spectrum on basis of the H_2 potential from Figure 1.8, assuming a tip with resonant frequency $f_0 = 25$ kHz and spring constant $k = 2000$ N/m and an infinitesimally small oscillation amplitude.

curve is related to the bond strength of the outermost atom of the tip with the atom of the sample underneath, this method allows for chemical identification of atoms [49]. Therefore, the force spectroscopy in this distance regime is usually referred to as chemical force spectroscopy.

A final note on AFM is that the depth of the $\Delta f(z)$ curve, and therefore the image contrast, depends on the reactivity of the tip. This can be utilized to enhance the Δf contrast by measuring with reactive metal tips. However, this is only possible if the molecules that are studied are bound to the surface strongly enough to avoid accidental pickup by the reactive tip (*i.e.*, due to bond formation between molecule and tip). When studying molecules that are not strongly bound to the surface, it is recommendable to use tips that are first functionalized with nonreactive species such as CO molecules [50]. The frequency shift spectra for such nonreactive tips have a different shape from the one presented in Figure 1.10, since

for nonreactive tips only van der Waals interaction and Pauli repulsion between tip and sample play a role, *i.e.*, to first order there is no chemical bond formation.

1.7. Electron microscopy, tomography, and computer-aided image analysis

Transmission electron microscopy (TEM) is probably the most used imaging technique in nanomaterials sciences. It is therefore no coincidence that when Binnig and Rohrer received the Nobel prize in 1986, they had to share it with Ernst Ruska for his work on the TEM. In its most basic form the TEM is very similar to an optical microscope ('light microscope'). The important difference is that an electron beam rather than a light beam is used to probe the sample. The wavelength of electrons is much smaller than the wavelength of light: electrons with an energy > 1.5 eV already have a wavelength < 1 nm. And since the maximum resolution in far field microscopy is determined by the diffraction limit $d \approx \lambda/2$, electron microscopy allows for sub-nanometer resolution, whereas ordinary optical microscopy is limited to several hundreds of nanometers.

The design of the transmission electron microscope is very similar to that of the optical microscope: an electron gun is used as 'light' source, after which a condenser lens is used to make the beam parallel. Then the beam is guided through a thin ($< \mu$m) specimen, collected by an objective lens and finally projected on a fluorescent screen or ccd camera. Image contrast is generated by scattering of the electrons by thicker parts of the sample, or by heavier elements in the sample. Imaging can be done in bright field or in dark field mode. In bright field mode the transmitted beam is recorded, resulting in scatterers being displayed as dark objects in a bright background. In dark field mode only the scattered electrons are recorded, resulting in the scatterers being imaged as bright objects in a dark background.

The transmission electron microscope can also be operated in a scanning mode (STEM). In this mode the electron beam is focused by an objective lens before going through the sample. The focal point of the beam is then raster scanned over the sample, and the transmitted or scattered signal is recorded. This allows for chemical mapping of the surface by means of energy dispersive X-ray (EDX) or electron energy loss spectroscopy (EELS). It also allows for annular dark field imaging, where the scattered beam is recorded by an annular detector. The contrast in dark field images is strongly influenced by the scattering mechanism. At relatively low scattering angles Bragg diffraction will dominate. This allows for

crystallographic analysis, either by just recording the electron diffractogram (ED) in the back focal plane, or by selecting certain scattering angles for dark field imaging. When recording electrons incoherently scattered at high angle, the dark field images are very sensitive to the scattering strength of the elements imaged. In this high-angle annular dark-field imaging (HAADF) STEM mode, the images have high contrast between chemical elements with different scattering strength.

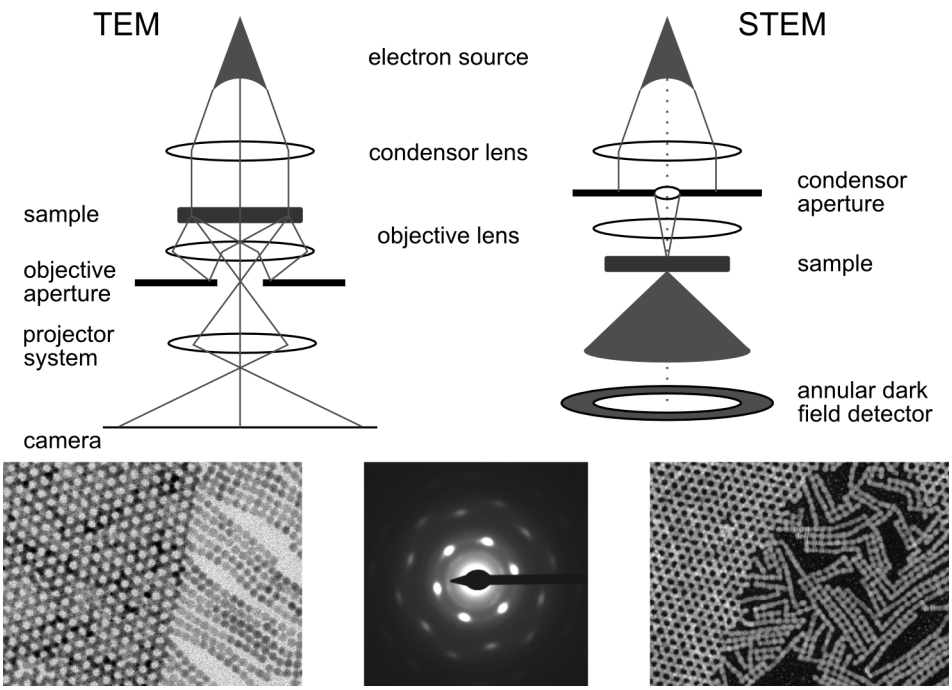

FIGURE 1.11. Schematic beam path in a transmission electron microscope and in a scanning transmission electron microscope equipped with an annular dark field detector. Bottom row shows images obtained in bright field mode (left) and dark field mode (right). The images depict oriented attachment of nanocrystals in honeycomb and string like fashion. The middle image shows an electron diffractogram obtained on a patch of nanocrystals packed in a honeycomb lattice. The clear spots originate from Bragg diffraction at, amongst others, the $\{2\bar{2}0\}$ crystal lattice planes of the nanocrystals, showing that the nanocrystals are atomically aligned. Adapted from Reference [51].

The main drawback of TEM is that the obtained images are a 2-D projection of a 3-D object. A way around this problem is the use of electron tomography. Here, transmission images are obtained at different incident beam angles by rotating the sample. In this way a tilt series of transmission images is obtained. According to the projection-slice theorem [52] the Fourier transform (FT) of each transmission image should be equal to a slice through the FT of the 3-D object at the incident beam angle. This implies that we can build the 3-D FT by combining the 2-D FTs over their respective tilt angles. Afterwards we can then reconstruct the 3-D image in real space by means of back projection algorithms [51]. A schematic illustration of this method is given in Figure 1.12.

A limiting factor in tomography is the incident beam angle. At high rotation angles the pathway of the beam through the sample becomes very large, resulting in decreasing contrast due to lack of transmission. High rotation angles may also lead to shadowing of the object of interest by the tomography holder or the TEM grid. For this reason tilt angles are usually restricted to ± 60–$70°$. This results in artifacts in the reconstruction in the direction of this missing 'wedge' of tilt angles, *e.g.*, elongation of objects in that direction (Figure 1.12). These artifacts greatly hamper computer-aided particle detection.

When a 3-D image of the object is reconstructed it contains all kind of information such as particle sizes, positions, and orientations. The images studied in this thesis often contain several hundreds of nanocrystals, making it impossible to extract all the information from the image by simply looking at it. Therefore computer-aided image analysis methods are applied to the reconstruction. The first step in such an analysis is the particle detection. In this thesis, this is done using image filtering by means of cross correlation. First a template object is constructed (*e.g.*, a dark sphere in a bright background). Then the cross-correlation of the 3-D reconstruction with the template is calculated. High correlation volumes then give a good approximation for the position of the particle. To account for size dispersion the analysis is done multiple times with a varying template size. The correlations are averaged and a cut off is applied. The coordinates of the nanoparticles are then recorded as the position of the center of mass of the high correlation volumes. Once the particle positions are obtained, further analysis can be done, *e.g.*, size determination by means of radial averaging of the intensity around the center position, crystal structure detection, etc. [53].

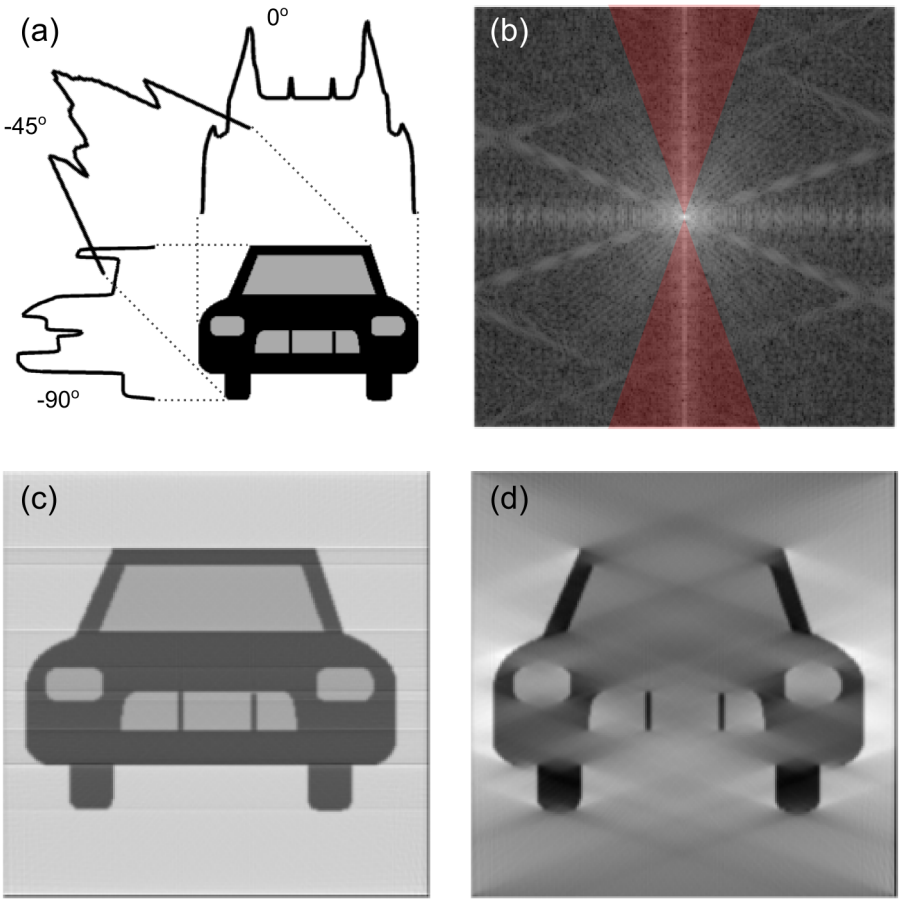

FIGURE 1.12. A 2-D schematic of the electron tomography technique. (a) Tilt series of transmission images in 2-D would result in line profiles of the transmission. (b) These line profiles can then be combined into a 2-D FT. Also indicated is the missing wedge (red), assuming a tilt series from ±70°. (c) The reconstruction of (b) using a simple back projection algorithm, resulting in the original image. (d) The reconstruction of (b) when excluding the missing wedge from the reconstruction algorithm. This results in artifacts looking like an elongation of the reconstructed objects.

1.8. LEED as a tool to probe surfaces in *k*-space

As already mentioned in Section 1.7, the scattering of an electron beam on a surface can provide information on the crystal structure of that surface. This is utilized in so-called low-energy electron diffraction (LEED) experiments, where a crystal surface is bombarded with electrons with an energy of typically 10–1000 eV [39]. The incident electrons then scatter on the crystal structure according to Bragg's law:

$$n\lambda = 2d\sin(\theta) \qquad (n = 1, 2, 3, \ldots). \tag{1.36}$$

Here λ is the wavelength of the electron, d is the distance between the crystal lattice planes, and θ is the angle of incidence. The typical energy range of 10–1000 eV results in an electron wavelength of 0.4–4 Å. This is a low enough wave length to probe atomic crystal lattices while still allowing for an energy low enough to only probe the outermost atomic layers. The scattering in this low energy regime is dominated by inelastically scattered electrons. However, these can easily be filtered on energy, allowing to record the scattering pattern originating from elastic collisions only. Scattering patterns obtained in this way look very similar to the ones obtained using electron diffraction in the TEM, see *e.g.*, Figure 1.11. Due to the low energy, the signal is dominated by collisions with the outer most atomic layers. This makes LEED an excellent tool to study surface reconstructions, oxides, or epitaxial overgrowth layers (*e.g.*, graphene). LEED can also be used as a quantitative technique, allowing to extract the full crystallographic data (*i.e.*, unit cell) of the outer most layers. This is done by measuring the intensity of the diffraction spots as a function of incident electron energy: LEED *I(V)*. There are several sophisticated methods to compare these curves to theoretical scattering curves, allowing for geometrical optimization of the theoretical unit cell [54–56]. In Chapter 3 we use this technique to reconstruct the full moiré unit cell for graphene on Ir(1 1 1). In order to perform this geometrical optimization, we need to describe the scattering potential relevant to LEED. A full description of this scattering potential is however unfeasible, since we would need to include the electrostatic contributions from all the atomic nuclei and electrons, including any exchange-correlation effects. Fortunately, LEED is dominated by scattering from the ionic cores rather than from the valence electrons [57, 58]. This allows us to describe the scattering potential with a 'muffin-tin' model, *i.e.*, using a potential like the one in Figure 1.4(a). A geometrical optimization is now feasible since the contribution of a single atom to the potential, once calculated, is mostly insensitive to the proximity of nearby atoms.

1.9. Bibliography

[1] Wallace, P. The band theory of graphite. *Physical Review* **71**, 622–634 (1947).

[2] McClure, J. W. Diamagnetism of graphite. *Physical Review* **104**, 666–671 (1956).

[3] DiVincenzo, D. P. & Mele, E. J. Self-consistent effective-mass theory for intralayer screening in graphite intercalation compounds. *Physical Review B* **29**, 1685–1694 (1984).

[4] Semenoff, G. W. Condensed-matter simulation of a three-dimensional anomaly. *Physical Review Letters* **53**, 2449–2452 (1984).

[5] Mermin, N. D. Crystalline order in two dimensions. *Physical Review* **176**, 250–254 (1968).

[6] Saito, R., Dresselhaus, G. & Dresselhaus, M. S. *Physical properties of carbon nanotubes* (Imperial College Press, London, 1998).

[7] Novoselov, K. S. *et al.* Electric field effect in atomically thin carbon films. *Science* **306**, 666–669 (2004).

[8] Novoselov, K. S. *et al.* Two-dimensional gas of massless Dirac fermions in graphene. *Nature* **438**, 197–200 (2005).

[9] Zhang, Y., Tan, Y.-W., Stormer, H. L. & Kim, P. Experimental observation of the quantum Hall effect and Berry's phase in graphene. *Nature* **438**, 201–204 (2005).

[10] Reich, S., Maultzsch, J., Thomsen, C. & Ordejón, P. Tight-binding description of graphene. *Physical Review B* **66**, 035412 (2002).

[11] Castro Neto, A. H., Peres, N. M. R., Novoselov, K. S. & Geim, A. K. The electronic properties of graphene. *Reviews of Modern Physics* **81**, 109–162 (2009).

[12] Beenakker, C. Colloquium: Andreev reflection and Klein tunneling in graphene. *Reviews of Modern Physics* **80**, 1337–1354 (2008).

[13] Dresselhaus, M. S. & Dresselhaus, G. Intercalation compounds of graphite. *Advances in Physics* **51**, 1–186 (2002).

[14] Forbeaux, I., Themlin, J.-M. & Debever, J.-M. Heteroepitaxial graphite on 6H-SiC(0001): Interface formation through conduction-band electronic structure. *Physical Review B* **58**, 16396–16406 (1998).

[15] Berger, C. *et al.* Ultrathin epitaxial graphite: 2D electron gas properties and a route toward graphene-based nanoelectronics. *The Journal of Physical Chemistry B* **108**, 19912–19916 (2004).

[16] Land, T., Michely, T., Behm, R., Hemminger, J. & Comsa, G. STM investigation of single layer graphite structures produced on Pt(111) by hydrocarbon decomposition. *Surface Science* **264**, 261–270 (1992).

[17] Nagashima, A. *et al.* Electronic states of monolayer graphite formed on TiC(111) surface. *Surface Science* **291**, 93–98 (1993).

[18] Busse, C. *et al.* Graphene on Ir(111): physisorption with chemical modulation. *Physical Review Letters* **107**, 036101 (2011).

[19] N'Diaye, A. T., Coraux, J., Plasa, T. N., Busse, C. & Michely, T. Structure of epitaxial graphene on Ir(111). *New Journal of Physics* **10**, 043033 (2008).

[20] Coraux, J. *et al.* Growth of graphene on Ir(111). *New Journal of Physics* **11**, 023006 (2009).

[21] Sun, Z. *et al.* Topographic and electronic contrast of the graphene moiré on Ir(111) probed by scanning tunneling microscopy and noncontact atomic force microscopy. *Physical Review B* **83**, 081415 (2011).

[22] Waser, R. (ed.) *Nanoelectronics and information technology* (Wiley-VCH, Weinheim, 2005), second edn.

[23] Binnig, G., Rohrer, H., Gerber, C. & Weibel, E. Tunneling through a controllable vacuum gap. *Applied Physics Letters* **40**, 178–180 (1982).

[24] Binnig, G. & Quate, C. F. Atomic force microscope. *Physical Review Letters* **56**, 930–933 (1986).

[25] Wiesendanger, R. *Scanning probe microscopy and spectroscopy: methods and applications* (Cambridge University Press, Cambridge, 1994), first edn.

[26] Bardeen, J. Tunnelling from a many-particle point of view. *Physical Review Letters* **6**, 57–59 (1961).

[27] Cohen, M., Falicov, L. & Phillips, J. Superconductive tunneling. *Physical Review Letters* **8**, 316–318 (1962).

[28] Chen, C. J. *Introduction to scanning tunneling microscopy* (Oxford Univ. Press, Oxford, 2008), second edn.

[29] Tersoff, J. & Hamann, D. R. Theory and application for the scanning tunneling microscope. *Physical Review Letters* **50**, 1998–2001 (1983).

[30] Tersoff, J. & Hamann, D. R. Theory of the scanning tunneling microscope. *Physical Review B* **31**, 805–813 (1985).

[31] Wahl, P., Diekhöner, L., Schneider, M. A. & Kern, K. Background removal in scanning tunneling spectroscopy of single atoms and molecules on metal surfaces. *Review of Scientific Instruments* **79**, 043104 (2008).

[32] Weymouth, A. J. *et al.* Atomic structure affects the directional dependence of friction. *Physical Review Letters* **111**, 126103 (2013).

[33] Costi, R., Cohen, G., Salant, A., Rabani, E. & Banin, U. Electrostatic force microscopy study of single Au-CdSe hybrid nanodumbbells: evidence for light-induced charge separation. *Nano Letters* **9**, 2031–2039 (2009).

[34] Frisbie, C. D., Rozsnyai, L. F., Noy, A., Wrighton, M. S. & Lieber, C. M. Functional group imaging by chemical force microscopy. *Science* **265**, 2071–2074 (1994).

[35] Rugar, D. *et al.* Magnetic force microscopy: general principles and application to longitudinal recording media. *Journal of Applied Physics* **68**, 1169–1183 (1990).

[36] Lister, T. E. & Pinhero, P. J. In vivo atomic force microscopy of surface proteins on deinococcus radiodurans. *Langmuir* **17**, 2624–2628 (2001).

[37] Lea, A. S., Higgins, S. R., Knauss, K. G. & Rosso, K. M. A high-pressure atomic force microscope for imaging in supercritical carbon dioxide. *Review of Scientific Instruments* **82**, 043709 (2011).

[38] Israelachvili, J. N. *Intermolecular and surface forces* (Academic Press, Elsevier, 2011), third edn.

[39] Kittel, C. *Introduction to solid state physics* (John Wiley & Sons, 2005), eight edn.

[40] Ternes, M. *et al.* Interplay of conductance, force, and structural change in metallic point contacts. *Physical Review Letters* **106**, 016802 (2011).

[41] Jelínek, P., Ondráček, M. & Flores, F. Relation between the chemical force and the tunnelling current in atomic point contacts: a simple model. *Journal of Physics: Condensed Matter* **24**, 084001 (2012).

[42] Sugimoto, Y. *et al.* Quantum degeneracy in atomic point contacts revealed by chemical force and conductance. *Physical Review Letters* **111**, 106803 (2013).

[43] Dewar, M. J. S. & Kelemen, J. LCAO MO theory illustrated by its application to H_2. *Journal of Chemical Education* **48**, 494–501 (1971).

[44] Huber, K. & Herzberg, G. Constants of diatomic molecules. In *Molecular Spectra and Molecular Structure* (Van Nostrand Reinhold Company, 1979), first edn.

[45] Koga, T. & Matsumoto, S. An exact solution of the van der Waals interaction between two ground-state hydrogen atoms. *The Journal of Chemical Physics* **82**, 5127–5132 (1985).

[46] Giessibl, F. J. Advances in atomic force microscopy. *Reviews of Modern Physics* **75**, 949–983 (2003).

[47] Giessibl, F. Forces and frequency shifts in atomic-resolution dynamic-force microscopy. *Physical Review B* **56**, 16010–16015 (1997).

[48] Giessibl, F. J. A direct method to calculate tip-sample forces from frequency shifts in frequency-modulation atomic force microscopy. *Applied Physics Letters* **78**, 123–125 (2001).

[49] Sugimoto, Y. *et al.* Chemical identification of individual surface atoms by atomic force microscopy. *Nature* **446**, 64–67 (2007).

[50] Gross, L., Mohn, F., Moll, N., Liljeroth, P. & Meyer, G. The chemical structure of a molecule resolved by atomic force microscopy. *Science* **325**, 1110–1114 (2009).

[51] Friedrich, H., de Jongh, P. E., Verkleij, A. J. & de Jong, K. P. Electron tomography for heterogeneous catalysts and related nanostructured materials. *Chemical Reviews* **109**, 1613–1629 (2009).

[52] Bracewell, R. N. Numerical transforms. *Science* **248**, 697–704 (1990).

[53] Friedrich, H. *et al.* Quantitative structural analysis of binary nanocrystal superlattices by electron tomography. *Nano Letters* **9**, 2719–2724 (2009).

[54] Van Hove, M., Lin, R. & Somorjai, G. Efficient scheme for calculation of low-energy electron-diffraction intensities in the presence of large superlattices, with application to the structural analysis of benzene adsorbed on Rh(111). *Physical Review Letters* **51**, 778–781 (1983).

[55] Rundgren, J. Optimized surface-slab excited-state muffin-tin potential and surface core level shifts. *Physical Review B* **68**, 125405 (2003).

[56] Moritz, W. *et al.* Structure determination of the coincidence phase of graphene on Ru(0001). *Physical Review Letters* **104**, 136102 (2010).

[57] Pendry, J. B. Ion core scattering and low energy electron diffraction I. *Journal of Physics C: Solid State Physics* **4**, 2501–2513 (1971).

[58] Pendry, J. B. Ion core scattering and low energy electron diffraction II. *Journal of Physics C: Solid State Physics* **4**, 2514–2523 (1971).

2

Graphene on iridium(111): atomic structure

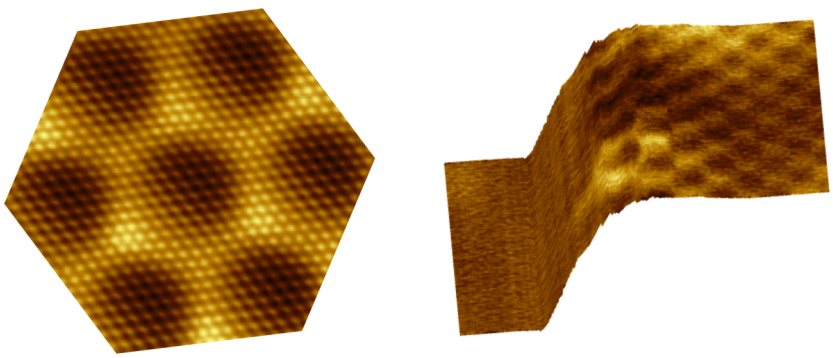

This chapter[1] describes the study of graphene grown on iridium(1 1 1) with AFM. Experiments with a reactive metal tip were compared to experiments with a CO-passivated tip to assess the effect of tip reactivity on the resulting AFM images. We show that the contrast in images obtained with a metal tip is largely determined by chemical bond formation. For the CO-terminated tip on the other hand, we show that the contrast is dominated by Pauli repulsion. Therefore measurements with a CO-terminated tip can be assumed to better reflect the actual atomic topography of the sample. Finally we show how the use of CO-terminated tips leads to improved imaging conditions at the edges of graphene islands.

[1]This chapter is based on M.P. Boneschanscher, J. van der Lit, Z. Sun, I. Swart, P. Liljeroth and D. Vanmaekelbergh, *ACS Nano* **6**, 10216–10221 (2012).

2.1. AFM on graphene and graphite shows a wide variety of atomic contrast patterns

The relationship between the atomic configuration and electronic structure in graphene nanostructures has attracted large interest [1–4]. While STM has proven useful in acquiring local electronic information [5–8], the study of the atomic structure with STM is complicated: the contrast in the tunneling current is more sensitive to the electronic structure close to the Fermi level than to the atomic geometry (see also Section 1.5) [9–11]. Using non-contact frequency modulation AFM [12] with sub-angstrom tip oscillation amplitudes [13–15] and chemically modified tips [14, 16–18] allows for imaging short-range forces, leading to improved spatial resolution (see also Section 1.6). AFM images of graphene and graphite show contrast with atomic periodicity [19–21]. However, the contrast patterns vary depending on the atomic termination of the AFM tip apex and the tip-sample distance, hampering the identification of the atomic positions [22–24].

Previous AFM experiments on carbon nanotubes and graphite showed a maximum attractive force between tip and sample on lattice sites with triangular periodicity, consistent with either the hollow sites or every other atom of the carbon lattice [21, 25, 26]. Using a Lennard–Jones model this attraction was explained to originate from the hollow site [27]. It was only with the advent of AFM imaging with tip oscillation amplitudes of the order of a few angstroms that image contrast with a honeycomb lattice was achieved on graphite [20, 23, 28]. Simultaneous AFM and STM experiments were used to measure both force and current landscapes above graphite and epitaxial graphene [19, 22]. However, the topographies were found to differ strongly depending on bias settings and tip-sample distance, making identification of the true positions of the atoms difficult.

The role of tip termination and reactivity in imaging graphene has not previously been studied experimentally. A recent theoretical paper based on density functional theory (DFT) calculations indicated that the tip reactivity should be a key factor for understanding the wide variety in measured topographies [24]. The model predicts that, for nonreactive tips, atomic scale contrast will only be observed in the repulsive regime. For reactive tips, an as-yet unobserved inversion of the atomic contrast upon variation of the tip-sample distance (d_{ts}) is anticipated. This inversion results from a change in interaction between tip and carbon atoms from maximum attraction at sufficiently large d_{ts} into a minimum attractive force when Pauli repulsion becomes important (at small d_{ts}).

Here, we present a study of the effect of tip reactivity in imaging the atoms of epitaxial graphene using a nonreactive, carbon monoxide (CO)-terminated tip and a reactive Ir tip. We examine the image contrast with both tips at various d_{ts}, ranging from the attractive regime to the onset of the Pauli repulsion regime. This allows us to provide a consistent interpretation of the atomic scale contrast patterns at any tip-sample distance and to identify the carbon atoms in the lattice and at edges of graphene.

2.2. Materials and methods

We grew epitaxial graphene on Ir(1 1 1) from ethylene using the temperature-programmed growth method [29]. The Ir(1 1 1) surface was cleaned by repetitive cycles of argon sputtering and flash heating to 1500 K. After the sample had cooled below 570 K, ethylene was deposited on the surface (3×10^{-6} mbar for 10 s). The temperature was then raised to 1200 K for 20 s to grow large, mostly defect-free graphene islands. After the growth, the sample was inserted into a low-temperature STM/AFM (T = 4.8 K, Omicron LT STM/QPlus AFM), housed within the same ultra-high vacuum system (base pressure $< 10^{-10}$ mbar). We used commercially available W tips mounted on a QPlus sensor (Omicron) with a resonance frequency f_0 of $\sim$ 24.5 kHz, a quality factor of 12000, and a peak-to-peak oscillation amplitude of $\sim$ 170 pm.

Series of constant height maps of the frequency shift Δf were recorded at different heights above the same area of graphene. A reference distance of $d_{ts} = 0$ was chosen for the closest tip-sample distance that could be achieved while keeping the tip stable. Frequency shift as a function of the tip-sample distance (Δf *vs* d_{ts}) curves were converted to force-distance curves using the Sader–Jarvis method [30]. The metal tip apex was formed by controlled contact with the iridium surface. The metallic nature of the tip was confirmed by conductance spectroscopy on the iridium surface. For the experiments with CO-terminated tips, the tip was prepared on a Cu(1 1 1) surface, resulting in a copper-coated metal tip [14, 18]. Then 10^{-9} mbar of CO was leaked in the vacuum chamber for 10 s, resulting in $\sim$ 1/10 monolayer of CO molecules on the copper surface. A single CO molecule was picked up as described previously [14]; the nature of the tip apex was confirmed by the observed contrast inversion in STM feedback of the imaged CO on the copper surface. Subsequently, the Cu(1 1 1) was exchanged for the graphene-coated Ir(1 1 1) sample, after which the CO tip was carefully approached. The stability of the CO molecule on the tip apex through the experiments on the graphene was

confirmed by changing back to the Cu(1 1 1) substrate with adsorbed CO molecules and checking the contrast above the CO on the copper in STM feedback. While making sure in this way that the tip was terminated with a CO molecule, we found that on the graphene on Ir(1 1 1) surface the presence of a CO molecule at the tip apex results in an inversion of the moiré contrast in STM feedback mode at low bias. This gives a simple qualitative indication of the tip termination (metal versus a CO molecule) on the graphene on Ir(1 1 1) system.

2.3. The role of tip reactivity on atomic contrast

2.3.1. The metal tip. Figure 2.1 shows a series of Δf images acquired at constant height using an iridium-terminated tip. A reference distance of $d_{ts} = 0$ is chosen for the closest tip-sample distance that could be achieved while keeping the tip stable. Upon approaching the tip further, changes in the tip-geometry result in unstable imaging conditions, preventing the acquisition of reliable data. The obtained contrast patterns reflect the periodicity of carbon atoms in graphene and on a larger length scale (~ 2.5 nm) a periodicity consistent with the moiré unit cell for graphene on Ir(1 1 1) [31]. The moiré pattern is set up by the lattice mismatch between graphene and the Ir(1 1 1) substrate, resulting in a topographic corrugation of the graphene layer, as illustrated in Figure 2.1(b) [19, 32]. For the metallic tip, atomic contrast can already be observed in the attractive regime. A triangular pattern of light yellow dots (smaller attraction) and dark spots (stronger attraction) is observed. Previously, such patterns were measured on carbon nanotubes and graphite; the sites corresponding to maximum attraction were interpreted as corresponding to the hollow sites [21, 23, 25]. Here, we present an interpretation that is in contrast with this: the positions of maximum attraction (dark points) correspond to the carbon atoms in the graphene lattice, while the spots of weaker attraction (light spots) correspond to the hollow sites. This interpretation will be corroborated by the results below. A more detailed comparison including simultaneously measured tunneling current can be found in Section 2.3.4.

At the smallest distance, the contrast pattern is drastically changed into a lighter honeycomb lattice (smaller attraction) with in-between darker spots (stronger attraction). The honeycomb lattice corresponds to the atomic backbone of the graphene. Hence, the positions with smallest attractive force (light) represent the carbon atoms. That the left and right images represent a true contrast inversion is proven by the frequency shift *vs* distance curves: position 1 on the honeycomb lattice and position 2 on top of a dark spot. The Δf *vs* d_{ts} curves

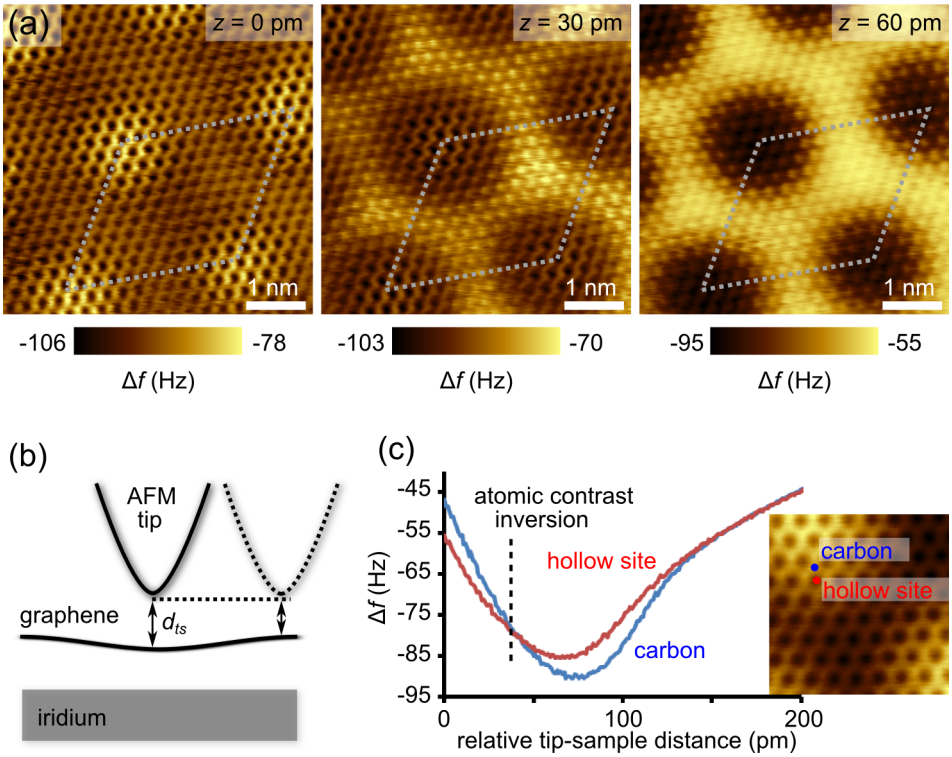

FIGURE 2.1. Constant height AFM imaging of epitaxial graphene on Ir(1 1 1) with a metallic tip. (a) Constant height Δf images acquired with a metallic iridium tip at varying d_{ts}. All scans are 5×5 nm^2, and the relative tip heights are indicated in the insets. The moiré unit cell is indicated by the dotted lines. Regions with brighter contrast correspond to less negative Δf (smaller attractive force). (b) Schematic of the variation of the tip-sample distance going from the middle to the corner of the moiré unit cell. (c) Frequency shift *vs* tip-sample distance measured above the positions of a carbon atom (blue curve) and a hollow site (red curve). The distance where the atomic scale contrast inverts is indicated by a dashed vertical line. The inset acquired in the repulsive regime shows the positions of the Δf *vs* d_{ts} curves.

[Figure 2.1(c)] acquired on these two positions show a crossing and hence reflect the inversion of the contrast pattern with distance. Similar curves are obtained at different regions of the moiré pattern, see Figure 2.2. We remark that this contrast inversion was predicted by DFT calculations [24]. The AFM image acquired at intermediate height [Figure 2.1(a), center] shows the honeycomb lattice on the atop regions in the corners of the moiré unit cell (typical for short distances, similar to the left picture), while in the lower parts, the contrast typically acquired at larger distances (similar to the right picture) is still visible. These results were reproduced using a number of different metal tips.

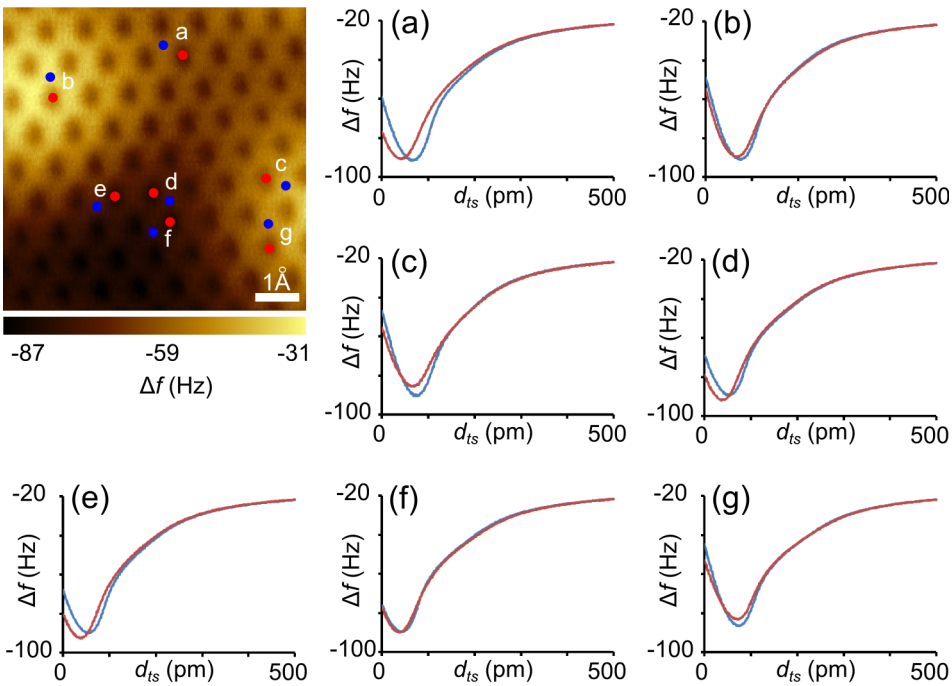

FIGURE 2.2. Metal tip Δf *vs* d_{ts} curves acquired on different spots in the moiré pattern. Red (blue) curves obtained on the hollow (carbon) sites indicated in the frequency shift window.

2.3.2. The CO-terminated tip. With nonreactive CO-terminated tips, the contrast patterns are remarkably different. At large d_{ts} [Figure 2.3(a), right], only the atop positions of the moiré unit cell are visible. Here d_{ts} is lowered locally due

to the outward buckling of the graphene, resulting in additional van der Waals attraction [more negative Δf, dark, see also Figure 2.3(b)]. When d_{ts} is lowered, repulsive interaction on sites forming a honeycomb lattice appears. At medium d_{ts}, this honeycomb lattice is only observed on atop positions in the moiré unit cell [Figure 2.3(a), middle]. At even smaller d_{ts}, the Pauli repulsion contributes significantly to the total force and the honeycomb lattice is observed over the entire moiré unit cell [Figure 2.3(a), left]. The honeycomb lattice can be interpreted as the carbon atoms of the graphene (*i.e.*, the electronic backbone) similar to what was observed on small organic molecules [14]. This is backed up by comparing the Δf with the simultaneous obtained current signal (Section 2.3.4). Figure 2.3(c) shows the Δf *vs* d_{ts} curves acquired with the CO-terminated tip on the carbon and hollow sites, located on a lower region of the moiré pattern. Similar results are obtained at atop regions of the moiré pattern (Figure 2.4).

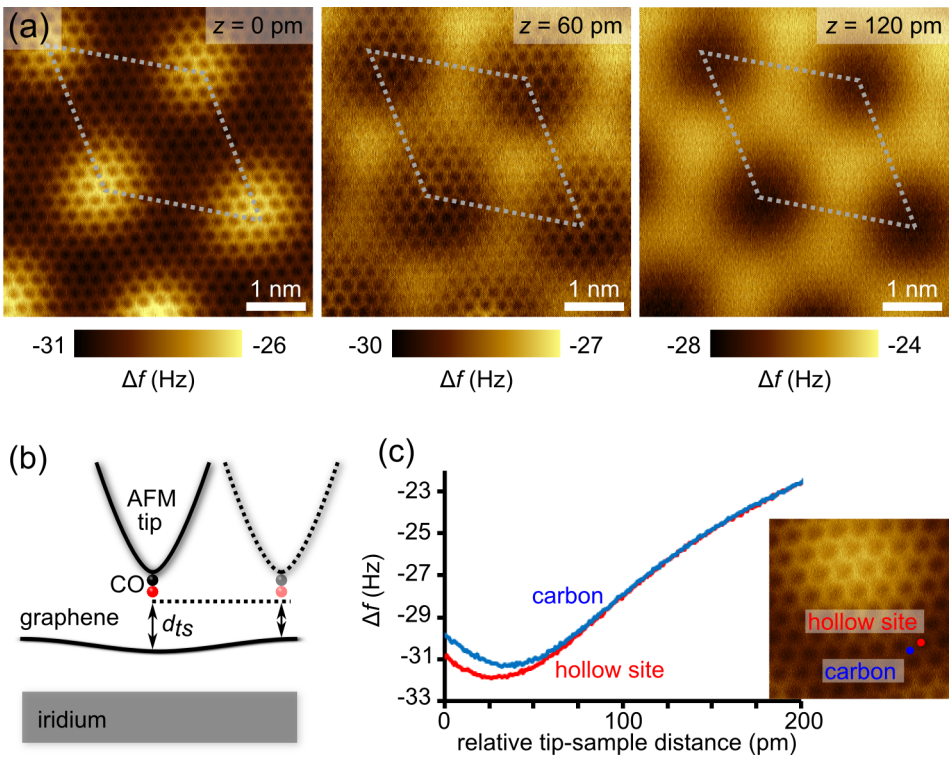

FIGURE 2.3. Constant height experiments with a CO-terminated tip. Labels are the same as in Figure 2.1.

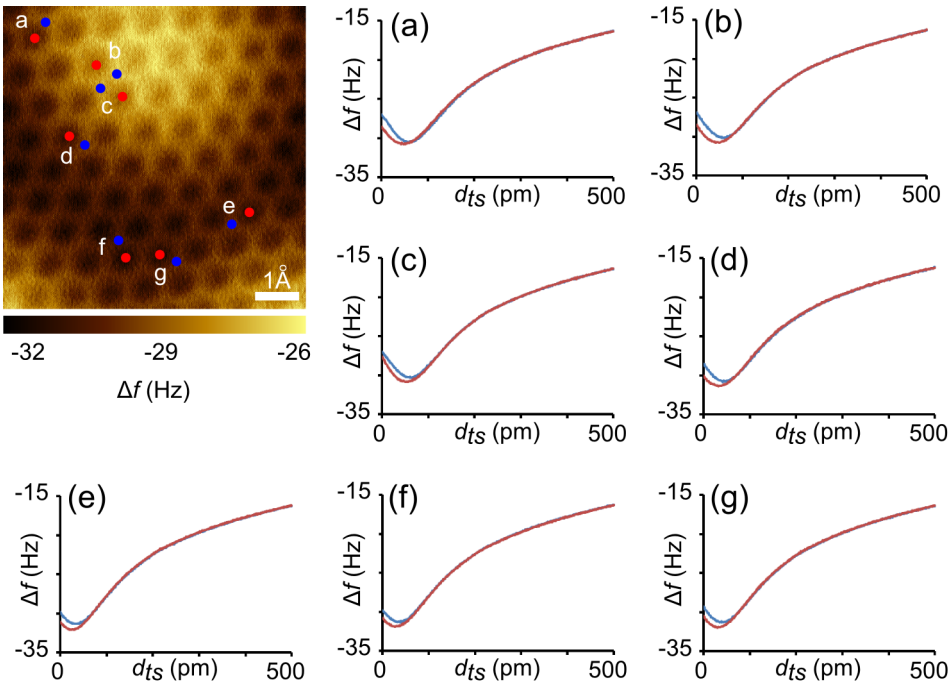

FIGURE 2.4. CO-terminated tip Δf *vs* d_{ts} curves acquired on different spots in the moiré pattern. Red (blue) curves obtained on the hollow (carbon) sites indicated in the frequency shift window.

2.3.3. Quantifying the effect of tip termination. Figures 2.1 and 2.3 demonstrate how the chemical reactivity of the tip apex controls the atomic scale contrast. To quantify the effect of tip termination we first integrated the Δf *vs* d_{ts} curves using the Sader–Jarvis method [30] to obtain force-distance curves (Figure 2.5). In the Sader–Jarvis integration, the long distance part of the Δf *vs* d_{ts} curves was fitted to a power law [33].

However, it is more insightful to first subtract the Δf *vs* d_{ts} curve measured on top of a hollow site from the Δf *vs* d_{ts} curve measured on top of a carbon atom. This corrects for the overall background van der Waals interaction between tip and sample, giving us a measure for the force between the outermost tip atom (or CO molecule) and the carbon atoms in the graphene lattice. The Δf *vs* d_{ts} and force-distance curves obtained in this way are presented in Figure 2.6. With the reactive iridium tip, we observe attractive atomic contrast in a 100 pm range of tip-sample

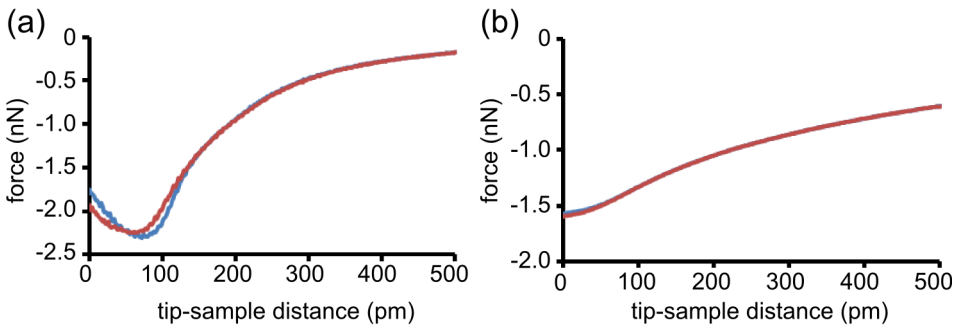

FIGURE 2.5. Force-distance curves calculated based on the Δf *vs* d_{ts} curves shown in Figures 2.1 and 2.3 for the metal (a) and CO-terminated tips (b), using the Sader–Jarvis method [30].

distances. This chemical interaction between the last tip atom and the carbon atoms of the graphene results in atomic contrast (attractive or repulsive) in a d_{ts} region as broad as 150 pm. We observe a maximum attractive force on top of the carbon atom of *ca.* 150 pN [Figure 2.6(b)]. This is in line with DFT calculations showing free iridium atoms adsorbing preferentially on top of the carbon atoms, not on the hollow sites [34, 35].

When d_{ts} is further reduced, we enter the regime in which Pauli repulsion becomes important. As the repulsion on carbon atoms is considerably stronger than on the hollow sites, this results in less overall attractive force (less negative Δf) on the carbon atoms. The difference in repulsion between the carbon atoms and hollow sites overcompensates the difference in the attractive forces leading to images with a honeycomb lattice. This can also be observed in the crossing of the Δf *vs* d_{ts} curves [Figure 2.1(c)] and is the reason for the change of sign in the Δf difference curve in Figure 2.6(a).

With the chemically passivated CO-terminated tip, chemical bond formation between the tip and graphene does not occur [Figure 2.6(a)]. The difference in van der Waals attraction for the carbon atoms and the hollow sites is too small to be visible as an atomic scale contrast in the image. Atomic contrast is only observed at smaller d_{ts}, in the Pauli repulsion regime. We find a maximum repulsive force on top of the carbon atoms of *ca.* 25 pN. This is in good agreement with the observed repulsive force contrast of *ca.* 10 pN with a CO-terminated tip on a pentacene molecule [14].

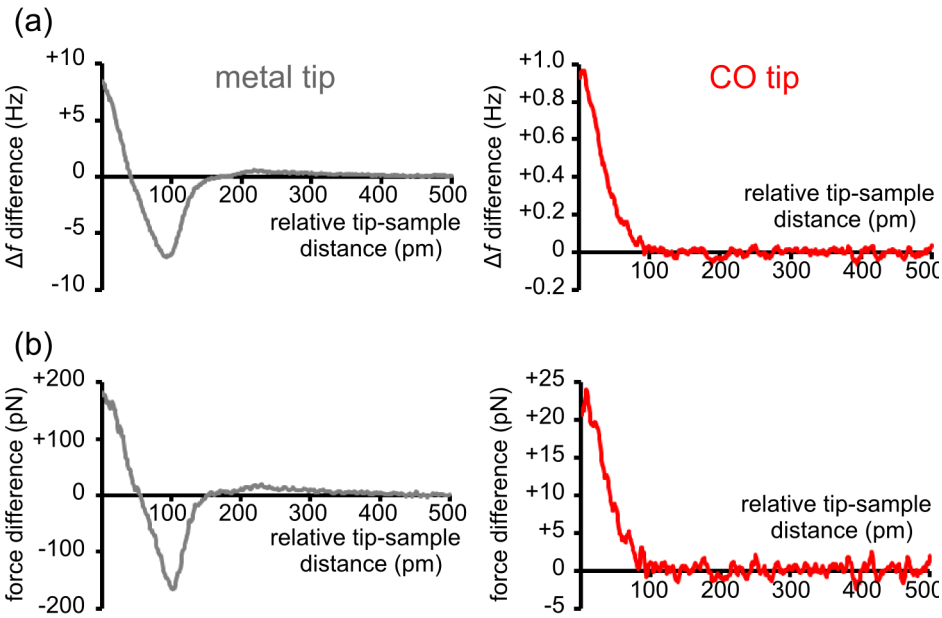

FIGURE 2.6. Force curves showing the formation of atomic scale contrast. (a) Frequency shift difference between carbon and hollow sites as a function of tip-sample distance. Measured with a metal tip (gray curve) and with a CO-terminated tip (red curve). (b) Force curves calculated from the frequency shift difference curves in (a) using the Sader–Jarvis method [30].

2.3.4. Comparison of Δf and current data. During the constant height experiment both frequency shift and current are recorded. The sample was positively biased with 0.2 mV with respect to the tip (tip connected to ground). The integration time per pixel in the image (7.5 ms) is *ca.* 2 orders of magnitude larger than the time per oscillation of the tip (1/24.5 kHz = 0.04 ms). Therefore the obtained tunneling current is an average over the full oscillation amplitude. For the metal tip, a current contrast is observed that roughly resembles the honeycomb lattice of graphene (Figure 2.7). On very close tip-sample distances, the current contrast over the carbon atoms gets smeared out, making it difficult to identify the atomic positions. Over the moiré unit cell, a stronger current is observed on the atop positions.

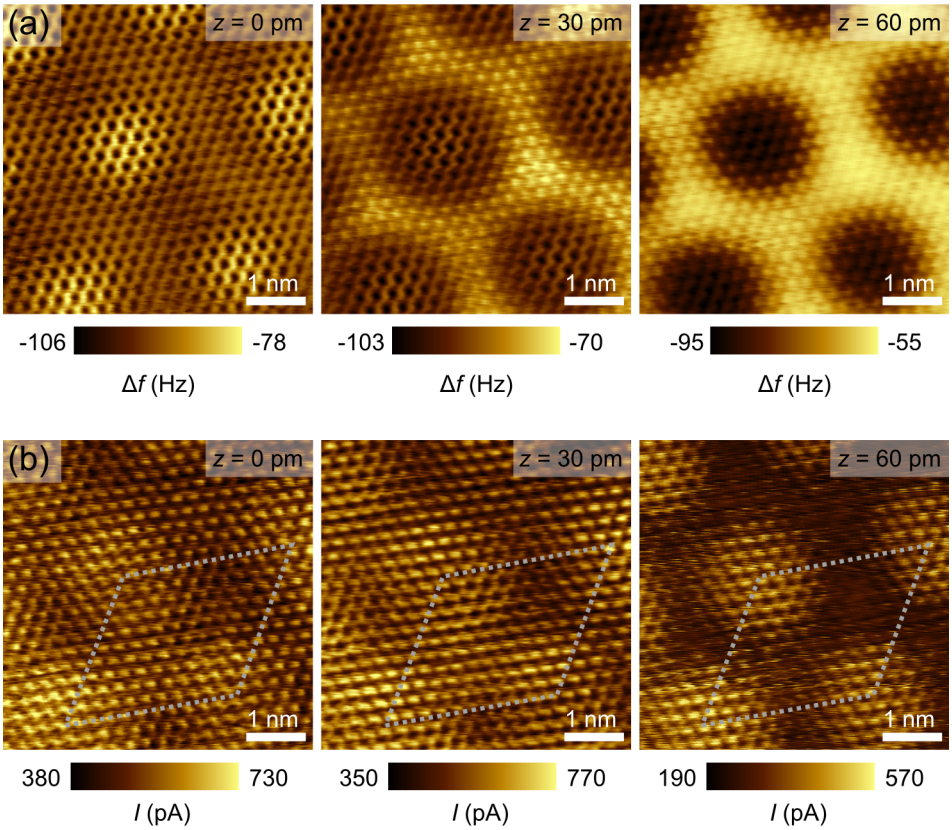

FIGURE 2.7. Comparison of the frequency shift and tunneling current acquired with a metal tip. (a) Frequency shift contrast obtained with a metal tip as a function of tip-sample distance (z-offset indicated in inset). (b) Simultaneous acquired tunneling current. A positive bias of 0.2 mV between tip and sample was applied (tip connected to ground).

For the CO-terminated tip, the simultaneous measured currents are *ca.* 2 orders of magnitude lower than for the metal tip (sub-pA for most distances considered here). The observed current contrast is inverted and shows a decrease in current over the honeycomb lattice of the graphene. Also the moiré scale contrast is inverted, showing a decrease in current when going to the atop positions. In the current contrast, a number of defects can be observed that are not visible in the

frequency shift contrast. These are probably related to defects in the underlying iridium lattice or impurities between the graphene and iridium (Figure 2.8).

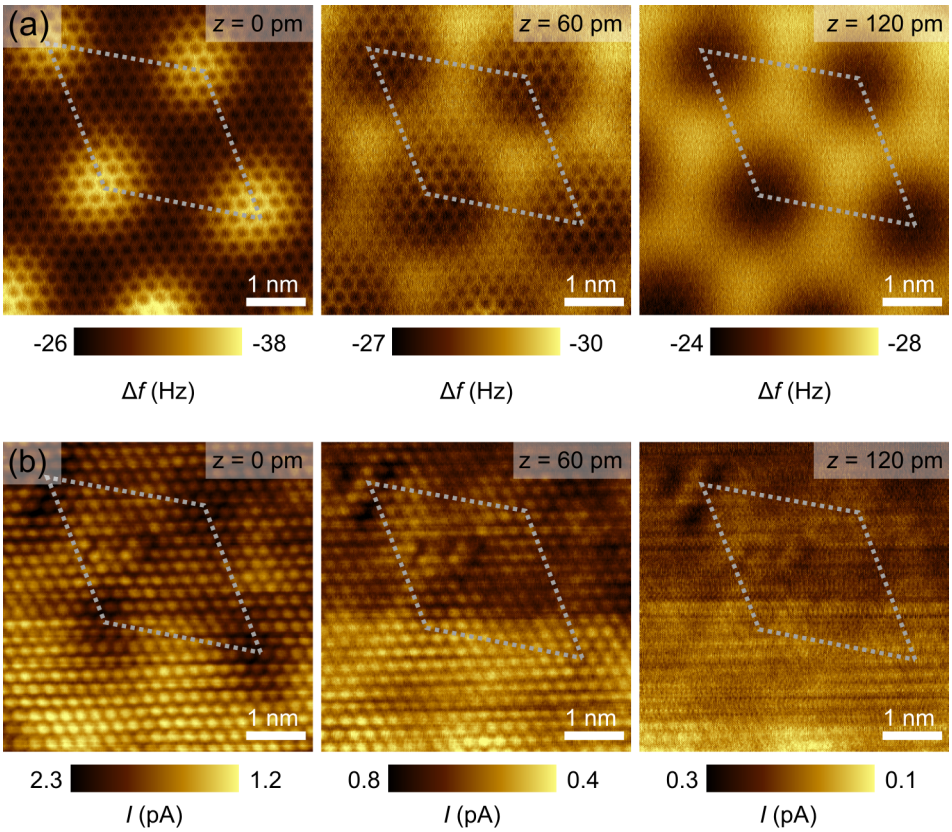

FIGURE 2.8. Comparison of the frequency shift and tunneling current acquired with a CO-terminated tip. (a) Frequency shift contrast obtained with a CO-terminated tip as a function of tip-sample distance (z-offset indicated in inset). (b) Simultaneous acquired tunneling current. A positive bias of 0.2 mV between tip and sample was applied (tip connected to ground).

2.4. Imaging graphene edges

Understanding the contrast formation on graphene enables us to analyze the edge structure of graphene nanostructures, which is one of the key challenges in realizing

graphene-based nanoelectronics [36, 37]. In Figures 2.9–2.11, we show first results obtained on graphene islands on Ir(1 1 1). The islands are terminated along the zigzag direction, but STM experiments have been unable to detect the theoretically predicted edge state. One possible reason for this is bonding between the graphene edge and the underlying iridium substrate [38].

Due to the changing slope of the Δf *vs* d_{ts} curve and strong changes in the tip-sample interaction, it is impossible to image the graphene edges in the Pauli repulsion regime using Δf feedback. We therefore developed an adaptive height scan method. Here, the overall shape of the graphene edge is determined in STM feedback. A height profile is extracted by averaging over a small window perpendicular to the graphene edge (Figure 2.9 and 2.10). The feedback is then switched off and the tip is scanned over the edge following the predetermined z-profile, recording current and Δf. This results in a more highly resolved image of the edge structure. However, for the metal tip, the strong attraction between the metal tip and the iridium substrate results in tip changes while scanning (Figure 2.9).

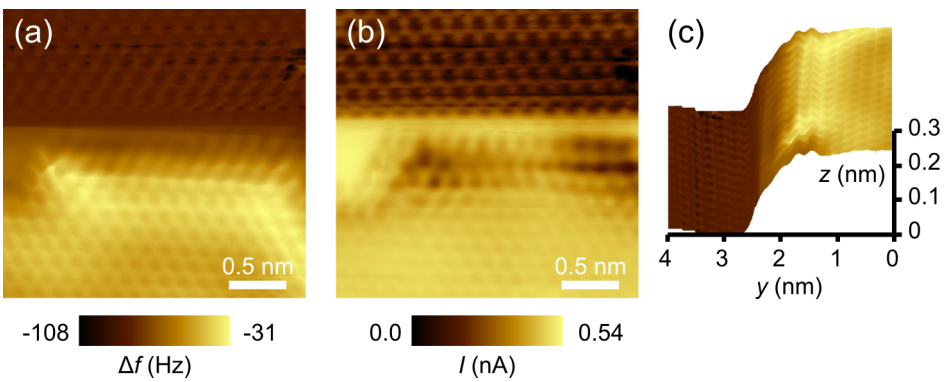

FIGURE 2.9. Adaptive height scans over a graphene edge with a metal tip. (a) Recorded frequency shift. The strong attraction between the metal tip and the iridium substrate results in tip changes while scanning. (b) Simultaneously recorded tunneling current. (c) Height profile that the tip follows while scanning over the edge. The height profile is determined using STM feedback (100 mV, 30 pA). The frequency shift data from (a) is mapped to the height profile.

In Figure 2.10, the same procedure is repeated with a CO-terminated tip. For this nonreactive tip, there is a much smaller difference in force between the positions on top of graphene and on top of iridium as compared to the more reactive metal tip. This allows for the stable imaging of the graphene edge and the adjacent iridium substrate. In the simultaneously recorded current scan, even the underlying iridium layer is atomically resolved [Figure 2.10(b)]. We are also able to atomically resolve one of the kinks [right side of Figure 2.10(a)], revealing that the kinks are in fact due to the onset of an additional row of benzene rings to the graphene. The distorted benzene rings and apparent changes in the carbon-carbon bond lengths are likely to result from the flexibility of the CO on the tip apex [18, 39].

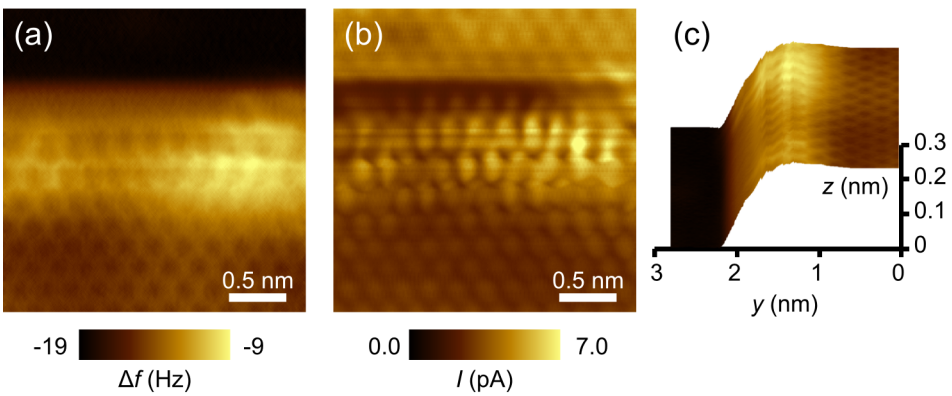

FIGURE 2.10. Adaptive height scans over a graphene edge with a CO-terminated tip. (a) Recorded frequency shift, revealing the position of the atoms along the edge. The darkening of the background after crossing over the edge is due to the strong increase in attraction that the tip experiences from the iridium. (b) Simultaneously recorded tunneling current. (c) Height profile that the tip follows while scanning over the edge. The height profile is determined using STM feedback (100 mV, 30 pA). The frequency shift data from (a) is mapped to the height profile.

2.5. Conclusions

In conclusion, we have studied how the graphene atomic contrast in AFM depends on tip termination and tip-sample distance. This allows us to identify the atoms from any contrast pattern as demonstrated by atomic resolution imaging of graphene edges. Combined STM and AFM measurements can now be used to unravel the effect of defects, distortions, and edges on the electrical properties of graphene nanostructures. For imaging of the edges of graphene flakes on Ir(1 1 1) we found that, for the metal tip, the best results were obtained using constant height scans over the graphene edge in the Pauli repulsion regime (see Figure 2.11). However, the strong bending of the graphene layer towards the Ir surface at the edge makes it very hard to determine the exact atomic geometry of the outermost row of carbon atoms. A possible solution for this problem is the use of adaptive height scans with a CO-terminated tip. Since the CO-terminated tip is chemically inert, the tip can be brought closer to the Ir(1 1 1) substrate while scanning over the edge. This finally allows imaging of the outermost row of carbon atoms, as shown in Figure 2.11(c). The graphene island is terminated by nonreconstructed zigzag edges that bend down by *ca.* 0.4 Å due to the increased interaction with the underlying Ir(1 1 1) substrate.

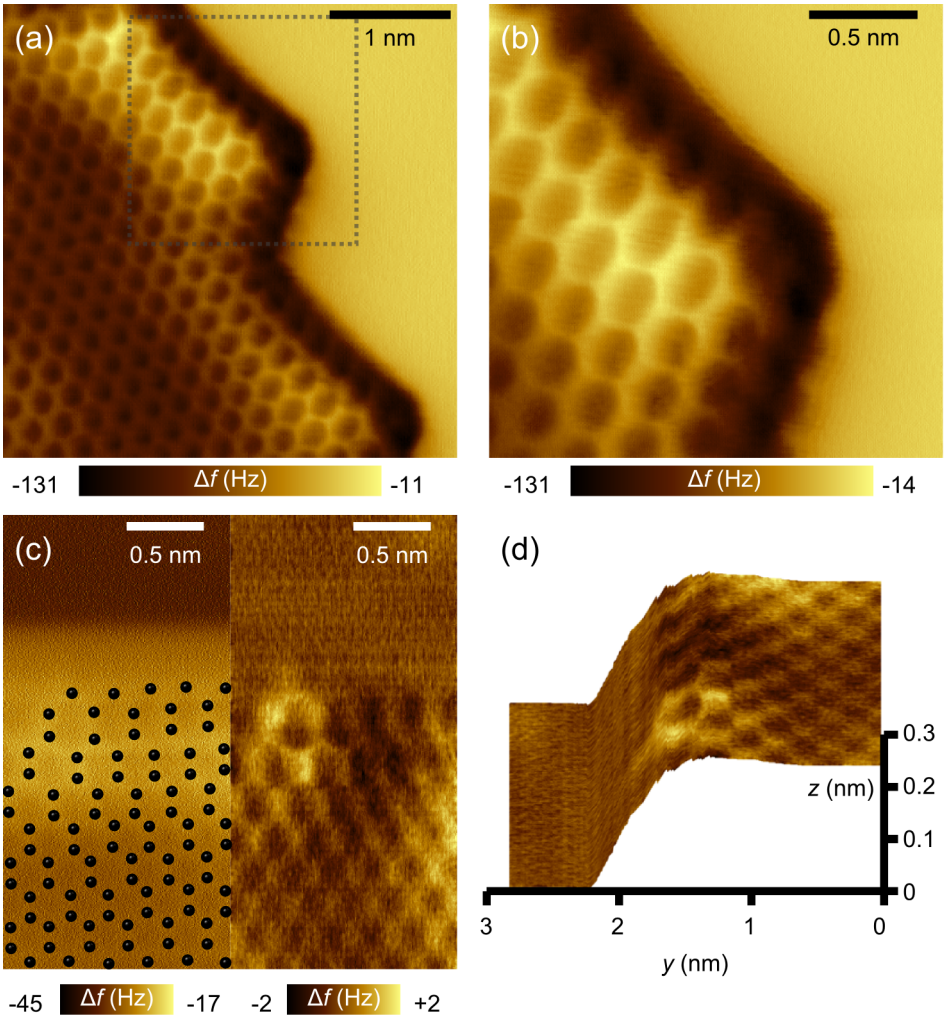

FIGURE 2.11. Frequency shift mapping of a graphene edge. (a) Constant height image of Δf over a graphene edge measured with an Ir-terminated tip. (b) Zoom-in on the indicated region in (a). (c) Adaptive height scan of Δf over a graphene edge measured with a CO-terminated tip. Left image is raw data with an overlaid schematic indicating the positions of the outermost benzene rings, right image after median line correction and filtering. (d) Filtered image from (c) mapped to the height profile that the tip followed while scanning over the edge. The height profile is determined prior to scanning using STM feedback (100 mV, 30 pA).

2.6. Bibliography

[1] Castro Neto, A. H., Peres, N. M. R., Novoselov, K. S. & Geim, A. K. The electronic properties of graphene. *Reviews of Modern Physics* **81**, 109–162 (2009).

[2] Geim, A. K. & Novoselov, K. S. The rise of graphene. *Nature Materials* **6**, 183–191 (2007).

[3] Levy, N. *et al.* Strain-induced pseudo-magnetic fields greater than 300 tesla in graphene nanobubbles. *Science* **329**, 544–547 (2010).

[4] Suenaga, K. & Koshino, M. Atom-by-atom spectroscopy at graphene edge. *Nature* **468**, 1088–1090 (2010).

[5] Hämäläinen, S. K. *et al.* Quantum-confined electronic states in atomically well-defined graphene nanostructures. *Physical Review Letters* **107**, 236803 (2011).

[6] Xue, J. *et al.* Scanning tunnelling microscopy and spectroscopy of ultra-flat graphene on hexagonal boron nitride. *Nature Materials* **10**, 282–285 (2011).

[7] Decker, R. *et al.* Local electronic properties of graphene on a BN substrate via scanning tunneling microscopy. *Nano letters* **11**, 2291–2295 (2011).

[8] Zhao, L. *et al.* Visualizing individual nitrogen dopants in monolayer graphene. *Science* **333**, 999–1003 (2011).

[9] Chen, C. J. *Introduction to scanning tunneling microscopy* (Oxford Univ. Press, Oxford, 2008), second edn.

[10] Hofer, W., Foster, A. & Shluger, A. Theories of scanning probe microscopes at the atomic scale. *Reviews of Modern Physics* **75**, 1287–1331 (2003).

[11] Ugeda, M. M. *et al.* Point defects on graphene on metals. *Physical Review Letters* **107**, 116803 (2011).

[12] Morita, S., Giessibl, F. J. & Wiesendanger, R. (eds.) *Noncontact atomic force microscopy.* NanoScience and Technology (Springer, Berlin, 2009).

[13] Giessibl, F. J. Advances in atomic force microscopy. *Reviews of Modern Physics* **75**, 949–983 (2003).

[14] Gross, L., Mohn, F., Moll, N., Liljeroth, P. & Meyer, G. The chemical structure of a molecule resolved by atomic force microscopy. *Science* **325**, 1110–1114 (2009).

[15] Welker, J. & Giessibl, F. J. Revealing the angular symmetry of chemical bonds by atomic force microscopy. *Science* **336**, 444–449 (2012).

[16] Gross, L. *et al.* Organic structure determination using atomic-resolution scanning probe microscopy. *Nature Chemistry* **2**, 821–825 (2010).

[17] Moll, N., Gross, L., Mohn, F., Curioni, A. & Meyer, G. The mechanisms underlying the enhanced resolution of atomic force microscopy with functionalized tips. *New Journal of Physics* **12**, 125020 (2010).

[18] Sun, Z., Boneschanscher, M. P., Swart, I., Vanmaekelbergh, D. & Liljeroth, P. Quantitative atomic force microscopy with carbon monoxide terminated tips. *Physical Review Letters* **106**, 046104 (2011).

[19] Sun, Z. *et al.* Topographic and electronic contrast of the graphene moiré on Ir(111) probed by scanning tunneling microscopy and noncontact atomic force microscopy. *Physical Review B* **83**, 081415 (2011).

[20] Hembacher, S., Giessibl, F. J., Mannhart, J. & Quate, C. F. Revealing the hidden atom in graphite by low-temperature atomic force microscopy. *Proceedings of the National Academy of Sciences* **100**, 12539–12542 (2003).

[21] Hölscher, H., Allers, W., Schwarz, U. D., Schwarz, A. & Wiesendanger, R. Interpretation of "true atomic resolution" images of graphite (0001) in noncontact atomic force microscopy. *Physical Review B* **62**, 6967–6970 (2000).

[22] Hembacher, S., Giessibl, F. J., Mannhart, J. & Quate, C. F. Local spectroscopy and atomic imaging of tunneling current, forces, and dissipation on graphite. *Physical Review Letters* **94**, 056101 (2005).

[23] Albers, B. J. *et al.* Three-dimensional imaging of short-range chemical forces with picometre resolution. *Nature Nanotechnology* **4**, 307–310 (2009).

[24] Ondráček, M. *et al.* Forces and currents in carbon nanostructures: are we imaging atoms? *Physical Review Letters* **106**, 176101 (2011).

[25] Ashino, M., Schwarz, A., Behnke, T. & Wiesendanger, R. Atomic-resolution dynamic force microscopy and spectroscopy of a single-walled carbon nanotube: characterization of interatomic van der Waals Forces. *Physical Review Letters* **93**, 136101 (2004).

[26] Allers, W., Schwarz, A., Schwarz, U. & Wiesendanger, R. Dynamic scanning force microscopy at low temperatures on a van der Waals surface: graphite (0001). *Applied Surface Science* **140**, 247–252 (1999).

[27] Hölscher, H., Allers, W., Schwarz, U., Schwarz, A. & Wiesendanger, R. Determination of tip-sample interaction potentials by dynamic force spectroscopy. *Physical Review Letters* **83**, 4780–4783 (1999).

[28] Kawai, S. & Kawakatsu, H. Surface-relaxation-induced giant corrugation on graphite (0001). *Physical Review B* **79**, 115440 (2009).

[29] Coraux, J. *et al.* Growth of graphene on Ir(111). *New Journal of Physics* **11**, 023006 (2009).

[30] Sader, J. E. & Jarvis, S. P. Accurate formulas for interaction force and energy in frequency modulation force spectroscopy. *Applied Physics Letters* **84**, 1801–1803 (2004).

[31] N'Diaye, A. T., Coraux, J., Plasa, T. N., Busse, C. & Michely, T. Structure of epitaxial graphene on Ir(111). *New Journal of Physics* **10**, 043033 (2008).

[32] Busse, C. *et al.* Graphene on Ir(111): physisorption with chemical modulation. *Physical Review Letters* **107**, 036101 (2011).

[33] Giessibl, F. Forces and frequency shifts in atomic-resolution dynamic-force microscopy. *Physical Review B* **56**, 16010–16015 (1997).

[34] Feibelman, P. Pinning of graphene to Ir(111) by flat Ir dots. *Physical Review B* **77**, 165419 (2008).

[35] Feibelman, P. Onset of three-dimensional Ir islands on a graphene/Ir(111) template. *Physical Review B* **80**, 085412 (2009).

[36] Wintterlin, J. & Bocquet, M.-L. Graphene on metal surfaces. *Surface Science* **603**, 1841–1852 (2009).

[37] Lacovig, P. *et al.* Growth of dome-shaped carbon nanoislands on Ir(111): the intermediate between carbidic clusters and quasi-free-standing graphene. *Physical Review Letters* **103**, 166101 (2009).

[38] Subramaniam, D. *et al.* Wave-function mapping of graphene quantum dots with soft confinement. *Physical Review Letters* **108**, 046801 (2012).

[39] Gross, L. *et al.* Bond-order discrimination by atomic force microscopy. *Science* **337**, 1326–1329 (2012).

3

Graphene on iridium(111): moiré structure

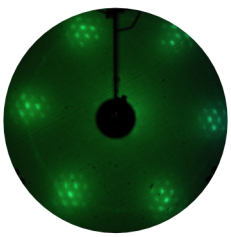

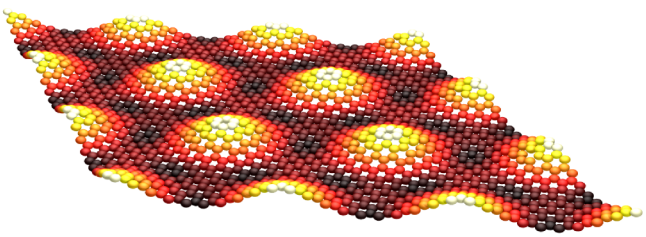

This chapter[1] describes the study of the moiré structure of epitaxial graphene grown on iridium(1 1 1) using LEED *I(V)* and AFM with a CO-terminated tip. Our LEED *I(V)* results yield the average positions of all the atoms in the surface unit cell and are in qualitative agreement with the structure obtained from density functional theory. The AFM experiments reveal local variations of the moiré structure: The corrugation varies smoothly over several moiré unit cells between 42 and 56 pm. We attribute these variations to the varying registry between the moiré symmetry sites and the underlying substrate. We also observe isolated outliers, where the moiré top sites can be offset by an additional 10 pm.

[1]This chapter is based on S.K. Hämäläinen, M.P. Boneschanscher, P.H. Jacobse, I. Swart, K. Pussi, W. Moritz, J. Lahtinen, P. Liljeroth and J. Sainio, *Physical Review B* **88**, 201406(R) (2013).

3.1. Two-dimensional overlayers and moiré patterns

Determination of the surface topography down to the atomic level is crucial in understanding the correlation between the electronic and geometric structure. Total structure determination is particularly challenging in the case of two-dimensional (2-D) overlayers, which are prominent due to the rise of graphene [1] and related materials such as hexagonal boron nitride [2] and silicene [3, 4].

These atomically thin materials typically exhibit a moiré pattern arising from the lattice mismatch with the substrate [2, 5, 6], which has been shown to cause a significant change in the electronic structure in the case of graphene [7–10]. Weakly interacting overlayers are generally not commensurate with the substrate, which might result in a longer length scale modulation of the moiré pattern and variation of the electronic properties. Determination of the surface structure by standard tools such as dynamic low-energy electron diffraction [LEED *I(V)*], scanning tunneling microscopy (STM), and atomic force microscopy (AFM) is complicated due to the large size of the moiré unit cell and the resulting variations in the local density of states and chemical reactivity [11–16]. These difficulties have been illustrated by numerous examples on epitaxial graphene on metal single crystal substrates [5, 17–21]. The graphene-substrate interaction depends on the metal, leading to a variation in the electronic and topographic structure of the moiré [5], and reactivity of the graphene layer [22–27].

The structure of the moiré on the weakly bound systems has proven to be particularly difficult to study experimentally. In STM the contrast of the moiré on graphene/Ir(1 1 1) inverts as a function of bias and tip termination [22, 23] and the results of AFM experiments depend on the tip reactivity and the tip-sample distance [22, 24, 28]. On molecular systems, chemical functionalization of the AFM tip apex with a CO molecule and working in the repulsive force regime have become the standard way to obtain atomic scale information [24, 29–33]. However, all these measurements with a CO tip in the repulsive force regime have been done at a constant height without AFM feedback and hence do not yield direct information on the actual topography of the surface.

Here, we use both LEED *I(V)* and scanning probe measurements to unravel the structure of the graphene/Ir(1 1 1) surface. The average adsorption height, registry, and moiré structure are obtained from LEED *I(V)* measurements where the atomic positions are described by Fourier components [15]. Finally, we use AFM in feedback mode with a CO-terminated tip to probe local variations in the moiré structure.

3.2. Materials and methods

The LEED measurements and graphene growth were conducted in a single ultra-high vacuum (UHV) system with a base pressure $\sim 10^{-10}$ mbar. The Ir(1 1 1) single crystal was cleaned by repeated cycles of sputtering with 1.5 kV Ar^+ ions and subsequent annealing to 1350 K. A full monolayer of graphene was grown on the clean Ir(1 1 1) surface by chemical vapor deposition (CVD) from ethylene at 1350 K, as described in Reference [17]. Prior to the LEED measurements, the quality of the sample was checked with an RHK UHV-750 variable temperature STM.

Princeton Research Instruments rear view LEED optics were used to measure the LEED patterns with the sample held at room temperature. The diffraction patterns were recorded in 2 eV steps from the phosphorescent screen with a computer controlled Nikon D70s camera using a flat gradation curve and a single exposure setting for all the images. Due to the small spacing of the moiré diffraction spots, the background of the adjacent spots could result in false peaks in the extracted *I(V)* spectra. This was avoided by taking cross sections over the spots and subtracting a linear background, similarly as in Reference [15]. The sum of the RGB channels of the color images were used as the intensity signal.

The AFM measurements were done using a separate UHV system with an Omicron LT-STM/AFM operated at 5 K using a QPlus tuning fork with an oscillation amplitude of ~ 85 pm. A submonolayer of graphene was grown on the iridium crystal in order to leave clean iridium for tip preparation. This was done by depositing a monolayer of ethylene on the clean Ir(1 1 1) and subsequently heating to 1500 K for 30 s [17]. AFM experiments were carried out in the constant frequency shift mode with a CO-terminated tip [34]. To prepare the tips, CO was deposited on the graphene/Ir(1 1 1) sample at 5 K by back filling the vacuum outside the cryostat to 10^{-9} mbar with CO, and opening a shutter on the radiation shield for 10 s. Sometimes this already resulted in a CO-terminated tip. If this was not the case, a CO molecule was picked up from the bare Ir by controlled contact with the tip. The presence of a CO molecule at the tip apex was confirmed as described in Chapter 2 [24]. In Section 3.3 the results of the LEED *I(V)* experiment will be discussed. The AFM data is presented in Section 3.4.

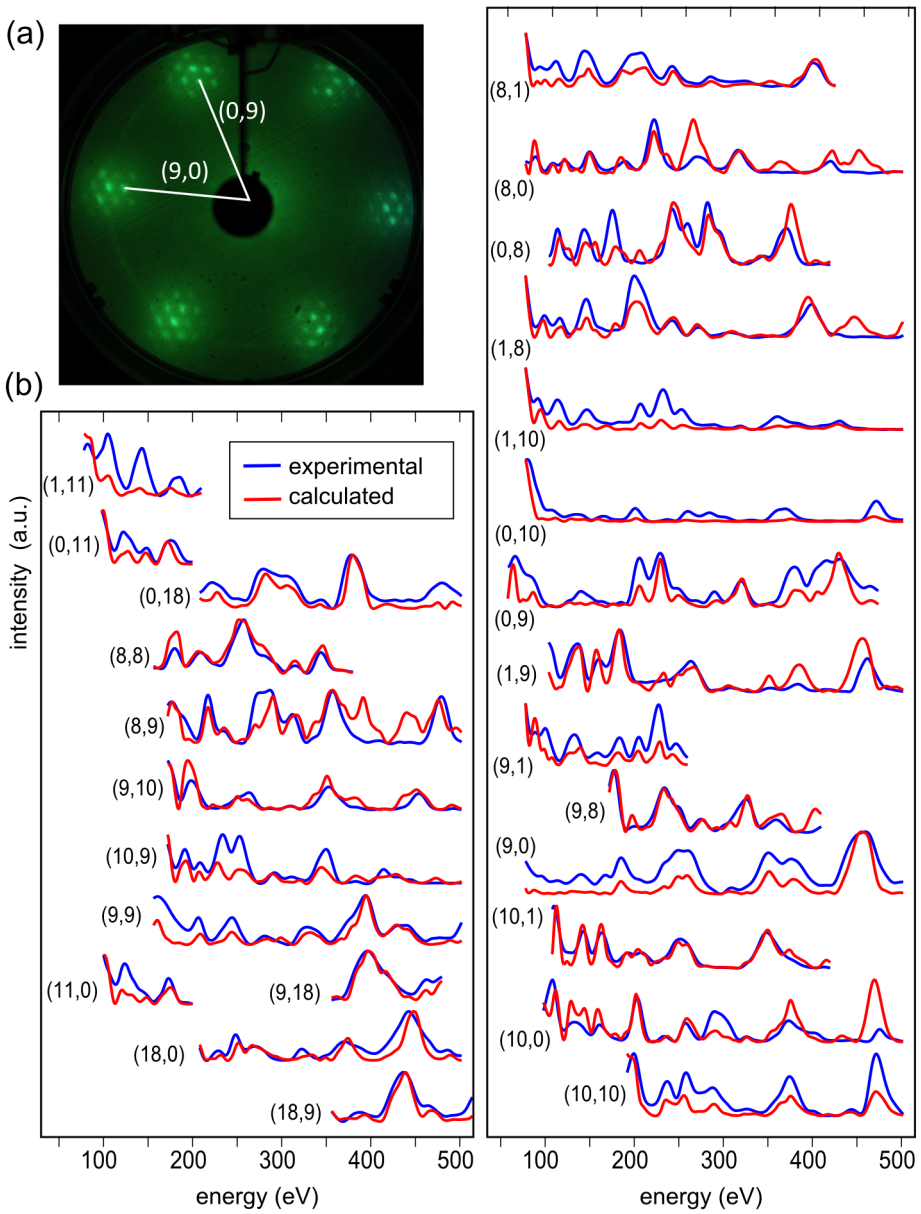

FIGURE 3.1. LEED *I(V)* measurements on graphene/Ir(1 1 1). (a) LEED pattern of graphene on Ir(1 1 1) (78 eV) showing the moiré spots. Illustrated indexed spots correspond to the first-order substrate spots. (b) Comparison of measured (blue) and calculated (red) *I(V)* curves for the best fit (7886 eV, $R_P = 0.39$).

3.3. The LEED *I(V)* experiment

The LEED structure analysis was performed for an Ir(1 1 1)-(9 × 9)-graphene-(10 × 10) structure involving 200 C atoms per unit cell and 243 Ir atoms from the three relaxed Ir layers. In reality, the system is incommensurate but the error made in the graphene lattice constant by forcing a commensurate structure is well under 1% [6, 23]. The dataset consisted of 26 beams presented in Figure 3.1 with an energy range between 40 and 520 eV. The total energy range of the set was 7886 eV.

LEED calculations were restricted to models with *p3m1* symmetry, which was experimentally observed. The beam set neglect method was used [35]. Convergence was checked by comparison with a full calculation for one model. The phase shifts were calculated from a superposition of atomic potentials using optimized muffin-tin radii [36]. Eleven phase shifts were used. A least-squares scheme was used to optimize the structural and thermal parameters in the graphene and top three substrate layers [37]. To reduce the number of free parameters, the modulation was described by Fourier coefficients limited to the third order. Higher-order Fourier coefficients did not improve the final agreement. Lateral shifts were considered for the top graphene layer only, but no clear improvement to the agreement was achieved. Overall, 12 independent Fourier components for lateral and vertical modulations in the graphene layer and in three substrate layers were optimized together with four interlayer distances.

The structure of the moiré unit cell obtained from the LEED *I(V)* calculations is presented in Figure 3.2 and the *I(V)* curves in Figure 3.1. The structure largely agrees with a previous van der Waals (vdW)-density functional theory (DFT) study [6]. Similar to other graphene/metal systems, the graphene Ir distance is largest where the center of the carbon ring is directly above an Ir atom (top site) [Figure 3.2(a)]. The smallest graphene-Ir separation is found in the bridge site region between the hcp and fcc sites [see Figure 3.2(a) for an explanation of the abbreviations]. This is in contrast to the vdW-DFT results where the bridge site region is higher than either of the hollow site regions. The R factor of the calculated LEED *I(V)* data is not very sensitive to the Fourier component causing this small (2 pm) dip around the bridge site, and hence this is likely to be an artifact in the model (see below for AFM results). Not taking into account the dip on the bridge site, the overall corrugation of the graphene layer in the model is 43 ± 9 pm. This is slightly higher, although within the error margins, than the value predicted by vdW-DFT (35 pm) [6].

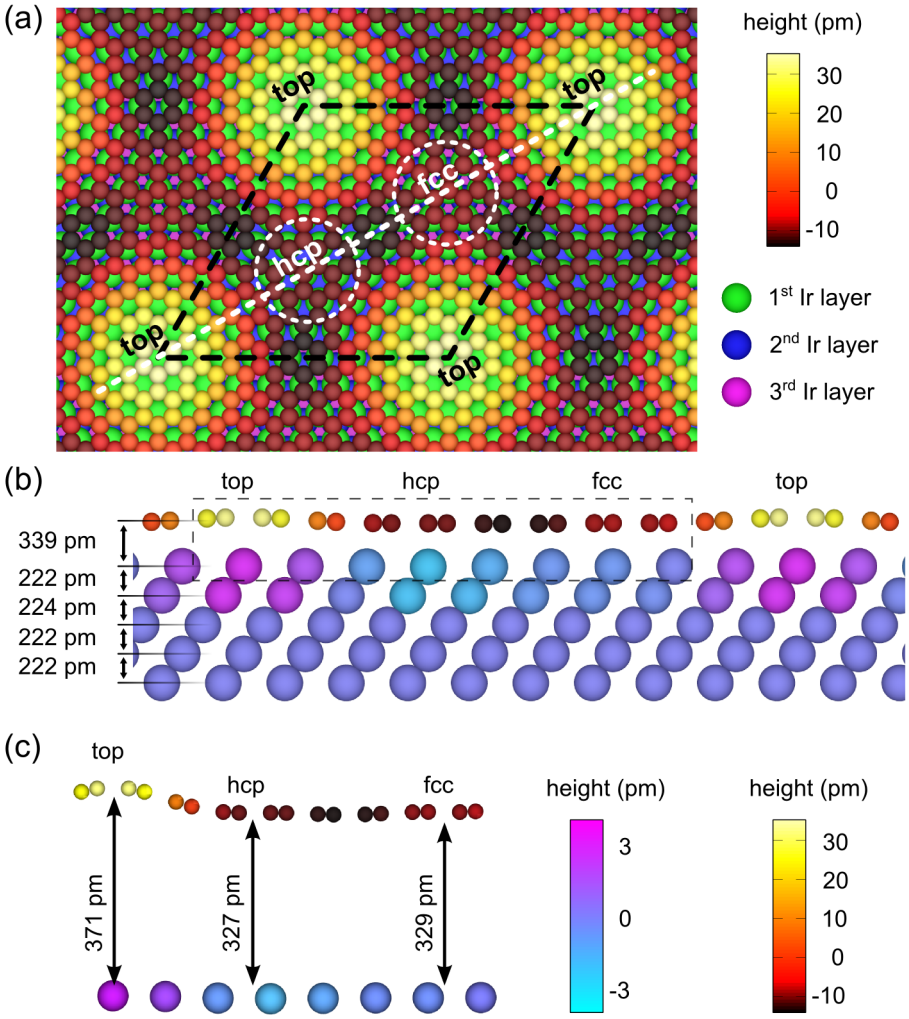

FIGURE 3.2. Structure of the moiré unit cell obtained from LEED *I(V)* calculations. (a) Topographic structure. (b) Cross section through the moiré unit cell along the white dashed line marked in (a). The color scales of the z positions of the atoms are relative to the mean height of the layer given on the left side of the image. (c) Magnification of the area marked with the dashed box in (b). The vertical scale in (c) is magnified fivefold to better illustrate the shape of the graphene layer.

The graphene-Ir separations in the hcp and fcc areas match exactly the values given by vdW-DFT (327 and 329 pm, respectively) [6]. It is worth noting that the optimization for the LEED structure was started from a completely flat layer of graphene not to introduce any bias in the structure. The larger corrugation in our results compared to vdW-DFT is caused by the height of the top site where the graphene-Ir separation from our LEED *I(V)* analysis is 371 pm compared to 362 pm given by vdW-DFT. The mean height of the graphene is 339 ± 3 pm, which is in excellent agreement with both X-ray standing wave (XSW) and vdW-DFT [6]. The first two Ir layers in the best fit LEED structure are also slightly corrugated in phase with the graphene layer. This corrugation is, however, within the limits of error of the LEED *I(V)* calculation. No significant changes in the C-C bond lengths were observed in the LEED model (Δ bond length < 0.3 pm), which is also in line with the DFT results [38].

3.4. The AFM experiment

In addition to LEED *I(V)*, we have used AFM with CO terminated tips to study the atomic scale corrugation of the moiré. As shown in Chapter 2, a CO molecule on the end of the AFM tip is chemically inert on the graphene/Ir(1 1 1) system [24]. When scanning very close to the surface, Pauli repulsion is the dominant force between the tip and carbon atoms [29]. Thus the AFM experiments yield the actual topography of the graphene surface not distorted by local variations in chemical reactivity or local density of states.

Figure 3.3(a) shows an AFM image acquired with a CO terminated tip. Qualitatively the structure is very similar to that obtained from LEED *I(V)* and predicted by vdW-DFT. We can relate the bright hills to the on top sites of the moiré unit cell by comparing to STM images acquired immediately before and after the AFM image. We assign the lower of the fcc and hcp sites to the hcp site, in line with LEED *I(V)* measurements and DFT calculations. In contrast to the LEED *I(V)* structure, the AFM images [cross section in Figure 3.3(b)] show that the bridge site is higher than the fcc and hcp sites, which is in agreement with the vdW-DFT results. Based on XSW measurements, it has been suggested that the moiré corrugation of graphene on Ir is not constant, but changes as a function of graphene coverage [6]. As a local probe AFM can be used to study the order and corrugation of individual graphene islands as a function of their size and environment. We have imaged 14 islands of various sizes and shapes in Figure 3.4, with some of them flowing over or growing from steps and others lying freely on

an iridium terrace. The obtained moiré corrugations as function of island size are plotted in Figure 3.4(a). The AFM measurements were all conducted with a CO tip with a detuning set point of 0 Hz, which corresponds to a repulsive interaction between the CO molecule on the tip and graphene. The tip was characterized before each image by measuring the frequency shift and current as a function of tip-sample distance. The corrugations were extracted from atomically resolved 8×8 nm^2 images by comparing the height of the topmost atoms from each top site to the lowest atoms of the neighboring three hcp sites.

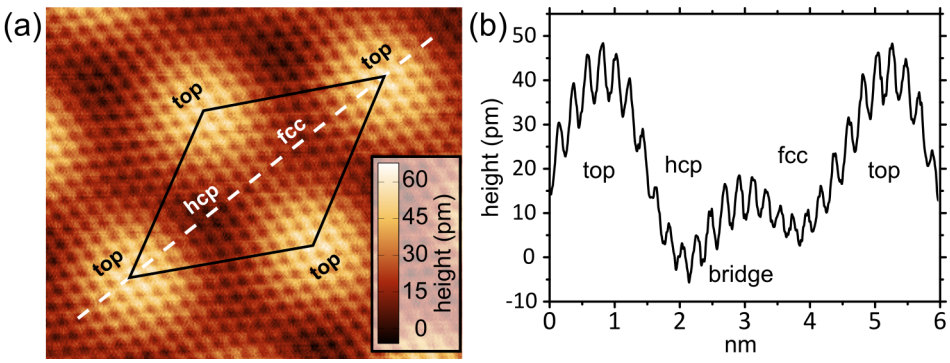

FIGURE 3.3. AFM imaging of the graphene moiré. (a) Constant Δf AFM image of the graphene moiré ($\Delta f = 0$ Hz, bias $= 0$ V). (b) AFM line profile over the moiré unit cell marked with a white dashed line in (a).

The data shown in Figure 3.4(a) shows no definite trend between the island size and moiré corrugation in the studied size range (420–8200 nm^2). What is surprising though is the spread of the measured corrugations (42–56 pm). Neither the moiré rotation, environment, nor island aspect ratio had any correlation with the measured corrugations. Based on the data shown in Figure 3.4, we obtain an estimate of the total corrugation of 47 ± 5 pm, which is in line with the LEED *I(V)* model. The height difference between the fcc and the hcp sites is 5 ± 2 pm.

While analyzing the corrugations we noticed that some of the images had outliers where the top site of one moiré unit cell was much higher than the rest [these cells were excluded from Figure 3.4(a) and from the average values above]. To study the outliers in detail we imaged a much larger area (24×24 nm^2) with atomic resolution from one of the islands [Figure 3.5(a)]. When limiting the contrast of the image to the top sites [Figure 3.5(b)], it is easy to distinguish the

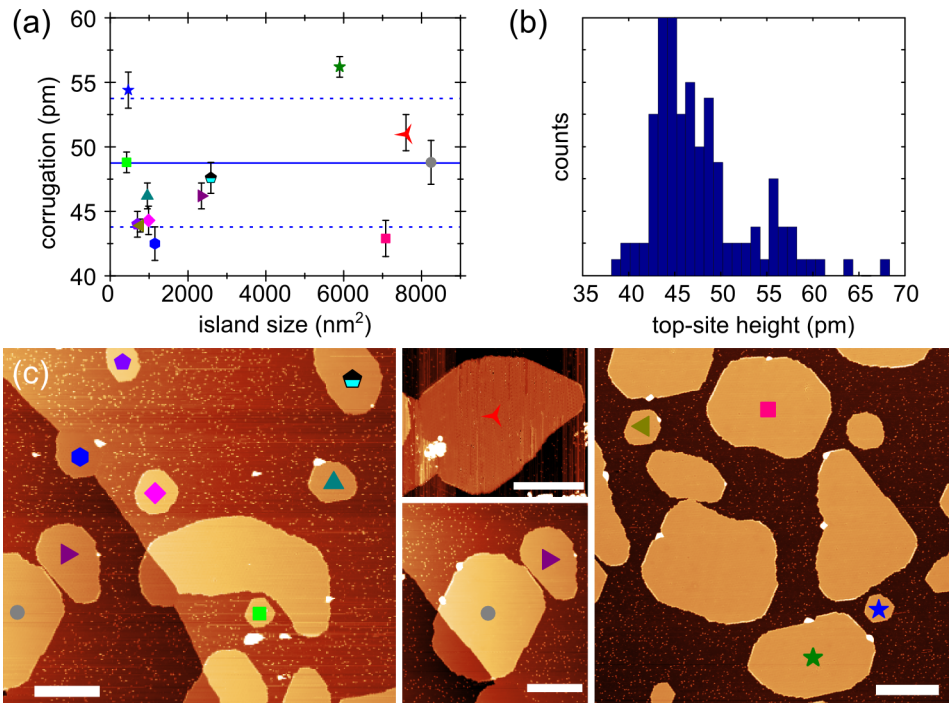

FIGURE 3.4. Comparison of the moiré corrugation for different graphene islands. (a) The moiré corrugation as a function of graphene island size excluding the outliers. The solid line is the average of the set and the dotted lines the standard deviation. (b) Distribution of all the individual top site heights extracted from the AFM images (including outliers). (c) Overview STM scans of the islands in the plot in (a). The scale bar is 50 nm in all images.

higher outliers which are randomly distributed around the scanned area. The atomic contrast on the outliers varies, which indicates that they do not correspond to a specific graphene-substrate registry. Figure 3.5(c) shows the height of each top site with respect to the neighboring hcp sites. As can be seen from the extracted heights, the outliers are all roughly the same height. This is even more evident when plotting the heights in a histogram [Figure 3.5(d)] where the outliers show up as a distinct peak some 10 pm higher than the rest of the top sites. A similar peak is visible in the histogram in Figure 3.4(b) with all the measured moiré heights.

In addition to the outliers, the top site heights in Figure 3.5(c) also exhibit a smooth variation over several moiré unit cells. This variation within one island is of the same magnitude as the differences between the different islands in Figure 3.4. There is a difference between the smooth long range variation and the outliers. The outliers are moiré unit cells where the top site is lifted higher, whereas in the longer range fluctuations the heights of both the top and the hcp site vary.

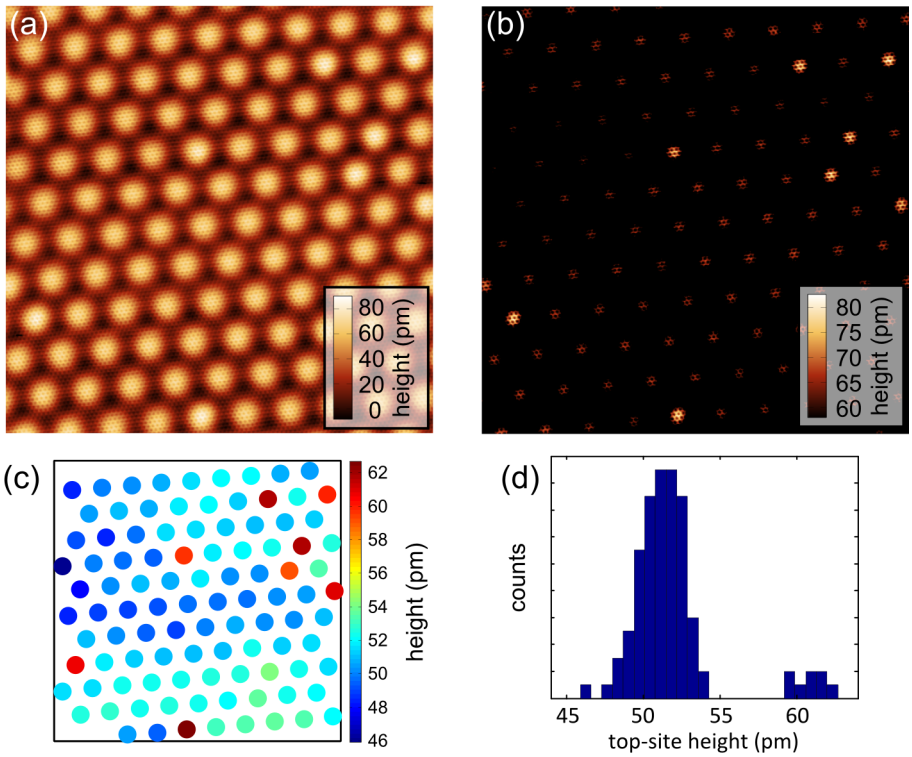

FIGURE 3.5. Deviations of the moiré corrugation within one island. (a) Constant Δf AFM image over a larger area ($\Delta f = 0$ Hz, bias = 0 V, 24×24 nm^2). (b) Same AFM image as in (a) but with the contrast adjusted to the top sites. (c) Heights of the top sites with respect to the neighboring hcp sites. (d) Distribution of the top site heights in (c).

3.5. Discussion and conclusions

There are possible sources of the observed variations in the moiré structure. The unit cell of the moiré structure of graphene/Ir is shown to be incommensurate with respect to both the graphene and Ir lattices [23, 39]. This means that the graphene carbon rings are not exactly on the symmetry sites which are used to describe the structure (top, hcp, fcc) but change slightly from one moiré to the next. In a very simple model, this should produce a repeating second-order moiré structure, where the symmetry sites are closer to the ideal case in some regions than in others. This could affect the local interaction between graphene and iridium, leading to variation in the adsorption heights of the different areas. This is a possible source for the long range variation in the observed moiré corrugation as it would most likely affect both the strongly and weakly bound [6] hollow and top sites of the moiré. The second-order moiré is not expected to be rigid and the structure would be likely to exhibit fluctuations, in line with the variations shown in Figure 3.5.

Spot profile analysis LEED has shown that graphene locks to the Ir substrate already at high temperatures, which upon cooling induces strain in the graphene lattice due to the mismatch in thermal expansion coefficients [40–42]. This locking most likely happens at the edges of the graphene island which strongly interact with the Ir substrate [24, 43, 44]. In large islands the strain is partially relieved by local delamination into wrinkles [45]. The islands we studied are so small that no wrinkling was observed in any of them. However, the outliers could be a way to relieve some strain before complete local delamination. The top sites are weakly bound by vdW forces [6] and hence would be the first sites to accommodate the strain. As the outliers do not correspond to a specific graphene-substrate registry, it is unlikely that they are related to the second-order moiré effect discussed above.

In conclusion, we present an experimental investigation on the local variations in the moiré structure of an incommensurate graphene layer. We attribute these variations to a second-order moiré structure where the exact registry of the moiré symmetry sites changes from one unit cell to the next, and to local strain relief. Our dynamic low-energy electron diffraction experiments yield the average structure and registry of the moiré pattern of epitaxial graphene on Ir(1 1 1). Comparing this structure with AFM experiments shows that AFM imaging can be used to directly yield the local surface topography with pm accuracy on 2-D structures. This type of information is likely to be important in a detailed understanding of the electronic properties of weakly interacting incommensurate 2-D structures, such as graphene on hexagonal boron nitride.

3.6. Bibliography

[1] Geim, A. K. & Novoselov, K. S. The rise of graphene. *Nature Materials* **6**, 183–191 (2007).

[2] Xue, J. *et al.* Scanning tunnelling microscopy and spectroscopy of ultra-flat graphene on hexagonal boron nitride. *Nature Materials* **10**, 282–285 (2011).

[3] Vogt, P. *et al.* Silicene: compelling experimental evidence for graphenelike two-dimensional silicon. *Physical Review Letters* **108**, 155501 (2012).

[4] Chen, L. *et al.* Evidence for Dirac fermions in a honeycomb lattice based on silicon. *Physical Review Letters* **109**, 056804 (2012).

[5] Wintterlin, J. & Bocquet, M.-L. Graphene on metal surfaces. *Surface Science* **603**, 1841–1852 (2009).

[6] Busse, C. *et al.* Graphene on Ir(111): physisorption with chemical modulation. *Physical Review Letters* **107**, 036101 (2011).

[7] Pletikosić, I. *et al.* Dirac cones and minigaps for graphene on Ir(111). *Physical Review Letters* **102**, 056808 (2009).

[8] Yankowitz, M. *et al.* Emergence of superlattice Dirac points in graphene on hexagonal boron nitride. *Nature Physics* **8**, 382–386 (2012).

[9] Ponomarenko, L. A. *et al.* Cloning of Dirac fermions in graphene superlattices. *Nature* **497**, 594–597 (2013).

[10] Dean, C. R. *et al.* Hofstadter's butterfly and the fractal quantum Hall effect in moiré superlattices. *Nature* **497**, 598–602 (2013).

[11] Wang, B., Bocquet, M.-L., Marchini, S., Günther, S. & Wintterlin, J. Chemical origin of a graphene moiré overlayer on Ru(0001). *Physical Chemistry Chemical Physics* **10**, 3530–3534 (2008).

[12] Berner, S. *et al.* Boron nitride nanomesh: functionality from a corrugated monolayer. *Angewandte Chemie International Edition* **46**, 5115–5119 (2007).

[13] Corso, M. *et al.* Boron nitride nanomesh. *Science* **303**, 217–220 (2004).

[14] Marchini, S., Günther, S. & Wintterlin, J. Scanning tunneling microscopy of graphene on Ru(0001). *Physical Review B* **76**, 075429 (2007).

[15] Moritz, W. *et al.* Structure determination of the coincidence phase of graphene on Ru(0001). *Physical Review Letters* **104**, 136102 (2010).

[16] Iannuzzi, M. *et al.* Moiré beatings in graphene on Ru(0001). *Physical Review B* **88**, 125433 (2013).

[17] Coraux, J. *et al.* Growth of graphene on Ir(111). *New Journal of Physics* **11**, 023006 (2009).

[18] Sutter, P., Sadowski, J. T. & Sutter, E. Graphene on Pt(111): growth and substrate interaction. *Physical Review B* **80**, 245411 (2009).

[19] Wu, M.-C., Xu, Q. & Goodman, D. W. Investigations of graphitic overlayers formed from methane decomposition on Ru(0001) and Ru(11.hivin.20) catalysts with scanning tunneling microscopy and high-resolution electron energy loss spectroscopy. *The Journal of Physical Chemistry* **98**, 5104–5110 (1994).

[20] Klink, C., Stensgaard, I., Besenbacher, F. & Laegsgaard, E. An STM study of carbon-induced structures on Ni(111): evidence for a carbidic-phase clock reconstruction. *Surface Science* **342**, 250–260 (1995).

[21] Land, T., Michely, T., Behm, R., Hemminger, J. & Comsa, G. STM investigation of single layer graphite structures produced on Pt(111) by hydrocarbon decomposition. *Surface Science* **264**, 261–270 (1992).

[22] Sun, Z. *et al.* Topographic and electronic contrast of the graphene moiré on Ir(111) probed by scanning tunneling microscopy and noncontact atomic force microscopy. *Physical Review B* **83**, 081415 (2011).

[23] N'Diaye, A. T., Coraux, J., Plasa, T. N., Busse, C. & Michely, T. Structure of epitaxial graphene on Ir(111). *New Journal of Physics* **10**, 043033 (2008).

[24] Boneschanscher, M. P. *et al.* Quantitative atomic resolution force imaging on epitaxial graphene with reactive and nonreactive AFM probes. *ACS Nano* **6**, 10216–10221 (2012).

[25] N'Diaye, A., Bleikamp, S., Feibelman, P. & Michely, T. Two-dimensional Ir cluster lattice on a graphene moiré on Ir(111). *Physical Review Letters* **97**, 215501 (2006).

[26] Altenburg, S. J. *et al.* Graphene on Ru(0001): contact formation and chemical reactivity on the atomic scale. *Physical Review Letters* **105**, 236101 (2010).

[27] Vázquez de Parga, A. *et al.* Periodically rippled graphene: growth and spatially resolved electronic structure. *Physical Review Letters* **100**, 056807 (2008).

[28] Voloshina, E. N. *et al.* Electronic structure and imaging contrast of graphene moiré on metals. *Scientific Reports* **3**, 1072 (2013).

[29] Gross, L. *et al.* Measuring the charge state of an adatom with noncontact atomic force microscopy. *Science* **324**, 1428–1431 (2009).

[30] Pavliček, N. *et al.* Atomic force microscopy reveals bistable configurations of dibenzo[a,h]thianthrene and their interconversion pathway. *Physical Review Letters* **108**, 086101 (2012).

[31] van der Lit, J. *et al.* Suppression of electron-vibron coupling in graphene nanoribbons contacted via a single atom. *Nature Communications* **4**, 2023 (2013).

[32] de Oteyza, D. G. *et al.* Direct imaging of covalent bond structure in single-molecule chemical reactions. *Science* **340**, 1434–1437 (2013).

[33] Schuler, B. *et al.* Adsorption geometry determination of single molecules by atomic force microscopy. *Physical Review Letters* **111**, 106103 (2013).

[34] Bartels, L. *et al.* Dynamics of electron-induced manipulation of individual CO molecules on Cu(111). *Physical Review Letters* **80**, 2004–2007 (1998).

[35] Van Hove, M., Lin, R. & Somorjai, G. Efficient scheme for calculation of low-energy electron-diffraction intensities in the presence of large superlattices, with application to the structural analysis of benzene adsorbed on Rh(111). *Physical Review Letters* **51**, 778–781 (1983).

[36] Rundgren, J. Optimized surface-slab excited-state muffin-tin potential and surface core level shifts. *Physical Review B* **68**, 125405 (2003).

[37] Over, H., Moritz, W. & Ertl, G. Optimization methods and their use in low-energy electron-diffraction calculations. *Physical Review B* **46**, 15438–15446 (1992).

[38] Seitsonen, A. P. & Busse, C. private communication (2013).

[39] Blanc, N. *et al.* Local deformations and incommensurability of high-quality epitaxial graphene on a weakly interacting transition metal. *Physical Review B* **86**, 235439 (2012).

[40] Hattab, H. *et al.* Interplay of wrinkles, strain, and lattice parameter in graphene on iridium. *Nano Letters* **12**, 678–682 (2012).

[41] Pozzo, M. *et al.* Thermal expansion of supported and freestanding graphene: lattice constant versus interatomic distance. *Physical Review Letters* **106**, 135501 (2011).

[42] Jean, F. *et al.* Effect of preparation on the commensurabilities and thermal expansion of graphene on Ir(111) between 10 and 1300 K. *Physical Review B* **88**, 165406 (2013).

[43] Lacovig, P. *et al.* Growth of dome-shaped carbon nanoislands on Ir(111): the intermediate between carbidic clusters and quasi-free-standing graphene. *Physical Review Letters* **103**, 166101 (2009).

[44] Li, Y. *et al.* Absence of edge states in covalently bonded zigzag edges of graphene on Ir(111). *Advanced materials* **25**, 1967–1972 (2013).

[45] N'Diaye, A. T. *et al.* In situ observation of stress relaxation in epitaxial graphene. *New Journal of Physics* **11**, 113056 (2009).

4

Can exact atomic positions be measured by non-contact AFM?

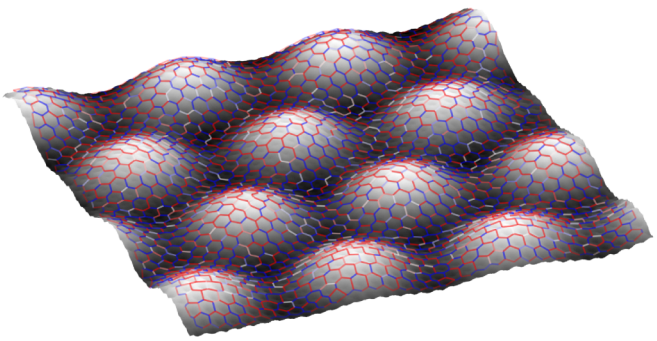

This chapter[1] describes the fundamental limits in precision for AFM imaging of atomic positions and chemical bonds using CO-terminated tips. Using epitaxial graphene as a model system, we demonstrate experimentally that the apparent atomic positions measured by AFM depend on the sample corrugation. Using molecular mechanics simulations, we explain these observations by the interplay of the CO bending and the non-linear background signal arising from the neighboring atoms. These effects depend non-trivially on the tip-sample distance and limit the achievable accuracy on the bond length determination based on AFM experiments.

[1]This chapter is based on M.P. Boneschanscher, S.K. Hämäläinen, P. Liljeroth, and I. Swart, *ACS Nano* **8**, 3006–3014 (2014).

4.1. The use of AFM with CO terminated tips in imaging single molecules

Imaging individual planar molecules with atomic resolution is now possible using frequency modulation atomic force microscopy (FM-AFM) [1–10]. Besides structure determination, AFM can also provide more quantitative information. For example, different atomic species can be identified [11–13], and the charge distribution inside a single molecule measured [3]. Recently, it was shown that the apparent height and length of bonds in planar molecules is correlated to the bond order [4]. It is even possible to visualize intermolecular hydrogen bonding using AFM [14]. Because of these new capabilities, AFM could be used for structural chemistry at the single molecule level [2, 7, 8, 10, 15].

In all cases where atomic resolution was demonstrated, the experiments were performed in constant height mode. In this mode, the tip is raster scanned over the surface on a fixed plane, *i.e.*, the tip does not follow the corrugation of the surface. Instead, the frequency shift is measured as a function of position. In addition, in all experiments chemically passivated tips were used, typically a carbon monoxide (CO) molecule adsorbed on the apex. Inert tips are essential to avoid accidental pick-up of the molecule of interest by the tip at the small distances and oscillation amplitudes required for atomic resolution imaging. The geometry of the CO in the junction depends on the tip-sample distance and on the crystallographic termination of the tip apex [16]. Attractive van der Waals and repulsive Pauli interactions can cause the CO molecule to bend [17, 18]. The direction of this bending depends also on the neighboring atoms: if their positions are not symmetric with respect to the atom directly under the AFM tip, there is a non-symmetric background force on the CO. This lateral force causes the CO molecule to bend and results in a shift in the apparent atomic positions. The quantitative details of how non-planarity and the associated degree of CO bending and background forces from the neighboring atoms affect the atomic positions extracted from AFM have not been established. Knowledge of these details is essential in assessing the experimentally achievable certainty in the atomic positions extracted from AFM measurements. This has a direct consequence in the validity of AFM as a tool in single molecule structural chemistry.

Here, we study experimentally and computationally how accurately the atomic positions can be extracted from AFM measurements using CO terminated tips. We use epitaxial graphene [19, 20] as a model system. This material is ideally suited for this investigation as, due to a lattice mismatch between graphene and the Ir(1 1 1) substrate, the epitaxial layer exhibits a periodic physical buckling. The vertical

corrugation is small enough to allow simultaneous atomic resolution imaging of both the top and valley sites in constant height mode, see also Chapter 2 [20, 21]. In addition, the exact atomic scale structure of this system is known, see also Chapter 3 [19, 22–24].

4.2. Materials and methods

Epitaxial graphene on Ir(1 1 1) was grown from ethylene using the temperature programmed growth method as described in Chapter 2 [25–29]. The experiments were performed using the low-temperature STM/AFM setup described in Chapter 2. All images were taken with a bias voltage of 0 V. Tip preparation was done as described in Chapter 3 [24].

In order to determine the bond lengths we used a combination of template matching, Voronoi analysis and spline fitting using MATLAB®. First, the experimental images are averaged over forward and backward scan direction and filtered with a Gaussian filter ($\sigma \leq 1$ Å) to remove 'salt-and-pepper' noise. A spherical mask is created, consisting of a dark ring matching the size of the hollow sites of the hexagons and a bright ring around it. The correlation coefficient for each pixel of the image is calculated according to

$$\rho_{AB} = \frac{\langle AB \rangle - \langle A \rangle \langle B \rangle}{\sigma_A \sigma_B} \tag{4.1}$$

where $\sigma_A = \left\langle A^2 \right\rangle - \langle A \rangle^2$, $\sigma_B = \left\langle B^2 \right\rangle - \langle B \rangle^2$ and A and B are the intensities of mask and masked area of the image, respectively. The resulting correlation image was binarized at a value of typically +0.35 and segmented by means of connected-component labeling. Finally, the centers of the hexagons were detected by taking the center of mass of each image segment. Then a Voronoi analysis was used to detect the nearest neighbors of each hexagon. The lines connecting each hexagon to its nearest neighbors were extracted as height/intensity profiles. The maximum of these profiles was detected by spline fitting, giving us the center position of each carbon-carbon bond in the image. The positions of the carbon atoms were then detected as the intersection of lines fitted through these points.

For the AFM simulations a MATLAB® code was used to simulate the CO bending and calculate the forces on the tip after CO relaxation. All forces were modeled with a Lennard–Jones-type 9–6 potential [30]. Four different force components were taken into account, namely CO–graphene, CO–bulk Ir substrate, bulk tip–graphene, and bulk tip–bulk Ir substrate. In order to relax the CO, the forces exerted on it were calculated in vector format while for the other forces

only the z-component was taken into account. The bulk tip was modeled as a continuum Ir sphere with a radius of 10 nm. Analytic formulas derived based on Reference [31] were used to calculate the bulk forces at each point. In simulations on graphene, the CO molecule was offset by 6 Å from the spherical bulk tip in order to mimic a micro tip most likely present in the measurements. This offset was set to zero in the simulations involving pentacene. The forces were calculated in a cube with a typical step size of around 5 pm in all directions. For the cross sections, a lateral step size of 1 pm was used. Only the force on the oxygen atom of the CO was taken into account in the relaxation. The oxygen atom was allowed to move on the spherical surface with a radius defined by the sum of the CO adsorption height and the bond length (3 Å). The displacement of the oxygen used in calculating the spring force of the CO was taken along the spherical surface, *i.e.*, not directly as the lateral displacement. The CO was relaxed self-consistently in each point of the cube until the lateral displacement between iterations was less than 5 fm or when the maximum of 80 iterations was reached. Usually the forces converged well before the maximum number of iterations was reached. Only in some cases at extremely close tip-sample distances the maximum number of iterations was reached.

4.3. Bond lengths in AFM measurements with a CO tip on a non-planar surface

The structure of graphene on Ir(1 1 1) as adapted from the dynamic low-energy electron diffraction [LEED-*I(V)*] measurements described in Chapter 3 [19, 24] is shown in Figure 4.1(a). The lattice mismatch between the graphene layer and the underlying Ir(1 1 1) substrate gives rise to a moiré pattern as described in Chapter 3. Different regions of the moiré unit cell have different graphene to Ir(1 1 1) registries and we follow the common practice in naming these areas: top (graphene hexagon on top of an underlying Ir atom), fcc and hcp regions within the moiré pattern [19, 32]. A schematic of the AFM experiment is shown in Figure 4.1(b) and an example of a constant-height AFM image obtained with a CO tip is shown in Figure 4.1(c). Besides the clear honeycomb arrangement of the carbon atoms, the periodic buckling of the graphene layer can be seen. This buckling corresponds to the moiré pattern [19, 24]. The moiré unit cell is indicated in Figure 4.1(c) along with the different areas indicated in Figure 4.1(a): top (green hexagon), hcp / fcc (red star / blue triangle) and bridge sites (purple line), respectively.

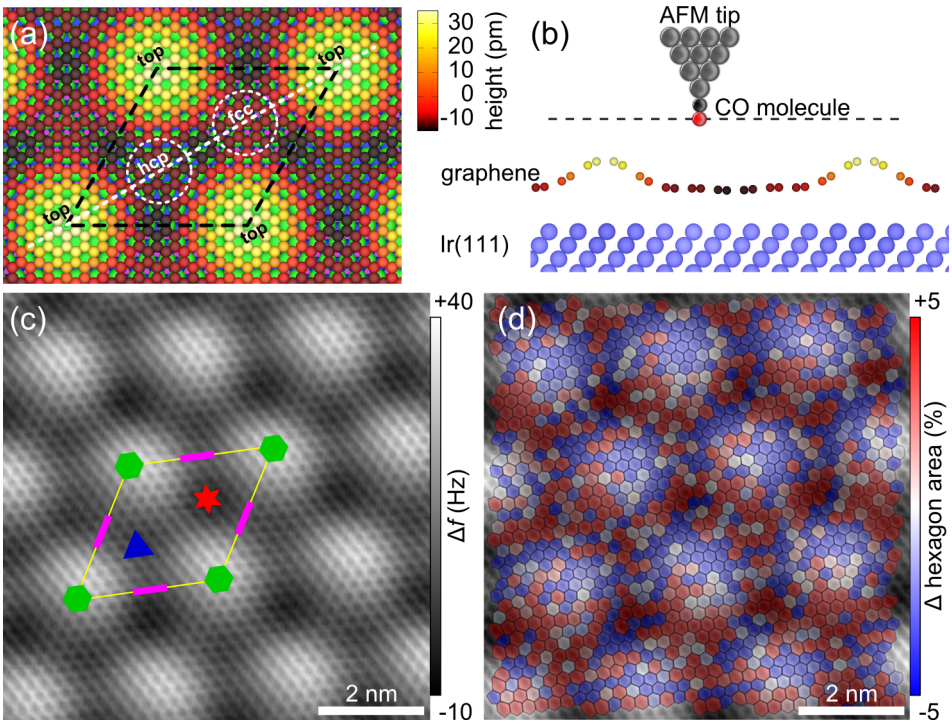

FIGURE 4.1. AFM experiments on epitaxial graphene on Ir(1 1 1). (a) Structure of the graphene on Ir(1 1 1) surface, where the moiré unit cell and the regions with different average graphene-Ir(1 1 1) registries are indicated. (b) Schematic of the AFM experiments with a CO-modified tip apex. (c) Constant height AFM image of the graphene/Ir(1 1 1) substrate obtained on the repulsive branch of the Δf *vs* tip-sample distance curve using a CO-terminated tip. The moiré unit cell is indicated by yellow lines. Green hexagons indicate top sites, purple lines bridge sites and blue triangle and red star fcc and hcp sites, respectively. (d) Color coded map of the apparent graphene hexagon area.

We analyzed the AFM data by extracting the area of each six-membered carbon ring (See Section 4.2). Figure 4.1(d) shows the same image as Figure 4.1(c), overlaid with hexagons color-coded to indicate the relative size of each cell compared to the average value. It is immediately clear that the hexagons at the moiré top sites are significantly smaller than the hexagons in the hcp and fcc sites. These

deviations from average can be as large as ±15%. This implies that the C-C bonds at the top sites of the moiré pattern should be shorter than those at the hcp and fcc sites. A difference in area of ±15% approximately corresponds to an average difference in bond length of 20 pm.

The 3-D structure of graphene on Ir(1 1 1) has been established by both DFT calculations and LEED-*I(V)*, see Chapter 3 [19, 22–24]. Both methods indicate that the variation in the C-C bond length across the moiré unit cell is very small: the difference between the shortest and longest bond is less than 0.3 pm. This is in strong contrast to the AFM result, where the difference between the longest and shortest bond can be as large as 15% of the bond length. This difference is of the same order as the difference in the bond length of C-C single (154 pm) and aromatic double bonds (139 pm) [33]. Such large differences between bonds in epitaxial graphene are unphysical. Considering the arguments outlined above, it is clear that the variations that we see in AFM are not due to actual differences in bond length but are instead related to the imaging mechanism.[2]

4.4. Shifting atoms: pentacene as a test case

In constant height AFM experiments, there are several variables that affect apparent bond lengths. First of all, it is well-known that the CO at the tip apex is flexible and can bend in response to attractive vdW and repulsive Pauli interactions [4, 17]. As the tip-sample distance varies in the constant height mode (the sample is vertically corrugated), the CO bending will vary and this might give rise to the observed changes in the bond lengths. Secondly, when the tip is exactly on top of a carbon atom, the distance to the neighboring atoms will be different if the sample is corrugated. This will give rise to a different background contribution to the measured force, which will also shift the apparent atomic positions.

We have investigated these effects in detail by constructing a model of the AFM experiments based on a molecular mechanics force field between the CO molecule and the sample (see Section 4.2 for details). The model system is depicted in Figure 4.2(a). The main tunable parameters are the lateral spring constant of the CO molecule at the tip apex (k_{CO}), the bulk tip radius of curvature (R_{tip}) and the offset between the CO molecule and the bulk tip apex (d_{CO}, due to,

[2]We would like to note here that the frequency shift on top of a bond in constant height mode has been used as an indicator for bond-order in addition to the bond length [4]. This parameter cannot be used for analyzing bonds on corrugated samples as it relies on constant tip-bond distance.

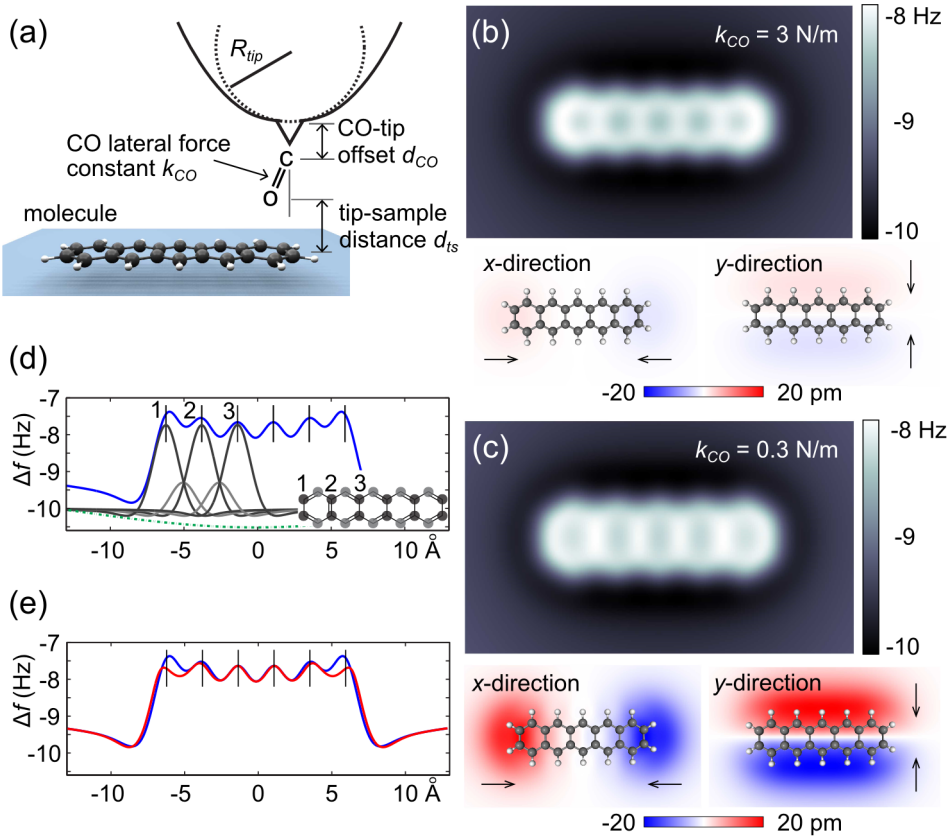

FIGURE 4.2. 'Ball-and-stick'-modeling of AFM imaging with a CO-terminated tip. (a) Schematic of the model setup and the relevant parameters. (b,c) Simulated constant height AFM images of pentacene (top) with a relatively stiff (b, $k_{CO} = 3$ N/m) and soft (c, $k_{CO} = 0.3$ N/m) CO lateral force constant and the corresponding maps of the CO bending (bottom). The arrows indicate the direction of the CO bending. (d) Extracted line profile along the center of the pentacene molecule for a non-flexible tip. The contributions from the individual dimers (black and gray lines, the corresponding atoms are indicated in the inset) and the overall vdW background between the CO molecule and the pentacene (green dotted line) have been shifted for clarity. (e) Extracted line profiles along the center of the pentacene molecule for the tips considered in panels (b) and (c). Blue and red lines correspond to lateral force constants of 3 and 0.3 N/m, respectively.

for example, the presence of a metal cluster at the end of the tip). The latter two parameters mostly affect the depth of the minimum of the Δf *vs* tip-sample distance (d_{ts}) curves. These have been selected such that reasonable agreement with experimental results is obtained. While this model is more simplistic than the DFT calculations performed in, for example, References [4, 17, 34, 35], the major advantage of the force field based modeling is that we can freely vary the lateral spring constant of the CO molecule at the tip apex, and thereby study the influence of the tip flexibility. In DFT calculations, this number is fixed by the choice of the metal cluster used as a tip model. Previous studies suggest the spring constant to be of the order of 0.1–3 N/m [4, 16] and we explore this range to assess its effect on the measured response. Finally, to facilitate direct comparison with experimental results, we convert the calculated force cube into Δf data [36, 37].

To validate the simulations and to check the predictions on a well-studied model system, we have first considered a pentacene molecule adsorbed directly on a metal (Figure 4.2). Calculated constant height Δf maps with two different lateral spring constants are shown in Figure 4.2(b,c). Both strongly resemble experimental AFM images of pentacene. Especially the result obtained with the smaller k_{CO} is in essentially quantitative agreement with the experiment [1]. The simulations accurately reproduce the three main experimental observations of deviations between the real pentacene bond lengths and the apparent bond lengths in the AFM experiments: (a) all the phenyl rings are elongated in the y-direction [1]; (b) the left and rightmost phenyl rings are also elongated in the x-direction [1]; (c) as the tip-sample distance is reduced, the bonds appear sharper in the constant height Δf maps [4].

The bottom panels of Figure 4.2(b,c) show the tip bending in the x- and y-direction for the stiffer and softer tips, respectively. The overall bending at the outer edge of the molecule is always towards the center of the molecule and is caused by the attractive vdW interaction between the CO molecule and the pentacene. A more detailed investigation reveals changes when going over the atoms as well: the tip can bend away from the nearest atom irrespective of the vdW background at sufficiently short tip-sample distances. The maximum tip displacement is of the order of a couple of pm for the stiffer tip, but can reach several tens of pm for the softer tip. This naturally depends on the tip-sample distance, with the CO bending more at smaller d_{ts}.

Before discussing the effect of CO bending in detail, we will first investigate how the background forces from the neighboring atoms affect the apparent atomic

positions. Figure 4.2(d) shows an extracted Δf line profile (blue line) along the center of the pentacene molecule for a non-flexible tip ($k_{CO} = \infty$). The peaks in Δf correspond to the apparent positions of the carbon dimers along the middle of the pentacene molecule. Their real positions are marked by vertical lines. The contributions to the total Δf signal from the individual dimers are given by the black solid lines (the gray lines give the response of the outer most carbon atoms, see inset for a schematic). The green dotted line gives the overall van der Waals attraction between the bulk Ir tip and the pentacene molecule.

It is immediately obvious that the peaks corresponding to the left and right-most carbon atoms are shifted towards the center of the molecule. This effect is large (the lateral shift is around 25 pm) and it is due to the asymmetric background signal from the neighboring atoms. The AFM measures the total Δf and the signal from the neighboring atoms (the last dimer has neighboring atoms on only one side) causes an apparent shift in the position of the C-C bond. The peak corresponding to dimer 2 is also shifted towards the left, *i.e.*, the outermost benzene ring is contracted on both sides. This small shift (around 5 pm depending on the tip height) is due to the slope of the vdW background between the tip and whole pentacene molecule. This effect is of course also present on the last dimer, but there the asymmetry in the neighboring atoms has the dominant contribution. In planar molecules, these effects will always cause an apparent contraction towards the center of the molecule of the outermost rings.

Finally, Figure 4.2(e) compares the extracted Δf line profiles along the center of the pentacene molecule, for both the case of a stiff ($k_{CO} = 3$ N/m, blue line) and soft ($k_{CO} = 0.3$ N/m, red line) CO tip. The results obtained with the stiffer tip are quantitatively very close to the non-flexible tip discussed in Figure 4.2(d). As k_{CO} becomes smaller, the bending of the CO increases. In general, the vdW attraction causes the molecule to bend towards the center of the pentacene. As a result, the outermost bonds appear stretched, both in x- and y-directions. Hence, the effect of tip flexibility is opposite to that of the asymmetric background forces. Which effect is dominant depends on the lateral force constant of the CO and on the tip-sample distance. Note that it is problematic to assess the effect of tip flexibility by DFT calculations, due to the difficulties in varying k_{CO}.

4.5. Shifting atoms: the graphene on Ir(1 1 1) moiré case

Having established the different mechanisms affecting the apparent locations of the bonds, we now turn to the buckled graphene moiré. Figure 4.3(a) shows a

simulated constant height image of the graphene/Ir(1 1 1) surface using coordinates adapted from the LEED-*I(V)* experiments described in Chapter 3 [24]. The left hand side of the image is obtained with a lateral spring constant of 0.6 N/m and the right hand side with 3 N/m. With the softer tip one can clearly see the sharpening of the bonds caused by the CO bending away from the carbon atoms near the top sites of the moiré where the tip-sample distance is the smallest. Comparison of the simulated and experimental images suggests that the tip in these experiments on graphene on Ir was laterally stiffer than the tip used for the experiments on pentacene [1]. A variation in the lateral spring constant is not surprising, as the stiffness depends on the exact atomic configuration of the tip and also on the on the tip material [4]. Here, the tip apex is likely to be coated by iridium atoms compared to the Cu tip used in the pentacene experiment.

We find that the CO at the tip apex generally bends towards the top sites due to the increased vdW attraction, in line with what we observed for the pentacene molecule. However, near the top sites of the moiré the tip-sample distance is smaller, causing the tip to flip from side to side when going over the carbon bonds. This results in bonds that appear sharper on the top sites in the constant height image. This sharpening is clearly seen in Figure 4.3(a) and in the cross section shown in Figure 4.3(b). The effect of the CO bending on the apparent bond lengths is difficult to observe directly in the simulated constant height images. This is caused by the fact that the same background will shift broader peaks more than sharp ones. While the local maximum of the Δf signal for the softer tip (blue line) is closer to the real atomic position [shift 11 pm in Figure 4.3(b) inset] than with the stiffer tip [shift 17 pm in Figure 4.3(b) inset], it is impossible to deconvolve the effects of the bond sharpening effect and the tip bending towards the top site, as both will always be present.

As can be seen in Figure 4.3(b), the bonds shift towards the nearest top site for both tip stiffnesses. Hence, benzene rings near the moiré top sites appear smaller, which is in qualitative agreement with the experimental data shown in Figure 4.1(d). The effect is similar to pentacene imaged with a stiff tip, where the non-homogeneous contribution from the neighboring atoms to the Δf signal dominates over the tip bending. The neighboring atoms around the moiré top site are closer to the tip and thus have a larger contribution to Δf signal. Hence, the contribution from the neighboring atoms to the total Δf signal can be positive, even when the force between the tip and these atoms is attractive.

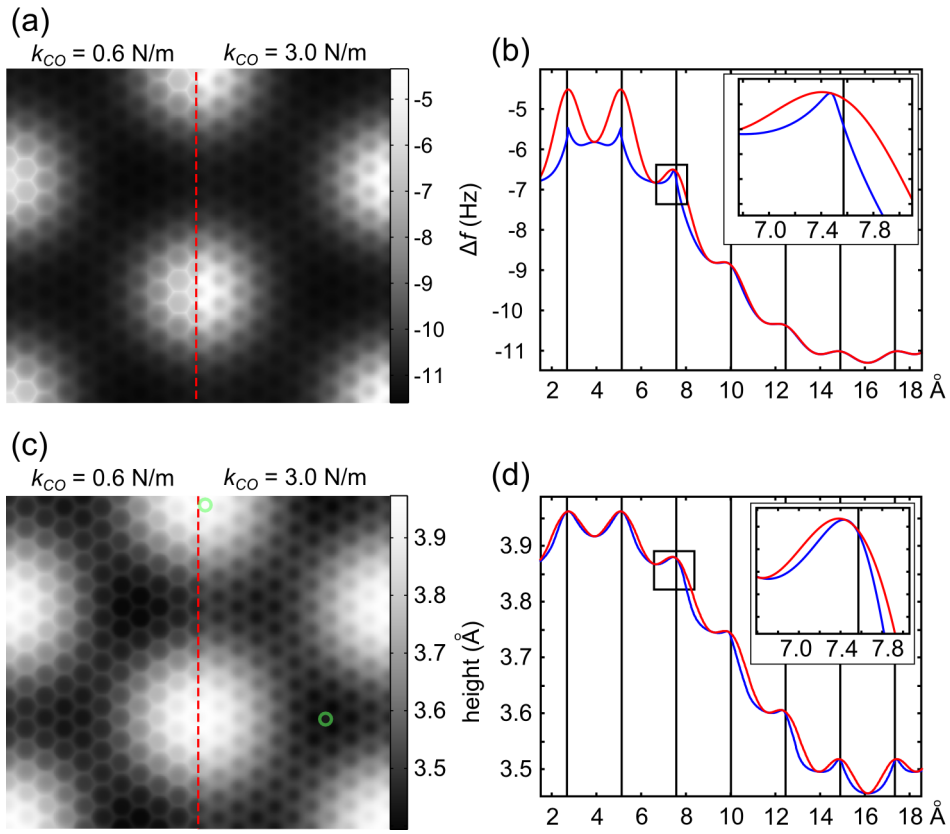

FIGURE 4.3. Simulated AFM images for the graphene moiré. (a) Simulated constant height images (average tip height with respect to the graphene top site is 3.8 Å) with a soft (left, $k_{CO} = 0.6$ N/m) and a stiff (right, $k_{CO} = 3$ N/m) tip. (b) Cross-section from the constant height image in panel (a) taken along the dotted line from top to bridge site for the two CO spring constants (blue 0.6 N/m, red 3 N/m). The black lines mark the real positions of the bonds in the input file for the simulation. The inset shows a close up of one of the bonds. (c) Simulated constant frequency shift images (at $\Delta f = -8$ Hz) with a soft (left, $k_{CO} = 0.6$ N/m) and a stiff (right, $k_{CO} = 3$ N/m) tip. (d) Cross-section along dotted line in panel (c) from top to bridge site for the two CO spring constants (blue 0.6 N/m, red 3 N/m). The black vertical lines denote the actual positions of the bonds. The inset shows a close up of one of the bonds.

The AFM can also be operated in feedback mode where the frequency shift Δf is kept constant by adjusting the height of the tip relative to the sample. To first order, this eliminates the spatial variation of the tip-sample distance for corrugated samples. Hence, the degree of the CO bending as the tip passes over a substrate atom should no longer be spatially dependent. As such, constant frequency shift experiments and simulations can give further insight into which factors are dominant for determining atomic positions. Figure 4.3(c) shows two simulated constant Δf images with different CO spring constants (0.6 N/m and 3 N/m) at $\Delta f = -8$ Hz (in the repulsive branch of the Δf *vs* d_{ts}). Compared to the constant height images in Figure 4.3(a), the atomic corrugation is more uniform across the unit cell since in constant-frequency shift mode the tip effectively follows the surface contours. As can be seen in Figure 4.3(d), the bonds are slightly contracted towards the top sites similarly to the constant height case. The softer tip is again closer to the true positions with the different bonds being shifted by 4–16 pm compared to 6–28 pm for the stiffer tip. Going closer to the sample by increasing the Δf setpoint decreases the shift somewhat but even when going extremely close, the bonds on the sloping part of the moiré are still shifted by over 10 pm. At very close distances the CO bending actually reverses: the CO starts bending outwards from the moiré top sites [Figure 4.4(a,b)]. This is the point where the CO finally starts to feel repulsion from the neighboring atoms. With a setpoint of -8 Hz, the tip just barely reaches this area where it bends outwards on top of the underlying bond at the very bottom of its oscillation cycle [dotted line in Figure 4.4(a)]. Whether this point is reached at a given Δf depends largely on the shape of the bulk tip and the oscillation amplitude of the tip.

Contrary to the constant height mode where the bonds appeared sharpest near the moiré top sites, the bonds in constant Δf are sharpest near the moiré hcp and fcc sites. This is especially clear for the softer tip [left hand side in Figure 4.3(c)]. The sharpness of the bonds is a consequence of a smaller tip-graphene distance. The reason for the tip being pushed closer is the increase of the long range vdW forces from the bulk tip. Even if the repulsive part of the force increases very sharply at close distances, the additive character of the vdW forces combined with the sheer size of the bulk tip is enough to push it closer. This effect is similar the one reported previously, where the modeling was done in the attractive side of the Δf *vs* d_{ts} slope and hence caused an inverse effect (underestimation of the moiré corrugation) [38].

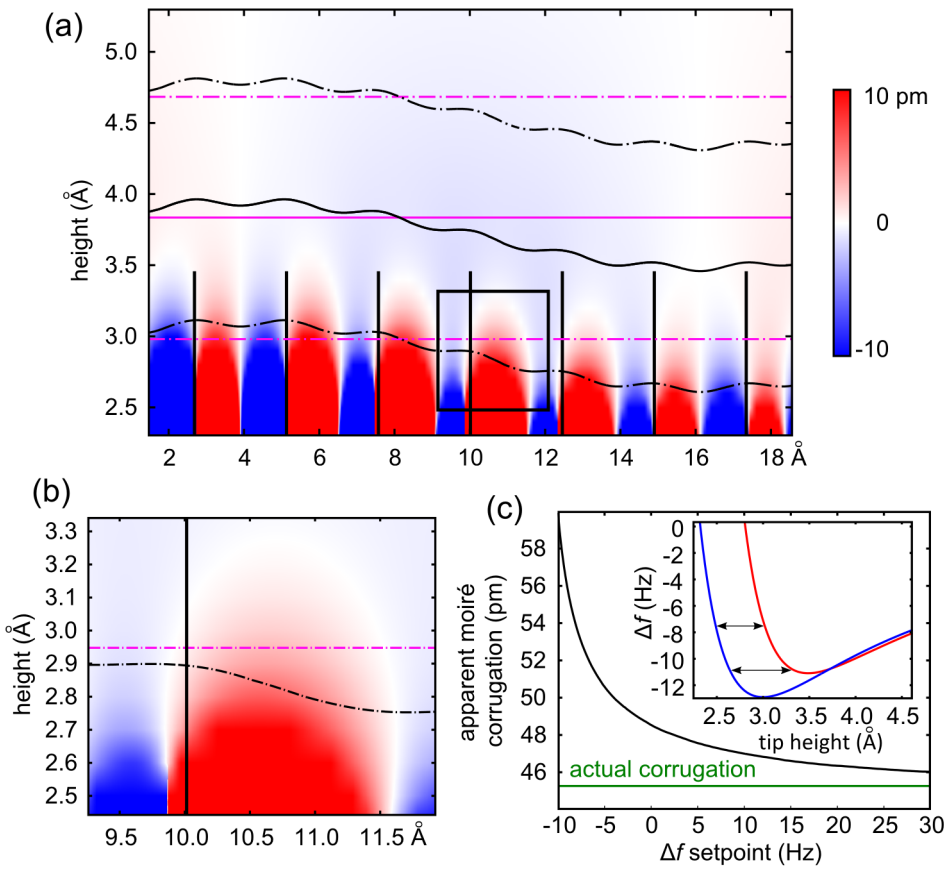

FIGURE 4.4. Slices from the simulated AFM images for the graphene moiré. (a) Bending of the CO along the same section as shown in Figure 4.3(b and d) with $k_{CO} = 3$ N/m. The solid lines correspond to the tip height (black line at $\Delta f = 8$ Hz and magenta line at constant height of 3.8 Å), while the dotted lines show the limits of the oscillation ($A = 0.85$ Å). (b) Close up of the bending near one of the bonds (indicated with a square in panel (a). (c) Apparent corrugation of the graphene moiré as a function of the Δf setpoint on the repulsive side of the Δf *vs* d_{ts} for a non-flexible tip. The inset shows Δf *vs* d_{ts} curves simulated at the points marked with green circles in Figure 4.3(c).

To study how accurately AFM can measure height differences in cases where the background forces change, we plotted the apparent height difference between the topmost and lowest atoms of the moiré (marked with green circles in Figure 4.3(c) as a function of the Δf setpoint. The resulting curve with a non-flexible tip is shown in Figure 4.4(c). At Δf setpoints corresponding to the bottom of the Δf *vs* d_{ts} curve, the moiré corrugation is overestimated significantly. As the tip-sample distance is reduced, the apparent corrugation gradually decreases towards the geometric corrugation. However, in the span of setpoints we have studied, it never reaches the true corrugation of ~ 45 pm. With reasonable values of Δf the corrugation is overestimated by almost 10%.

Awareness of the background forces arising from the substrate is also necessary in measuring adsorption geometries of molecules on surfaces. For example, when the molecule adsorbs in a non-planar configuration, the background force has to be considered for a correct determination of the angle between the molecular plane and the substrate [34]. In the case of molecules, this background force can be simply measured on the bare substrate adjacent to the molecule [34], which is difficult for extended two-dimensional layers such as graphene.

4.6. The influence of background corrections on apparent bond length

According to our simulations, both constant height and constant frequency shift AFM measurements detect apparent changes in the atomic positions on corrugated surfaces. As explained above, in the case of the graphene on Ir(1 1 1) experiments, we get best correspondence between theory and experiment when using a relatively large lateral spring constant. The apparent changes in the atomic positions are then caused by the asymmetric background signal from the neighboring atoms that are at different heights. This suggests that an appropriate background correction or subtraction could remedy the situation and allow us to extract the actual atomic positions from the experiments. We have tested this idea using the simulations and the results are summarized in Figures 4.5 and 4.6. We have removed the moiré corrugation from the simulated images using different filtering schemes. Examples on the results of background subtracted constant frequency shift and constant height images are shown in Figure 4.5(a). Here, the background was removed by either estimating the background by heavily blurring the original images by a Gaussian filter and subtracting this from the original image or with a Laplacian of Gaussians (LoG) filter which removes the long wave-length moiré corrugation (it essentially gives the second derivative of the sample corrugation).

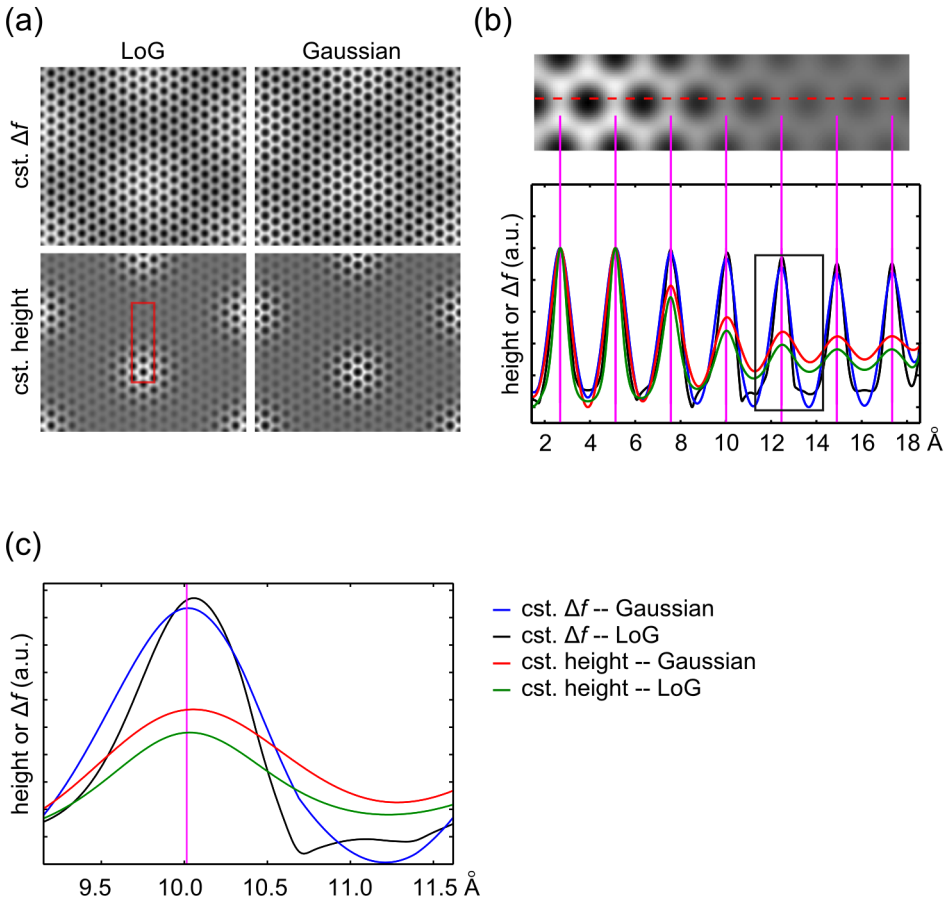

FIGURE 4.5. The effect of background subtraction on the apparent bond positions in simulated AFM images with a stiff tip (k_{CO} = 3 N/m). (a) Background subtracted constant Δf (Δf = 0 Hz) and constant height (average tip height 3.65 Å) images using either a heavily Gaussian blurred background ($\sigma = 1$ Å) or a Laplacian of Gaussians filter ($\sigma = 0.6$ Å). (b) Normalized cross-sections of the images in panel (a) in the red square. The vertical lines mark the positions of the bonds. (c) Zoom-in on one of the bonds showing how the bonds on the constant height image are shifted out from the top sites.

Figure 4.5(b) shows cross-sectional profiles of the background corrected images for two different filtering schemes. A zoom-in on one of the bonds is shown in Figure 4.5(c). As can be seen in the images, background subtraction of AFM images results in an apparent expansion of the top sites, *i.e.*, the trend from non-corrected data is reversed. In both the constant frequency shift and constant height data, background correction improves the match between the apparent and real bond positions. The apparent positions in background corrected data can be as close as 1 pm from the real bond positions; however, typically the difference is of the order of 3–5 pm. While these differences depend on the exact form of the background, the tip-sample distance, the lateral force constant of the tip etc., it appears that using the Gaussian blurred image as the background in constant frequency shift images results in very accurate estimation of the bond positions to within < 2 pm.

4.7. The influence of CO bending on apparent bond length

As the background subtraction significantly reduces the effect of the background forces, we are now able to study the effect of the CO bending on the graphene moiré. To enhance the effect of CO bending, we have calculated two constant frequency shift images with a softer tip ($k_{CO} = 0.6$ N/m). Figure 4.6(a) shows a height cross-section along the same line as in Figure 4.5(b) calculated with two different Δf setpoints (-8 Hz and -10 Hz on the repulsive branch). The main difference is that at $\Delta f = -8$ Hz, the CO reaches the region where it starts to bend away from the top sites (red background) at the bottom of its oscillation cycle while in the $\Delta f = -10$ Hz image the CO remains bent towards the top site over the full oscillation cycle. This can clearly be seen in the zoomed-in image in Figure 4.6(b). Figure 4.6(c) shows the cross-section of the same zoom-in after background correction with the two methods described above. In the case of the $\Delta f = -8$ Hz image the bonds now appear closer to the top site whereas for the $\Delta f = -10$ Hz image they are farther from it. This is in line with the tip bending away and towards the top site, respectively. In addition, the flexibility of the CO causes the bonds to appear sharper at the shorter tip-sample distance. Since this also has a slight effect on the apparent bond positions after background subtraction, the bond shift in Figure 4.6(c) cannot fully be attributed to the tip bending alone. However, the shift in Figure 4.6(c) is ~ 20 pm, which is larger than the typical shifts due to changes in the peak shape.

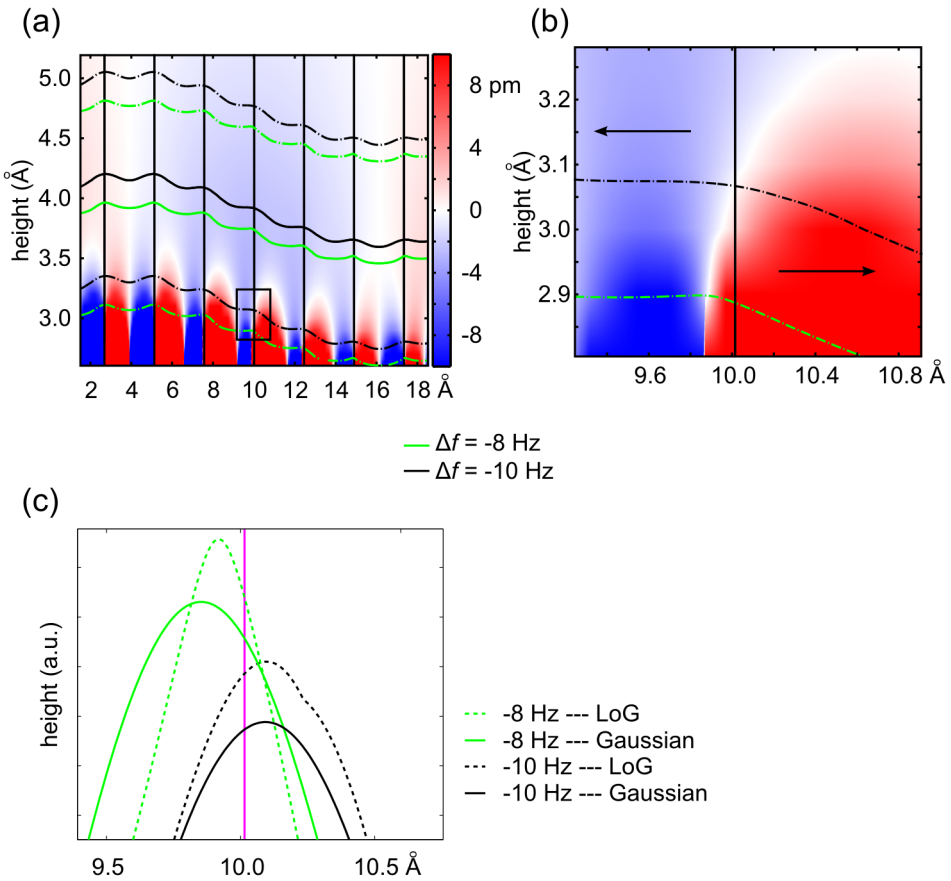

FIGURE 4.6. The effect of background subtraction on the apparent bond positions in simulated constant Δf AFM images with a stiff tip (k_{CO} = 3 N/m). (a) Cross-section along the line in Figure 4.5(b) for a more flexible tip (k_{CO} = 0.6 N/m) calculated at two different Δf setpoints [$\Delta f = -8$ Hz (green) and $\Delta f = -10$ Hz (black)]. The background color corresponds to the bending of the CO along the same section. (b) Close-up of the bending in the area marked with a square in panel (a). (c) Zoom-in to the background corrected cross-section on the same bond after background subtraction for the two different Δf setpoints.

4.8. Testing the background correction on experimental images

We can demonstrate the effect of the background subtraction in the experimental images as shown in Figure 4.7. A constant frequency shift AFM image of the graphene on Ir(1 1 1) surface acquired with a CO-terminated tip is shown in Figure 4.7(a). Background subtracted images using the Gaussian blurred background and LoG filtering are shown in Figure 4.7(b) and 4.7(c), respectively. The extracted apparent hexagon areas are displayed in Figures 4.7(d) to 4.7(f). It is apparent that the trend of smaller top sites is reduced, and even reversed in the background corrected data, consistent with the LoG filtered simulated images. The remaining differences in the apparent hexagon areas ($\pm$ 5 %) convert into $\pm$ 3 pm changes in the graphene bond lengths. This is close to the results from the simulated images and close to the typical noise levels of a low-temperature scanning probe microscope.

4.9. Conclusions

We have studied the limits of achievable accuracy in the determination of the surface atomic positions by non-contact AFM with a CO-terminated tip. The precision is limited by the background forces arising from the neighboring atoms and the flexibility of the CO at the tip apex. Using epitaxial graphene as a model system, we demonstrate experimentally and by the use of molecular mechanics simulations that the asymmetric background forces are the limiting factor in our experiments. While non-background corrected data gives errors of the order of 20 pm in the atomic positions, suitable background correction can reduce this to the level of a couple of pm for a relatively stiff tip. Our work has a direct bearing on the accuracy of total structure determination at the single molecule level using non-contact AFM with functionalized tips.

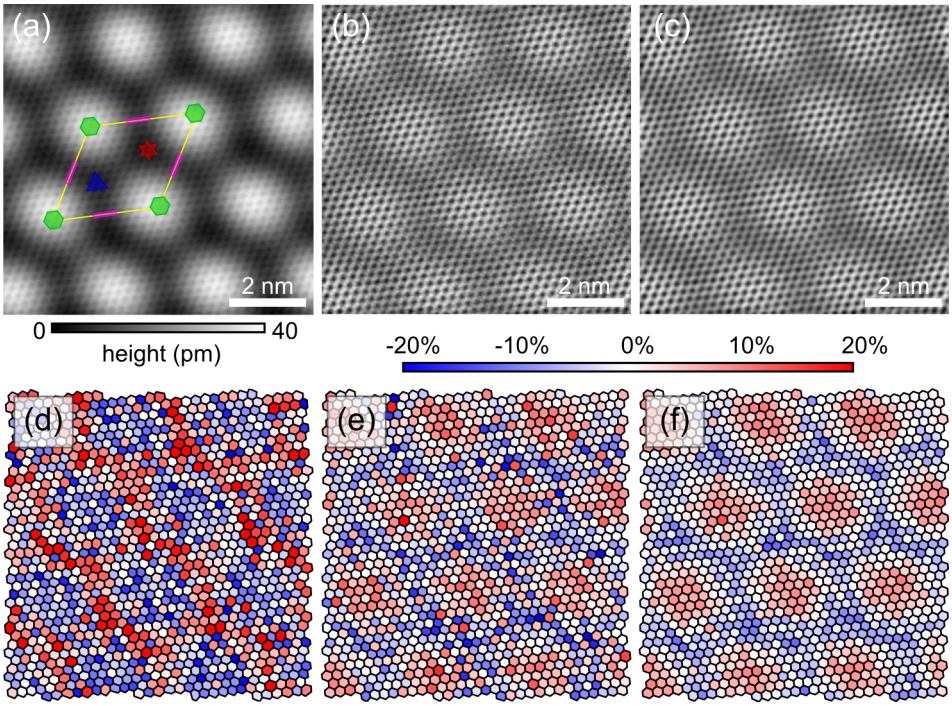

FIGURE 4.7. Effect of background subtraction on the experimental AFM images. (a) Constant frequency shift AFM image of graphene on Ir(1 1 1) with a CO terminated tip obtained at a feedback setpoint of $\Delta f = 0$ Hz. (b,c) Image from panel (a) after background subtraction using Gaussian blurring with $\sigma = 1$ Å (b) or a Laplacian of a Gaussian with $\sigma = 0.6$ Å (c). (d–f) Color coded maps of the apparent graphene hexagon area as extracted from (d), the constant frequency shift image in panel (a), or (e) and (f) the background subtracted images in panels (b) and (c).

4.10. Bibliography

[1] Gross, L., Mohn, F., Moll, N., Liljeroth, P. & Meyer, G. The chemical structure of a molecule resolved by atomic force microscopy. *Science* **325**, 1110–1114 (2009).

[2] Gross, L. *et al.* Organic structure determination using atomic-resolution scanning probe microscopy. *Nature Chemistry* **2**, 821–825 (2010).

[3] Mohn, F., Gross, L., Moll, N. & Meyer, G. Imaging the charge distribution within a single molecule. *Nature Nanotechnology* **7**, 227–231 (2012).

[4] Gross, L. *et al.* Bond-order discrimination by atomic force microscopy. *Science* **337**, 1326–1329 (2012).

[5] de Oteyza, D. G. *et al.* Direct imaging of covalent bond structure in single-molecule chemical reactions. *Science* **340**, 1434–1437 (2013).

[6] Guillermet, O. *et al.* STM and AFM high resolution intramolecular imaging of a single decastarphene molecule. *Chemical Physics Letters* **511**, 482–485 (2011).

[7] Pavliček, N. *et al.* Atomic force microscopy reveals bistable configurations of dibenzo[a,h]thianthrene and their interconversion pathway. *Physical Review Letters* **108**, 086101 (2012).

[8] Albrecht, F., Neu, M., Quest, C., Swart, I. & Repp, J. Formation and characterization of a molecule-metal-molecule bridge in real space. *Journal of the American Chemical Society* **135**, 9200–9203 (2013).

[9] van der Lit, J. *et al.* Suppression of electron-vibron coupling in graphene nanoribbons contacted via a single atom. *Nature Communications* **4**, 2023 (2013).

[10] Riss, A. *et al.* Local electronic and chemical structure of oligo-acetylene derivatives formed through radical cyclizations at a surface. *Nano letters* Article ASAP (2014).

[11] Sugimoto, Y. *et al.* Chemical identification of individual surface atoms by atomic force microscopy. *Nature* **446**, 64–67 (2007).

[12] Welker, J., Weymouth, A. J. & Giessibl, F. J. The influence of chemical bonding configuration on atomic identification by force spectroscopy. *ACS Nano* **7**, 7377–7382 (2013).

[13] Lantz, M. A. *et al.* Quantitative measurement of short-range chemical bonding forces. *Science* **291**, 2580–2583 (2001).

[14] Zhang, J. *et al.* Real-space identification of intermolecular bonding with atomic force microscopy. *Science* **342**, 611–614 (2013).

[15] Mohn, F. *et al.* Reversible bond formation in a gold-atom–organic-molecule complex as a molecular switch. *Physical Review Letters* **105**, 266102 (2010).

[16] Welker, J. & Giessibl, F. J. Revealing the angular symmetry of chemical bonds by atomic force microscopy. *Science* **336**, 444–449 (2012).

[17] Sun, Z., Boneschanscher, M. P., Swart, I., Vanmaekelbergh, D. & Liljeroth, P. Quantitative atomic force microscopy with carbon monoxide terminated tips. *Physical Review Letters* **106**, 046104 (2011).

[18] Mohn, F., Schuler, B., Gross, L. & Meyer, G. Different tips for high-resolution atomic force microscopy and scanning tunneling microscopy of single molecules. *Applied Physics Letters* **102**, 073109 (2013).

[19] Busse, C. *et al.* Graphene on Ir(111): physisorption with chemical modulation. *Physical Review Letters* **107**, 036101 (2011).

[20] Boneschanscher, M. P. *et al.* Quantitative atomic resolution force imaging on epitaxial graphene with reactive and nonreactive AFM probes. *ACS Nano* **6**, 10216–10221 (2012).

[21] Dedkov, Y. & Voloshina, E. Multichannel scanning probe microscopy and spectroscopy of graphene moiré structures. *Physical Chemistry Chemical Physics* Accepted Manuscript (2013).

[22] Meng, L. *et al.* Multi-oriented moiré superstructures of graphene on Ir(111): experimental observations and theoretical models. *Journal of Physics: Condensed Matter* **24**, 314214 (2012).

[23] Voloshina, E. N. *et al.* Electronic structure and imaging contrast of graphene moiré on metals. *Scientific Reports* **3**, 1072 (2013).

[24] Hämäläinen, S. K. *et al.* Structure and local variations of the graphene moiré on Ir(111). *Physical Review B* **88**, 201406(R) (2013).

[25] Coraux, J. *et al.* Growth of graphene on Ir(111). *New Journal of Physics* **11**, 023006 (2009).

[26] Subramaniam, D. *et al.* Wave-function mapping of graphene quantum dots with soft confinement. *Physical Review Letters* **108**, 046801 (2012).

[27] Pletikosić, I. *et al.* Dirac cones and minigaps for graphene on Ir(111). *Physical Review Letters* **102**, 056808 (2009).

[28] Lacovig, P. *et al.* Growth of dome-shaped carbon nanoislands on Ir(111): the intermediate between carbidic clusters and quasi-free-standing graphene. *Physical Review Letters* **103**, 166101 (2009).

[29] Altenburg, S. J. *et al.* Local gating of an Ir(111) surface resonance by graphene islands. *Physical Review Letters* **108**, 206805 (2012).

[30] Yang, J., Ren, Y., Tian, A.-m. & Sun, H. COMPASS force field for 14 inorganic molecules, He, Ne, Ar, Kr, Xe, H_2, O_2, N_2, NO, CO, CO_2, NO_2, CS_2, and SO_2, in liquid phases. *The Journal of Physical Chemistry B* **104**, 4951–4957 (2000).

[31] Hamaker, H. The London–van der Waals attraction between spherical particles. *Physica* **4**, 1058–1072 (1937).

[32] N'Diaye, A. T., Coraux, J., Plasa, T. N., Busse, C. & Michely, T. Structure of epitaxial graphene on Ir(111). *New Journal of Physics* **10**, 043033 (2008).

[33] Lide, D. *Handbook of chemistry & physics* (CRC Press LLC, Boca Raton, 2002), 83rd edn.

[34] Schuler, B. *et al.* Adsorption geometry determination of single molecules by atomic force microscopy. *Physical Review Letters* **111**, 106103 (2013).

[35] Moll, N., Gross, L., Mohn, F., Curioni, A. & Meyer, G. The mechanisms underlying the enhanced resolution of atomic force microscopy with functionalized tips. *New Journal of Physics* **12**, 125020 (2010).

[36] Giessibl, F. Forces and frequency shifts in atomic-resolution dynamic-force microscopy. *Physical Review B* **56**, 16010–16015 (1997).

[37] Sader, J. E. & Jarvis, S. P. Accurate formulas for interaction force and energy in frequency modulation force spectroscopy. *Applied Physics Letters* **84**, 1801–1803 (2004).

[38] Sun, Z. *et al.* Topographic and electronic contrast of the graphene moiré on Ir(111) probed by scanning tunneling microscopy and noncontact atomic force microscopy. *Physical Review B* **83**, 081415 (2011).

5

Graphene on iridium(111): electronic structure

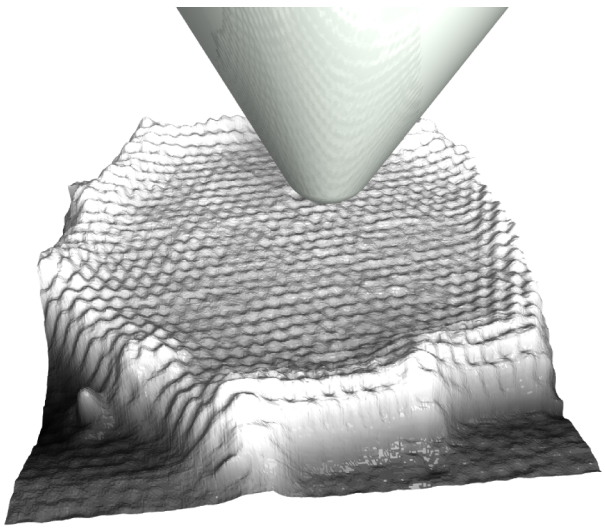

This chapter[1] describes measurements of the local density of states (LDOS) of small (< 20 nm diameter) graphene islands on Ir(1 1 1). The results can be quantitatively modeled by a relativistic wave equation and atomistic tight-binding calculations. The observed states are analogous to the solutions of the textbook 'particle-in-a-box' problem applied to relativistic massless fermions.

[1]This chapter is based on S.K. Hämäläinen, Z. Sun, M.P. Boneschanscher, A. Uppstu, M. Ijäs, A. Harju, D. Vanmaekelbergh, and P. Liljeroth, *Physical Review Letters* **107**, 236803 (2011).

5.1. Measuring the electronic properties of well-defined graphene nanostructures

Graphene, a monolayer of carbon atoms that is a 2-D metal where the charge carriers behave as massless relativistic electrons, has attracted enormous scientific and technological interest [1–4]. Despite the potential of graphene nanostructures in electronic applications [5–12], the study of quantum-confined electronic states in atomically well-defined graphene nanostructures remains an experimental challenge. Basic questions, such as the relation between the atomic configuration of graphene nanostructures and the spatial distribution and energy of their electronic states, have not been experimentally addressed.

In previous experiments, macroscopic graphene sheets have been studied by scanning tunneling microscopy (STM) and spectroscopy (STS), focusing on the electronic structure and scattering processes in epitaxial graphene [13, 14] and the density of states and charge puddles in graphene sheets deposited on an insulator [15–18]. It is, however, also possible to grow much smaller graphene nanostructures [graphene quantum dots (GQDs)] by chemical vapor deposition (CVD) and characterize them with scanning probe methods [10, 19–21].

In this chapter, we present low-temperature STM and STS experiments on GQDs with well-defined atomic structures grown by CVD on an Ir(1 1 1) substrate. We can readily access individual GQDs and measure their atomic structure with STM. Measurement of the local density of states (LDOS, proportional to the dI/dV_b signal) allows us to probe the spatial structure and energy of the quantum-confined energy levels for GQDs with variable size and shape. The measured LDOS maps can be reproduced by tight-binding (TB) calculations, where we use the exact atomic structure of the GQDs as determined by STM, and by the Klein–Gordon (KG) equation, which is a continuum model describing particles with linear dispersion.

5.2. Materials and methods

Graphene islands on Ir(1 1 1) were prepared as described in Chapter 2. The GQD size could be controlled by the growth temperature [21]: larger (smaller) GQDs were grown by heating the sample to 1470 K (1170 K) for 10 s. After the CVD growth of the GQDs, the sample was inserted into the low-temperature STM setup described in Chapter 2. We used cut PtIr tips, and the bias voltage (V_b) was defined as sample voltage with respect to the tip. The dI/dV_b signal was recorded with a lock-in amplifier by applying a small sinusoidal variation to the

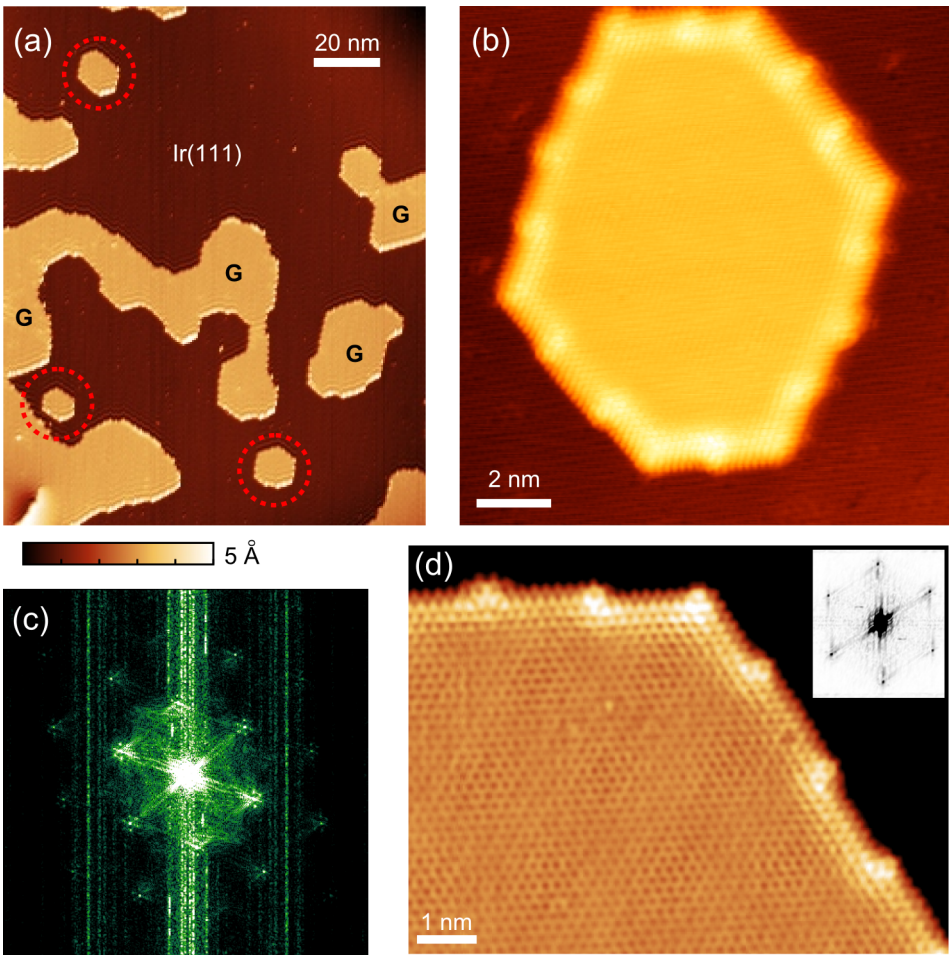

FIGURE 5.1. Growth of graphene islands on Ir(1 1 1). (a) Overview STM image of graphene islands (G) on Ir(1 1 1), $I = 40$ pA, $V_b = 1.0$ V. Small GQDs are indicated by red circles.(b) Atomically resolved STM image of the GQD studied in more detail in Figure 5.5 (5 mV / 1 nA). The contrast is enhanced by an adsorbed molecule on the tip, which also inverts the atomic contrast. (c) Square root of the modulus of the FFT of the panel (b). (d) Atomic resolution STM image (50 mV / 200 pA) of a larger graphene flake edge where the kinks of one atomic row are clearly visible. The inset shows the FFT spectrum of the image.

bias voltage (typically 30 mV rms at 660 Hz). This gives an energy resolution of $\sim$ 75 meV in our experiments [22]. To ensure that the modulation would not couple to the feedback loop, a 300 Hz low-pass filter was used for the feedback input. The experimental dI/dV_b images are averages of the trace and retrace scans (Figure 5.3) and of the trace and retrace scans of two consecutive images (up and down, Figure 5.5) to increase the signal-to-noise ratio.

Figure 5.1(a) shows a large-scale overview scan of a typical sample. We find interconnected graphene patches (indicated by G) as well as small isolated GQDs (red dotted circles). The CVD growth yields a relatively broad distribution of different GQD sizes ranging from a couple of nanometers up to $\sim$ 20 nm, most of them with a roughly hexagonal shape. The lattices of all the grown GQDs were roughly aligned with the underlying Ir lattice, which is the predominant growth phase of graphene on Ir [23]. This can be clearly seen in atomically resolved STM images and their Fourier transforms [Figures 5.1(b) and 5.1(c)]. The Fourier transforms show intensity maxima in a hexagonal pattern around the maxima produced by the graphene lattice. These spots arise from the lattice mismatch between graphene and iridium and are analogous to the diffraction pattern of graphene on Ir observed in low-energy electron diffraction (LEED) as described in Chapter 3 [24, 25]. In our case, these hexagons are aligned with the maxima from the graphene lattice indicating that the two lattices are aligned. The mismatch in lattice constants is also observed in the real space STM images as a moiré pattern on graphene islands with a period of around 2.5 nm, see also Chapter 3 [14, 24, 25]. All the GQD edges were terminated in the zigzag direction [corresponding to the close-packed atomic rows of the underlying Ir(1 1 1) surface]. This could be verified from FFT spectra of the GQDs, where the first order maxima were always oriented perpendicular to the graphene flake edges [*e.g.*, Figure 5.1(d)]. The edges always had 120 degree corners; no 60 degree corners were observed. Thus all GQDs had an overall hexagonal shape and no triangular QDs were observed. We see kinks of one or two atomic rows at the GQD edges, which we ascribed to the onset of an additional row of benzene rings in Chapter 2.

5.3. Edge states in small GQDs

Closer inspection of a small GQD [Figures 5.2(a) and 5.2(b)] at a bias voltage close to zero bias shows that the edges are bright both in the actual STM topography image (left) as in the simultaneously recorded dI/dV_b image (right). The enhanced conductance is due to edge states that are expected for zigzag or reconstructed

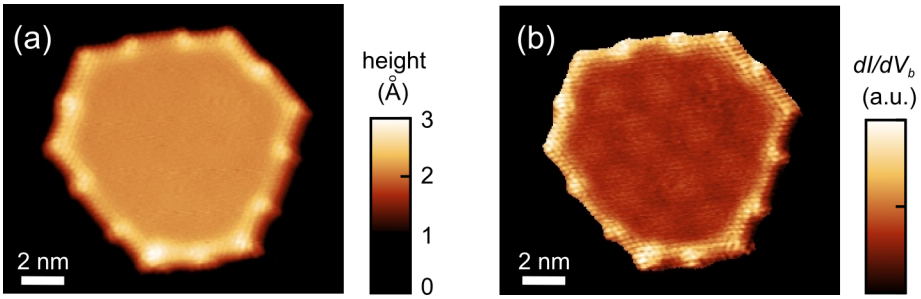

FIGURE 5.2. STM measurements on edge states in small GQDs. (a) STM topography of an isolated GQD flake (100 pA / 50 mV). (b) Simultaneously acquired dI/dV_b map under constant-current STM feedback.

zigzag edges [2, 26–28]. We observe a higher LDOS at the corner and kink sites compared to the other edge sites, while atomistic tight-binding modeling predicts highest intensity at the middle of the edges with vanishing intensity in the corners of the GQD [29]. This disagreement is likely to be related to the remaining coupling of the GQDs with the Ir(1 1 1) substrate. Angle-resolved photoemission spectroscopy (ARPES) experiments have shown that close to the Fermi-level, there is an onset of an Ir(1 1 1) surface state that interacts with the graphene layer [30, 31]. At negative bias voltages, but before the onset of the delocalized states in the interior of the GQD, the experimental results on the edge-state LDOS agree with the predictions from tight-binding calculations. Bias-dependent imaging indicates that the edge states have a very flat dispersion, *i.e.*, their spatial (exponential) decay away from the edges of the GQD is roughly energy independent with a decay constant of ~ 0.5 nm. Generally, we can observe the intrinsic properties of GQDs with little interference from the substrate in the bias region below -0.1 V.

5.4. Quantum confinement in GQDs

We now focus on the delocalized, quantum-confined states inside the GQDs. We can map the atomic structure of the GQD by STM as shown for a small GQD with perfect hexagonal symmetry with 7 benzene ring long edges in Figure 5.3(a). The LDOS can be accessed through $d\ln I/d\ln V_b$ measurements as shown in Figure 5.3(b); we clearly observe an increased and spatially dependent LDOS on the GQDs. There is a pronounced maximum of the LDOS measured in the center of the GQD [blue line in Figure 5.3(b)] at a bias of -0.6 V. Moving away from the

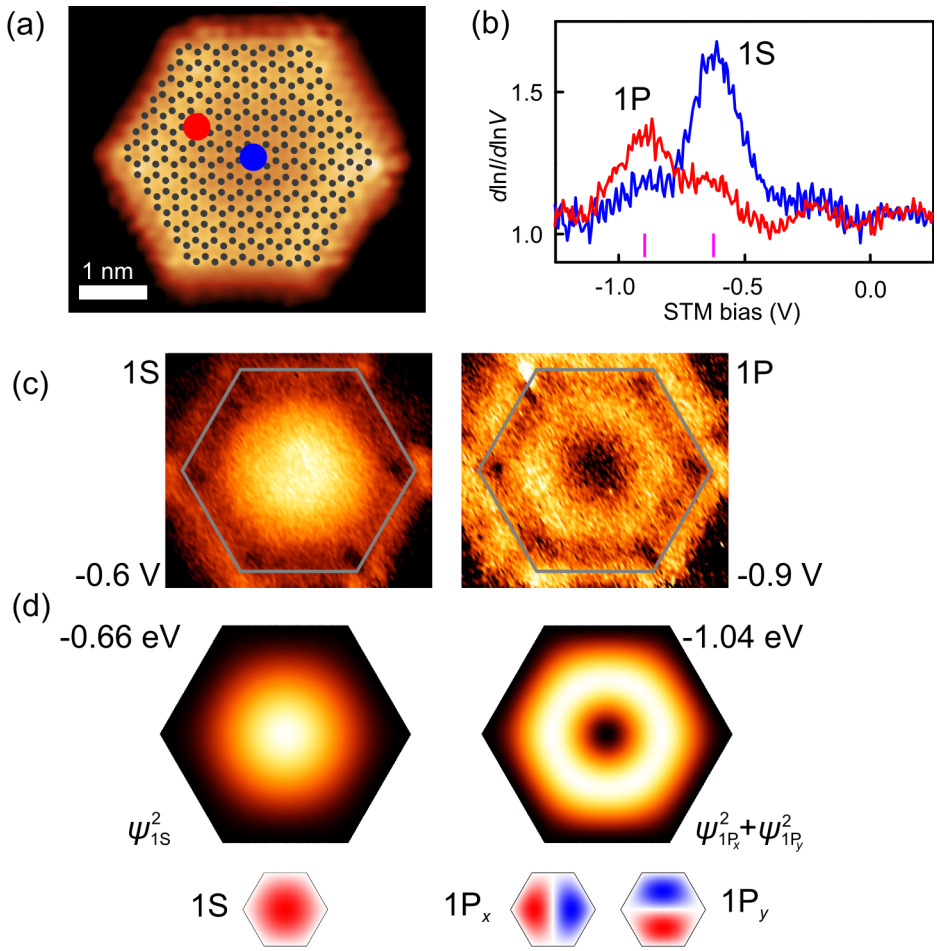

FIGURE 5.3. STM and STS on small GQDs. (a) STM topography of a small GQD (−50 mV, 100 pA) with overlaid atomic model; hexagonal symmetry, 7 benzene ring long edges. (b) $d\ln I/d\ln V_b$ spectra measured on the points indicated in (a). Purple bars indicate the bias voltages corresponding to the LDOS maps shown in (c). (c) Measured LDOS maps (gray lines indicate edges of the GQD) at bias voltages corresponding to the two resonances in the spectra shown in (b). (d) Corresponding LDOS maps for a particle in a box at the indicated energies, and underlying eigenstates.

center of the GQD, the intensity of this peak is reduced and another resonance emerges at a bias of −0.9 V (red line). We can map the spatial shape of the orbitals responsible for these resonances by measuring the dI/dV_b signal during STM imaging under constant-current feedback at biases corresponding to the resonances [Figure 5.3(c)]. These states have the familiar appearance of the lowest energy levels of the textbook particle-in-a-box problem and can be characterized using symmetry labels borrowed from atomic physics. The lowest state has 1S symmetry (no nodal planes) and the first excited state is composed of two 1P type orbitals ($1P_x$ and $1P_y$) which are degenerate in this case of a perfect hexagonal GQD. STM probes the sum of the squared wave functions $\psi^2_{1P_x} + \psi^2_{1P_y}$ leading to a doughnut-shaped dI/dV_b signal as we observe in the experiment.[2]

These experiments can be reproduced by both TB calculations and by a continuum model for particles with linear dispersion confined to a GQD. For the latter we use the KG equation [29, 33]

$$-\nu_F^2 \hbar^2 \nabla^2 \psi_i = E_i^2 \psi_i \tag{5.1}$$

where ν_F is the Fermi velocity (10^6 m/s in isolated graphene) and the boundary condition is given by $\psi_i = 0$ at the edges of the GQD. A more accurate boundary condition would be needed to take into account the sublattice pseudospin and the interaction with the Ir substrate. It is clear that the KG equation cannot be used to model the edge states (in contrast to the Dirac equation and TB calculations [2, 26, 27]). However, as shown below, the LDOS plots from the KG equation are remarkably similar to the TB calculations and the experimental results, although the number of states in a given energy interval is too small. We use the experimentally determined geometries of the GQD in our calculations. The lowest energy solutions of Equation 5.1 are plotted in Figure 5.3(d) as the squared wave functions corresponding to the experimentally measured LDOS $\propto \sum_{\delta E} \psi_i^2$, where δE is the energy resolution of the experiment [34].

[2]We note here that at positive bias, electronic resonances with clear peaks in the dI/dV_b spectrum cannot be observed. Based on density-functional theory calculations on Ir(1 1 1), there is a dense set of energy bands above the Fermi energy at the K point of the Brillouin zone. It is likely that interaction with these states masks the intrinsic graphene states at positive bias [32].

5.5. Modeling the quantum confinement

Atomic models of the GQDs were created for the TB calculations. For the smallest hexagonal GQDs, this procedure was straight-forward as the hexagons can be readily identified by counting the carbon rings along each edge of the GQD. An example of the smallest observed GQD with its corresponding atomic model is shown in Figure 5.4(a). For the larger and more complex GQDs, a rough estimate of the structure was first created by measuring the coordinates of all the kinks and corners of the QGD from the STM image. An atomic model based on the coordinates was then created and compared to the atomically resolved image. As there might be an uncertainty in the STM piezo calibrations or some residual thermal drift, the model was then further refined by comparing the number of carbon rings in the image and model along the edges of the GQD. These models correspond to the actual GQD geometry with an uncertainty of 1 carbon atom row. The kinks and other features on the edge are nevertheless produced with atomic precision. An example of this is shown in Figure 5.4(b).

For solving the Klein–Gordon equation (which does not include atomic details), the shape and size were taken directly from the STM images for the larger QDs. The kinks on the edges of the larger flakes were also taken into account. The symmetric smaller QDs were modeled as perfect hexagons with sharp corners, where the edges run along the outermost atoms of the atomic model [hexagon surrounding the atomic model in Figure 5.4(a)].

The Klein–Gordon equation was solved numerically by the finite element method (FEM) using the commercial software Comsol Multiphysics (v. 3.5). Eigenstates of the Klein–Gordon equation were calculated up to 2 eV (using $\nu_F = 6.2 \times 10^5$ m/s). LDOS maps for a given energy E were created by weighing each eigenstate ψ_i by the energy difference of the eigenvalue E_i and E using a Gaussian distribution

$$\mathrm{LDOS}(E, x, y) = \sum_i \left\{ \exp\left[-\frac{(E - E_i)^2}{2\sigma^2} \right] \psi(x, y)_i^2 \right\} \tag{5.2}$$

We checked the effect of the width σ on the calculated LDOS maps: 100 meV was found to give the best match with the experimental results and was thus used for all of the calculations.

We used a single-electron tight-binding (TB) model, suitable for describing the π-electrons of graphene. Hoppings up to third-nearest neighbors were included, with the original parameters being $t_1 = -2.7$ eV, $t_2 = -0.20$ eV, and $t_3 = -0.18$ eV

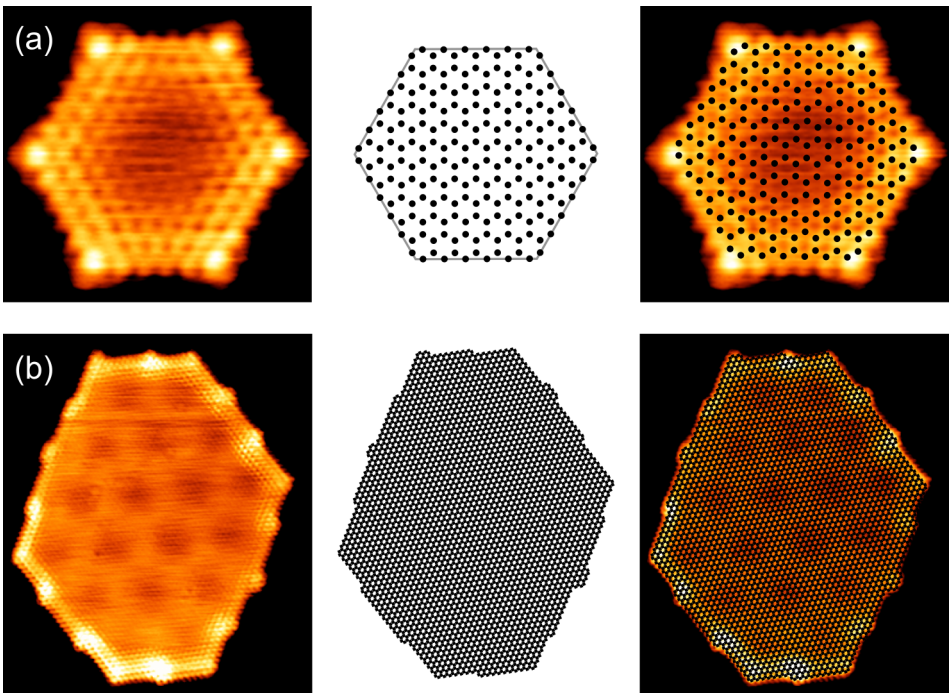

FIGURE 5.4. Examples of the atomic models created for two different GQDs. (a) Atomic model created directly from the STM image for a GQD with 6 carbon rings per edge. The grey hexagon around the atomic model (middle column) represents the area used for the FEM calculation of the Klein–Gordon equation. (b) Example of a larger GQD where the atomic model has first been created from the coordinates of the edges and kinks and then refined to better match the actual atomic structure on the edges of the STM image.

for first, second, and third-nearest neighbors, respectively [35]. In order to match the experimental energy scale, the parameters were scaled to $t_1 = -2.26$ eV, $t_2 = -0.168$ eV, and $t_3 = -0.151$ eV, keeping their ratios constant. In 2-D graphene, these parameters correspond to a Fermi velocity of about 6.3×10^5 m/s. The LDOS was computed with a 100 meV Lorentzian broadening of the spectrum. In Figure 5.5, the LDOS from the TB model has been averaged over the sites in each hexagon of the graphene lattice.

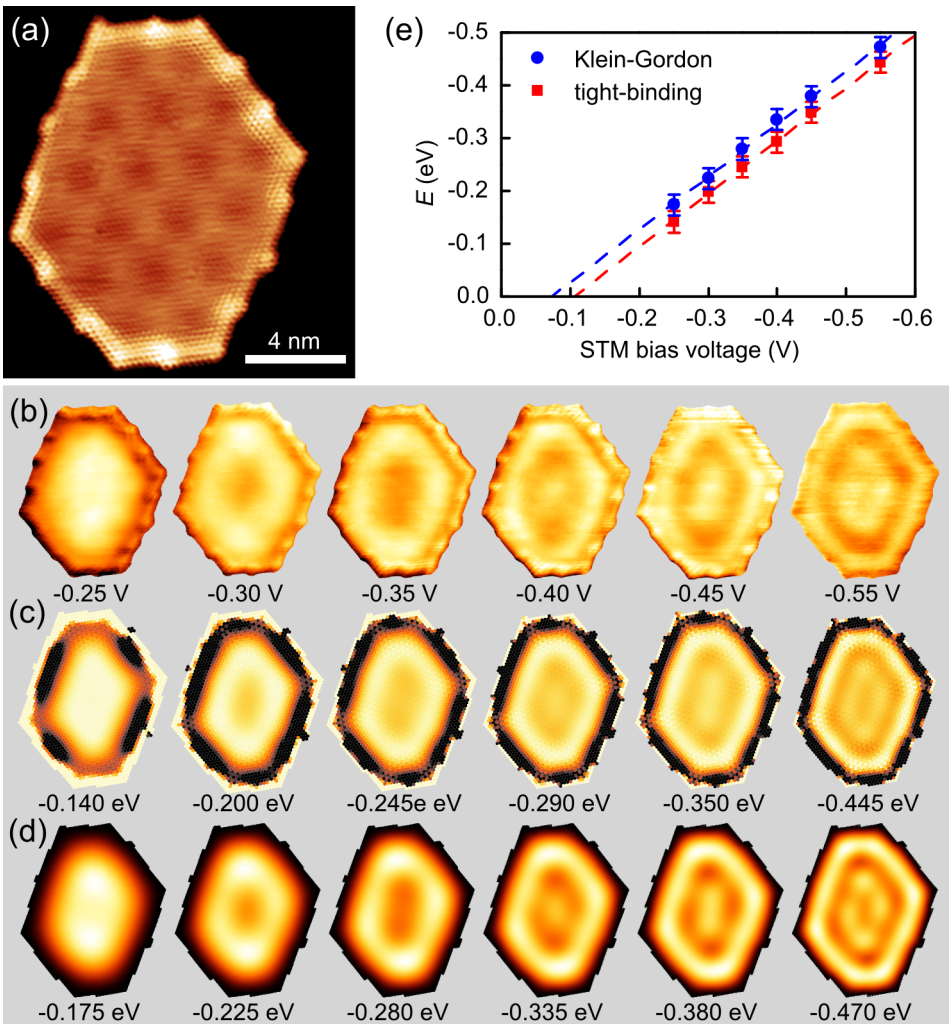

FIGURE 5.5. Detailed comparison between STM/STS experiments and computational results on a large GQD. (a) Atomically resolved STM image of the GQD ($I = 3$ nA, $V_b = 1$ mV). (b) dI/dV_b maps recorded under constant-current STM feedback at the bias voltages indicated in the figure ($I = 1$ nA). (c,d) Corresponding LDOS plots at the indicated energies calculated using a TB model (c) and the KG equation (d) as described in the text. (e) Correspondence between the experimental and the calculated energies based on TB (red squares) and the KG equation (blue circles) calculated with $\nu_F = 6.2 \times 10^5$ m/s.

5.6. Comparing the measurement to the different models

We have measured the LDOS at different bias voltages on a larger GQD shown in Figure 5.5(a). The periodic variation with a period of 2.5 nm seen on the topographic STM images is a moiré pattern resulting from the lattice mismatch between graphene and Ir, as described in depth in Chapter 3 [14, 21]. The STM contrast results mostly from the small ($\sim$ 45 pm) geometric modulation of the graphene structure as described in Chapter 3 [14, 25]. Our calculations neglecting this moiré-induced potential modulation yield quantitative agreement with the experiment, and the expected potential modulation due to the moiré pattern is small compared to the confinement energy in our GQDs. It has been reported that the size and shape of the GQDs is influenced by the moiré pattern and the edges prefer to run along the fcc and hcp regions of the moiré [21, 24]. We also observe GQDs that are smaller than the moiré period (6×6 and 7×7). For larger GQDs, the kinks on the edges are spaced by roughly one moiré period.

The asymmetry of the GQD breaks the degeneracies (*e.g.*, $1P_x$ and $1P_y$ states) of the purely hexagonal GQD. This can be seen in the measured LDOS maps shown in Figure 5.5(b) (the Ir substrate has been removed in the images using the simultaneously acquired STM topography image as a mask): after the 1S state (bias -0.25 V), we observe increased intensity at the top and bottom end of the GQD consistent with the $1P_y$ envelope wave function along the long GQD axis (at -0.30 V). At more negative bias, the $1P_x$ state also contributes and the long GQD edges are brighter (-0.35 V). Subsequently, the next eigenstate becomes relevant, which is seen as an increased intensity in the middle of the QD (bias -0.4 V).

In order to compare experiment and theory in detail, we have generated a series of theoretical LDOS maps, which are calculated as a weighted and broadened sum of squares of TB molecular orbitals (MOs) or KG eigenstates close to a given energy [see Figures 5.5(c) and 5.5(d)]. This broadening is justified due to the intrinsic resolution of the measurement (75 meV) and the lifetime broadening of the states. In the case of the calculations based on the KG equation, the eigenfunctions are given by the solution of Equation 5.1 using the overall shape of the GQD. In the TB calculations (we use third-nearest-neighbor TB) [2, 26, 35], they correspond to the calculated MOs for the GQD with an exact atomic structure as obtained from experiment [Figure 5.5(a)]. It can be seen that the eigenstates of the KG equation (overall geometry) match with clusters of TB MOs (exact atomic lattice). Furthermore, there is a remarkable agreement in how both calculated LDOS maps evolve with energy and how the experimental conductance maps evolve with bias.

To find the correspondence between the measured and calculated states the LDOS maps were visually compared. This was done by calculating several LDOS maps in relatively small energy steps (6 meV) and comparing these to each of the measured dI/dV_b maps. Since in most cases the calculated states change fairly little between such small energy steps, a range of possible matches was picked for each measured dI/dV_b map. The energy in the middle of the range was used as the best match. The width of the range of the corresponding experimental and calculated LDOS maps was typically 0.05 eV. An example of this procedure is shown in Figure 5.6, where the best match is indicated by the green bar.

Based on a comparison between the experimental and computed LDOS maps, we have identified energy-bias voltage pairs that give the same spatial features in the LDOS with an associated error estimate indicated by error bars in Figure 5.5(e). It is clear that with the Fermi velocity ν_F as the only adjustable parameter (in the case of TB calculations, ν_F is directly related to the value of the hopping integrals), both calculations agree strikingly well with the experiments. This is also evident from Figure 5.5(e), where we show the correspondence between the experimental bias voltages and the theoretical energies. This gives the Fermi velocity $\nu_F = (6.2 \pm 0.1) \times 10^5$ m/s as the best fit to both the KG equation and the TB calculations. The two theories yield slightly different values for the doping of the GQD, *i.e.*, the intercept of the y-axis, due to the differences in the theoretical approaches.

5.7. The charge carriers in GQDs

Do we see the peculiar nature of the charge carriers in graphene in these LDOS maps? In fact, the Schrödinger equation predicts wave functions with an identical spatial shape as the KG equation since both are second order differential equations; the corresponding eigenenergies are related as $E_S = E_{KG}^2/2m\nu_F^2$. This also explains the different dispersion relations for free electrons, which are either parabolic (Schrödinger) or linear (Klein–Gordon). Moreover, the energy of the lowest (and the other) quantum-confined state scales as $1/A^{1/2}$ (A is the area of the GQD) in the case of the relativistic massless particles, instead of $1/A$ for the particles obeying the Schrödinger equation. We demonstrate in Figure 5.7 that the charge carriers in our GQDs fulfill the conditions of $E \propto 1/A^{1/2}$ and have a linear dispersion. Figure 5.7(a) shows the bias voltage corresponding to the lowest quantum-confined energy level (determined by the peak position in dI/dV_b *vs* V_b spectra acquired at the center of the GQD) on many different GQDs [topographies

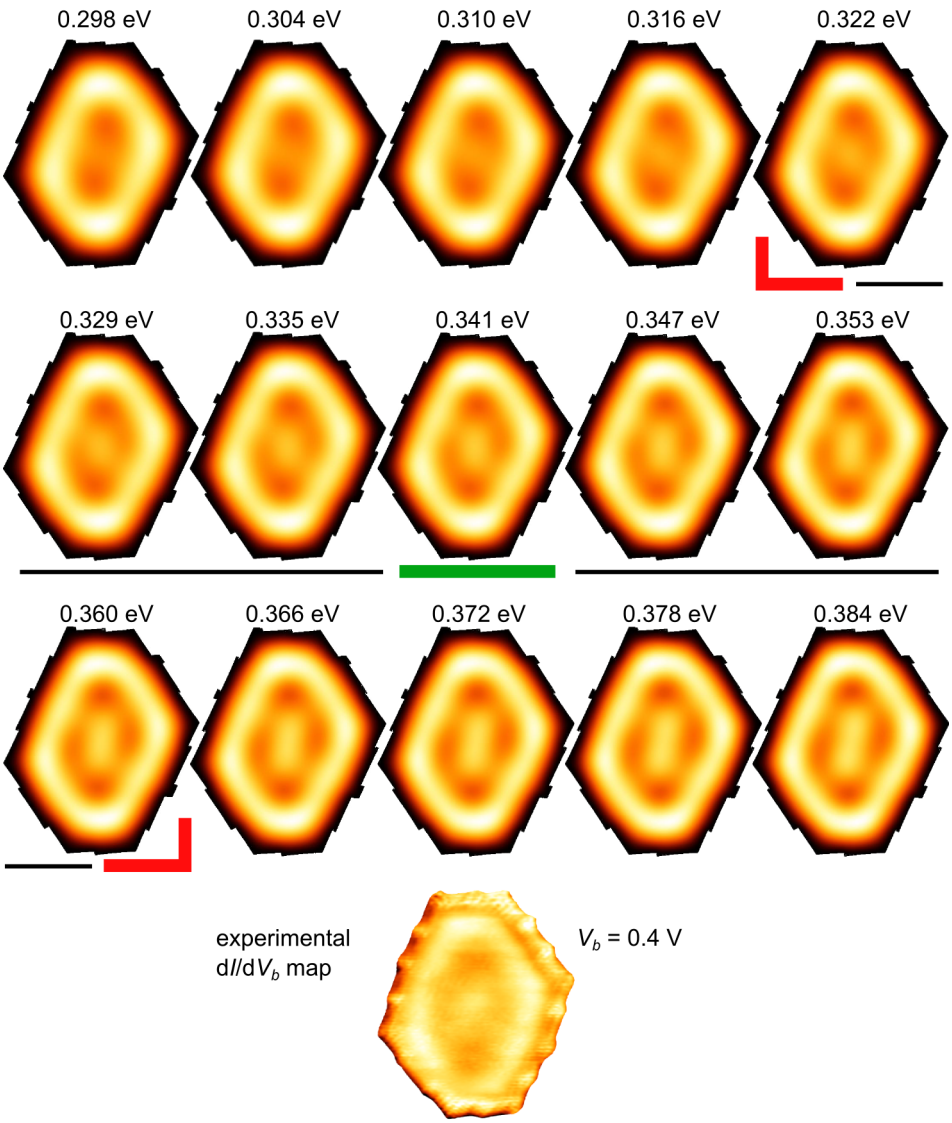

FIGURE 5.6. LDOS maps calculated based on the KG equation. Map at the energy of 0.341 eV (green underline) is taken as the best match to the measured dI/dV_b map. The red markers denote the limits of error for the visual match.

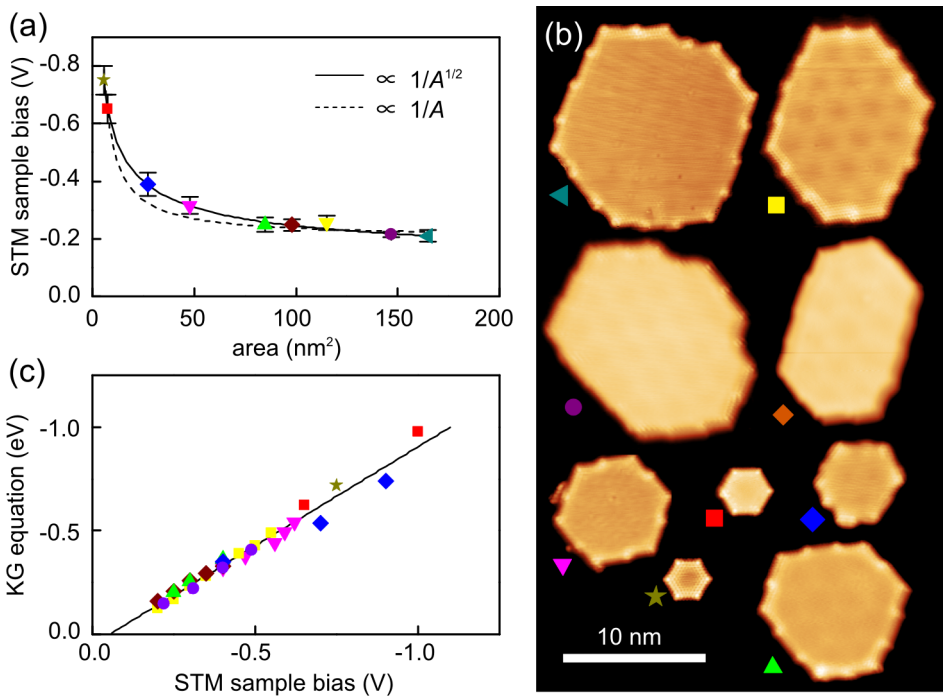

FIGURE 5.7. Electronic structure of GQDs as a function of their size. (a) STM sample bias corresponding to the S state as a function of the area A of the GQD. The solid and dashed lines are fits to $1/A^{1/2}$ and $1/A$ scaling, respectively. (b) Composition of the STM topographies of the GQDs used in (a) (with different scan parameters). (c) A plot of the bias voltages from the STM experiments (x-axis) and the energies that give comparable LDOS calculated from the Klein–Gordon equation using a single value for $\nu_F = 6.2 \times 10^5$ m/s (y axis).

shown in Figure 5.7(b)] as a function of the experimentally determined area. The solid line showing the expected $1/A^{1/2}$ scaling fits the data clearly better than the $1/A$ (dashed line) behavior.

In Figure 5.7(c), we present the correspondence between experimental bias voltages (x-axis) and the theoretical energies calculated with the KG equation (y-axis) for many states on several GQDs. The one-to-one correspondence confirms

that the experimental data are consistent with the linear dispersion of the Klein–Gordon equation. The corresponding Fermi velocity $\nu_F = (6.2 \pm 0.3) \times 10^5$ m/s is slightly smaller than the previous results on macroscopic graphene samples on Ir(1 1 1) obtained by ARPES (6.5×10^5 to 9.2×10^5 m/s) [30, 31, 36]. Possible reasons for this discrepancy are that our STM measurements probe the average Fermi velocity around the Dirac cone (in contrast to ARPES) and our experiments are carried out on GQDs instead of bulk graphene. Remarkably, ν_F remains constant down to the smallest structures that we have measured. The intercept with the y-axis in Figure 5.7(c) and the extrapolation to infinite GQD area in Figure 5.7(a) indicate that GQDs on Ir(1 1 1) are n doped by ~ 0.1 eV.

5.8. Conclusion

In summary, we have presented low-temperature STM and STS experiments aimed at understanding the quantum-confined energy levels and their spatially resolved wave functions in atomically well-defined graphene quantum dots. The measured resonances and corresponding LDOS maps correspond to a number of molecular orbitals close in energy, calculated by TB for the exact atomic geometry. The energy position and LDOS structure of these clustered states can also be calculated from the relativistic wave equation for massless particles. Our results provide experimental verification of the physics relevant for graphene-based optoelectronics where wave function engineering via well-defined nanostructuring is likely to be a central issue. In addition, our experiments indicate that the intrinsic electronic states of graphene can be studied on weakly interacting metal substrates [*e.g.*, Ir(1 1 1)]. These systems can act as future test beds for studying the effects of chemical modifications or doping of graphene.

5.9. Bibliography

[1] Geim, A. K. & Novoselov, K. S. The rise of graphene. *Nature Materials* **6**, 183–191 (2007).

[2] Castro Neto, A. H., Peres, N. M. R., Novoselov, K. S. & Geim, A. K. The electronic properties of graphene. *Reviews of Modern Physics* **81**, 109–162 (2009).

[3] Li, X. *et al.* Large-area synthesis of high-quality and uniform graphene films on copper foils. *Science* **324**, 1312–1314 (2009).

[4] Schwierz, F. Graphene transistors. *Nature Nanotechnology* **5**, 487–496 (2010).

[5] Han, M., Özyilmaz, B., Zhang, Y. & Kim, P. Energy band-gap engineering of graphene nanoribbons. *Physical Review Letters* **98**, 206805 (2007).

[6] Rycerz, A., Tworzydlo, J. & Beenakker, C. W. J. Valley filter and valley valve in graphene. *Nature Physics* **3**, 172–175 (2007).

[7] Ponomarenko, L. A. *et al.* Chaotic Dirac billiard in graphene quantum dots. *Science* **320**, 356–358 (2008).

[8] Jiao, L., Zhang, L., Wang, X., Diankov, G. & Dai, H. Narrow graphene nanoribbons from carbon nanotubes. *Nature* **458**, 877–880 (2009).

[9] Kosynkin, D. V. *et al.* Longitudinal unzipping of carbon nanotubes to form graphene nanoribbons. *Nature* **458**, 872–876 (2009).

[10] Ritter, K. A. & Lyding, J. W. The influence of edge structure on the electronic properties of graphene quantum dots and nanoribbons. *Nature materials* **8**, 235–242 (2009).

[11] Cai, J. *et al.* Atomically precise bottom-up fabrication of graphene nanoribbons. *Nature* **466**, 470–473 (2010).

[12] Sprinkle, M. *et al.* Scalable templated growth of graphene nanoribbons on SiC. *Nature nanotechnology* **5**, 727–731 (2010).

[13] Rutter, G. M. *et al.* Scattering and interference in epitaxial graphene. *Science* **317**, 219–222 (2007).

[14] Sun, Z. *et al.* Topographic and electronic contrast of the graphene moiré on Ir(111) probed by scanning tunneling microscopy and noncontact atomic force microscopy. *Physical Review B* **83**, 081415 (2011).

[15] Martin, J. *et al.* Observation of electron-hole puddles in graphene using a scanning single-electron transistor. *Nature Physics* **4**, 144–148 (2008).

[16] Zhang, Y. *et al.* Giant phonon-induced conductance in scanning tunnelling spectroscopy of gate-tunable graphene. *Nature Physics* **4**, 627–630 (2008).

[17] Deshpande, A., Bao, W., Miao, F., Lau, C. & LeRoy, B. Spatially resolved spectroscopy of monolayer graphene on SiO_2. *Physical Review B* **79**, 205411 (2009).

[18] Zhang, Y., Brar, V. W., Girit, C., Zettl, A. & Crommie, M. F. Origin of spatial charge inhomogeneity in graphene. *Nature Physics* **5**, 722–726 (2009).

[19] Wang, B., Ma, X., Caffio, M., Schaub, R. & Li, W.-X. Size-selective carbon nanoclusters as precursors to the growth of epitaxial graphene. *Nano Letters* **11**, 424–430 (2011).

[20] Eom, D. *et al.* Structure and electronic properties of graphene nanoislands on Co(0001). *Nano letters* **9**, 2844–2848 (2009).

[21] Coraux, J. *et al.* Growth of graphene on Ir(111). *New Journal of Physics* **11**, 023006 (2009).

[22] Morgenstern, M. Probing the local density of states of dilute electron systems in different dimensions. *Surface Review and Letters* **10**, 933–962 (2003).

[23] Coraux, J., N'Diaye, A. T., Busse, C. & Michely, T. Structural coherency of graphene on Ir(111). *Nano letters* **8**, 565–570 (2008).

[24] N'Diaye, A. T., Coraux, J., Plasa, T. N., Busse, C. & Michely, T. Structure of epitaxial graphene on Ir(111). *New Journal of Physics* **10**, 043033 (2008).

[25] Hämäläinen, S. K. *et al.* Structure and local variations of the graphene moiré on Ir(111). *Physical Review B* **88**, 201406(R) (2013).

[26] Son, Y.-W., Cohen, M. L. & Louie, S. G. Energy gaps in graphene nanoribbons. *Physical Review Letters* **97**, 216803 (2006).

[27] Brey, L. & Fertig, H. Electronic states of graphene nanoribbons studied with the Dirac equation. *Physical Review B* **73**, 235411 (2006).

[28] Koskinen, P., Malola, S. & Häkkinen, H. Self-passivating edge reconstructions of graphene. *Physical Review Letters* **101**, 115502 (2008).

[29] Heiskanen, H. P., Manninen, M. & Akola, J. Electronic structure of triangular, hexagonal and round graphene flakes near the Fermi level. *New Journal of Physics* **10**, 103015 (2008).

[30] Pletikosić, I. *et al.* Dirac cones and minigaps for graphene on Ir(111). *Physical Review Letters* **102**, 056808 (2009).

[31] Starodub, E. *et al.* In-plane orientation effects on the electronic structure, stability, and Raman scattering of monolayer graphene on Ir(111). *Physical Review B* **83**, 125428 (2011).

[32] Pletikosić, I. *et al.* Photoemission and density functional theory study of Ir(111); energy band gap mapping. *Journal of physics: Condensed matter*

22, 135006 (2010).

[33] Barbier, M., Peeters, F., Vasilopoulos, P. & Pereira, J. Dirac and Klein–Gordon particles in one-dimensional periodic potentials. *Physical Review B* **77**, 115446 (2008).

[34] Tersoff, J. & Hamann, D. R. Theory of the scanning tunneling microscope. *Physical Review B* **31**, 805–813 (1985).

[35] Hancock, Y., Uppstu, A., Saloriutta, K., Harju, A. & Puska, M. J. Generalized tight-binding transport model for graphene nanoribbon-based systems. *Physical Review B* **81**, 245402 (2010).

[36] Rusponi, S. *et al.* Highly anisotropic Dirac cones in epitaxial graphene modulated by an island superlattice. *Physical Review Letters* **105**, 246803 (2010).

6

Tomography resolves a novel crystal structure in a binary nanocrystal superlattice

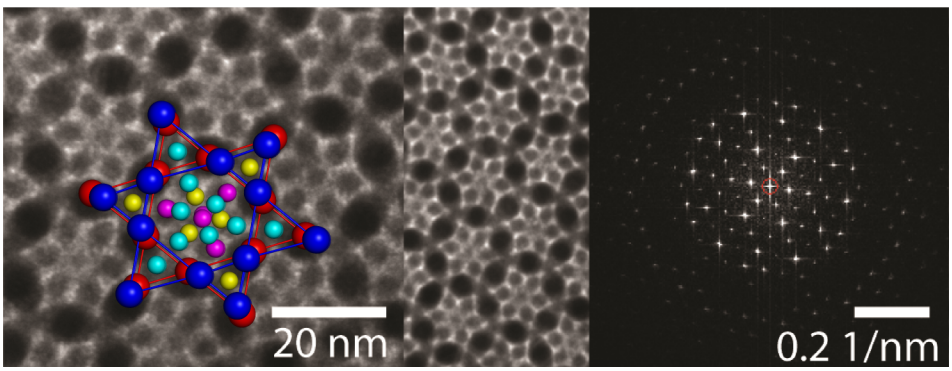

The self-assembly of different nanocrystals into a binary superlattice is of interest for both colloidal science and nanomaterials science. Identification of the superlattice structure including its defects is of key interest in understanding the electrical and optical properties of these systems. TEM has been instrumental to reach this goal but fails for complex crystal structures and buried defects. Here[1], we use electron tomography to resolve the three-dimensional crystal structure of a binary superlattice that could not be resolved by TEM only. The structure with a $[PbSe]_6[CdSe]_{19}$ stoichiometry has no analogue in the atomic world.

[1]This chapter is based on M.P. Boneschanscher, W.H. Evers, W. Qi, J.D. Meeldijk, M. Dijkstra, and D. Vanmaekelbergh, *Nano Letters* **13**, 1312–1316 (2013).

6.1. Self-assembly of binary nanocrystal superlattices

As technology's demand for more sophisticated materials with versatile properties steadily increases, the interest in nanocrystal-based materials has grown rapidly in recent years. A cheap and versatile route for the preparation of these structures is the bottom-up approach based on self-assembly of colloidal nanocrystals. The versatility of this approach originates from two separate steps; first colloidal nanocrystals (NCs) of a metallic, semiconductor and/or magnetic compound are prepared from molecular precursors; second, any conceivable combination of these nanocrystals can be used to achieve binary nanocrystal superlattices (NCSL) by self-assembly [1–3]. In these systems, new properties can emerge from the quantum mechanical and dipolar interactions between the building blocks that are in close contact and ordered in three dimensions [4–8]. In order to understand the colloidal crystallization, and the electrical and optical properties of the resulting superlattices, it is essential to characterize the superlattice structure in detail, including its deformations and crystal defects.

Previous studies have shown that NCSL can be formed in a plethora of different crystal structures that are known from the atomic world [9]. However, NCSL often show slight variations and distortions depending on the details of the self-assembly conditions [8, 10–12]. This feature is very different from atomic lattices where even slight modulations referred to the ideal lattice structure are energetically forbidden due to the nature of the covalent and ionic bonding. The deformations and polymorphs present in self-assembled NCSL, though interesting from a purely scientific viewpoint, hamper the identification and classification of NCSL crystal structures. For instance, they result in blurring of both transmission images and of characteristic spots in scattering techniques.

Structural analysis based on transmission electron microscopy (TEM) has proven to be an important tool for progress in this field. For instance, by careful analysis of the superlattice structures formed by two types of semiconductor NCs with different size and comparing these structures with the predictions of the hard-sphere model, it was concluded that entropy can be an important driving force for the NC self-assembly [13]. Another example: the understanding of self-doping in a binary NCSL of PbTe and Ag_2Te NCs also required a detailed structural analysis [14]. Being a technique that provides direct and local information, TEM is the first choice for structural characterization of such systems. It has, however, the inherent drawback of being a projection method. This first of all means that all information along the beam axis is averaged out, making it very difficult to

study buried lattice defects and distortions. Furthermore, the TEM projections of self-assembled NCSL are, though astoundingly beautiful, often very complex and variable. As a consequence, the direct determination of the crystal structure by identification of different projection patterns is challenging.

In order to further our understanding of the formation and properties of self-assembled NCSL, a complete 3-D structural characterization with a method that provides local information is highly desirable. In electron tomography, a three-dimensional reconstruction of a crystal structure is obtained from a series of 2-D TEM projections acquired at different angles between the incoming electron beam and the lattice (see also Chapter 1) [15, 16]. Hence, one can study the local three-dimensional structure of a lattice including the buried defects and boundaries. This has been demonstrated for binary as well as ternary NCSL [17–20].

Here, we show how electron tomography enabled us to resolve a complex crystal structure formed by self-assembly of PbSe and CdSe NCs. The structure has no analogue in the atomic world. Moreover, we show that the interpretation of TEM projections can be clouded by planar defects and misorientations in the superlattice, but that this can be overcome by an analysis based on tomography. The observed superlattice structure resembles that of a jammed phase that can be simulated using mixtures of hard spheres with the same size ratio. However, modeling the structure with hard spheres results in a filling fraction considerably lower than that of a face-centered cubic (fcc) single component structure. This provides an indication that next to entropic, also enthalpic driving forces could play a role in the crystal structure formation [21–26].

6.2. Materials and methods

Oleic acid capped PbSe and trioctylphosphine oxide/hexadecylamine capped CdSe NCs were prepared according to literature [27, 28]. The as prepared NCs had an inorganic core size of 6.5 ± 0.4 nm (PbSe) and 3.4 ± 0.3 nm (CdSe) and an effective size of 9.4 ± 0.3 nm (PbSe) and 5.8 ± 0.3 nm (CdSe). Effective sizes, giving an estimate for the contribution of the soft ligand shell, were determined by measuring the center-to-center distance of the NCs in a hexagonally packed single-component monolayer.

The NCSL were prepared by solvent evaporation as reported previously [13]. In short, suspensions of the PbSe and CdSe NCs in tetrachloroethylene were mixed at a concentration ratio of 1:4 PbSe:CdSe. Colloidal crystallization was achieved by evaporation of the solvent under reduced pressure ($\sim$ 10 mbar) and elevated

temperature (70 °C) while keeping the substrate (a Pioloform coated TEM-grid) under an angle of 30° with respect to the surface plane. All syntheses were performed in an nitrogen purged glovebox.

Electron tomography was performed in a similar way as described in detail previously [17]. Transmission images and tilt series were acquired in bright-field mode using a Tecnai 20 electron microscope with a LaB_6 electron source (FEI Company, Eindhoven). The tilt series were acquired over ±65° with a 1° increment. The entire object was imaged in underfocus throughout the tilt series.

Particle detection was done using template matching in MATLAB® as described by Friedrich *et al.* [17]. Following the particle detection, a statistical analysis of the unit cell was performed. The unit vectors were determined by averaging over the nearest neighbor distances that were determined by a Voronoi analysis. Nanocrystal positions were then expressed as a distance from the origin of their respective unit cells. Averaging over these distances resulted in the final coordinates. Since the spread in the CdSe positions was very large, we used an additional detection criterion. This was to only include positions that were separated over at least one CdSe diameter (inorganic core diameter) from other CdSe positions within the same unit cell.

6.3. Binary NCSL of PbSe and CdSe at a size ratio of 0.61–0.67

Self-assembly of PbSe and CdSe NCs with an effective size ratio in the range of 0.61–0.67 (r_{CdSe}/r_{PbSe}) resulted in a plethora of different crystal structures showing long-range ordering as observed by TEM (Figure 6.1). Although the grain size of the structures can go up to several micrometers, a lot of different structures are observed within one synthesis. An overview of some typical crystal structures/orientations observed on a single TEM grid is shown in Figure 6.2. We should furthermore note that — despite the variety in crystal structures observed and their long range ordering — the average overall surface coverage of binary NCSL at this size ratio range is very small ($< 1\%$).

6.4. Selection of three different crystal structures for tomography

Figure 6.3 shows different TEM projections taken from parts of self-assembled superlattices formed by the PbSe and CdSe NCs with a size-ratio range of 0.61–0.67. Figure 6.3(a) shows a clear hexagonally symmetric structure (structure 1), as is also confirmed by the clear pattern in the FFT (inset). Figure 6.3(b) (structure 2) shows features that are less sharp, resulting in a much more diffuse FFT.

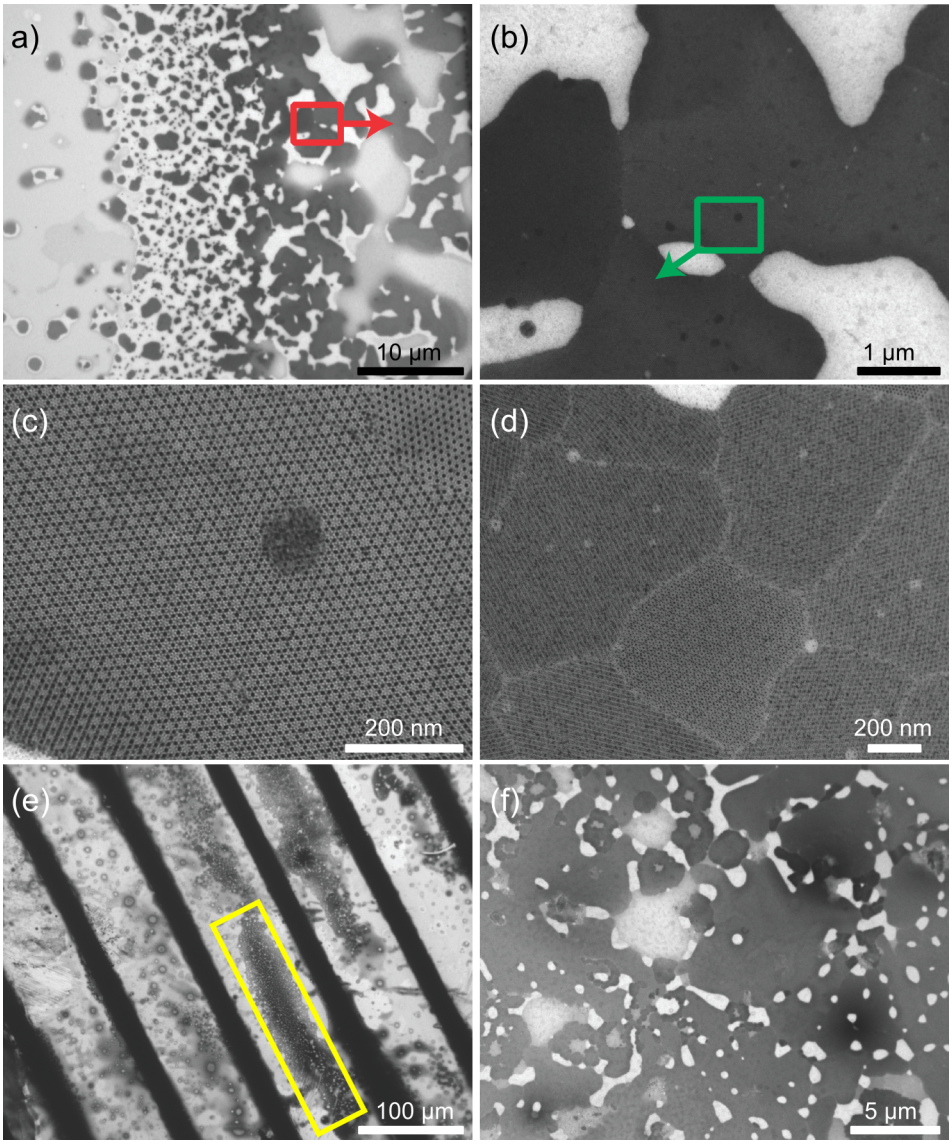

FIGURE 6.1. Overview TEM images of binary NCSL with size ratios 0.61–0.67. (a-c) Micrometer sized domains of various crystal structures/orientations. (b) Zoom-in on the red square in (a). (c) Zoom-in on the green square in (b). (d) Various small crystal domains. (e) Overview indicating the region where the crystallites shown in (d) can be found (yellow box). (f) Zoom-in of (e) showing crystallites (dark) next to thin disordered regions (bright).

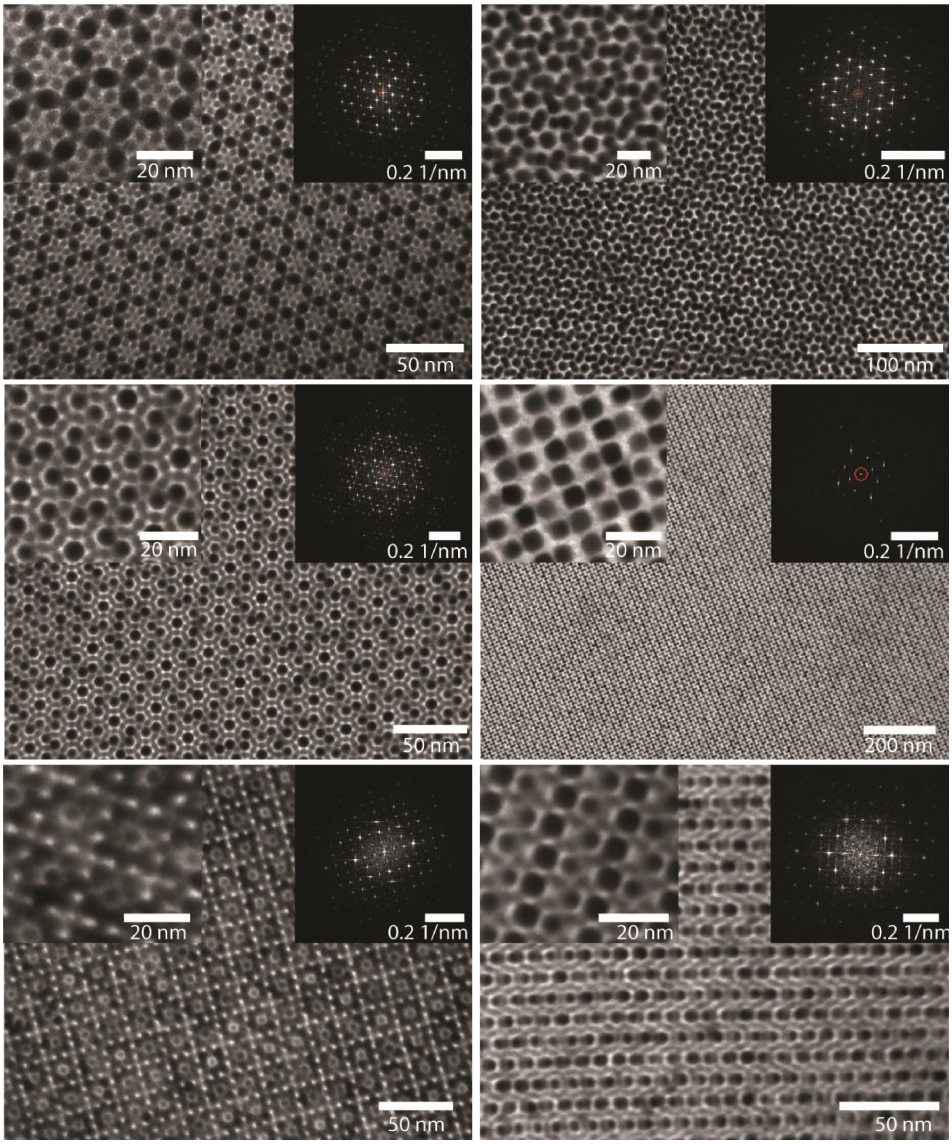

FIGURE 6.2. Excerpt of TEM images of (unknown) binary crystal structures / orientations observed in the size ratio range 0.61–0.67. In the insets a zoom-in and FFT of the obtained superlattices is given. All structures are observed on a single TEM grid. The structure shown in the very first panel will be analyzed in detail in the remainder of this chapter.

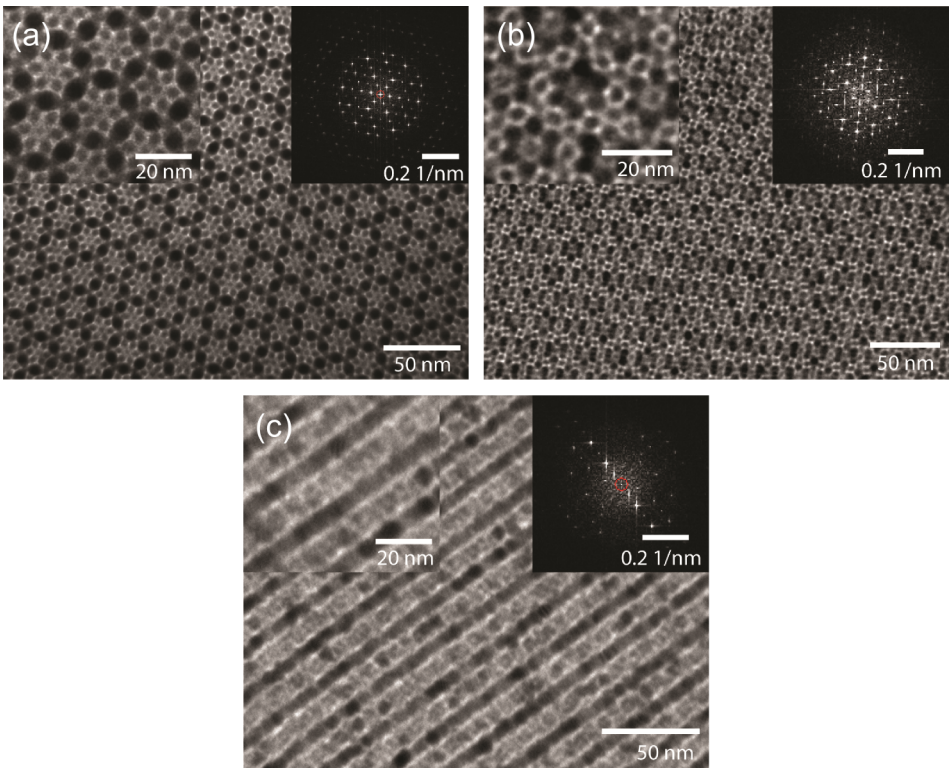

FIGURE 6.3. Three selected binary NCSL with size ratio 0.61–0.67. (a) Structure 1 showing clear hexagonal symmetry. (b) Structure 2 showing a more complex pattern but still hexagonal symmetry. (c) Structure 3 showing repetitions in two directions with no sign of hexagonal symmetry.

However, still a hexagonal symmetry is observed. Figure 6.3(c) shows a superlattice (structure 3) that is under such an angle with the surface that almost no information about the structure can be extracted from the TEM image. These TEM images and the ones presented in Figure 6.2 suggest that at this size-ratio PbSe and CdSe form several different superlattices, very different from our findings in other size-ratio regions where the same types of nanocrystals only lead to one or two binary crystal structures that were in agreement with predictions for hard-sphere mixtures [13]. Notice that these complex TEM images do not allow to identify the unit cell and crystal structure of these superlattices.

6.5. The A_6B_{19} crystal structure

Using electron tomography and computer-aided particle detection, the average unit cell vectors for structure 1 can be estimated. The position of the larger PbSe NCs is relatively easy to find since the heavy Pb atoms lead to high image contrast. Using the particle detection method as described in Reference [17], the positions of 466 individual PbSe NCs were determined. The unit vector distance between each of them was calculated and used to transpose all detected PbSe nanocrystal positions into one unit cell. This unit cell was then used to determine the relative positions of the smaller CdSe NCs. For the CdSe NCs, 1852 positions were determined. The relative distance to the unit cell's origin was used to transpose all determined positions into one unit cell. After this, their average position within the unit cell was calculated. The CdSe NCs are much harder to detect due to their smaller size and lower contrast in TEM: Cd is a much weaker electron scatterer than Pb. This results in a wider spread in the detected Cd positions. The final crystal structure is presented in Figure 6.4, and the coordinates of the primitive unit cell are presented in Figure 6.5 and Tables 6.1 and 6.2. The structure has the remarkable PbSe:CdSe stoichiometry of 6:19.

Looking at the structure in more detail shows that the PbSe NCs form an ABA stacking of equivalent kagome-like lattices with three larger and three smaller triangles attached to a hexagon. Notice that the A (blue) and B (red) layers are rotated 60° with respect to each other, *i.e.*, small triangles in layer A overlap with large triangles in layer B. The CdSe NCs form an ABCBA stacking of three different hexagonally symmetric layers. Here A (cyan) and C (yellow) are in the same plane as the PbSe layers, and B (purple) occupies one fcc and three defect positions in between A and C. The total volume of the unit cell is 5365 nm^3. Using the effective radius of the NCs we find a packing fraction of 0.85. This dense stacking suggests that the crystal structure might be stable in the hard-sphere framework. However, it is to be noted that using the effective radius of the NCs is known to lead to an overestimation of the packing fraction due to the extra degree of freedom the NC ligands have in three dimensions with respect to two dimensions [17]. A thorough search through various crystal databases reveals that the A_6B_{19} crystal structure has no counterpart in the atomic world. However, although no exact atomic equivalent was found, the crystal structure presented here resembles the $Gd_3Ru_4Al_{12}$ and the $U_3Co_{12-x}Y_4$ (Y = Si, Ge) structures, both of which are ternary variants of the $EuMg_{5.2}$ structure family [Figure 6.4(e)] [29–31].

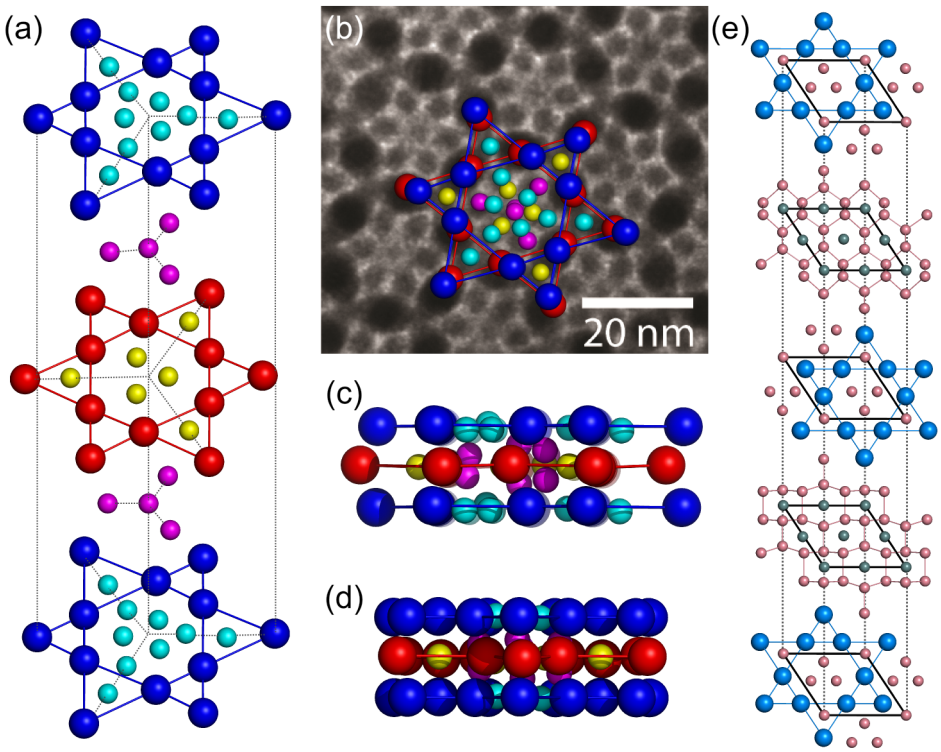

FIGURE 6.4. The A_6B_{19} structure. (a) The PbSe positions (large spheres) form an ABA stacking of a kagome-like structure with a 60° rotation between A (blue) and B (red). The CdSe positions (small spheres) form three different layers. The first layer (cyan) is in the same plane as the PbSe positions indicated in blue. The second layer (yellow) is in plane with the PbSe positions indicated in red. The third layer (purple) is located in between the PbSe layers, occupying one fcc position and three defect positions. Note that the spheres are not drawn to scale for better visibility. (b) Top view of the A_6B_{19} structure aligned with the TEM projection. (c,d) The respective side views of the structure. (e) Crystal structure of the $U_3Co_{12-x}Y_4$ (Y = Si, Ge) crystal, showing quite some resemblance to the A_6B_{19} structure described here. The primitive unit cell is indicated in black, U atoms in blue, Co atoms in pink, Si/Ge atoms in green.

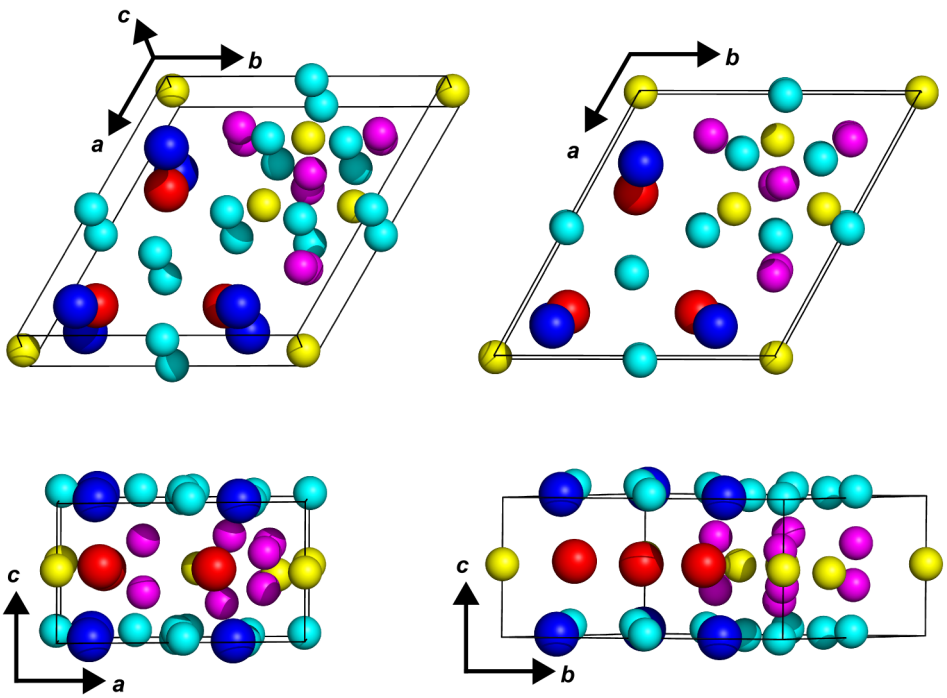

FIGURE 6.5. Three dimensional, top, and different side views of the detected unit cell. Spheres with the same color depict nanocrystals within the same layer (PbSe in blue and red, CdSe in cyan, magenta and yellow). Unit vectors are defined as $\boldsymbol{a}$ in the xy-plane at $-120°$ with the x-axis, $\boldsymbol{b}$ along the x-axis and $\boldsymbol{c}$ along the z-axis.

TABLE 6.1. Lattice parameters given in Cartesian coordinates, lengths and angles.

unit vector	$\boldsymbol{x}$ **(nm)**	$\boldsymbol{y}$ **(nm)**	$\boldsymbol{z}$ **(nm)**	**length (nm)**	**angle (°)**
$\boldsymbol{a}, \alpha$	-9.4 ± 0.7	-22.3 ± 0.6	-0.2 ± 0.8	24.2 ± 0.7	89.2 ± 2.8
$\boldsymbol{b}, \beta$	22.4 ± 0.7	2.3 ± 0.8	-0.3 ± 0.7	22.5 ± 0.7	89.4 ± 1.8
$\boldsymbol{c}, \gamma$	0.3 ± 0.9	-0.4 ± 0.9	11.2 ± 0.7	11.2 ± 0.8	118.7 ± 2.5

TABLE 6.2. The 25 unique nanocrystal positions within the unit cell given in both Cartesian coordinates and fractions of the unit vectors. Color coding refers to Figure 6.4 (b = blue, r = red, c = cyan, m = magenta, y = yellow).

nano-crystal	x **(nm)**	y **(nm)**	z **(nm)**	a	b	c
PbSe (b)	-5.1 ± 0.7	-19.3 ± 0.9	-0.2 ± 0.9	0.88 ± 0.03	0.14 ± 0.04	0.00 ± 0.08
PbSe (b)	7.9 ± 0.7	-18.0 ± 0.9	-0.4 ± 0.6	0.88 ± 0.03	0.72 ± 0.04	0.00 ± 0.05
PbSe (b)	0.6 ± 1.0	-5.7 ± 0.7	0.0 ± 0.6	0.27 ± 0.04	0.14 ± 0.03	0.01 ± 0.05
PbSe (r)	6.5 ± 1.0	-17.3 ± 0.9	5.4 ± 0.9	0.83 ± 0.04	0.63 ± 0.04	0.51 ± 0.08
PbSe (r)	0.6 ± 1.2	-8.3 ± 0.9	5.2 ± 0.9	0.38 ± 0.05	0.18 ± 0.04	0.48 ± 0.08
PbSe (r)	-3.8 ± 1.2	-18.3 ± 1.1	5.6 ± 1.0	0.83 ± 0.05	0.17 ± 0.05	0.52 ± 0.09
CdSe (c)	0.8 ± 1.0	-14.5 ± 0.7	0.4 ± 0.9	0.68 ± 0.04	0.32 ± 0.03	0.06 ± 0.08
CdSe (c)	6.1 ± 1.0	-10.5 ± 0.7	0.2 ± 0.9	0.52 ± 0.04	0.49 ± 0.03	0.04 ± 0.08
CdSe (c)	12.2 ± 1.0	-10.7 ± 0.7	10.6 ± 0.4	0.52 ± 0.04	0.76 ± 0.03	0.98 ± 0.04
CdSe (c)	-4.8 ± 1.0	-11.4 ± 0.7	0.3 ± 0.7	0.51 ± 0.04	0.00 ± 0.03	0.04 ± 0.06
CdSe (c)	8.9 ± 1.2	-4.4 ± 0.7	10.8 ± 0.7	0.23 ± 0.05	0.48 ± 0.03	0.98 ± 0.06
CdSe (c)	14.9 ± 1.0	-3.8 ± 0.9	-0.2 ± 0.7	0.25 ± 0.04	0.77 ± 0.04	0.01 ± 0.06
CdSe (c)	11.6 ± 1.2	1.0 ± 0.7	0.1 ± 1.0	0.01 ± 0.05	0.52 ± 0.03	0.02 ± 0.09
CdSe (m)	11.6 ± 0.7	-6.4 ± 0.7	2.4 ± 0.4	0.35 ± 0.03	0.66 ± 0.03	0.24 ± 0.04
CdSe (m)	6.1 ± 1.0	-3.1 ± 0.7	3.2 ± 0.8	0.17 ± 0.04	0.34 ± 0.03	0.30 ± 0.07
CdSe (m)	12.4 ± 1.0	-13.2 ± 0.7	3.6 ± 0.9	0.67 ± 0.04	0.83 ± 0.03	0.36 ± 0.08
CdSe (m)	17.1 ± 1.0	-2.0 ± 0.7	3.6 ± 0.9	0.17 ± 0.04	0.83 ± 0.03	0.35 ± 0.08
CdSe (y)	0.2 ± 1.0	-0.2 ± 1.1	5.6 ± 1.1	0.00 ± 0.04	0.00 ± 0.05	0.50 ± 0.10
CdSe (y)	8.6 ± 0.7	-8.7 ± 0.4	5.2 ± 0.4	0.44 ± 0.03	0.56 ± 0.02	0.49 ± 0.04
CdSe (y)	11.4 ± 1.0	-2.9 ± 0.7	5.2 ± 0.4	0.18 ± 0.04	0.58 ± 0.03	0.48 ± 0.04
CdSe (y)	15.7 ± 1.0	-8.0 ± 1.1	4.7 ± 0.7	0.44 ± 0.04	0.88 ± 0.05	0.45 ± 0.06
CdSe (m)	12.3 ± 1.0	-6.3 ± 0.9	7.8 ± 0.6	0.34 ± 0.04	0.68 ± 0.04	0.72 ± 0.05
CdSe (m)	6.1 ± 1.2	-3.1 ± 0.9	7.4 ± 0.8	0.16 ± 0.05	0.33 ± 0.04	0.67 ± 0.07
CdSe (m)	12.3 ± 1.0	-13.7 ± 0.7	6.6 ± 0.7	0.69 ± 0.04	0.83 ± 0.03	0.62 ± 0.06
CdSe (m)	17.3 ± 1.0	-2.3 ± 0.7	7.0 ± 0.6	0.18 ± 0.04	0.84 ± 0.03	0.65 ± 0.05

6.6. Space group assignment of the A_6B_{19} structure

To assign the correct space group to the A_6B_{19} crystal structure the dedicated software tool FINDSYM [32] was used. The unit vectors as given in Table 6.1 and the positions as given in Table 6.2 were used as input. As additional input parameters we used a tolerance of 1.7 nm, a random centering and an hexagonal axes system. Using these tolerance settings, the symmetry operations possible

showed that the A_6B_{19} structure can be classified in the $P\bar{6}m2$ space group (no. 187). Forcing this symmetry upon the structure, the occupation of the unit cell can be given in Wyckoff positions (Table 6.3).

Comparing the measured crystal structure with the structure after forcing $P\bar{6}m2$ symmetry we note that, in order to force the $P\bar{6}m2$ symmetry we had to move the nanocrystals over distances that fall well below the standard deviation in our measurement as presented in Table 6.2 (see also Figure 6.6). We therefore conclude that the deviation of the measured crystal structure from $P\bar{6}m2$ symmetry is more likely to be a measurement error than a physical phenomenon.

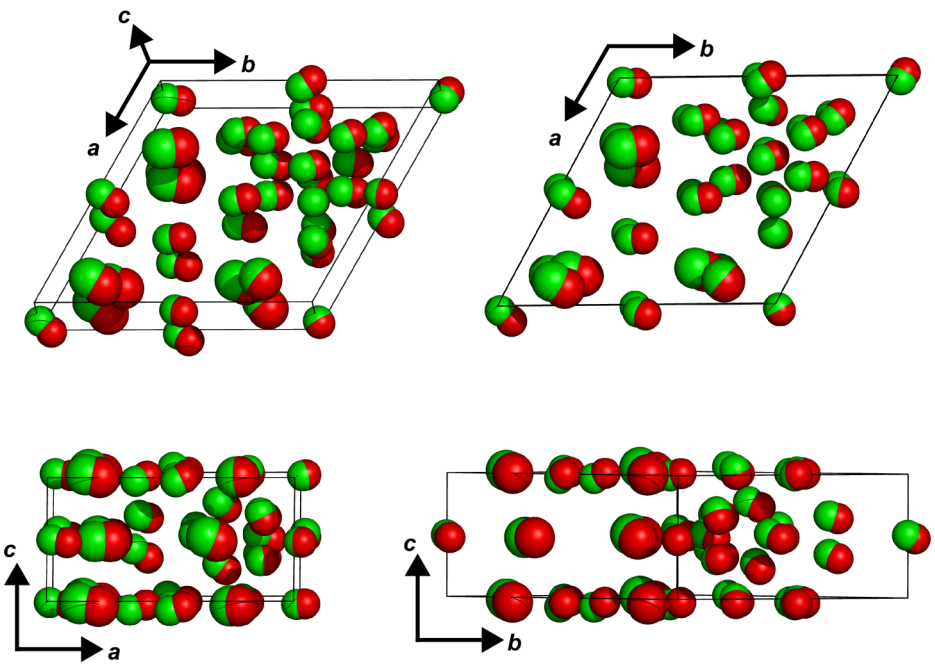

FIGURE 6.6. Comparison of the detected unit cell before (green) and after (red) forcing $P\bar{6}m2$ symmetry. Note that the spheres are not drawn to scale, to better visualize the differences. The shifts in positions in order to force $P\bar{6}m2$ symmetry are well below the standard deviations of the measured positions.

TABLE 6.3. The nanocrystal positions within the unit cell when forcing $P\bar{6}m2$ symmetry. The unit cell vectors are $\boldsymbol{a} = \boldsymbol{b} = 23.36$ nm, $\boldsymbol{c} = 11.21$ nm with $\alpha = \beta = 90°$ and $\gamma = 120°$. Color coding refers to Figure 6.4 (b = blue, r = red, c = cyan, m = magenta, y = yellow).

nanocrystal	***a***	***b***	***c***	**nanocrystal**	***a***	***b***	***c***
Wyckoff position $\boldsymbol{j}, x = -0.135$				**Wyckoff position** $\boldsymbol{k}, x = -0.182$			
PbSe (b)	0.270	0.135	0.000	PbSe (r)	0.363	0.182	0.500
PbSe (b)	0.865	0.135	0.000	PbSe (r)	0.818	0.182	0.500
PbSe (b)	0.865	0.730	0.000	PbSe (r)	0.818	0.637	0.500
Wyckoff position $\boldsymbol{e}$				**Wyckoff position** $\boldsymbol{b}$			
CdSe (c)	0.667	0.333	0.000	CdSe (y)	0.000	0.000	0.500
Wyckoff position $\boldsymbol{j}, x = -0.497$				**Wyckoff position** $\boldsymbol{j}, x = 0.237$			
CdSe (c)	0.503	0.007	0.000	CdSe (c)	0.237	0.473	0.000
CdSe (c)	0.503	0.497	0.000	CdSe (c)	0.237	0.763	0.000
CdSe (c)	0.993	0.497	0.000	CdSe (c)	0.572	0.763	0.000
Wyckoff position $\boldsymbol{k}, x = 0.430$				**Wyckoff position** $\boldsymbol{h}, z = -0.260$			
CdSe (y)	0.140	0.570	0.500	CdSe (m)	0.333	0.667	0.260
CdSe (y)	0.430	0.570	0.500	CdSe (m)	0.333	0.667	0.740
CdSe (y)	0.430	0.860	0.500				
Wyckoff position $\boldsymbol{n}, x = 0.166, z = -0.345$							
CdSe (m)	0.166	0.332	0.345				
CdSe (m)	0.166	0.834	0.345				
CdSe (m)	0.668	0.834	0.345				
CdSe (m)	0.166	0.332	0.655				
CdSe (m)	0.166	0.834	0.655				
CdSe (m)	0.668	0.834	0.655				

6.7. On the stability of the A_6B_{19} structure

To evaluate whether the experimentally observed A_6B_{19} structure is stable for a binary mixture of hard spheres, Monte Carlo (MC) simulations were performed. The configuration of the experimental results and a size ratio of 0.695 were used as initial parameters for the simulations [Figure 6.7(a)]. Subsequently the system was compressed to a higher pressure of $PV/kT = 1 \times 10^6$ using 3×10^5 MC steps. The most dense packing fraction obtained in our simulation is 0.641. Although

this is higher than the experimental values for the inorganic cores only, it is still much below the 0.85 we find using the effective sizes. Figure 6.7(b) shows the densest structure obtained in our simulations. Compared to the experimental configuration, some of the small CdSe nanocrystals moved out of position and the structure becomes more disordered. If the nanocrystals are only allowed to move in the xy-direction, the A_6B_{19} structure seems to be stable. The maximum packing fraction obtained in this case is 0.575.

In addition to the simulations described above, we performed Monte Carlo simulations with a variable box shape [23] to predict the crystal structure using the hard-sphere model. Statistical analysis of 100 independent simulation cycles shows the formation of jammed phases with maximum packing fractions in the range of 0.668–0.686 (Figure 6.8). These phases resemble the A_6B_{19} crystal structure with the position of the PbSe NCs mostly being preserved. However the positions of the CdSe NCs shift with respect to their position in the A_6B_{19} structure.

Our finding that MC simulations with hard spheres are unable to reproduce the experimentally found structure can be attributed to complications in the modeling due to the large system size. In addition, this finding may point out that

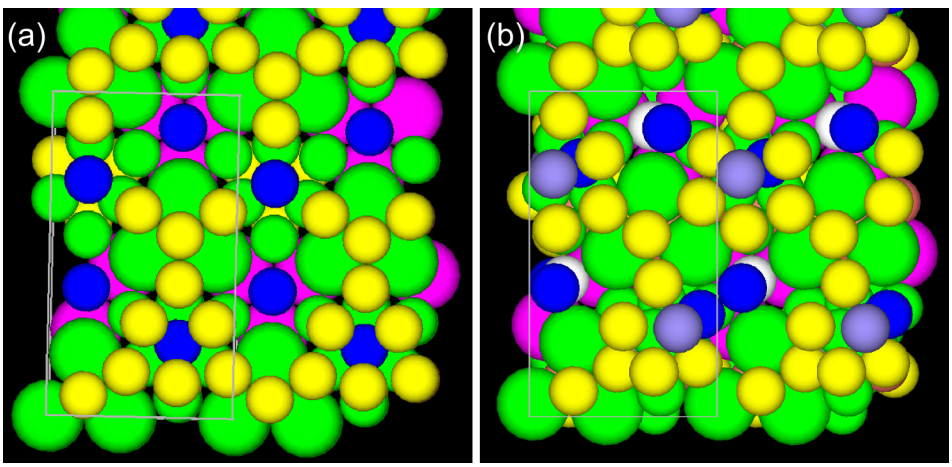

FIGURE 6.7. Monte Carlo simulations of the A_6B_{19} structure. (a) Top view of the initial configuration obtained from experiment. The color coding of the particles corresponds to the particular height of their center of mass. (b) Most dense packing structure obtained by MC simulations using a square box.

the system actually cannot be modeled with hard spheres. This would imply that the formation of the observed crystal structure cannot be explained by entropy alone. If this is true, than it would be contradicting our earlier work [13] where we describe how, for exactly the same nanocrystals and the same chemical environment but different size-ratios, we mainly do find superlattice structures of which the formation can be explained with entropy only. We would like to point out that in the size ratio regime of 0.61–0.67 used in this study, no stable structures of hard spheres have been predicted. As such, the formation of the crystal structure described in this work does not need to compete with entropy driven crystallization. Therefore we do not think that the enthalpic interaction between the nanocrystals necessarily needs to be large to explain the observed superlattice crystal structure. Rather, we think that enthalpy plays a bigger role in this superlattice crystal formation, simply due to the lower entropic contribution. We would furthermore like to remark that for the more complex structures with larger unit cells, like $NaZn_{13}$ and the Laves phases, the packing fraction of the structure alone is not an adequate measure anymore for the stability of the crystal. In fact, the Laves phases are with their packing fraction of 0.710 significantly below the 0.741 of the single component fcc structures. Nonetheless, free energy calculations show that the Laves phases are stable in a size-ratio range of 0.76–0.84 [33].

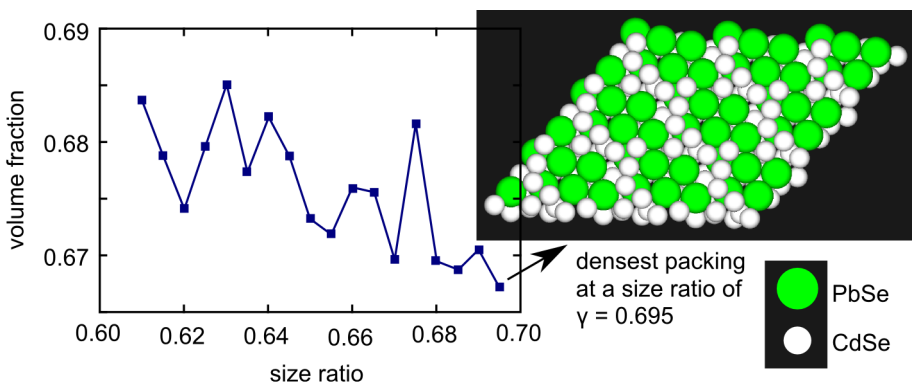

FIGURE 6.8. Most dense volume fraction as a function of particle size ratio in the region 0.61–0.69 using MC simulations with a variable box shape.

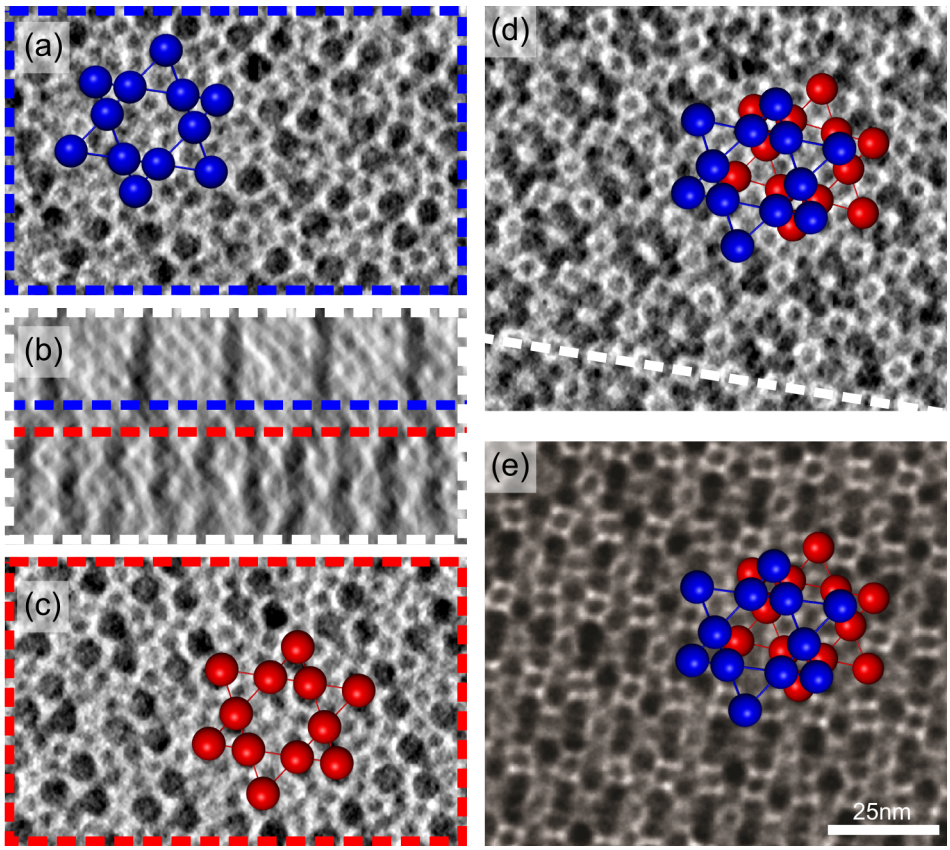

FIGURE 6.9. Tomographic reconstruction of structure 2. Horizontal reconstruction slices along the first PbSe layer above (a) and below (c) the planar defect. (b) A vertical reconstruction slice showing the planar defect and the position of the horizontal reconstruction slices. (d) Average of the two horizontal slices showing that the two PbSe kagome layers are not just rotated but also shifted with respect to each other. The white line indicates the position of the vertical slice (b). (e) The original TEM image of structure 2 showing the same pattern as (d).

6.8. Electron tomography on two more structures

Analyzing the electron tomogram of structure 2 [Figure 6.3(b)] directly shows the added value of electron tomography: a comparison of the reconstruction slices of

the electron tomograms of structure 1 and 2 readily shows that they are actually the same structure in disguise. What makes the TEM images so different however [compare Figure 6.3(a) and 6.3(b)], is that a planar defect runs through the middle of structure 2 (Figure 6.9). This planar defect is in fact a stacking fault where the next kagome structure of PbSe NCs was not just rotated over 60°, but also translated by the small PbSe–PbSe distance over both the in-plane unit cell axes. Since the planar defect is located roughly in the middle of the crystal, both orientations contribute equally to the scattering of the electron beam. This results in a TEM picture showing a complicated pattern misleadingly suggesting two different crystal structures in Figure 6.3.

We found that structure 3 was built up from the same kagome-like layers of PbSe as structure 1, with the difference that the layers in structure 3 are stacked under an angle of 43° with respect to the substrate (Figure 6.10). In earlier work by Smith *et al.* [34] and Friedrich *et al.* [17] drying forces resulting in strong compression in the direction of the surface normal were observed. In the present case however, the drying forces resulted in a lamellar offset of the different PbSe layers, thus distorting the crystal in the direction along the kagome layers rather than in the direction of the surface normal. The fact that the kagome layers are preserved hints toward stronger intralayer interactions than interlayer interactions, something that could also account for the stacking fault in structure 2. The lamellar distortion does not significantly influence the unit cell volume, which is only 5.8% larger than the unit cell volume for structure 1. However, combined with the difference in orientation with respect to the electron beam it makes a reliable interpretation of the TEM image [Figure 6.3(c)] impossible.

6.9. Conclusion

PbSe and CdSe nanocrystals with a size ratio of 0.67 were found to assemble into a complicated binary nanocrystal superlattice, of which the structure could not be determined by TEM. Electron tomography in combination with computer-aided particle tracking enabled us to determine the crystal lattice in three dimensions: the crystal with A_6B_{19} stoichiometry is formed by stacked layers of a kagome-like lattice of PbSe NCs with interstitial CdSe NCs. This work shows that electron tomography is an indispensable tool for the advanced study of nanocrystal solids, a very broad class of emerging nanostructured materials.

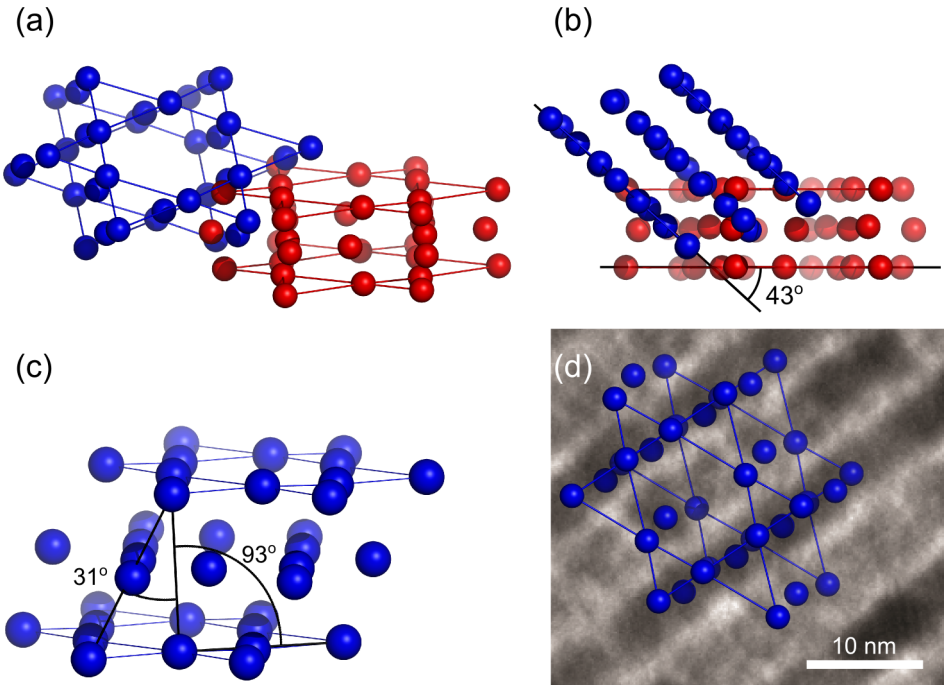

FIGURE 6.10. Analysis of structure 3. (a) Comparison of the distorted structure 3 (blue) with structure 1 (red). (b) The same layered kagome structure of the PbSe NCs is formed (blue), but the layer stacking direction is rotated 43° with respect to the stacking direction of structure 1 (red). (c) Drying forces acting on the crystal resulted in a lamellar displacement of the different PbSe layers. (d) Comparison of the detected unit cell to the TEM image.

6.10. Bibliography

[1] Talapin, D. V., Lee, J.-S., Kovalenko, M. V. & Shevchenko, E. V. Prospects of colloidal nanocrystals for electronic and optoelectronic applications. *Chemical Reviews* **110**, 389–458 (2010).

[2] Rogach, A. *et al.* Organization of matter on different size scales: monodisperse nanocrystals and their superstructures. *Advanced Functional Materials* **12**, 653–664 (2002).

[3] Vanmaekelbergh, D. Self-assembly of colloidal nanocrystals as route to novel classes of nanostructured materials. *Nano Today* **6**, 419–437 (2011).

[4] Overgaag, K. *et al.* Binary superlattices of PbSe and CdSe nanocrystals. *Journal of the American Chemical Society* **130**, 7833–7835 (2008).

[5] Redl, F. X., Cho, K.-S., Murray, C. B. & O'Brien, S. Three-dimensional binary superlattices of magnetic nanocrystals and semiconductor quantum dots. *Nature* **423**, 968–971 (2003).

[6] Kiely, C. J., Fink, J., Brust, M., Bethell, D. & Schiffrin, D. J. Spontaneous ordering of bimodal ensembles of nanoscopic gold clusters. *Nature* **396**, 444–446 (1998).

[7] Chen, Z., Moore, J., Radtke, G., Sirringhaus, H. & O'Brien, S. Binary nanoparticle superlattices in the semiconductor-semiconductor system: CdTe and CdSe. *Journal of the American Chemical Society* **129**, 15702–15709 (2007).

[8] Shevchenko, E. V., Talapin, D. V., O'brien, S. & Murray, C. B. Polymorphism in AB_{13} nanoparticle superlattices: an example of semiconductor-metal metamaterials. *Journal of the American Chemical Society* **127**, 8741–8747 (2005).

[9] Shevchenko, E. V., Talapin, D. V., Kotov, N. A., O'Brien, S. & Murray, C. B. Structural diversity in binary nanoparticle superlattices. *Nature* **439**, 55–59 (2006).

[10] Talapin, D. V. *et al.* Quasicrystalline order in self-assembled binary nanoparticle superlattices. *Nature* **461**, 964–967 (2009).

[11] Ye, X., Chen, J. & Murray, C. B. Polymorphism in self-assembled AB_6 binary nanocrystal superlattices. *Journal of the American Chemical Society* **133**, 2613–2620 (2011).

[12] Bodnarchuk, M. I., Shevchenko, E. V. & Talapin, D. V. Structural defects in periodic and quasicrystalline binary nanocrystal superlattices. *Journal of the American Chemical Society* **133**, 20837–20849 (2011).

[13] Evers, W. H. *et al.* Entropy-driven formation of binary semiconductor-nanocrystal superlattices. *Nano Letters* **10**, 4235–4241 (2010).

[14] Urban, J. J., Talapin, D. V., Shevchenko, E. V., Kagan, C. R. & Murray, C. B. Synergism in binary nanocrystal superlattices leads to enhanced p-type conductivity in self-assembled PbTe/Ag_2 Te thin films. *Nature Materials* **6**, 115–121 (2007).

[15] Midgley, P. A. & Weyland, M. 3D electron microscopy in the physical sciences: the development of Z-contrast and EFTEM tomography. *Ultramicroscopy* **96**, 413–431 (2003).

[16] Friedrich, H., de Jongh, P. E., Verkleij, A. J. & de Jong, K. P. Electron tomography for heterogeneous catalysts and related nanostructured materials. *Chemical Reviews* **109**, 1613–1629 (2009).

[17] Friedrich, H. *et al.* Quantitative structural analysis of binary nanocrystal superlattices by electron tomography. *Nano Letters* **9**, 2719–2724 (2009).

[18] Evers, W. H., Friedrich, H., Filion, L., Dijkstra, M. & Vanmaekelbergh, D. Observation of a ternary nanocrystal superlattice and its structural characterization by electron tomography. *Angewandte Chemie International Edition* **48**, 9655–9657 (2009).

[19] Florea, I. *et al.* 3D quantitative analysis of platinum nanocrystal superlattices by electron tomography. *ACS nano* **6**, 2574–2581 (2012).

[20] Bals, S. *et al.* Three-dimensional atomic imaging of colloidal core-shell nanocrystals. *Nano Letters* **11**, 3420–3424 (2011).

[21] Hopkins, A., Jiao, Y., Stillinger, F. & Torquato, S. Phase diagram and structural diversity of the densest binary sphere packings. *Physical Review Letters* **107**, 125501 (2011).

[22] Hopkins, A., Stillinger, F. & Torquato, S. Densest binary sphere packings. *Physical Review E* **85**, 021130 (2012).

[23] Filion, L. *et al.* Efficient method for predicting crystal structures at finite temperature: variable box shape simulations. *Physical Review Letters* **103**, 188302 (2009).

[24] Hudson, T. S. & Harrowell, P. Dense packings of hard spheres of different sizes based on filling interstices in uniform three-dimensional tilings. *Journal of Physical Chemistry B* **112**, 8139–8143 (2008).

[25] Hudson, T. S. & Harrowell, P. Structural searches using isopointal sets as generators: densest packings for binary hard sphere mixtures. *Journal of Physics: Condensed Matter* **23**, 194103 (2011).

[26] O'Toole, P. I. & Hudson, T. S. New high-density packings of similarly sized binary spheres. *Journal of Physical Chemistry C* **115**, 19037–19040 (2011).

[27] Houtepen, A. J., Koole, R., Vanmaekelbergh, D., Meeldijk, J. & Hickey, S. G. The hidden role of acetate in the PbSe nanocrystal synthesis. *Journal of the American Chemical Society* **128**, 6792–6793 (2006).

[28] de Mello Donegá, C., Hickey, S. G., Wuister, S. F., Vanmaekelbergh, D. & Meijerink, A. Single-step synthesis to control the photoluminescence quantum yield and size dispersion of CdSe nanocrystals. *Journal of Physical Chemistry B* **107**, 489–496 (2003).

[29] Gladyshevskii, R. E., Strusievicz, O. R., Cenzual, K. & Parthé, E. Structure of $Gd_3Ru_4Al_{12}$, a new member of the $EuMg_{5.2}$ structure family with minority-atom clusters. *Acta Crystallographica Section B Structural Science* **49**, 474–478 (1993).

[30] Soudé, A., Tougait, O., Pasturel, M., Kaczorowski, D. & Noël, H. Crystal structure and electronic properties of the new compounds $U_3Co_{12-x}X_4$ with X=Si, Ge. *Journal of Solid State Chemistry* **183**, 1180–1185 (2010).

[31] Erassme, J. & Lueken, H. Strontium and europium polynuclear units in intermetallic compounds with magnesium. Structural refinements and relationships. *Acta Crystallographica B* **43**, 244–250 (1987).

[32] Stokes, H. T. & Hatch, D. M. FINDSYM : program for identifying the space-group symmetry of a crystal. *Journal of Applied Crystallography* **38**, 237–238 (2005).

[33] Hynninen, A.-P., Filion, L. & Dijkstra, M. Stability of LS and LS_2 crystal structures in binary mixtures of hard and charged spheres. *The Journal of chemical physics* **131**, 064902 (2009).

[34] Smith, D. K., Goodfellow, B., Smilgies, D.-M. & Korgel, B. A. Self-assembled simple hexagonal AB_2 binary nanocrystal superlattices: SEM, GISAXS, and defects. *Journal of the American Chemical Society* **131**, 3281–3290 (2009).

7

Single crystal honeycomb superlattices obtained by oriented attachment

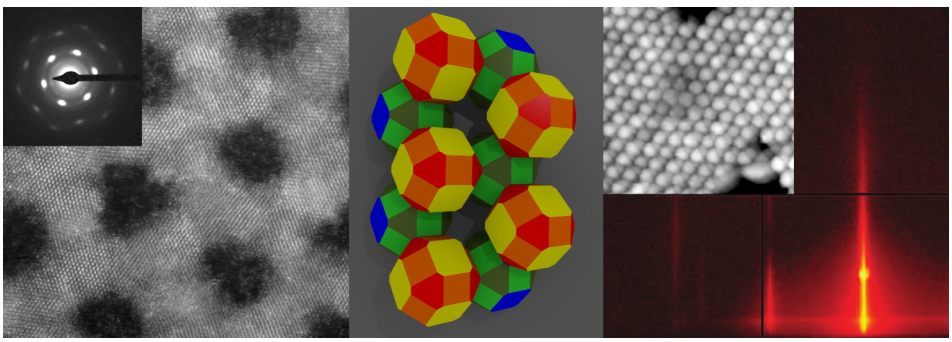

In this chapter[1] we present an atomic and nanoscale analysis of PbSe and CdSe superlattices with honeycomb nanogeometry. Extensive atomic and nanoscale imaging using different techniques shows that the honeycomb structures are atomically coherent, have bond angles of 90°, and a nanogeometry that bears analogy with silicene. The nanocrystals elongate in the direction of the bonds, providing evidence of neck-formation and vast atomic motion during the attachment process. We provide a route to a unique class of semiconductors, with a band structure determined by the honeycomb nanogeometry.

[1]This chapter is based on M.P. Boneschanscher, W.H. Evers, J.J. Geuchies, T. Altantzis, B. Goris, F.T. Rabouw, S.A.P. van Rossum, H.S.J. van der Zant, L.D.A. Siebbeles, G. van Tendeloo, J. Hilhorst, I. Swart, A. Pethukov, S. Bals, and D. Vanmaekelbergh *submitted*.

7.1. Oriented attachment of nanocrystals

Oriented attachment is a process in which two adjacent nanocrystals form a single one, due to an atomically matched bond formation between two specific facets. The oriented attachment of nanocrystals of transition metal (hydro)oxides [1–3] and of calcium salts [4, 5] in aqueous media has been studied in detail, as it is a widespread process in biomineralization. In colloid nanoscience, pre-synthesized nanocrystals with well-defined facets dispersed in organic solvents have been used [6, 7]. Controlled oriented attachment is currently emerging as a route to form extended one- and two-dimensional single-crystalline semiconductors of II-VI and IV-VI compounds [8–12], which are of interest in opto-electronics.

With truncated nanocubes of the Pb-chalcogenide family, 2-D atomically coherent ultra-thin quantum wells [11] as well as superlattices with long-range square or honeycomb nanogeometry [12] were recently reported. The formation of such systems is highly remarkable, as several demanding conditions have to be fulfilled: the nanocrystal building blocks must be nearly monodisperse in size and shape, and attachment should only occur with a geometrically defined subset of nanocrystal facets of one sort. The high degree of atomic and nanoscale order in such systems is far from understood. This is most obvious for extended, atomically coherent PbSe superlattices with honeycomb nanogeometry. In this case, immediate questions emerge on the large-scale crystallographic orientation of the nanocrystals, the role of surface passivation of specific facets, and the atomic mechanism of attachment.

In this chapter, we report on the atomic and nanoscale analysis of atomically coherent PbSe and CdSe honeycomb superlattices. Using HAADF-STEM tomography, we show that the honeycomb structures are buckled, *i.e.*, have nanocrystals occupying two parallel planes, and hence show nanoscale analogy with the atomic silicene honeycomb structure. The specific orientation of the nanocrystals in the 2-D superlattice extends over hundreds of unit cells, suggesting that such types of single crystals must be formed from a pre-ordered state, *e.g.*, at the suspension/air interface. We show that the nanocrystals in the honeycomb structure are considerably elongated in the direction of the nanocrystal-nanocrystal bond, compared to the native building blocks. This points to a bond formation via necking accompanied with a gradual release of the capping molecules and vast atomic motion. Moreover, the 2-D honeycomb structures of PbSe with a rock-salt atomic lattice are robust enough to be transformed into 2-D CdSe lattices with a zinc blende atomic lattice by cation-exchange, keeping the honeycomb nanogeometry intact.

This opens a route to a new class of 2-D semiconductors with tunable composition. In these structures the nanoscale honeycomb geometry has been predicted to result in conduction bands that can be filled with Dirac-type charge carriers as in graphene, with — in contrast to graphene — strong spin-orbit coupling [13]. Such nanoscale honeycomb semiconductors cannot be created by other means.

7.2. Materials and methods

7.2.1. Nanocrystal synthesis. As a starting material for the oriented attachment, PbSe nanocrystals were prepared using the method described by Steckel *et al.* [14]. The synthesis was performed in a water and oxygen free environment. (a) 1.54 g of lead acetate trihydrate (99.999% Aldrich), 3.34 g of oleic acid (OA, 90% Aldrich) and 12.86 g octadecene (ODE, 90% Aldrich) were heated to 130 °C under low pressure (10^{-3} bar) for $\sim$ 3 hours. (b) A second mixture containing 1.12 g Se (99.999% Alfa Aesar), 14.87 ml trioctylphosphine (TOP, 90% Fluka) and 0.13 ml diphenylphosphine (DPP, 98% Aldrich) was prepared by dissolving the Se. Subsequently, solution (a) was heated in a three-necked round-bottom flask to 180 °C, and solution (b) was injected into solution (a). The reaction mixture was kept at a constant temperature of 150 °C. After 40 seconds the reaction mixture was quenched with 20 ml butanol. The crude synthesis mixtures were washed twice by precipitation with methanol, centrifugation, and redispersion of the sediment in toluene. Nanocrystals with diameter of 4–9 nm have the shape of a cantellated cube, approaching that of a rhombicuboctahedron (Figure 7.1).

7.2.2. Honeycomb crystal synthesis. Single crystal thin films of PbSe with a honeycomb nanogeometry were prepared by oriented attachment, in a method adapted from the one reported previously [12]. A glass petri-dish (Ø 27 mm) was filled with 6.5 ml of ethylene glycol. Then a volume of 350 μl of the nanocrystal suspension with an initial concentration of 1.76×10^{-7} mol/l was placed on top of the ethylene glycol solution. The ethylene glycol serves as an immiscible liquid substrate for the nanocrystal solution. Then the solvent was allowed to evaporate, as depicted in Figure 7.2. Subsequently, the liquid was heated to 30–80 °C for 15 minutes to anneal the sample and improve attachment. After annealing, a sample was taken from the ethylene glycol layer at the center of the petri-dish, and placed under vacuum to evaporate the residual ethylene glycol. All experiments were performed in a nitrogen purged glove box (oxygen and water concentration $<$ 1 ppm).

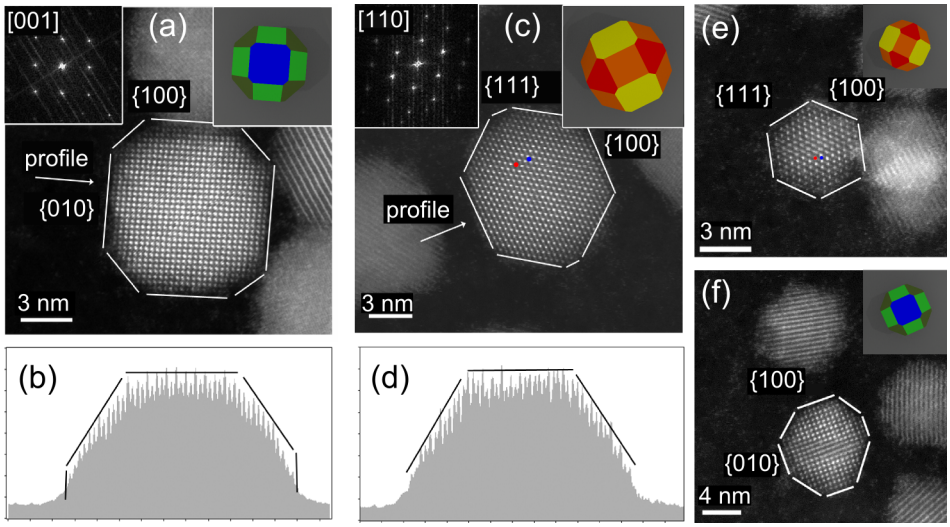

FIGURE 7.1. High resolution HAADF-STEM pictures resolve the atomic structure and outer shape of PbSe nanocrystals in the size range of 4–9 nm. (a) Large ($\sim$ 9 nm) PbSe nanocrystal projected along the [0 0 1] direction. The bright spots are caused by atomic columns consisting of alternating Pb and Se atoms. (b) Intensity profile along the [0 1 0] direction indicated in (a). (c) Large ($\sim$ 9 nm) PbSe nanocrystal projected along the [1 1 0] direction. The bright spots are columns of Pb atoms (indicated by a red dot). The less intense spots in between the Pb columns are columns of Se atoms (indicated by a blue dot). (d) Intensity profile along the [1 0 0] direction indicated in (c). (e,f) Small ($\sim$ 5 nm) PbSe nanocrystals with the same shape as (a) and (c). Insets show the orientation of the nanocrystals modeled with cantellated cubes and the selected area electron diffraction.

7.2.3. Determination of nanocrystal size. To have a user independent determination of the initial nanoparticle size, we used a computerized particle detection method [15, 16] on several bright field TEM images, each containing $>$ 100 nanoparticles. The TEM images were first low-pass filtered with a 2-D Gaussian ($\sigma < 0.5$ nm). We then detected the nanoparticle positions by means of cross-correlation with a disk-shaped template. The cross-correlation images were tresholded at a correlation value of +0.5. The binarized image was segmented, and

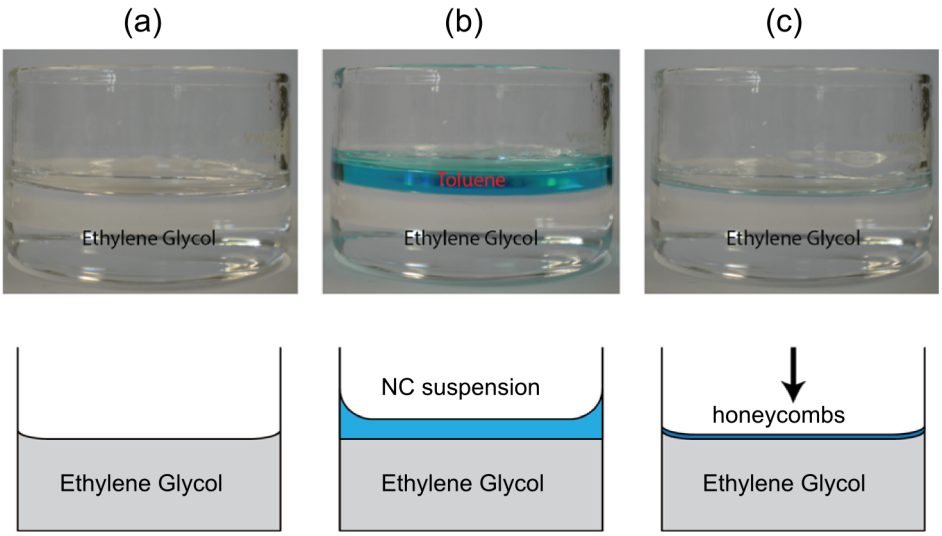

FIGURE 7.2. Cartoon and pictures of the self-assembly process induced by controlled solvent evaporation. (a) Ethylene glycol is placed in a petri-dish. (b) The PbSe nanocrystal suspension is added on top of the glycol layer. To illustrate solvent evaporation the amount of suspension has been exaggerated and dyed. (c) When the solvent of the nanocrystal suspension is evaporated completely the temperature is raised to 30–80 °C for 15 minutes. Finally, a sample is taken in the center of the petri-dish at the air/liquid interface. The entire experiment takes place in a nitrogen-purged glovebox (oxygen and water concentration < 1 ppm).

the nanoparticle positions were taken as the center of mass of each segment. From each nanoparticle center a radially averaged intensity profile was extracted. The nanocrystal radius was then determined as the position where the intensity profile had dropped to $1/e$ of the intensity at the nanoparticle center (Figure 7.3). Using this method we measured in total > 1000 nanoparticles used for the honeycomb synthesis, and found their diameter to be 5.4 ± 0.4 nm.

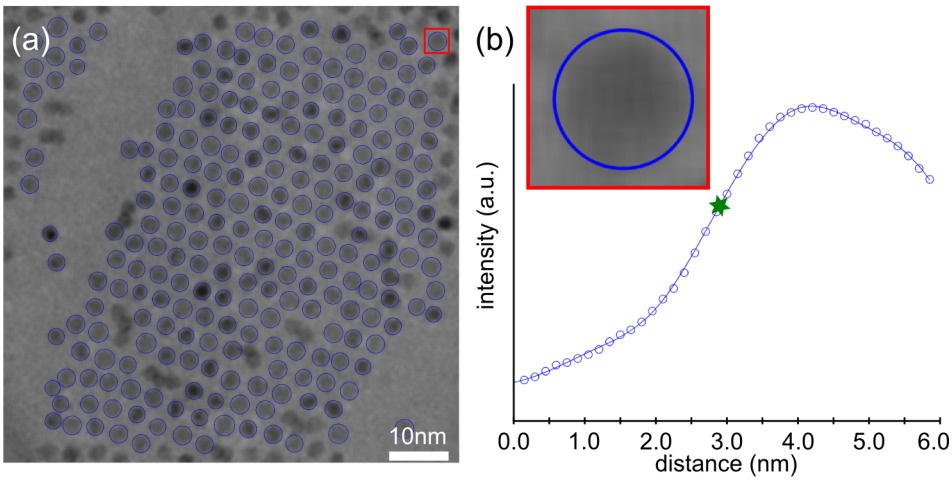

FIGURE 7.3. Computer-aided measurements of nanoparticle sizes on TEM images. (a) Input TEM picture, taken in slight underfocus to enhance contrast. Overlaid blue rings indicate detected nanoparticle size. (b) Radially averaged intensity profile of the nanoparticle indicated with a red box in (a). The intensity is lowest at the nanoparticle center (0 nm), and increases when moving out of the center. The observed maximum in intensity (4 nm) is caused by the underfocus of the TEM. The full signal is taken as the difference between minimum and maximum intensity of the profile. The nanoparticle edge is then defined as the position where the signal has dropped to $1/e$ of the full signal (green star, 2.8 nm).

7.2.4. Electron microscopy and tomography. Nanocrystals and honeycombs were imaged using both bright field TEM and HAADF-STEM. The conventional TEM images were obtained using a FEI Tecnai 12, FEI Tecnai 20, and a Philips CM30T microscope. The HAADF-STEM and tomography measurements were performed using a double aberration corrected FEI TITAN operated at 300 kV. The semi convergence angle of the electron probe used during acquisition was 21.4 mrad.

Both electron tomography series were acquired in HAADF-STEM mode using a double aberration corrected cubed FEI Titan 50–80 electron microscope operated at 300 kV. For the acquisition of the PbSe series, a tilt range from −50 to

+56 and an increment of 2 degrees were used and for the CdSe sample a tilt range from −64 to +60 and increment of 2 degrees respectively. A Fischione model 2040 tilt rotation holder was used for the acquisition of both tilt series and the reconstruction of them was performed using the Simultaneous Iterative Reconstruction Technique (SIRT) as implemented in Inspect 3D software.

For the HAADF-STEM images, it is to be noted that the ability to resolve the atomic columns in each nanocrystal sensitively depends on the precise nanocrystal orientation (Figure 7.4), *e.g.*, a slight misorientation can already blur the atomic contrast.

7.2.5. Computer-aided particle detection. Particle detection was done using template matching in MATLAB® as described by Friedrich *et al.* [15]. The cross-correlation of the 3-D reconstruction with a 3-D template containing a spherical step-function was calculated. The resulting cross-correlation profile was truncated at a value of +0.5 and binarized. The center of mass of the remaining spots was assumed to represent the coordinates of the nanocrystals. From the obtained coordinates a Voronoi cell was calculated in order to detect neighbors and next-nearest neighbors of each nanocrystal. Bond lengths and angles were calculated for particles with 3 nearest neighbors only.

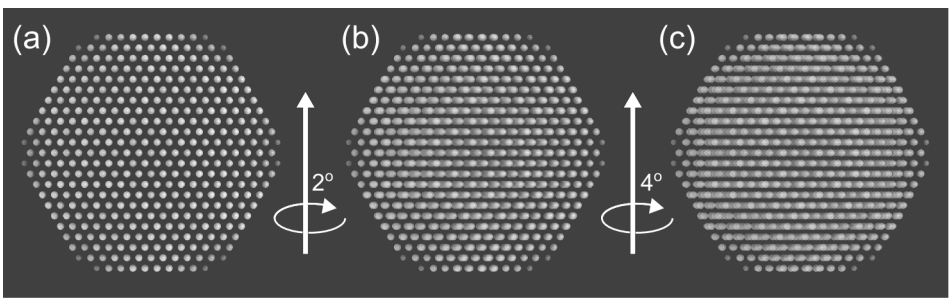

FIGURE 7.4. Simulated transmission images of an atomic model to illustrate the effect of slight nanocrystal rotations on the observed HAADF-STEM projections. (a) Simulated transmission image of a PbSe nanocrystal model observed along a ⟨1 1 1⟩ direction. (b) Same model but now with the model rotated 2°. (c) Same model but now rotated 4°.

7.2.6. Estimation of the effect of the missing wedge on the automated particle detection. A common problem in electron tomography is that the tilt range of the object is limited due to shadowing effects. This results in a lack of transmission images at high tilt angles: the missing wedge. This missing wedge translates into an uncertainty of position in the z direction of the reconstruction, and smears of contrast along the missing wedge (Figure 7.5).

Here, we show that the automated particle detection is not influenced by the missing wedge. We constructed a model of spheres mimicking our measurements. We then calculated transmission images over a tilt range of $\pm 50^\circ$ with a 2° increment. From the transmission images the backprojection was reconstructed [Figure 7.5(a)]. The size of the spheres and the resolution of the reconstruction are chosen to match the experiment. Using the same automated particle detection scripts as for the measurement, we successfully detected the position of all the spheres in the reconstruction [Figure 7.5(b)]. When comparing the initial coordinates with the detected coordinates, we find a randomly distributed error that is below 2 pixels in each direction [Figure 7.5(c)]. This is well below the standard deviation in our measurement.

7.3. Atomically coherent PbSe honeycomb structures

Figure 7.6 presents the honeycomb structure obtained by oriented attachment of PbSe nanocrystal building blocks [12]. The initial building blocks have the shape of a cantellated cube, approaching that of a rhombicuboctahedron. This implies that the nanoparticle is terminated with $\{1\,0\,0\}$, $\{1\,1\,0\}$, and $\{1\,1\,1\}$ facets. To estimate the nanoparticle size we determined the radially averaged diameter of the TEM projections, and found this to be 5.4 ± 0.4 nm. The oriented attachment of these nanoparticles results in structures with long range periodicity, as visualized by means of an equilateral triangle spanning the same number of unit cells at each vertex in the HAADF-STEM image [Figure 7.6(a)]. Zooming in on the honeycomb structure [Figure 7.6(b)] reveals that the $\langle 1\,1\,1 \rangle$ axes of the nanocrystals are perpendicular to the substrate, and that the $\langle 1\,\bar{1}\,0 \rangle$ axes are perpendicular to the nanocrystal-nanocrystal bonds. This is also corroborated by the recorded electron diffraction (ED) patterns [Figure 7.6(c)]. Furthermore the structures have a high degree of crystallinity, as observed by the occurrence of sharp spots in ED patterns recorded on selected areas with a diameter of 200 nm [Figure 7.6(c), for a more elaborate discussion of the ED patterns see Section 7.7].

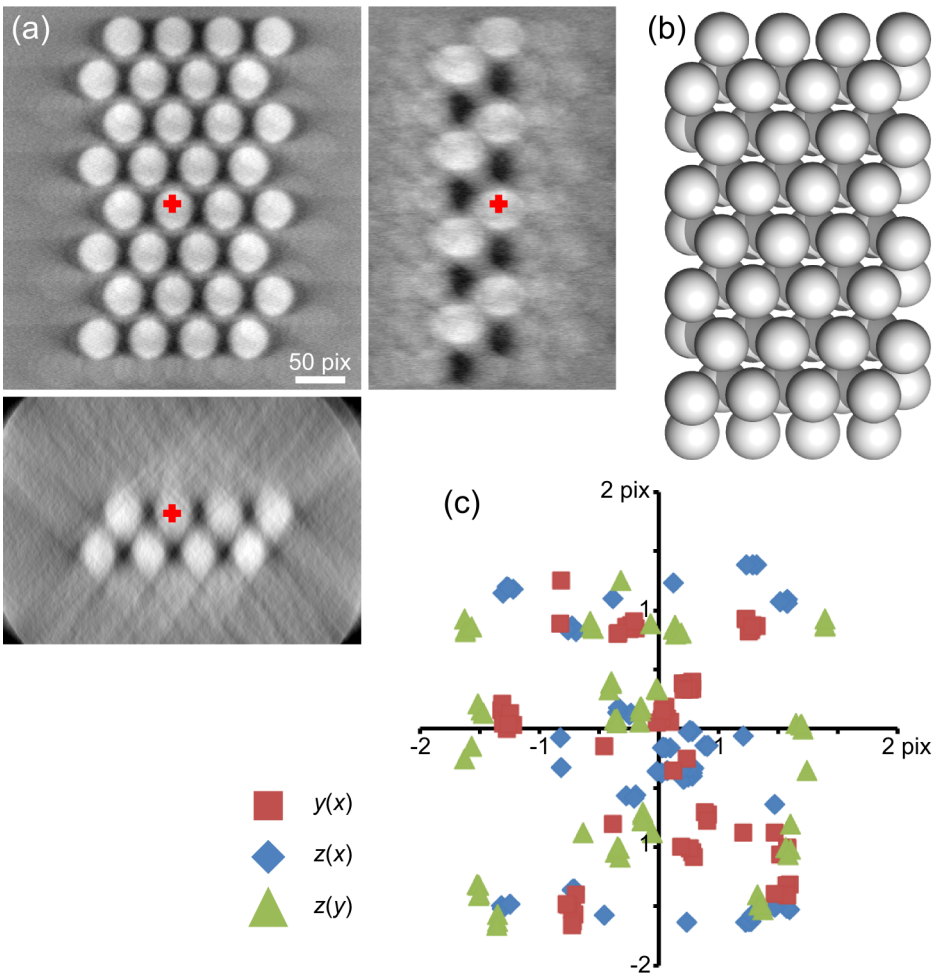

FIGURE 7.5. Testing the effect of the missing wedge on automated particle detection. (a) Reconstruction of a tilt series over $\pm 50°$ with a $2°$ increment, calculated for a model of two touching layers of hexagonally ordered spheres. The red cross marks the same particle throughout the xy, yz and xz planes. (b) The model as detected by automated particle detection. (c) The difference between initial and detect coordinates are random in all three dimensions and fall below 2 pixels.

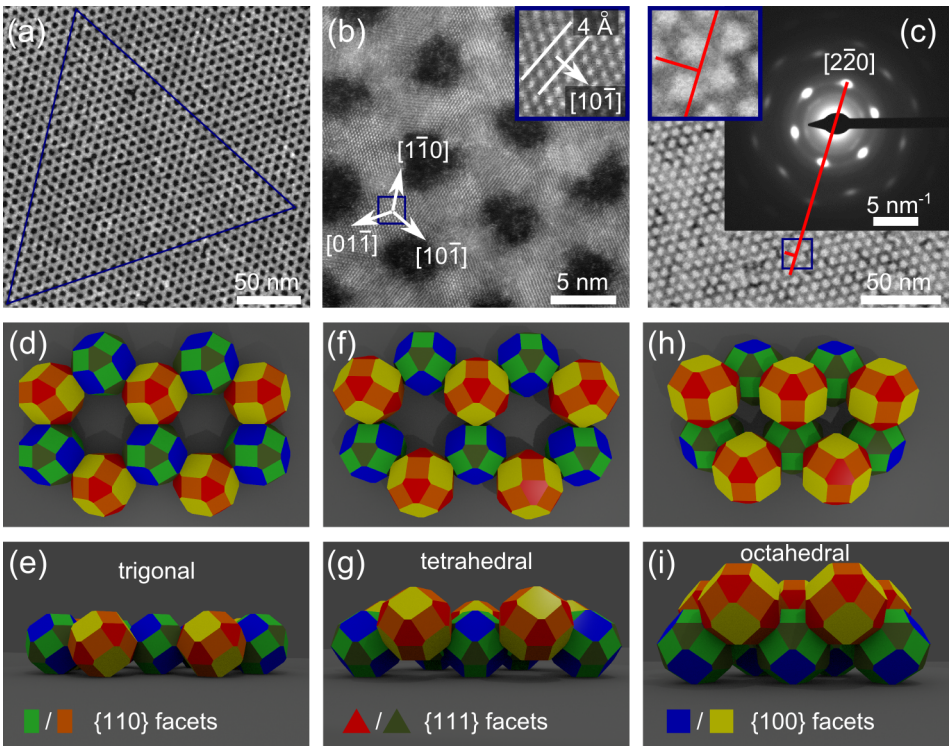

FIGURE 7.6. Single crystalline PbSe honeycomb structures created by oriented attachment. (a) HAADF-STEM image of the honeycomb structure (bright on a dark background). The equilateral triangle shows the long range ordering of the structure. (b) High resolution HAADF-STEM image showing that the $\langle 1\,1\,1 \rangle$ nanocrystal axes are perpendicular to the substrate, and the $\langle 1\,\bar{1}\,0 \rangle$ axes are perpendicular to the nanocrystal bonds. Inset: zoom-in on the area indicated by the blue box. (c) Electron diffraction pattern showing the high degree of crystallinity. TEM image in the background shows the area on which the ED pattern was recorded (the honeycomb appears dark on a bright background). Red line and inset show the orientation of the diffraction spots with respect to honeycomb structure, confirming that the $\langle 1\,\bar{1}\,0 \rangle$ axes are perpendicular to the nanocrystal bonds. (d-i) Models of the honeycomb structure with cantellated cubes as nanocrystals. The two inequivalent sites in the honeycomb lattice are indicated by yellow/red and blue/green nanocrystals.

There are three different models for attachment of the nanocrystals that result in a honeycomb structure with the nanocrystal $\langle 1\,1\,1\rangle$ axes perpendicular to the substrate, being attachment via the $\{1\,\bar{1}\,0\}$, $\{1\,1\,1\}$, or $\{1\,0\,0\}$ facets, respectively [Figure 7.6(d–i)]. The three models look similar from the top, but have a very different 3-D shape. The first model is a planar, trigonal structure with bond angles between the nanocrystals of 120° [Figure 7.6(d,e)]. The second model is slightly buckled, with a tetrahedral symmetry and nanocrystal bond angles of 109.5° [Figure 7.6(f,g)]. The third model is highly buckled, with an octahedral symmetry and nanocrystal bond angles of 90° [Figure 7.6(h,i)]. In the following, we will use various imaging techniques to show that the experimental structure is of the octahedral type, and that it has bond lengths that are longer than expected on basis of a simple block model.

7.4. Resolving the honeycomb lattice

In the trigonal model the attachment takes place via the $\{1\,\bar{1}\,0\}$ facets, meaning that it has the $\langle 1\,\bar{1}\,0\rangle$ axes parallel to the nanocrystal bonds. However, both the high resolution HAADF-STEM images and the electron diffraction patterns show that in our experiment the $\langle 1\,\bar{1}\,0\rangle$ axes are perpendicular to the nanocrystal bonds. This allows us to discard the trigonal model. Another indication is found in the buckling of the honeycomb: in the HAADF-STEM images we sometimes observe additional scattering strength on the nanocrystal bonds, indicating a larger than average thickness of the sample at that position. However, both the tetrahedral and octahedral model are buckled and have the $\langle 1\,\bar{1}\,0\rangle$ nanocrystal axes perpendicular to the nanocrystal bonds, making it impossible to discriminate between the two on basis of electron diffraction or the 2-D projections from high resolution HAADF-STEM.

The ability to discriminate between the tetrahedral and octahedral honeycomb structure is essential for understanding the oriented attachment, as it shows which facets play an active role in this process. Also, the orientation of the atomic lattice with respect to the nanogeometry influences the electronic properties of the honeycomb lattice [13]. Here, we use a combination of transmission electron microscopy (TEM), scanning tunneling microscopy (STM), grazing-incidence small-angle X-ray scattering (GISAXS), and electron tomography to fully resolve the honeycomb structure. STM measurements show that the honeycomb structure is indeed buckled [Figure 7.7(a,b)]. However, since the topography in STM

is a complicated convolution of nanocrystal height and tip radius, no quantitative height data could be extracted (see Section 7.4.1). Although this means that we cannot measure bond lengths and angles directly in STM, we can extract the next-nearest neighbor (NNN) distances and find these to be 8.5 ± 0.8 nm. From GISAXS we find scattering peaks arising from the hexagonal order of the holes in the honeycomb structure with relative positions of $1{:}\sqrt{3}{:}2{:}\sqrt{7}$, as expected from a honeycomb structure [Figure 7.7(c,d)]. Scattering in the direction normal to the surface [Figure 7.7(e)] provides information about the electron density of the sample in that direction. However, this information is obscured by multiple scattering events (see Section 7.4.2). Looking at the absolute peak positions in Figure 7.7(d) we find a hole-hole distance of 8.5 nm, in accordance with the NNN distances observed in STM. The hole-hole distances can of course also be measured from TEM images. This is done in Section 7.4.3. Also here we find a hole-hole distance of 8.5 ± 0.4 nm. Assuming perfect honeycomb models, this distance would correspond to a bond length of 5.2 nm for the tetrahedral and 6.0 nm for the octahedral honeycomb structure. This is a remarkable result, since it means that the bond lengths are either shorter (in the tetrahedral model), or larger (in the octahedral model), than the initial nanocrystal diameter of 5.4 ± 0.4.

7.4.1. STM measurements. Scanning tunneling microscopy measurements were performed using an Omicron LT-STM at temperatures < 4.5 K and a base pressure $< 10^{-10}$ mbar. The as-prepared honeycomb samples were placed on a highly-oriented pyrolithic graphite (HOPG) substrate. To further facilitate the imaging the samples were annealed in the UHV chamber at temperatures of ~ 100 °C for > 24 hours.

Topographic measurements were performed in current-feedback mode using cut PtIr tips at typical feedback settings of 3.5 V and 20 pA. Depending on the sharpness of the tip we were able to resolve all nanocrystals in the honeycomb structure [Figure 7.8(a,b)], or only the nanocrystals of the top layer of the honeycomb structure [Figure 7.8(c,d)]. The high degree of buckling is immediately apparent in the STM topographic images. However, it is not possible to give a quantitative measure for the difference in nanocrystal height, since the tip sharpness largely determines the height at which we see the different nanocrystals. When the tip radius is comparable to, or lower than, the nanocrystal radius, the tip is able to resolve the nanoparticles in the lower lying sublattice [Figure 7.8(a,b)]. However, when the tip approaches the lower lying nanocrystal, current will also flow to any close-by nanocrystals from the top layer, rendering quantitative height

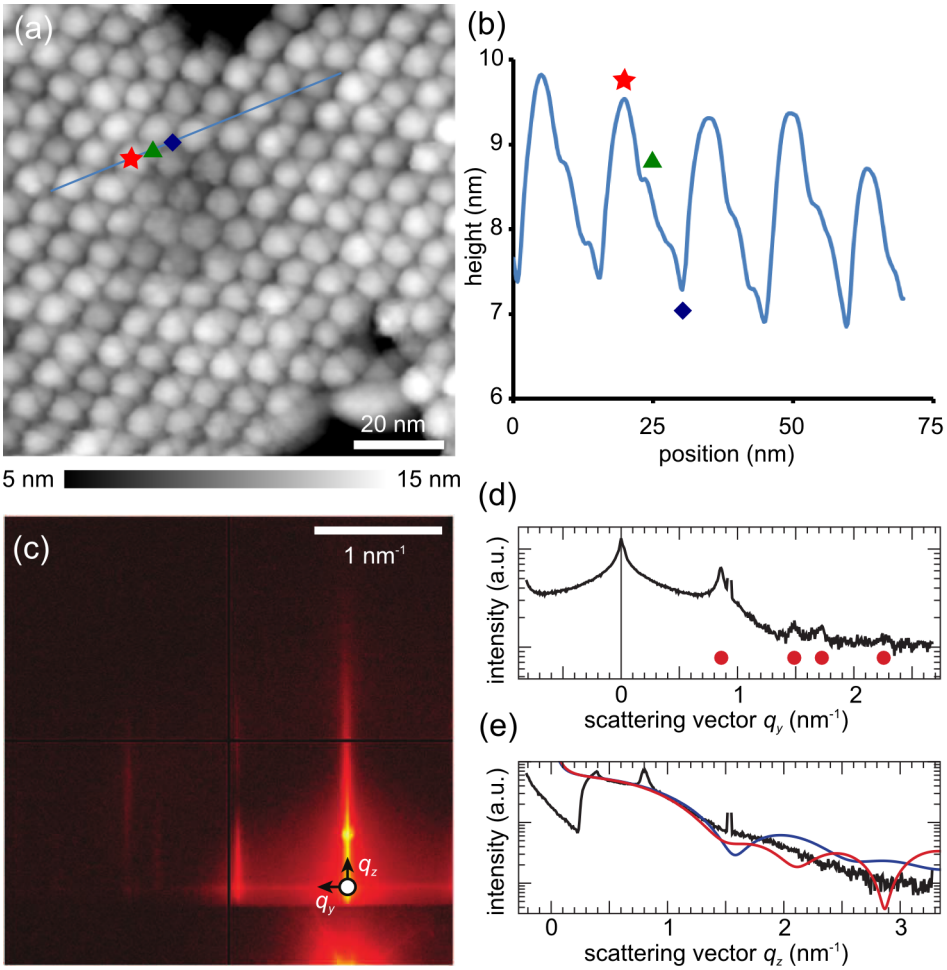

FIGURE 7.7. STM and GISAXS measurements on the PbSe honeycomb structures. (a) STM topography showing high (red star) and low (green triangle) nanocrystals forming a honeycomb structure (3.5 V/20 pA). (b) Height profile along the blue line in (a). (c) GISAXS pattern of a honeycomb structure on top of a Si(1 0 0) substrate. (d) Line trace along q_y, revealing the in-plane order. Red disks mark diffraction peaks with relative positions of $1{:}\sqrt{3}{:}2{:}\sqrt{7}$, arising from the hexagonal order of holes in the structure. (e) Line trace in along q_z, representing the electron density profile in the direction normal to the surface. Red (blue) lines are calculated Fourier transforms of the electron density of the octahedral (tetrahedral) honeycomb structure.

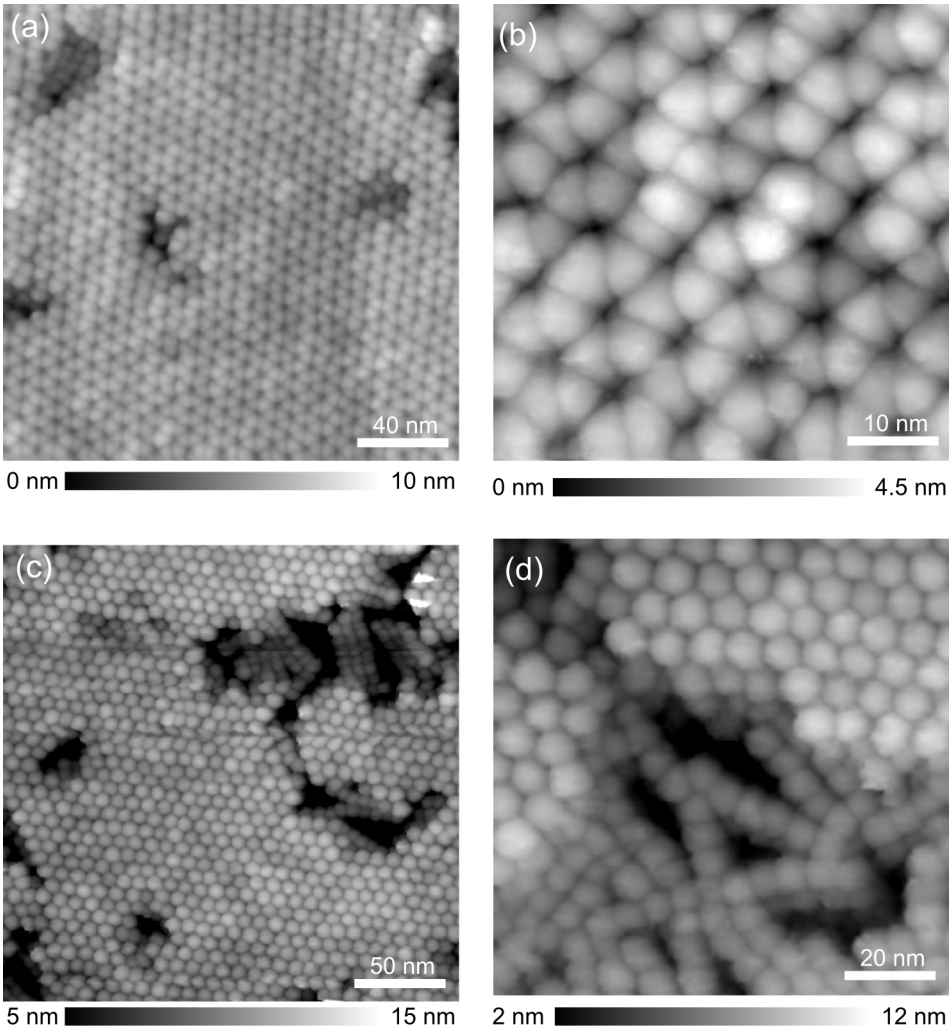

FIGURE 7.8. Scanning tunnelling microscopy images of the honeycomb structures. The ability to resolve the nanocrystals from the different sublattices largely depends on the sharpness of the tip, rendering measurement of nanocrystal height differences impossible. (a,b) Images taken with a sharp STM tip, allowing the imaging of nanocrystals from the lower sublattice. (c,d) Images taken with a blunter STM tip. Only at defect sites or cracks in the honeycomb layer the edges of the lower lying sublattice will be visible.

measurements impossible. When the tip radius is larger than the nanocrystal radius, only nanocrystals from the top sublattice will be visible. Only at defect sites, or cracks in the honeycomb layer, the edges of the lower lying sublattice can be resolved [Figure 7.8(c,d)].

Nonetheless, we can extract bond lengths and next-nearest neighbor bond lengths from the STM images. Here, we find bond lengths of 6.1 ± 0.3 nm as determined from single nanocrystal wires as observed in Figures 7.8(c) and 7.8(d), and next-nearest neighbor bond lengths of 8.5 ± 0.8 nm as determined from the top layer particles in Figure Figures 7.8(c) and 7.8(d), or from the different layers in Figures 7.8(a) and 7.8(b). These numbers are comparable to what we find using GISAXS, TEM, and tomography.

7.4.2. GISAXS measurements. GISAXS patterns were recorded at beamline ID01 at the European Synchrotron Radiation Facility (ESRF) in Grenoble. We used an X-ray beam with an energy of 9 keV incident at a grazing angle of 0.7°. The scattered intensity was recorded by a Maxipix single photon counting detector, consisting of 4 chips of 256×256 pixels each with a pixel size of 55×55 μm^2.

The line trace in the vertical direction presented in Figure 7.7(e) is, to first approximation, the Fourier transform of the electron density profile in the direction normal to the surface. In Figure 7.9(a) we plot the vertical scattering profile of the honeycomb structure [red; reproduced from Figure 7.7(e)] and of a flat monolayer of the same PbSe nanocrystals (green). Figure 7.9(b) shows the electron density profiles of a flat monolayer of nanocrystals (green), a tetrahedral honeycomb structure (blue) and an octahedral honeycomb structure (red). The corresponding Fourier transforms are plotted in Figure 7.9(c). The curves for the monolayer (green line) and the tetrahedral honeycomb (blue line) show a pronounced minimum around 1.6 nm^{-1}. We do indeed observe this minimum in the GISAXS pattern of the monolayer [green line in panel (a)], but not in the pattern of the honeycomb structure [red line in panel (a)]. Hence, we conclude that vertical GISAXS intensity is only consistent with the electron density profile of an octahedral honeycomb.

7.4.3. TEM measurements. In order to have an independent way of measuring the hole-hole distances in TEM images, and to measure a statistically significant amount of hole-hole distances, we used the computer-aided image analysis method as described in Section 7.2.3. However, now we detected the positions of

holes rather than nanoparticles in TEM pictures of the honeycomb lattice. Using a Voronoi method, we then detected the hole-hole distances for nearest neighbors. To minimize the effect of defects in the honeycomb lattice, we restricted the measurement to holes with six neighbors only.

Figure 7.10(a) shows an overview TEM picture of the PbSe honeycomb lattice. Using the method described above, we detected the position of > 2000 holes in the

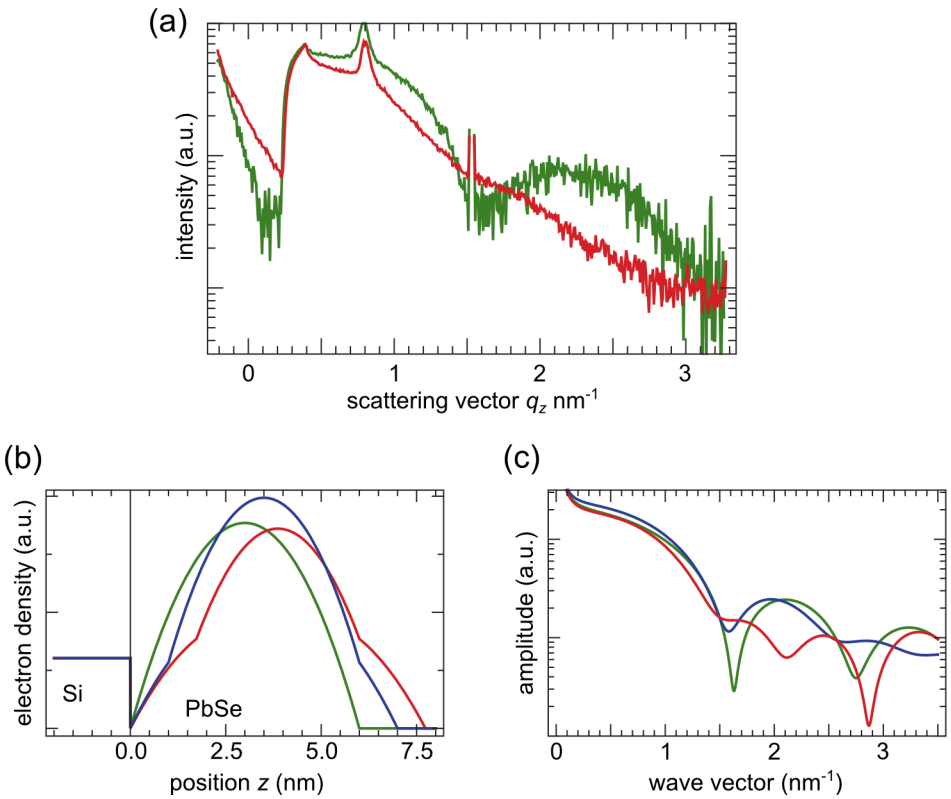

FIGURE 7.9. Vertical line traces from GISAXS. (a) Scattering profile of the PbSe honeycomb structure (red) compared to that of a flat monolayer of the same PbSe nanocrystals (green). (b) Electron density profile of a model of a flat monolayer of nanocrystals (green), a tetrahedral honeycomb (blue), and an octahedral honeycomb structure (red). (c) The Fourier transform of the electron density profiles plotted in (b).

picture, and calculated their Voronoi cells. We then selected the Voronoi cells with 6 neighbors only [indicated in green in Figure 7.10(a)] and measured the center-to-center distance between neighboring cells. In this way we measured 12396 hole-hole distances, showing an average of 8.5 ± 0.4 nm [Figure 7.10(b)]. This measurement confirms the measured hole-hole distances of 8.5 nm by GISAXS and the NNN distances of 8.5 ± 0.8 nm obtained by STM. Since these distances and the electron density profiles from GISAXS only allow an indirect distinction between the two honeycomb models, we also performed electron tomography measurements.

7.4.4. Tomography measurements. Figure 7.11 shows the tomographic reconstruction of a PbSe honeycomb structure obtained by electron tomography [15–17]. Panel 7.11(a) shows an overview of the honeycomb structure obtained

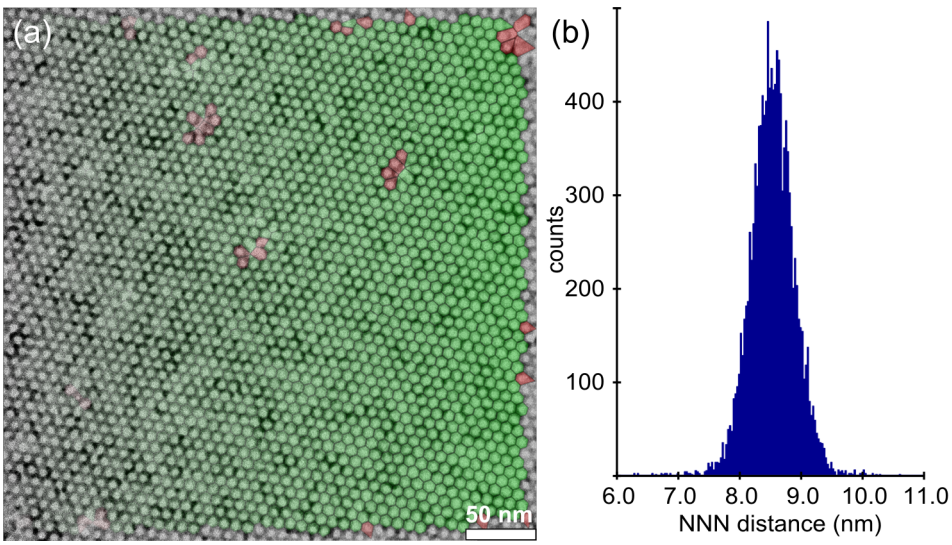

FIGURE 7.10. TEM measurements of the honeycomb lattice. (a) Overview TEM image with overlaid Voronoi cells. To better show the underlying honeycomb structure the Voronoi cells are made partially transparant, and Voronoi cells at the edge of the image are omitted. The Voronoi cells are colored green if they have exactly six neighboring cells, otherwise they are colored red. (b) Histogram of the center-to-center distances of the Voronoi cells indicated in green in panel (a), showing an average hole-hole distance of 8.5 ± 0.4 nm.

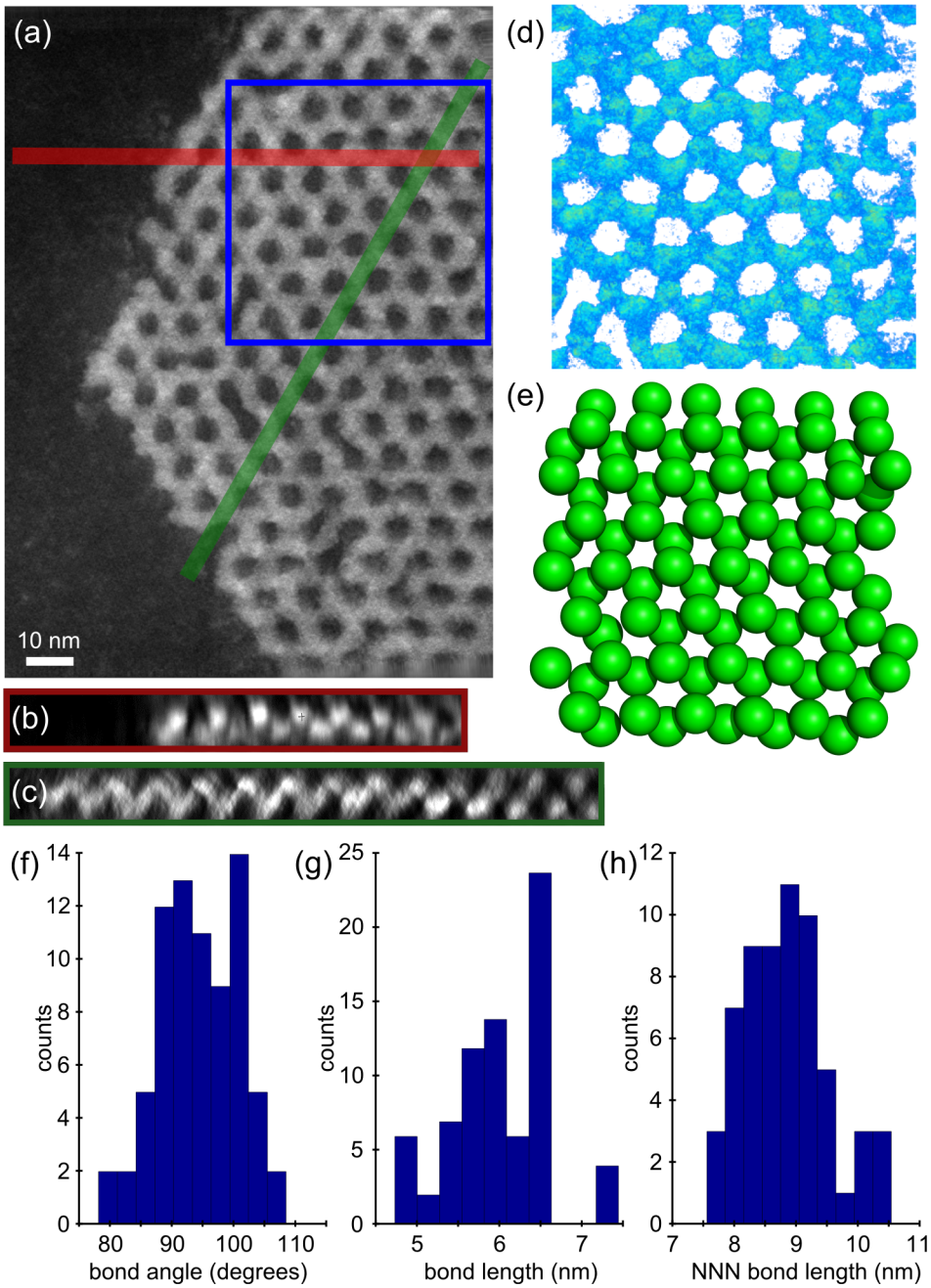

FIGURE 7.11. HAADF-STEM tomography on a PbSe honeycomb structure. See Section 7.4.4 for an explanation of the panels.

by averaging the tomographic reconstruction in the direction perpendicular to the substrate. Panels 7.11(b) and (c) show slices through the tomogram perpendicular to panel (a), along the red line (b), or green line (c) indicated in Figure 7.11(a). These slices clearly indicate that the two inequivalent nanocrystals in the honeycomb unit cell are located on different heights.[2] Panel 7.11(d) shows the iso-volume rendering of the tomographic reconstruction in the region indicated with the blue box in panel (a). Panel (e) shows equally sized spheres plotted on the coordinates obtained by automated particle detection (see Section 7.2.5) in the region indicated in blue in panel (a). Finally, using a Voronoi method, we can measure important parameters like bond angle, bond length and next-nearest neighbor bond length [Figure 7.11(f–h)] from the coordinates shown in panel (e). We measured bond angles of $95 \pm 5°$ [panel (f)], nearest neighbor bond lengths of 6.0 ± 0.5 nm [panel (g)], and bond lengths to next-nearest neighbors (NNN) of 8.9 ± 0.6 nm [panel (h)].

The measured bond angle of $95 \pm 5°$ [panel (f)] proves that the honeycomb structure is of the octahedral type, with bonds between the $\{1\,0\,0\}$ facets. We can furthermore compare the ratio between bond length (6.0 ± 0.5 nm) and next-nearest neighbor bond length (8.9 ± 0.6 nm) that we find with the theoretical values for the different structures — for the octahedral type one would expect $1{:}\sqrt{2}$, for the tetrahedral type $1{:}\sqrt{8/3}$, and for the trigonal type $1{:}\sqrt{3}$. The ratio we find here (1:1.48) is a bit higher than the expected ratio for an octahedral structure, in accordance with the bond angles being slightly higher than 90°. We attribute these higher than expected values to the defects in the structure imaged in this particular tomogram. The same measurement on a tomogram of a CdSe honeycomb structure shows bond angles of $85 \pm 6°$, slightly lower than expected (see Section 7.6.2).

7.5. Why are the bond lengths in the honeycomb larger than the initial nanocrystals?

We now have established that the nanocrystals attach via the $\{1\,0\,0\}$ facets into a honeycomb structure with octahedral symmetry [Figure 7.6(h,i)]. This allows to again look into the bond lengths of the honeycomb structure, as extracted from

[2] We would like to note here that the PbSe honeycombs suffer from beam damage, making it hard to obtain high quality tomographic reconstructions. CdSe on the other hand is more stable under the electron beam, resulting in higher quality tomographic reconstructions. Compare, *e.g.*, Figure 7.11 and Figure 7.14 that are obtained under the same imaging conditions.

TEM, STM, GISAXS, and tomography as described above. Knowing that the honeycomb structure has bond angles of 90°, we can then calculate the bond lengths from the measured NNN bond lengths (or hole-hole distances). All four techniques give an independent measure of 6.0 nm for the nanocrystal bond lengths, an increase of 11% of the original nanocrystal diameter. The increased bond lengths shed light on the microscopic mechanism of facet-to-facet atomic attachment. D. Li *et al.* [3] showed that, in the process of oriented attachment, the nanocrystals are continuously rotating and moving in close proximity by means of Brownian motion, in this way trying to find an optimum configuration before robust attachment takes place. We propose that, during the rotation and Brownian motion as described by D. Li *et al.* [3], atomic scale necking takes place as a first step in the attachment. After necking has started, the remaining capping molecules on the facet can be gradually removed and the neck extends perpendicular to the bond axis by vast atomic motion. For PbSe nanocrystals considerable atomic reconfigurations have been monitored by high resolution TEM in vacuum [18, 19]. The necking explains the elongation of the bond lengths, which also results in considerably more open honeycomb structure than can be obtained from geometric attachment of rigid block models [compare Figure 7.6(h) with the real structures in Figures 7.6, 7.11 and 7.12]. In the mechanism that we propose, not all the capping molecules have to be released at once from a facet, allowing for attachment pathways with lower activation energy. We note that oriented attachment accompanied with neck formation has been reported before as a pathway for the growth of various metal nanoparticles [20, 21].

7.6. Transformation of PbSe into CdSe honeycomb structures

To place our findings in a broader perspective, we will show that through a cation exchange reaction [22, 23] we can transform the PbSe honeycombs into CdSe. Nanoscale honeycomb structures of CdSe are predicted to have Dirac-type conduction bands [13]. In fact, since the emergence of graphene as an unconventional, physically interesting and useful material [24], there is a general interest in the properties of electrons confined in a honeycomb lattice [25–29]. Our work describes a general two-step method to obtain a variety of 2-D semiconductors with a nanoscale honeycomb geometry: assembly and oriented attachment of Pb-chalcogenide nanocrystals with truncated cubic shape, eventually followed by

cation exchange. We note that the first PbS honeycomb structures have been prepared (see section 7.8). These systems are of interest as this material should have a Dirac-type band structure and exhibit strong spin-orbit coupling [13, 30, 31].

Figure 7.12 presents the successful exchange of a PbSe honeycomb lattice into a CdSe honeycomb. The complete transformation of the PbSe lattice into CdSe is confirmed by means of energy-dispersive X-ray (EDX) spectroscopy [Figure 7.12(a)]. HAADF-STEM and electron diffraction measurements show that the orientation of the Se anion lattice with respect to the honeycomb periodicity is preserved [Figures 7.12(b–d)]. This is in line with earlier described mechanisms where the anion lattice is preserved during cation exchange [32, 33], and is corroborated by high resolution HAADF-STEM measurements of honeycomb structures at intermediate stages of cation exchange (Figure 7.13).

7.6.1. Details on the cation exchange. The conversion of the rock-salt PbSe honeycomb structures into zinc blende CdSe honeycomb structures was done by placing the PbSe sheet on a substrate (SiN TEM-grid), which was then immersed in a 0.1 mol/l Cd-oleate solution in 1-octadecene and heated to 150 °C for 1 hour. Subsequently, the solution was heated to 170 °C for 15 minutes. Finally, the substrate was cleaned several times by immersion in toluene → a 1:2 mixture of methanol/butanol → methanol.

To visualize the ion exchange mechanism, we also performed partial ion exchange where the sample was heated to only 110 °C for 45 minutes. We then analyzed the samples with TEM, EDX and high resolution HAADF-STEM. As can be observed in Figure 7.13(a,b) the ion exchange starts on the surface of the sample, leaving some PbSe cores if aborted prematurely. The boundary from the PbSe cores to the CdSe shells, as observed in the contrast change in the HAADF-STEM picture, is smooth [Figure 7.13(b)], showing the preservation of the anion lattice of the Se. This indicates that the cation exchange consists simply of removal of the Pb atoms from the octahedral sites in the fcc Se anion lattice, replacing them by Cd atoms in the tetrahedral sites. Furthermore, chemical characterization by means of EDX was performed. Consecutive EDX spectra show a gradual decrease of Pb concentration during ion exchange [Figure 7.13(a)], until there is a total absence of Pb peaks and a Cd:Se ratio of 1:1 [Figure 7.13(c)], demonstrating the success of the cation-exchange. The Cu peaks in the spectrum are background signal of the TEM grid holder.

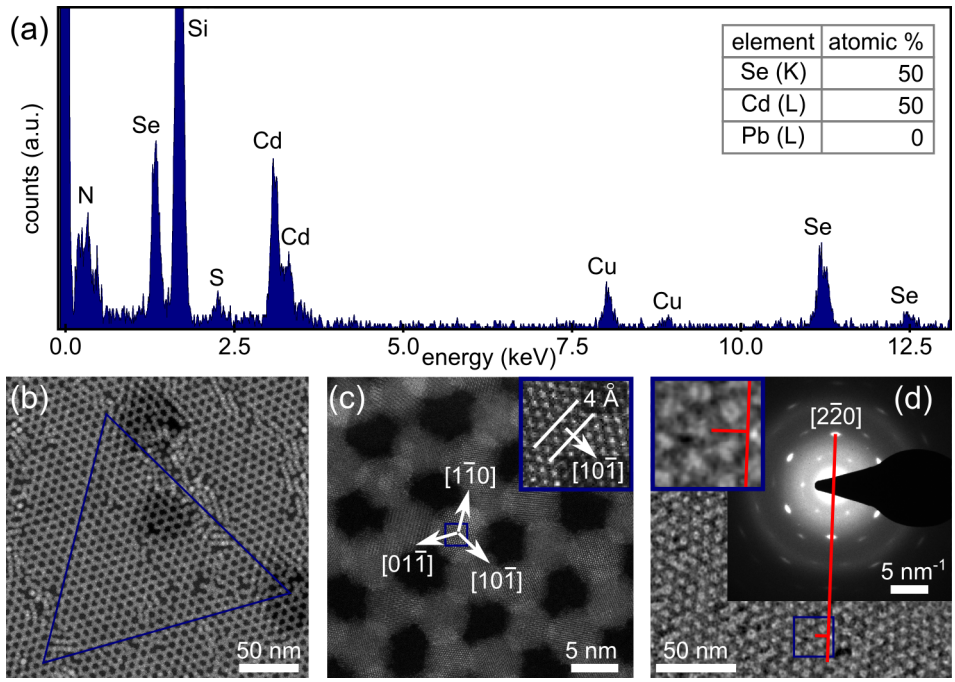

FIGURE 7.12. Single crystalline CdSe honeycomb structures created by cation exchange. (a) EDX spectrum of the CdSe honeycomb structure, showing a total absence of Pb and a 1:1 ratio of Cd:Se. (b) HAADF-STEM image of the CdSe honeycomb structure. The honeycomb appears bright on a dark background. The equilateral triangle shows that the long range ordering of the structure is retained. (c) High resolution HAADF-STEM image showing that orientation of the Se anion lattice with respect to the nanogeometry is preserved. Inset: zoom-in on the area indicated by the blue box. (d) Electron diffraction pattern showing that the high degree of crystallinity is preserved. TEM image in the background shows the area on which the ED pattern was recorded (the honeycomb appears dark on a bright background). Red line and inset show the orientation of the diffraction spots with respect to honeycomb structure, confirming that the $\langle 1\,\bar{1}\,0\rangle$ axes are perpendicular to the nanocrystal bonds.

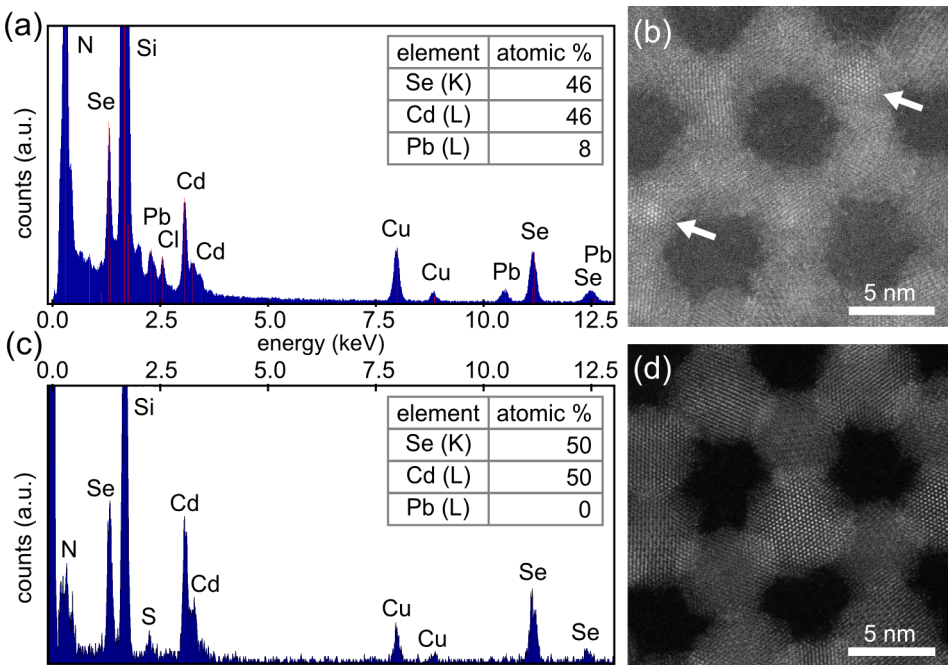

FIGURE 7.13. Preparation of CdSe thin films with a honeycomb nanogeometry via cation exchange. (a) EDX spectrum for partial ion exchanged sample (b) HAADF-STEM image showing a smooth transition in contrast of the atomic columns when going from the PbSe cores to the CdSe shells. (c) EDX spectrum for the fully ion exchanged sample, showing a total absence of Pb and a 1 : 1 ratio of Cd:Se. (d) HAADF-STEM image showing a lack of PbSe cores, and a preservation of the atomic coherency of the nanocrystals.

7.6.2. Tomography on the CdSe honeycomb structure. In addition to the electron tomography measurements on PbSe honeycombs, we also performed measurements on CdSe. The results are presented in Figure 7.14. Panel 7.14(a) shows an overview of the honeycomb structure obtained by averaging the tomographic reconstruction in the direction perpendicular to the substrate. Panel 7.14(b) shows a slice through the tomogram perpendicular to the honeycomb plane, along the red line indicated in 7.14(a). Panel 7.14(c) shows the iso-volume rendering of the tomographic reconstruction in the region indicated with the blue box in

panel 7.14(a). Panel 7.14(d) shows equally sized spheres plotted on the coordinates obtained by automated particle detection in the region indicated in blue in panel 7.14(a).

When looking at the quantitative information obtained from the coordinates plotted in 7.14(d), we find that the octahedral honeycomb structure is preserved upon ion exchange: the measured bond angles are $85 \pm 6°$ 7.14(e). However, the measured bond lengths [Figure 7.14(f)] and next-nearest neighbor bond lengths [Figure 7.14(g)] are remarkably high: 6.7 ± 0.3 and 9.1 ± 0.6 nm, respectively. For this increased length we do, as of yet, not have a satisfactory explanation.

7.7. Detailed analysis of the ED patterns

From the electron diffraction (ED) patterns [Figures 7.6(c) and 7.12(d)] we can extract the orientation of the atomic lattice with respect to the nanogeometry. In principle, ED also allows to differentiate between different crystal structures, but the difference in unit cell size for PbSe and CdSe is so small (< 0.1 Å), that the expected differences in diffraction position fall well below the standard deviation in our measurement (see Table 7.1). However, we can find some information on the most generally occurring defects in both structures.

Both ED patterns (Figure 7.15) are dominated by the $\{2\,\bar{2}\,0\}$ diffraction peaks, as expected from the orientation of the nanocrystals in the honeycomb structure (the $\langle 1\,1\,1\rangle$ axes perpendicular to the substrate). The $\{4\,\bar{2}\,\bar{2}\}$, $\{4\,\bar{4}\,0\}$ and $\{6\,\bar{4}\,\bar{2}\}$ spots confirm this orientation. However, for PbSe there is a weak diffraction spot corresponding to diffraction at the $\{2\,0\,0\}$ planes, indicating that the defects in PbSe are oriented either with their $\langle 1\,0\,0\rangle$ or their $\langle 1\,1\,0\rangle$ axes perpendicular to the substrate. For the CdSe sample we also observe spots corresponding to diffraction from the $\{1\,1\,1\}$, $\{1\,3\,1\}$ and $\{3\,3\,1\}$ facets. The fact that we observe sharp spots rather than diffraction rings suggests the existence of preferred defect orientations: two different defect orientations with their $\langle 1\,1\,0\rangle$ axes perpendicular to the substrate, but with a 90° rotation around the z-axis between them. The corresponding lattice distances are indicated in Table 7.1.

The defect spots in the CdSe ED could also be caused by a partial transformation of the CdSe from the zinc blende to the wurtzite phase. If this is the case, then the wurtzite phase makes up only a small fraction of the crystal, since all the high resolution HAADF-STEM images show a hexagonal arrangement of atomic columns as expected for zinc blende (ABC stacking) and not a honeycomb arrangement as expected for wurtzite (ABAB stacking).

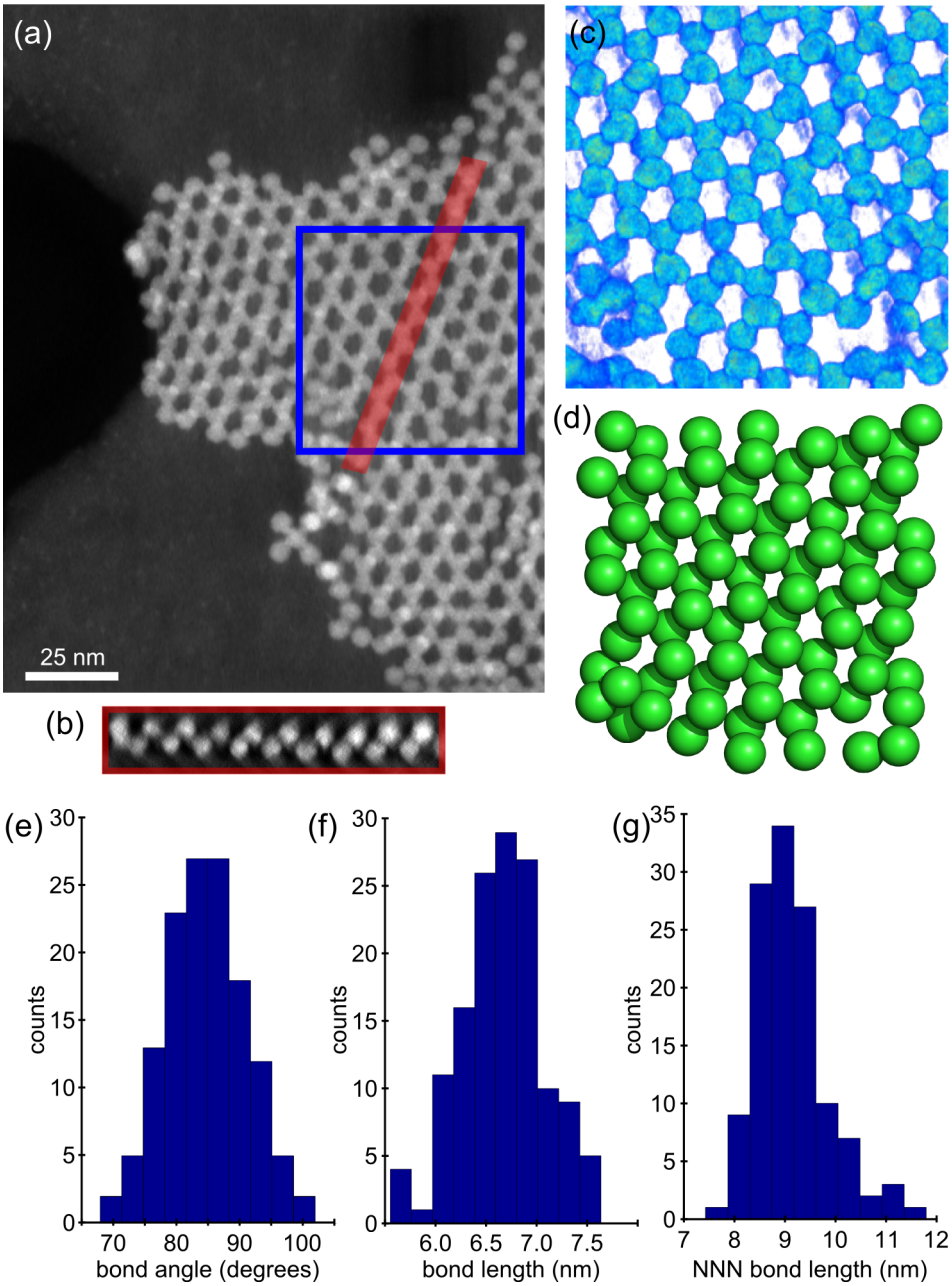

FIGURE 7.14. HAADF-STEM tomography on a CdSe honeycomb structure. See section 7.6.2 for an explanation of the panels.

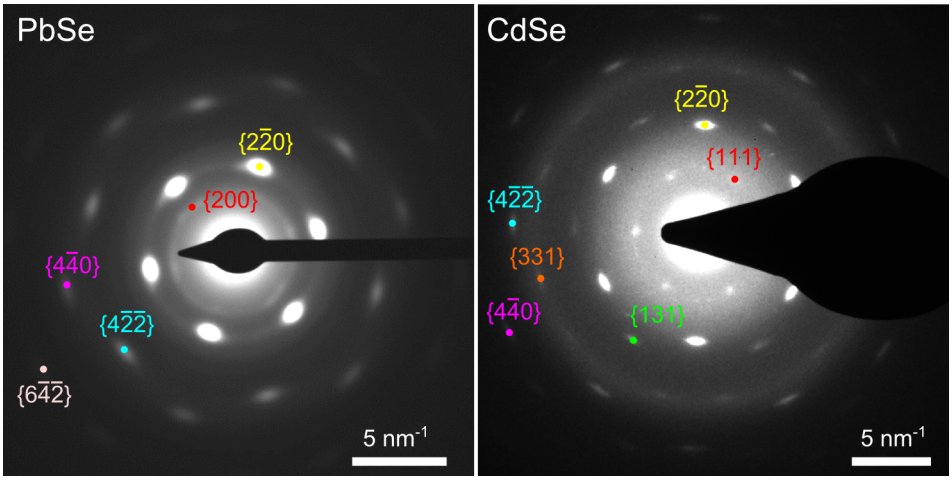

FIGURE 7.15. Electron diffraction patterns from Figures 7.6(c) and 7.12(d), with spot assignment. For the corresponding lattice distances see Table 7.1.

TABLE 7.1. Distances in the electron diffraction patterns.

Spot index PbSe	**distance (Å)**	**expected (Å)**	**Spot index CdSe**	**distance (Å)**	**expected (Å)**
{2 0 0}	3.02±0.10	3.06	**{1 1 1}**	3.64±0.16	3.49
{2 $\bar{2}$ 0}	2.18±0.15	2.17	**{2 $\bar{2}$ 0}**	2.17±0.22	2.14
{4 $\bar{2}$ $\bar{2}$}	1.26±0.12	1.25	**{1 3 1}**	1.86±0.13	1.82
{4 $\bar{4}$ 0}	1.09±0.22	1.08	**{3 3 1}**	1.39±0.31	1.39
{6 $\bar{4}$ $\bar{2}$}	0.83±0.24	0.82	**{4 $\bar{2}$ $\bar{2}$}**	1.25±0.42	1.23
			{4 $\bar{4}$ 0}	1.08±0.35	1.07

7.8. First results on the preparation of PbS honeycomb structures

The oriented attachment process described above should in principle work for all nanocrystals with a truncated cubic shape. As a proof of principle, we present here the first results obtained using PbS nanocrystals.

PbS nanocrystals were synthesized using a hot injection method based on the work of Abel *et al.* [34]. The synthesis was performed in a water and oxygen free environment. For the lead precursor 0.39 mg of lead acetate trihydrate (99.999%

Aldrich), 1.28 ml of oleic acid (OA, 90% Aldrich), 2.0 ml trioctylphosphine (TOP, 90% Aldrich), and 12.5 ml octadecene (ODE, 90% Aldrich) were heated to 130 °C under low pressure for ∼ 1.5 hours in a 50 ml erlenmeyer. This mixture was poured in a 50 ml three-necked round-bottom flask and was heated to 120 °C. At that point 16 μl bis(trimethylsilyl) sulfide [$(TMS)_2S$, synthesis grade Aldrich] was rapidly injected under vigorous stirring. The mixture immediately colored brown-black. After 2 min the mixture was cooled down to 60 °C and was quenched with 20 mL acetone; the mixture directly turned turbid brown. The mixture was washed twice by centrifugation using methanol as antisolvent and hexane as solvent. Finally, the PbS nanocrystals were dissolved in hexane. The PbS nanocrystals were analyzed by TEM in a similar way as described for the PbSe nanocrystals (six TEM images were used, and in total > 1000 nanoparticles were analyzed), and found to have a diameter of 5.5 ± 0.4 nm (Figure 7.16).

For oriented attachment a similar procedure as described for the PbSe was used: a glass test-tube (Ø 10 mm) was filled with 1 ml of ethylene glycol and subsequently heated to 30 °C. Then a volume of 50 μl of the PbS nanocrystal

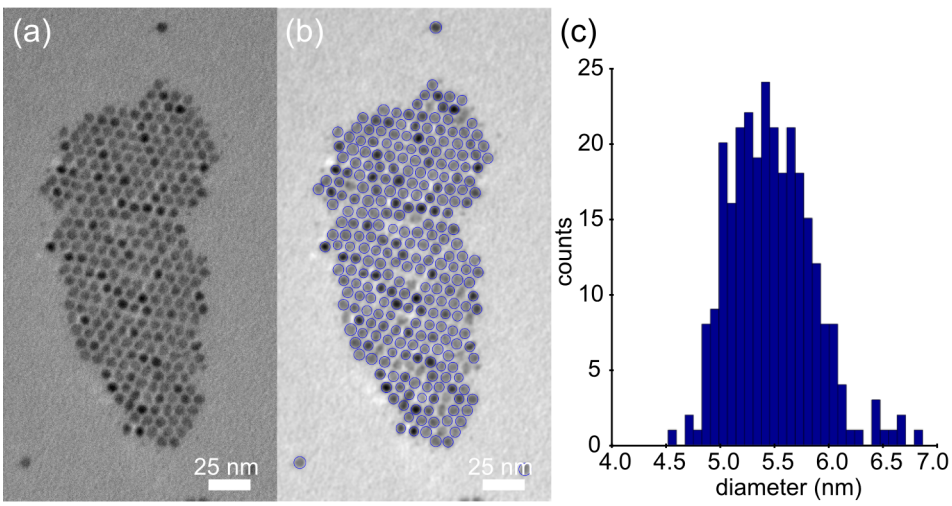

FIGURE 7.16. Computer-aided analysis of PbS nanocrystals. (a) TEM picture of the as-synthesized PbS nanocrystals. (b) Image with the detected sizes overlaid as blue circles. (c) Histogram showing the detected diameters of 5.5 ± 0.4 nm.

suspension with an initial concentration of 3.10×10^{-7} mol/l was placed on top of the ethylene glycol solution. After 1 hour, a sample was taken from the ethylene glycol layer at the center of the test-tube and placed under vacuum to evaporate the residual ethylene glycol. All experiments were performed in a nitrogen purged glove box (oxygen and water concentration < 1 ppm). The formation of single crystalline honeycomb structures was observed by TEM and ED (Figure 7.17).

The prepared PbS honeycomb structure seems to be of the tetrahedral or octahedral type [the two different sublattices at different height, similar to silicene, see Figure 7.6(f–i)]. This is indicated by the orientation of the diffraction spots in the ED with respect to the honeycomb structure, showing that the $\langle 1\,\bar{1}\,0\rangle$ axes are perpendicular to the nanocrystal bonds [Figure 7.17(a)]. Mind that from the three possible attachments, this was only the case for the tetrahedral and octahedral structures (see Section 7.4). Remarkably, when measuring the hole-hole distances

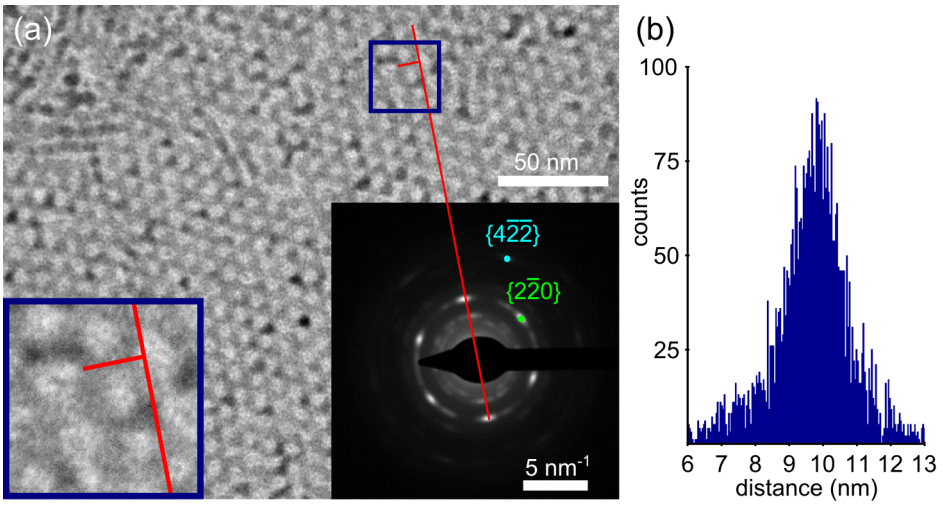

FIGURE 7.17. Single crystal PbS honeycomb structures. (a) TEM and ED of the PbS honeycomb. The ED shows that the honeycomb is single crystalline, and oriented with the $\langle 1\,1\,1\rangle$ direction normal to the substrate. The orientation of the spots in ED with respect to the nanogeometry in TEM shows that the $\langle 1\,\bar{1}\,0\rangle$ direction is perpendicular to the nanocrystal bonds, indicative for a tetrahedral or octahedral honeycomb structure. (b) Hole-hole distances calculated from (a) showing an average of 9.8 ± 1.7 nm.

in a similar way as described in Section 7.4.3, we find distances of 9.8 ± 1.7 nm [Figure 7.17(b), a total of 4536 distances was measured]. Comparing this with the initial nanocrystal size of 5.5 ± 0.4 nm shows a ratio of bond length:NNN bond length of 0.56. Comparing this to the ratios expected for the tetrahedral ($1{:}\sqrt{8/3}$) and octahedral ($1{:}\sqrt{2}$) model shows a significantly lower value than expected. The fact that this value is lower than expected can again be explained by neck-formation. Depending on the model, the bond length shows an increase of 9% (tetrahedral model) or 25% (octahedral model) — recall that for the PbSe nanocrystals of comparable size we found an increase of 11%.

It is to be noted that the work on the PbS honeycomb structures is still in an early stage. Although the above measurements prove the formation of single crystalline honeycomb structures of PbS nanocrystals, they should be reproduced for multiple structures. Moreover, electron tomography measurements on the PbS structures are needed in order to distinguish between the tetrahedral and octahedral structure, and to determine the amount of neck-formation in this attachment.

7.9. Conclusion

In this chapter we have provided a general route to the formation of atomically coherent honeycomb structures of different chemical constituents with a periodicity in the range of 5–10 nm. We have studied the honeycomb structure obtained by oriented attachment of PbSe in detail, using various atomic and nanoscale characterization techniques. We have shown that these PbSe honeycomb structures have an octahedral symmetry, resulting in a buckled structure similar to silicene. Furthermore, we have proven that neck-formation plays an important role in the oriented attachment of these structures. Finally, we have shown the general applicability of our approach, by combining the oriented attachment with cation exchange to prepare CdSe honeycomb structures with a zinc blende atomic structure, and by showing some first results on the formation of PbS honeycomb structures.

7.10. Bibliography

[1] Penn, R. L. & Banfield, J. F. Imperfect oriented attachment: dislocation generation in defect-free nanocrystals. *Science* **281**, 969–971 (1998).

[2] Banfield, J. F., Welch, S. A., Zhang, H., Ebert, T. T. & Penn, R. L. Aggregation-based crystal growth and microstructure development in natural iron oxyhydroxide biomineralization products. *Science* **289**, 751–754 (2000).

[3] Li, D. *et al.* Direction-specific interactions control crystal growth by oriented attachment. *Science* **336**, 1014–1018 (2012).

[4] Pouget, E. M. *et al.* The initial stages of template-controlled $CaCO_3$ formation revealed by cryo-TEM. *Science* **323**, 1455–1458 (2009).

[5] Dey, A. *et al.* The role of prenucleation clusters in surface-induced calcium phosphate crystallization. *Nature Materials* **9**, 1010–1014 (2010).

[6] Zhang, J., Huang, F. & Lin, Z. Progress of nanocrystalline growth kinetics based on oriented attachment. *Nanoscale* **2**, 18–34 (2010).

[7] Niederberger, M. & Cölfen, H. Oriented attachment and mesocrystals: non-classical crystallization mechanisms based on nanoparticle assembly. *Physical Chemistry Chemical Physics* **8**, 3271–3287 (2006).

[8] Pacholski, C., Kornowski, A. & Weller, H. Self-assembly of ZnO: from nanodots to nanorods. *Angewandte Chemie International Edition* **41**, 1188–1191 (2002).

[9] Cho, K.-S., Talapin, D. V., Gaschler, W. & Murray, C. B. Designing PbSe nanowires and nanorings through oriented attachment of nanoparticles. *Journal of the American Chemical Society* **127**, 7140–7147 (2005).

[10] Koh, W.-k., Bartnik, A. C., Wise, F. W. & Murray, C. B. Synthesis of monodisperse PbSe nanorods: a case for oriented attachment. *Journal of the American Chemical Society* **132**, 3909–3913 (2010).

[11] Schliehe, C. *et al.* Ultrathin PbS sheets by two-dimensional oriented attachment. *Science* **329**, 550–553 (2010).

[12] Evers, W. H. *et al.* Low-dimensional semiconductor superlattices formed by geometric control over nanocrystal attachment. *Nano Letters* **13**, 2317–2323 (2013).

[13] Kalesaki, E. *et al.* Dirac cones, topological edge states, and nontrivial flat bands in two-dimensional semiconductors with a honeycomb nanogeometry. *Physical Review X* **4**, 011010 (2014).

[14] Steckel, J. S., Yen, B. K. H., Oertel, D. C. & Bawendi, M. G. On the mechanism of lead chalcogenide nanocrystal formation. *Journal of the American*

Chemical Society **128**, 13032–13033 (2006).

[15] Friedrich, H. *et al.* Quantitative structural analysis of binary nanocrystal superlattices by electron tomography. *Nano Letters* **9**, 2719–2724 (2009).

[16] Boneschanscher, M. P. *et al.* Electron tomography resolves a novel crystal structure in a binary nanocrystal superlattice. *Nano Letters* **13**, 1312–1316 (2013).

[17] Midgley, P. A. & Weyland, M. 3D electron microscopy in the physical sciences: the development of Z-contrast and EFTEM tomography. *Ultramicroscopy* **96**, 413–431 (2003).

[18] van Huis, M. A. *et al.* Low-temperature nanocrystal unification through rotations and relaxations probed by in situ transmission electron microscopy. *Nano Letters* **8**, 3959–3963 (2008).

[19] van Huis, M. A. *et al.* Atomic imaging of phase transitions and morphology transformations in nanocrystals. *Advanced Materials* **21**, 4992–4995 (2009).

[20] Yuk, J. M. *et al.* High-resolution EM of colloidal nanocrystal growth using graphene liquid cells. *Science* **336**, 61–64 (2012).

[21] Yuk, J. M. *et al.* In situ atomic imaging of coalescence of Au nanoparticles on graphene: rotation and grain boundary migration. *Chemical Communications* **49**, 11479–11481 (2013).

[22] Luther, J. M., Zheng, H., Sadtler, B. & Alivisatos, A. P. Synthesis of PbS nanorods and other ionic nanocrystals of complex morphology by sequential cation exchange reactions. *Journal of the American Chemical Society* **131**, 16851–16857 (2009).

[23] Beberwyck, B. J., Surendranath, Y. & Alivisatos, A. P. Cation exchange: a versatile tool for nanomaterials synthesis. *The Journal of Physical Chemistry C* **117**, 19759–19770 (2013).

[24] Castro Neto, A. H., Peres, N. M. R., Novoselov, K. S. & Geim, A. K. The electronic properties of graphene. *Reviews of Modern Physics* **81**, 109–162 (2009).

[25] Gomes, K. K., Mar, W., Ko, W., Guinea, F. & Manoharan, H. C. Designer Dirac fermions and topological phases in molecular graphene. *Nature* **483**, 306–310 (2012).

[26] De Simoni, G. *et al.* Delocalized-localized transition in a semiconductor two-dimensional honeycomb lattice. *Applied Physics Letters* **97**, 132113 (2010).

[27] Gibertini, M. *et al.* Engineering artificial graphene in a two-dimensional electron gas. *Physical Review B* **79**, 241406 (2009).

[28] Park, C.-H., Yang, L., Son, Y.-W., Cohen, M. L. & Louie, S. G. New generation of massless Dirac fermions in graphene under external periodic potentials. *Physical Review Letters* **101**, 126804 (2008).

[29] Park, C.-H. & Louie, S. G. Making massless Dirac fermions from a patterned two-dimensional electron gas. *Nano Letters* **9**, 1793–1797 (2009).

[30] Nádvorník, L. *et al.* From laterally modulated two-dimensional electron gas towards artificial graphene. *New Journal of Physics* **14**, 053002 (2012).

[31] Sushkov, O. P. & Castro Neto, A. H. Topological insulating states in laterally patterned ordinary semiconductors. *Physical Review Letters* **110**, 186601 (2013).

[32] Bals, S. *et al.* Three-dimensional atomic imaging of colloidal core-shell nanocrystals. *Nano Letters* **11**, 3420–3424 (2011).

[33] Casavola, M. *et al.* Anisotropic cation exchange in PbSe/CdSe core/shell nanocrystals of different geometry. *Chemistry of Materials* **24**, 294–302 (2012).

[34] Abel, K. A., Shan, J., Boyer, J.-C., Harris, F. & van Veggel, F. C. J. M. Highly photoluminescent PbS nanocrystals: the beneficial effect of trioctylphosphine. *Chemistry of Materials* **20**, 3794–3796 (2008).

8 Outlook

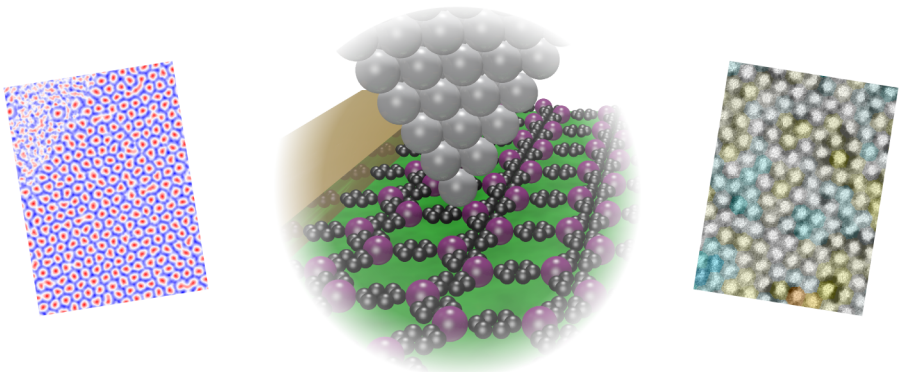

This chapter describes prospects for future research and an outlook on the research presented in this thesis. The chapter will follow the outline of the thesis: it will first deal with the future role of AFM and STM in atomic resolution imaging of honeycomb structures, followed by a study of future prospects for the nanocrystal-based honeycomb structures. It will also shortly address some possible applications of the automated image analysis methods used throughout this study.

8.1. Future use of AFM and STM for atomic-scale honeycomb systems

The first part of this thesis mostly dealt with the fundamentals of AFM imaging of atomic-scale honeycomb systems, in particular when using functionalized AFM tips [1–3]. Our contribution to the field should be considered in the broader context of elucidating the mechanisms underlying atomically resolved AFM imaging [4–9]. Combining this knowledge with the abilities of AFM/STM to resolve individual atoms chemically [10, 11] and to manipulate atoms [12] and molecules [13–16] should allow for the preparation of artificial honeycomb structures of various atoms and/or molecules. This offers a tunable platform for studying massless Dirac fermions and their topological and correlated phases. Indeed, the very first steps in this direction have already been taken, by using molecules to superimpose a honeycomb structure on a metal surface state [17].

It should be noted that, already before the interest in artificial honeycomb structures, there has been much study into the design of networks of organic molecules at metal surfaces by means of self-assembly [18]. However, since these systems are prepared on the metal surface directly there is strong coupling between the electronic states of the metal and these 2-D metal-organic frameworks. This makes it impossible to study the electronic properties of the framework itself. This can be resolved by using a buffer layer like NaCl, hexagonal boron nitride, or even an epitaxial graphene layer itself.

The self-assembly approach makes the preparation of larger films of artificial honeycombs possible, allowing to study them not only with the STM tip but also in *e.g.*, field-effect devices. For an artist impression of such a device see Figure 8.1. Combining the self-assembly approach with the ability of molecular manipulation allows for the design of well-defined nanostructures or edges, also in the field-effect device.

8.2. Automated image analysis for nanocrystal characterization

Despite the fact that (approximately) spherical colloidal quantum dots are the very basic material in nanoscience and nanotechnology, there is not a standardized way to determine their exact size. Of course, it is possible to determine the exact size of quantum dots from high-resolution TEM images where one can simply count the atomic lattice planes. Also analytical ultracentrifugation was found to be able to resolve nanocrystal sizes that differ by a single atomic plane [19]. However, these techniques are expensive and time consuming, and not readily available in all laboratories. Therefore the common practice is to take some TEM images and

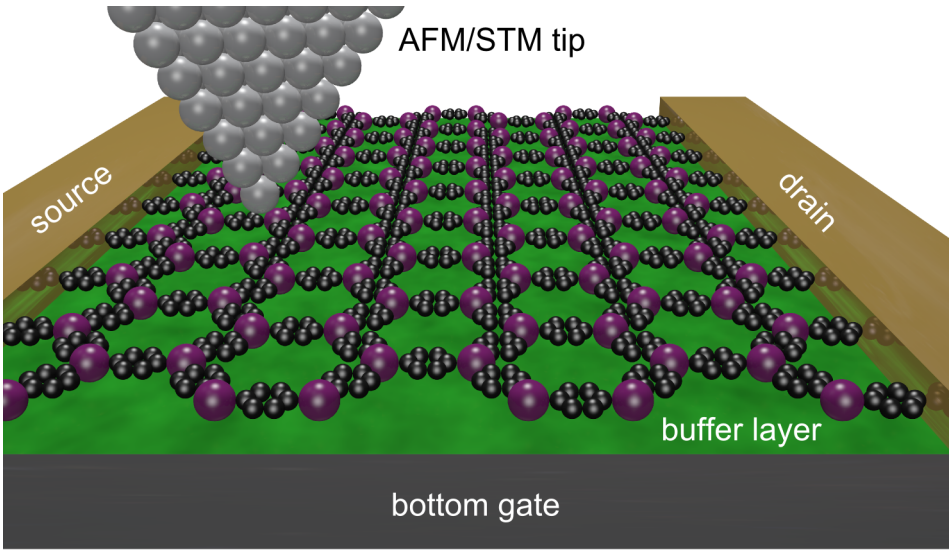

FIGURE 8.1. Artist impression of a field effect device with an artificial honeycomb structure consisting of metal atoms (purple) linked by benzene rings (black) on a buffer layer (green). The AFM/STM tip allows to atomically resolve the honeycomb structure, to measure the LDOS, or to manipulate the structure into well-defined nanopatterns between the source and drain.

to measure the size of a large number of quantum dots by hand. This method has also been used to relate the optical properties to the quantum dot size [20, 21], allowing for size determination by means of optical spectroscopy — assuming that the initial calibration by hand was correct.

My personal experience is that such a measurement of quantum dot sizes by hand is very user dependent, resulting in differences between determined quantum dot diameter in the order of a nanometer. Therefore we developed an automated, user independent method to determine the quantum dot size from TEM pictures. The method is inspired by the work of Friedrich *et al.* as described in Reference [22]. We applied this method in the work described in Chapter 7.

The method that we propose is based on cross-correlation (Figure 8.2). First a mask is created that resembles the object of interest on the TEM image. For bright field TEM images of (approximately) spherical quantum dots this can simply be a dark disk in a bright background, possibly with an even brighter ring around the

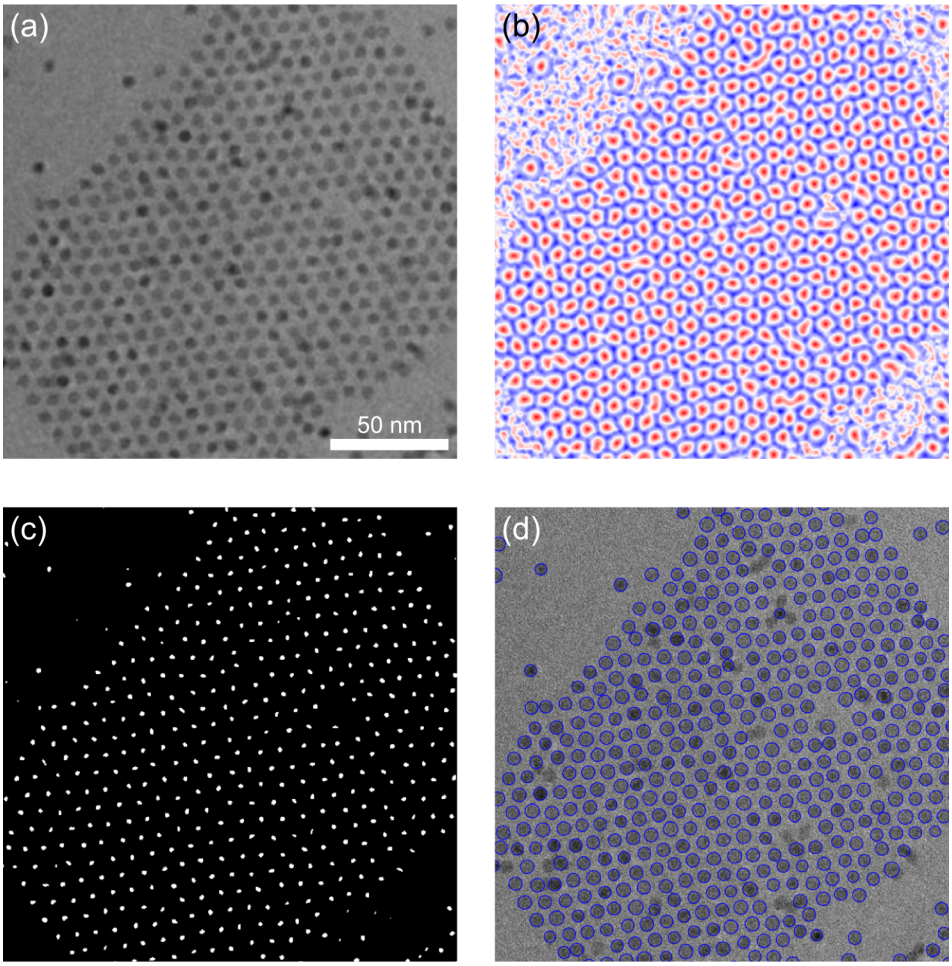

FIGURE 8.2. Automated particle detection of PbSe quantum dots in a TEM picture. (a) The original TEM image, Gaussian filtered with $\sigma = 0.5$ nm. (b) The cross-correlation profile. Red (blue) color coding means a positive (negative) correlation. (c) Black and white image after tresholding at a correlation value of +0.35. (d) The original image (unfiltered) overlaid with circles showing the size of the detected quantum dot.

disk to mimic the effect of the slight underfocus that is regularly used to enhance contrast in bright field electron microscopy. Then the correlation coefficient for each pixel of the image is calculated according to

$$\rho_{AB} = \frac{\langle AB \rangle - \langle A \rangle \langle B \rangle}{\sigma_A \sigma_B} \tag{8.1}$$

where $\sigma_A = \left\langle A^2 \right\rangle - \langle A \rangle^2$, $\sigma_B = \left\langle B^2 \right\rangle - \langle B \rangle^2$ and A and B are the intensities of mask and masked area of the image, respectively. The resulting correlation image has values in the range of $+1$ (perfect correlation) to -1 (perfect anticorrelation), with zero meaning a total lack of correlation. Depending on the dispersion in size and shape of the nanocrystals in the image, the correlation image is binarized at values typically between $+0.25$ and $+0.75$.

The binarized image is then segmented by means of connected-component labeling, where the centers of the quantum dots are assumed to be at the center of mass of each image segment. For each quantum dot center a radially averaged intensity profile is calculated, from which the quantum dot size is determined. In the work presented in Chapter 7 we defined the edge of a quantum dot to be at the position where the intensity profile had dropped to $1/e$ of its original intensity. From the few HAADF-STEM images that we have, this seems to be a reasonable definition. However, this should be investigated more rigorously by using a larger set of high resolution images. Nonetheless, the method we present here is independent of the final definition of where the edge of a quantum dot is, and could serve as a way to standardize the determination of nanocrystal sizes from TEM images. The method is easy to implement (a MATLAB® script of 300 lines is now freely available within the CMI group) and not demanding in terms of computation time (depending on particle size and resolution of the image the computation time ranges from a few seconds up to some minutes).

8.3. Opportunities for the nanocrystal-based honeycombs

Although the high carrier mobility of graphene holds great promise for applications in, *e.g.*, logic devices and radio frequency electronics, graphene has one large drawback: the lack of a band gap [23, 24]. This results in a low on-off resistance ratio and high leakage current for graphene transistors [25]. Numerous efforts have been taken to create a band gap in graphene by means of doping [26], atomic or molecular adsorption [27, 28], chemical modification [29, 30], and nanopatterning [31, 32]. However, these methods either lower the graphene device performance, are highly labor-intensive and thus costly, or are simply unable to create a significantly large

band gap for reasonable device performance [24, 25]. And although progress is made in the field of logic transistors by means of altering the graphene transistor architecture [33], the inherent problem itself is far from solved.

For the reasons outlined above, the nanocrystal based honeycomb systems described in Chapter 7 — having a significant and even tunable band gap — provide a real breakthrough, not only in the field of high-performance integrated logic circuits, but also in integrated optoelectronic devices. Tight-binding calculations on similar CdSe nanocrystal honeycomb structures as the ones presented in Chapter 7 show that a honeycomb pattern of such nanocrystals gives rise to not only one, but two Dirac bands at the conduction band side of the energy spectrum [34]. These Dirac bands are separated by a band gap of ~ 300 meV, have a dispersion of ~ 100 meV, and are well-separated (> 2 eV) from the lower lying valence bands (Figure 8.3, adapted from [34]).

Before the artificial honeycomb structures described in Chapter 7 can be integrated into devices, several issues need to be addressed. First of all, the fabrication of the honeycomb structures needs to be scaled up, made more robust, and tested for different semiconductor materials. This issue is being addressed by a collaboration between the Utrecht University and Delft University of Technology, and a first parameter study has already been published [35]. Also, the fabrication of honeycombs from different semiconductor materials is already partially addressed in Chapter 7. Secondly, to gain more insight in the rich physics underlying the band structure of such artificial honeycomb systems, more modeling and theoretical studies need to be undertaken. A collaboration between several research groups is working on this, the first result of which has lead to the band structures presented in Figure 8.3 [34]. Finally, the band structure of the samples need to be measured, in order to test it against the predictions made by theory. For this, initial studies are started using STM, and microwave and terahertz spectroscopy.

8.4. Automated image analysis for honeycomb characterization

Another issue that needs to be addressed is the understanding of the effects of atomic and nanoscale disorder. In order to model the effect of these forms of disorder on the electronic band structure, we first need to know what realistic parameters are. Here, I will present a method to analyze the nanoscale disorder in the honeycomb systems described in Chapter 7 using a similar approach as described in Section 7.4.3. The method combines the cross-correlation technique as

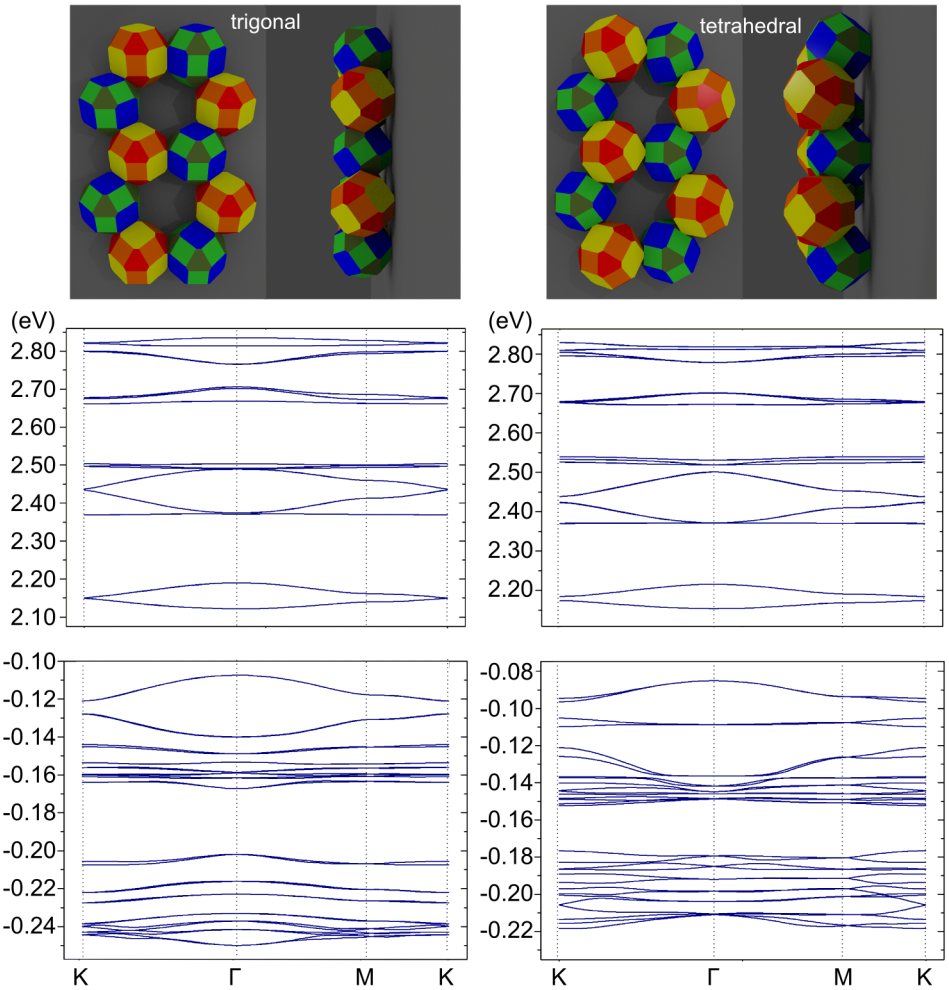

FIGURE 8.3. Band structure predicted by tight-binding for honeycomb superlattices of CdSe nanocrystals with a trigonal (nanocube diagonal = 4.3 nm, left) and tetrahedral (nanocube diagonal = 5.3 nm, right) shape. Adapted from [34].

described previously with a Voronoi analysis [Figure 8.4(a)] to determine parameters like nearest neighbor distances and hexagon areas. Scaling these quantities to their average in the picture provides a good insight into the disorder of the system. This can be visualized in the form of a color-coded overlay of the hexagon areas [Figure 8.4(b)] and nanocrystal-nanocrystal bonds [Figure 8.4(c)], or more

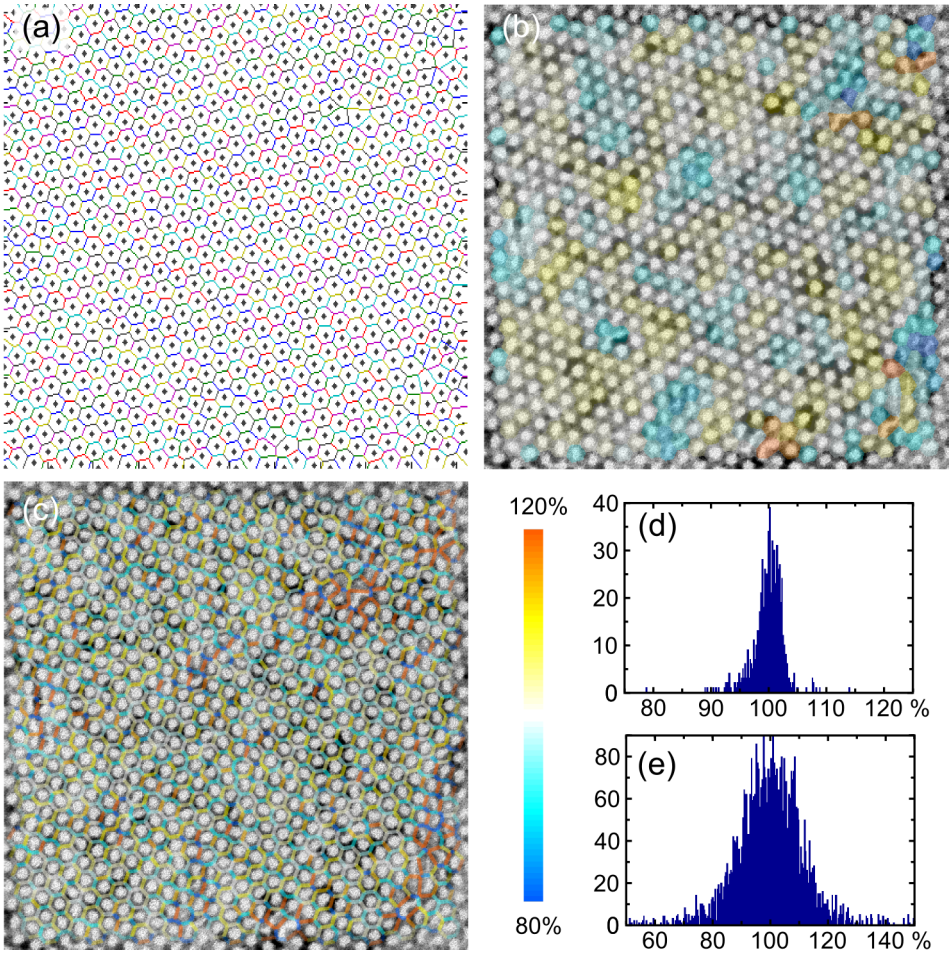

FIGURE 8.4. Voronoi analysis of the nanocrystal-based honeycomb structures. (a) Voronoi diagram of the detected hexagon centers in a TEM image of a PbSe honeycomb structure. (b) Color-coded overlay of the detected hexagon areas normalized to the average hexagon area. (c) Color-coded overlay of the detected nanocrystal-nanocrystal bonds normalized to the average bond length. (d,e) Histograms of the measured hexagon areas (d) and bond lengths (e).

quantitatively in histograms [Figure 8.4(d,e)]. As can be observed in Figure 8.4, the disorder (taken to be the full width at half maximum of the histograms) in this particular TEM image is $\sim 5\%$ of the average hexagon area, and $\sim 20\%$ of the average nanocrystal-nanocrystal bond length.

The information from Figure 8.4(d) and (e) allows to estimate reasonable input parameters for modeling the disorder. However, it is also important to know if the disorder in the honeycomb structures is completely random over the sample, or if there is a spatial correlation in the disorder. That is, is the honeycomb sheet stretched in certain areas and compressed in others, or is the distribution in hexagon area divided randomly over the sample? In order to test this, we again use Equation 8.1, and calculate the cross-correlation between the area of every hexagon and its n^{th} nearest neighbor [Figure 8.5, the correlation for a hexagon area with itself (n = 0) is one]. This was done for a total of six TEM images obtained on the same PbSe honeycomb sample. The data was averaged [Figure 8.5(b)] and a free exponential decay was fitted to the data resulting in a best fit of $y = a + b\exp(-\lambda x)$ with $a = -0.02$, $b = 1.03$, and $\lambda = 0.95$. Therefore we can safely conclude that, for this sample, there is no significant correlation in the hexagon disorder.

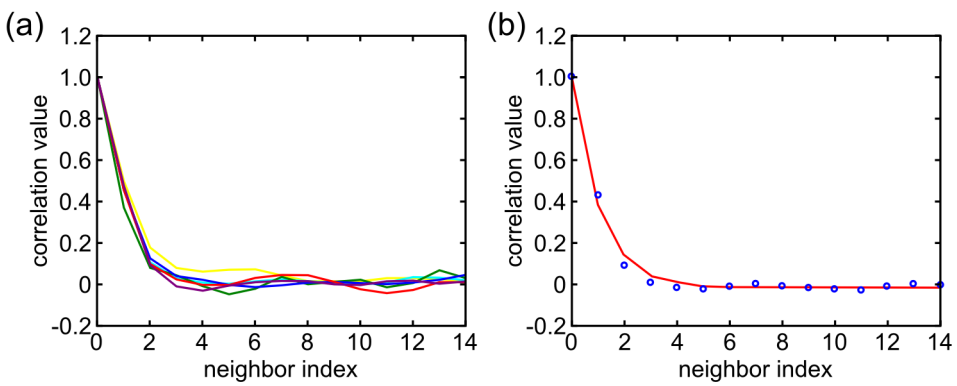

FIGURE 8.5. Correlation of disorder in hexagon area. (a) Cross-correlation value for the area of each hexagon with its n^{th} nearest neighbor. The analysis was performed for six TEM pictures (blue line represents the data from Figure 8.4). (b) Circles are the average of the data in panel (a), with the red line showing a free exponential decay fitted to the data (decay constant = 0.95).

8.5. Conclusion

This chapter reviewed the prospects for future research and provided an outlook on the research presented in this thesis. First, the principal insights gained in the imaging mechanism of AFM using functionalized tips were found to be directly applicable in future studies of nanopatterned graphene, molecules, and molecular networks. This holds in particular for the study of artificial graphene prepared from molecular networks, where atomically resolved images are indispensable for understanding the underlying physics. Combining this ability to precisely resolve the atomic structure with the possibility to manipulate the molecular structure, to chemically resolve the atoms in the structure, and to measure local electronic information, makes that the combined AFM/STM is an invaluable tool for the study of such systems. Second, it was shown that automated image analysis can serve as a valuable tool to facilitate and standardize the characterization of spherical nanocrystals. Finally, some future opportunities for the nanocrystal-based honeycomb structures were discussed. Although the development and study of this material is still in a very early stage, it was shown that the predicted material properties are very promising, surpassing those of regular graphene. Furthermore, we addressed the key issues that need attention before the material can be integrated into devices. The issue of disorder was dealt with in more depth, showing that also here automated image analysis can serve as a valuable tool, measuring the nanoscale disorder and spatial disorder correlation.

8.6. Bibliography

[1] Boneschanscher, M. P. *et al.* Quantitative atomic resolution force imaging on epitaxial graphene with reactive and nonreactive AFM probes. *ACS Nano* **6**, 10216–10221 (2012).

[2] Hämäläinen, S. K. *et al.* Structure and local variations of the graphene moiré on Ir(111). *Physical Review B* **88**, 201406(R) (2013).

[3] Boneschanscher, M. P., Hämäläinen, S. K., Liljeroth, P. & Swart, I. Sample corrugation affects the apparent bond lengths in atomic force microscopy. *ACS nano* **8**, 3006–3014 (2014).

[4] Gross, L., Mohn, F., Moll, N., Liljeroth, P. & Meyer, G. The chemical structure of a molecule resolved by atomic force microscopy. *Science* **325**, 1110–1114 (2009).

[5] Moll, N., Gross, L., Mohn, F., Curioni, A. & Meyer, G. The mechanisms underlying the enhanced resolution of atomic force microscopy with functionalized tips. *New Journal of Physics* **12**, 125020 (2010).

[6] Sun, Z., Boneschanscher, M. P., Swart, I., Vanmaekelbergh, D. & Liljeroth, P. Quantitative atomic force microscopy with carbon monoxide terminated tips. *Physical Review Letters* **106**, 046104 (2011).

[7] Guillermet, O. *et al.* STM and AFM high resolution intramolecular imaging of a single decastarphene molecule. *Chemical Physics Letters* **511**, 482–485 (2011).

[8] Mohn, F., Gross, L., Moll, N. & Meyer, G. Imaging the charge distribution within a single molecule. *Nature Nanotechnology* **7**, 227–231 (2012).

[9] Gross, L. *et al.* Bond-order discrimination by atomic force microscopy. *Science* **337**, 1326–1329 (2012).

[10] Sugimoto, Y. *et al.* Chemical identification of individual surface atoms by atomic force microscopy. *Nature* **446**, 64–67 (2007).

[11] Welker, J., Weymouth, A. J. & Giessibl, F. J. The influence of chemical bonding configuration on atomic identification by force spectroscopy. *ACS Nano* **7**, 7377–7382 (2013).

[12] Custance, O., Perez, R. & Morita, S. Atomic force microscopy as a tool for atom manipulation. *Nature Nanotechnology* **4**, 803–810 (2009).

[13] Liljeroth, P., Swart, I., Paavilainen, S., Repp, J. & Meyer, G. Single-molecule synthesis and characterization of metal-ligand complexes by low-temperature STM. *Nano Letters* **10**, 2475–2479 (2010).

[14] Swart, I., Gross, L. & Liljeroth, P. Single-molecule chemistry and physics explored by low-temperature scanning probe microscopy. *Chemical Communications* **47**, 9011–9023 (2011).

[15] Swart, I., Sonnleitner, T., Niedenführ, J. & Repp, J. Controlled lateral manipulation of molecules on insulating films by STM. *Nano Letters* **12**, 1070–1074 (2012).

[16] Albrecht, F., Neu, M., Quest, C., Swart, I. & Repp, J. Formation and characterization of a molecule-metal-molecule bridge in real space. *Journal of the American Chemical Society* **135**, 9200–9203 (2013).

[17] Gomes, K. K., Mar, W., Ko, W., Guinea, F. & Manoharan, H. C. Designer Dirac fermions and topological phases in molecular graphene. *Nature* **483**, 306–310 (2012).

[18] Bartels, L. Tailoring molecular layers at metal surfaces. *Nature Chemistry* **2**, 87–95 (2010).

[19] Lees, E. E. *et al.* Experimental determination of quantum dot size distributions, ligand packing densities, and bioconjugation using analytical ultracentrifugation. *Nano Letters* **8**, 2883–2890 (2008).

[20] Norris, D. & Bawendi, M. Measurement and assignment of the size-dependent optical spectrum in CdSe quantum dots. *Physical Review B* **53**, 16338–16346 (1996).

[21] Moreels, I. *et al.* Composition and size-dependent extinction coefficient of colloidal PbSe quantum dots. *Chemistry of Materials* **19**, 6101–6106 (2007).

[22] Friedrich, H. *et al.* Quantitative structural analysis of binary nanocrystal superlattices by electron tomography. *Nano Letters* **9**, 2719–2724 (2009).

[23] Novoselov, K. S. *et al.* Electric field effect in atomically thin carbon films. *Science* **306**, 666–669 (2004).

[24] Novoselov, K. S. *et al.* A roadmap for graphene. *Nature* **490**, 192–200 (2012).

[25] Schwierz, F. Graphene transistors. *Nature Nanotechnology* **5**, 487–496 (2010).

[26] Chang, C.-K. *et al.* Band gap engineering of chemical vapor deposited graphene by in situ BN doping. *ACS Nano* **7**, 1333–1341 (2013).

[27] Balog, R. *et al.* Bandgap opening in graphene induced by patterned hydrogen adsorption. *Nature Materials* **9**, 315–319 (2010).

[28] Samuels, A. J. & Carey, J. D. Molecular doping and band-gap opening of bilayer graphene. *ACS Nano* **7**, 2790–2799 (2013).

[29] Elias, D. C. *et al.* Control of graphene's properties by reversible hydrogenation: evidence for graphane. *Science* **323**, 610–613 (2009).

[30] Loh, K. P., Bao, Q., Ang, P. K. & Yang, J. The chemistry of graphene. *Journal of Materials Chemistry* **20**, 2277 (2010).

[31] Han, M., Özyilmaz, B., Zhang, Y. & Kim, P. Energy band-gap engineering of graphene nanoribbons. *Physical Review Letters* **98**, 206805 (2007).

[32] Hicks, J. *et al.* A wide-bandgap metal-semiconductor-metal nanostructure made entirely from graphene. *Nature Physics* **9**, 49–54 (2012).

[33] Britnell, L. *et al.* Field-effect tunneling transistor based on vertical graphene heterostructures. *Science* **335**, 947–950 (2012).

[34] Kalesaki, E. *et al.* Dirac cones, topological edge states, and nontrivial flat bands in two-dimensional semiconductors with a honeycomb nanogeometry. *Physical Review X* **4**, 011010 (2014).

[35] Evers, W. H. *et al.* Low-dimensional semiconductor superlattices formed by geometric control over nanocrystal attachment. *Nano Letters* **13**, 2317–2323 (2013).

Summary

The work described in this thesis was that of a quest to structurally resolve honeycomb systems — both on the atomic and on the nanometer scale. The first part included the use of AFM and STM to resolve graphene on Ir(111): to understand the atomic contrast, quantify the distortions due to the moiré pattern, explain the imaging mechanism of CO-terminated tips, and finally to measure the electronic properties of small graphene islands. The second part was devoted to the use of electron tomography to resolve nanoscale honeycomb systems: both weakly coupled, few-layer thick superlattices of PbSe and CdSe nanocrystals, and covalently bound single layer honeycombs of PbSe, CdSe, and PbS.

Chapter 1 provided a scope and outline of this thesis, followed by a short introduction to graphene. The interest in graphene was motivated by deriving its band structure, using a simple nearest-neighbor tight-binding model. Also the preparation of graphene by means of chemical vapor deposition was shortly addressed. Then the concept of quantum confinement was illustrated for different confinement geometries and it was shown how the density of states changes with confinement geometry. The concept of tunneling and the scanning tunneling microscope were introduced. Following this, the different forces playing a role at the atomic scale were addressed, and the atomic force microscope was introduced. The electron microscope was discussed for both bright-field and dark-field applications, and the theory behind electron tomography was shortly addressed. Finally, low-energy electron diffraction was introduced as a tool to probe surfaces in reciprocal space.

Chapter 2 described how the image contrast obtained with nc-AFM on graphene depends on tip reactivity and tip-sample distance. Experimental results obtained with a metallic tip were presented. At large tip-sample distances only van der Waals attraction with the moiré periodicity was observed. When

decreasing the tip-sample distance, an atomic-scale honeycomb pattern of attractive force was observed. This was attributed to chemical bond formation between the metallic tip and the carbon atoms of the graphene. When decreasing the tip-sample distance even further, the contrast was found to invert. This was attributed to a faster rise of Pauli repulsion on top of the carbon atoms than on the hollow sites in between the carbon atoms. When performing the same experiment with a chemically inert CO-modified tip, no attractive interaction at the atomic scale was observed. However, at the onset of repulsion the honeycomb lattice of graphene was observed. This was again attributed to a faster rise in Pauli repulsion on top of the carbon atoms than on the hollow sites in between the carbon atoms. The chemical forces associated with the bond formation and the Pauli repulsion were quantified, and found to be in line with reports of such forces in literature. Finally, using a CO-passivated tip, the edge of a graphene island was resolved atomically.

Chapter 3 was dedicated to resolving the moiré superstructure of graphene on Ir(111). The atomic structure within the moiré unit cell was resolved using dynamic LEED, and was found to be in line with predictions made in literature using van der Waals corrected DFT and X-ray standing wave measurements. AFM with CO-modified tips was used as a complementary technique to study local variations in the moiré pattern. It was found that random top sites of the moiré pattern were much higher (10 pm) than other top sites in the same area. Also a smooth variation in the moiré corrugation was observed (up to 5 pm), extending over several unit cells in a large island and resulting in a spread in observed corrugations for different island sizes. Neither the smooth variation nor the random outliers could be related to island size, or their environment (growing over, or being connected to a step edge in the iridium). Finally, formation of a second order moiré pattern and strain relief were discussed as possible sources for these local variations in the observed moiré corrugation.

Chapter 4 discussed the fundamental limits of AFM imaging with CO-modified tips, using epitaxial graphene as a model system. First it was demonstrated that the experimentally observed contrast pattern of graphene on Ir(111) consisted of much smaller hexagons on the top sites than on the bottom sites. These differences in area would correspond to unphysically large bond length changes over the sample. Using molecular mechanics simulations and pentacene as a simple model system, these changes in bond length could be attributed to the CO bending caused by the non-linear background signal arising from neighboring atoms. The experimental observations on the graphene on Ir(111) system could

be reproduced with the model, using physically reasonable parameters. Finally, the effect of background subtraction by means of filtering was tested, and suitable background subtraction was proposed as a means to bring the observed contrast patterns closer to the real atomic positions.

Chapter 5 reported quantum confined electronic states in small graphene islands on Ir(111), resembling standing wave patterns expected for the particle in a 2-D box problem. The quantum confined states were reproduced both by atomistic tight binding modeling and by solving the Klein–Gordon equation for confinement areas matching the size and shape of the experimentally measured graphene islands. To study the nature of the charge carriers in the graphene islands, the relationship between the energy of the lowest quantum confined state (the S state) and the area of confinement was measured. It was found that the energy of this S state evolved with area as $1/\sqrt{A}$, indicative for the behavior of massless Dirac fermions and a linear $E(\boldsymbol{k})$ dispersion. The corresponding Fermi velocity was found to be slightly smaller than previous results obtained by ARPES.

Chapter 6 showed the potential of electron tomography for nanomaterial analysis by resolving a novel crystal structure made by self-assembly of PbSe and CdSe nanocrystals. First, it described how the formation of binary nanocrystal superlattices reported in literature thus far could be understood in terms of the hard-sphere model. Then it reported how various binary crystal structures were observed using a nanocrystal size ratio that, according to hard-sphere theory, should not result in binary crystal structure formation. From the TEM images, the crystal structure could not be resolved. However, using electron tomography, the crystal structure of three different patches observed in TEM was resolved. It was found that the first patch consisted of staggered layers of PbSe and CdSe nanocrystals forming a kagome lattice (hexagons connected by triangles), with CdSe nanocrystals sandwiched in between these layers. The crystal structure had a stoicheometry of $[PbSe]_6[CdSe]_{19}$. Although the structure showed resemblance with minerals from the $EuMg_{5.2}$ family, there was no counterpart observed in the atomic world. Initial Monte Carlo simulations could not account for the stability of the crystal structures in terms of the hard-sphere model. However, these simulations were hampered by the large and complex unit cell of the structure. Electron tomography on the second patch showed that this was in fact also consisting of the $[PbSe]_6[CdSe]_{19}$ crystal structure. However, a crystallographic defect resulted in the top half of the structure being transposed with respect to the bottom half. This made that the resulting TEM image showed a complicated pattern that was

very different from the TEM image obtained on the first patch. The third patch was found also to consist of the $[PbSe]_6[CdSe]_{19}$ crystal structure. However, here the crystal was grown in a different orientation with respect to the TEM grid, and drying forces had distorted the unit cell of the crystal.

Chapter 7 presented a thorough atomic and nanoscale analysis of atomically coherent honeycomb structures prepared by oriented attachment of nanocrystals. First it described the synthesis of PbSe nanocrystals and a honeycomb thereof, while also providing a HAADF-STEM analysis of the initial PbSe nanocrystal shape. It was shown that, in the relevant size regime, the rock salt lattice of PbSe resulted in nanocrystals with a cantellated cubic shape. This shape exposes three different crystal facets, providing a route for three different oriented attachment schemes, each resulting in a different honeycomb structure. From these three models, the flat, trigonal mode could quickly be discarded, since the orientation of the atomic lattice with the honeycomb geometry was found to differ from what was experimentally observed in high-resolution HAADF-STEM images and electron diffraction patterns. The other two models, with tetrahedral and octahedral symmetry, both showed profound buckling of the honeycomb structure. This buckling was also observed in STM experiments. However, experimental limitations did not allow to quantify the buckling, making a distinction between the two models on basis of STM impossible. A GISAXS analysis of the honeycomb structure indicated that the octahedral structure was more likely than the tetrahedral one. However, electron tomography combined with automated particle detection provided real evidence that the honeycombs indeed possessed octahedral symmetry. The next-nearest neighbor (NNN) distances observed in STM, GISAXS, and TEM, and the ratio between nanocrystal bond length and NNN distance implied by the octahedral model, implied that the nanocrystal-nanocrystal bonds in the honeycomb structure were longer than the initial nanocrystal size. This was corroborated by the results from electron tomography. This increase in bond length was explained by a model of oriented attachment by means of self-assembly followed by neck formation before robust attachment takes place. To demonstrate the versatility of the honeycomb structures, cation exchange was used to transform the PbSe honeycomb lattices into CdSe. Analysis by means of electron diffraction, HAADF-STEM, and electron tomography demonstrated that the atomic lattice was transformed into zinc blende, while the nanogeometry and the orientation of the atomic lattice with respect to the honeycomb lattice were preserved. As a

final demonstration of the versatility of this method to prepare nanoscale honeycomb structures from ordinary semiconductors, the first results obtained with PbS nanocrystals were presented.

Chapter 8 finally presented an outlook of the research described in this thesis. It speculated on how the gained knowledge of the imaging mechanism of AFM with CO-modified tips could be used in the preparation and analysis of atomic-scale honeycomb structures by scanning probe microscopy. Then it provided insight in the computer-aided image analysis method used throughout this research, and demonstrated how this method could be applied to various problems. Also, the prospects of the nanocrystal-based honeycomb structures were presented. Potential applications of the honeycomb structures for various devices were discussed, and issues that need attention before the honeycomb structures can be integrated into devices were addressed. In particular, the issue of disorder was addressed, and a first analysis of the nanoscale disorder was presented.

Samenvatting in het Nederlands

De afgelopen vier jaar heb ik met veel plezier fundamenteel onderzoek mogen doen. Fundamenteel wil zeggen dat mijn onderzoek puur gedreven werd door nieuwsgierigheid, in dit geval nieuwsgierigheid naar de werking van de natuur tot op het niveau van enkele atomen. Tegelijkertijd laat ik in het laatste hoofdstuk van dit proefschrift zien dat inzichten uit nieuwsgierigheidsgedreven onderzoek wel degelijk tot allerlei nieuwe toepassingen kunnen leiden.

Dit proefschrift heeft als thema tweedimensionale materialen met honingraatgeometrie. Tweedimensionaal betekend simpelweg vlak: de onderzochte materialen hebben een dikte variërend van enkele nanometers tot slechts één enkel atoom. Ter illustratie: een meter verhoudt zich tot een nanometer als de diameter van de aarde tot die van een knikker. Als we de grootte van de knikker op één nanometer stellen hebben de nanodeeltjes uit dit onderzoek de grootte van een tennisbal en de koolstofatomen in grafeen de grootte van een speldenknop.

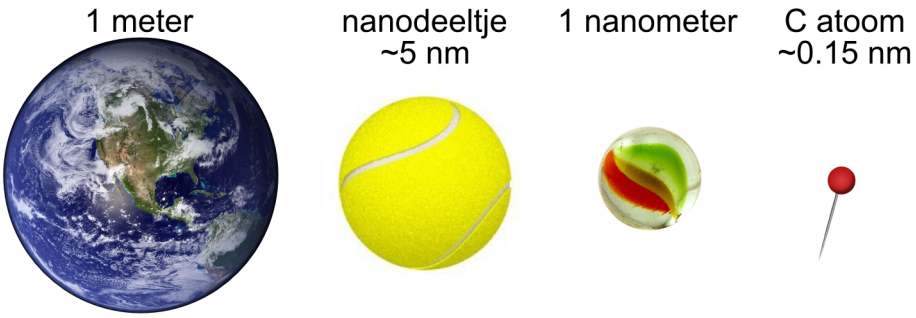

De verhouding van 1 meter tot 1 nanometer is gelijk aan de verhouding van de aarde tot een knikker.

Wat is er interessant aan de honingraat-geometrie?

Het kernwoord in deze scriptie is honingraat, wat leidt tot de logische vraag waarom de honingraatstructuur nu zo interessant is. Het antwoord op deze vraag is te vinden in de manier waarop deze structuren stroom geleiden, ofwel elektronen transporteren. Om dit te begrijpen moeten we eerst accepteren dat elektronen niet alleen lijken op deeltjes die we kunnen beschrijven met een massa en een snelheid (zoals bijvoorbeeld biljartballen), maar dat ze zich ook kunnen gedragen als golven die we moeten beschrijven met een golfvector (richting en golflengte) en een amplitude. Als we een elektron alleen zouden zien als een biljartbal, dan zouden we een elektrische spanning als het equivalent van een keu kunnen gebruiken om het elektron met een willekeurige snelheid en richting over de biljarttafel te stoten. Nu we het elektron ook als golf moeten beschouwen, moeten we rekening houden met de interactie tussen de elektrongolf en het onderliggende atoomrooster. Als we dit doen blijkt dat de energie van het elektron afhankelijk is van de richting waarmee het zich door het rooster beweegt. Stel je voor dat de richting waarin een bal zich mag verplaatsen over de biljarttafel opeens afhangt van zijn energie (snelheid en massa) — dat zou de sport in elk geval interessanter maken. Een mooi voorbeeld van dit gedrag is te zien in de breking van licht in een prisma: rood licht (met een iets lagere energie) en blauw licht (met een iets hogere energie) hebben na breking door het prisma elk een andere richting gekregen.

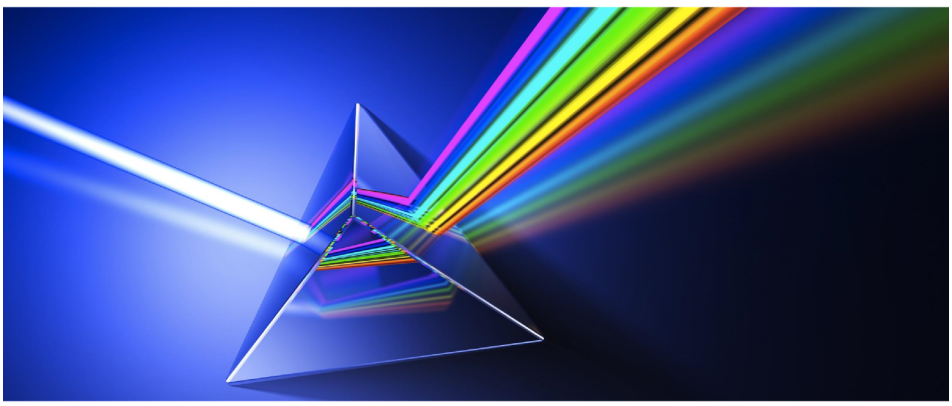

Dispersie van licht aan een driehoekig prisma.

Het verband tussen de golfvector en energie van een golf noemen we de dispersierelatie. Deze relatie is niet uniek: er zijn meerdere energiën toegestaan bij één en dezelfde golfvector, die in een grafiek elk hun eigen band vormen. We kunnen veel van de eigenschappen van het materiaal begrijpen door nu de bandenstructuur op te vullen met de elektronen die er in het materiaal aanwezig zijn. Elektronen zullen daarbij altijd de nog vrije toestand met een zo laag mogelijke energie aannemen, waardoor we de banden van laag naar hoog met elektronen zullen bezetten. Als we halverwege een energieband al door de elektronen heen zijn spreken we van een metaal. Omdat niet alle toestanden in die band gevuld zijn kost het maar weinig energie om een elektron uit die band een bepaalde richting aan te laten nemen en dus zal het materiaal goed stroom geleiden. De elektronen in deze band noemen we daarom ladingsdragers. De elektronen in de lagere energiebanden spelen geen rol in de geleiding, maar vormen de bindingen die het metaal bij elkaar houdt. In het geval van een halfgeleider zijn alle elektronen betrokken in de bindingen van het materiaal en zijn de bezette banden dus allemaal helemaal gevuld. Om een halfgeleider stroom te laten geleiden moet er dus eerst een elektron uit zo'n bindende toestand aangeslagen worden naar de eerstvolgende lege band. Daarom noemen we de laatst gevulde band de valentieband en de eerstvolgende lege band de geleidingsband. Als de energiekloof tussen deze twee banden heel groot is spreken we niet meer van een halfgeleider maar van een isolator.

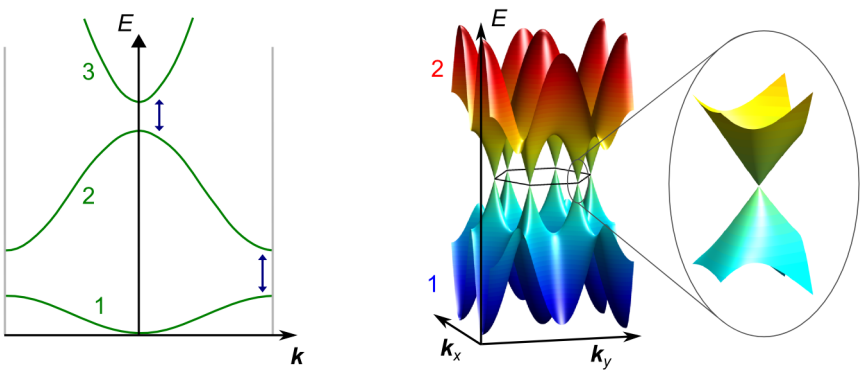

Links: de bandenstructuur van een 1-dimensionale keten van atomen. De energiekloof tussen verschillende banden is met een blauwe pijl weergegeven. Rechts: de bandenstructuur van de valentie- en geleidingsband van grafeen.

De interesse in honingraatstructuren is terug te leiden op onderzoek aan grafeen, een honingraatstructuur gevormd uit koolstofatomen. De bandenstructuur van grafeen is namelijk heel bijzonder: allereerst raken de valentieband en de geleidingsband elkaar net aan, waardoor grafeen een zogenaamd semimetaal is. Omdat een semimetaal minder ladingsdragers heeft dan een metaal zal het normaal gesproken minder goed stroom geleiden. Grafeen blijkt echter juist heel goed te zijn in het geleiden van stroom, zelfs veel beter dan de best geleidende metalen zilver en koper. Dit komt doordat de dispersierelatie in grafeen, rondom het punt waar valentie- en geleidingsband elkaar raken, over een significante afstand lineair is. Een lineaire dispersierelatie is kenmerkend voor deeltjes die met de snelheid van het licht reizen omdat ze geen massa hebben (bijvoorbeeld fotonen). Grafeen blijkt dan ook in staat tot ballistisch transport van ladingsdragers, dat wil zeggen dat de ladingsdragers tijdens transport nauwelijks ergens tegen terugkaatsen en dat grafeen dus zo goed als geen weerstand heeft. Verder leidt de dispersierelatie van grafeen tot diverse andere bijzondere eigenschappen, bijvoorbeeld een goede geleiding van elektronspinstromen en bijzondere interacties met een magnetisch veld.

Instrumentatie

Omdat de onderzochte structuren zo klein zijn, kun je ze niet met het blote oog waarnemen. Sterker nog, de onderzochte structuren zijn vele malen kleiner dan de golflengte van licht, waardoor je ze ook niet met een conventionele lichtmicroscoop zult kunnen bestuderen. De microscopen die zijn gebruikt voor dit onderzoek werken dan ook fundamenteel anders dan een lichtmicroscoop.

Allereerst heb ik veel gebruik gemaakt van de rastertunnelmicroscoop (Engels: scanning tunneling microscope, of STM) en de atoomkrachtmicroscoop (Engels: atomic force microscope, of AFM). De werking van deze microscopen lijkt meer op de werking van een ouderwetse platenspeler dan op die van een lichtmicroscoop: een scherpe naald wordt gebruikt om informatie van een oppervlak af te lezen.

In de rastertunnelmicroscoop gebeurt dit aflezen door slim gebruik te maken van het kwantummechanische tunneleffect. Dit tunneleffect is af te leiden uit het onzekerheidsprincipe van Heisenberg dat stelt dat het onmogelijk is om van een deeltje tegelijkertijd de positie en de energie met volkomen zekerheid te weten. Stel dat een deeltje zich geplaatst ziet voor een barrière die zo hoog is dat het deeltje niet genoeg energie heeft om deze over te steken. De onzekerheid in positie van het deeltje maakt dan dat er toch een bepaalde kans is dat het zich opeens aan de andere kant van de barrière bevindt. Deze kans is extreem gevoelig voor

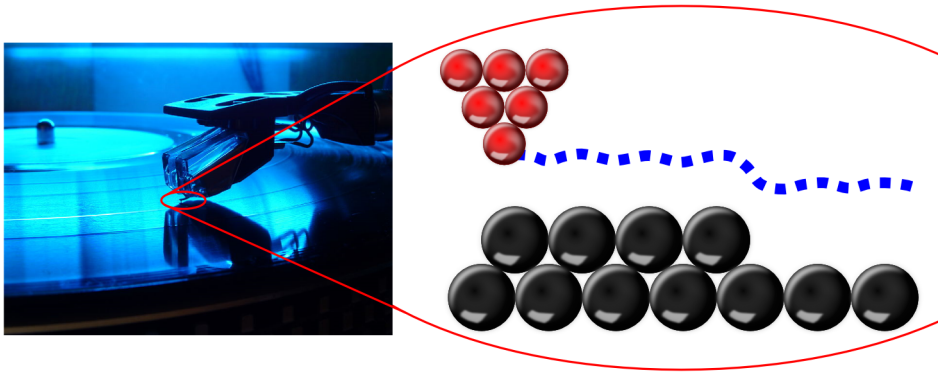

De werking van de rastertunnelmicroscoop en de atoomkrachtmicroscoop doet denken aan die van een platenspeler.

de breedte van de barrière, waardoor de tunnelstroom door de barrière gebruikt kan worden om zeer nauwkeurig veranderingen in de breedte daarvan te meten. In de rastertunnelmicroscoop is de afstand tussen het uiterste atoom van de naald en de atomen van het te meten oppervlak bepalend voor de breedte van de energie barrière. Door een zwakke spanning aan te leggen tussen de naald en het oppervlak kunnen we de tunnelende elektronen meten in de stroom. Als we nu de naald in een raster over het oppervlak scannen kunnen we de stroom registreren om een plaatje te maken van het oppervlak (constante hoogte modus). Ook kunnen we met een terugkoppelingsproces tijdens het scannen de hoogte van de naald aanpassen om een constante stroom te houden (constante stroom modus). In dat geval wordt de hoogte van de naald weergegeven om een plaatje van het oppervlak te maken. Het feit dat er een elektrische stroom nodig is om te kunnen meten is een nadeel van de rastertunnelmicroscoop: hierdoor kunnen namelijk alleen maar metingen aan geleidende oppervlakken gedaan worden.

De atoomkrachtmicroscoop gebruikt ook een scherpe naald om informatie van een oppervlak af te lezen, maar gebruikt in plaats van de tunnelstroom de kracht tussen naald en oppervlak om hier een afbeelding van te maken. Deze kracht kan bijvoorbeeld veroorzaakt worden door elektrostatische effecten (ladingen die elkaar aantrekken of afstoten), Van der Waals effecten (aantrekkende krachten tussen permanente en/of geïnduceerde dipolen, bijvoorbeeld gecorreleerde beweging tussen elektronen van twee verschillende atomen), magnetische krachten, formatie van een chemische binding tussen het uiterste atoom van de naald en het oppervlak,

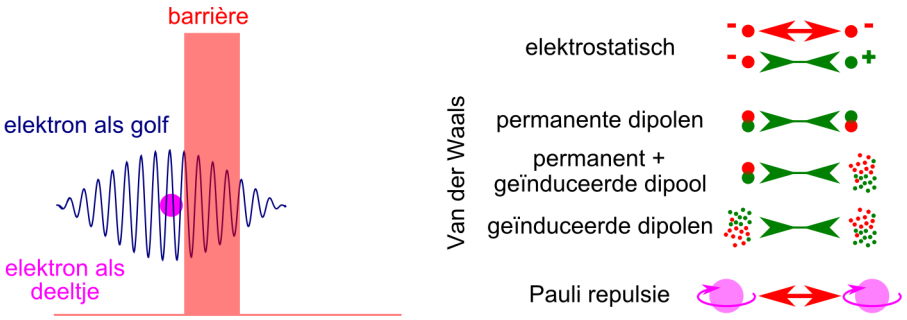

Links: de amplitude van een elektrongolf geeft de kans het elektron aan te treffen. De elektrongolf strekt zich hier uit tot voorbij de barrière, waardoor het elektron kan tunnelen naar de andere kant. Rechts: illustratie van enkele krachten relevant voor de atoomkrachtmicroscoop.

of Pauli repulsie: afstoting doordat twee elektronen met gelijke kwantumgetallen zich niet op dezelfde plaats kunnen bevinden. Deze krachten worden in de atoomkrachtmicroscoop gemeten door de naald op een veerarm (cantilever) te plaatsen en die te laten trillen met zijn eigenfrequentie. Als de trillende naald in dicht contact met het oppervlak wordt gebracht, zal de kracht tussen naald en oppervlak zorgen voor een verandering van de trilling van de naald. In onze opstelling houden we de amplitude van de trilling constant en meten we de verandering in frequentie. Nu kunnen we opnieuw een raster meten in constante hoogte modus en zo een afbeelding genereren van de frequentieverschuiving (Δf) over het oppervlak. Ook kunnen we de hoogte van de naald reguleren aan de hand van de gemeten frequentieverschuiving om zo in constante Δf modus te meten. Het voordeel van de atoomkrachtmicroscoop is dat er ook aan niet-geleidende materialen gemeten kan worden.

Om de naald de minieme afstanden voor het scannen en aanpassen van de hoogte te laten maken gebruiken we een piëzo-elektrisch kristal. Onder invloed van een elektrische spanning krimpen deze kristallen, of zetten ze juist uit. Hierdoor zijn ze geschikt om nauwkeurig hele kleine bewegingen uit te voeren. Ten slotte: doordat we in de atoomkrachtmicroscoop gebruik maken van een zeer stijve veerarm kunnen we meten bij heel kleine amplitudes. Daardoor kunnen we de naald zo

dicht bij het oppervlak brengen dat we ook tegelijkertijd de tunnelstroom kunnen meten.

Een andere techniek die een grote rol speelt in dit onderzoek is transmissie-elektronenmicroscopie (TEM). Elektronenmicroscopie lijkt al meer op lichtmicroscopie dan de hierboven beschreven technieken, maar omdat elektronengolven een veel kortere golflengte hebben dan die van licht kunnen we met deze techniek wel afbeeldingen maken van objecten op de nanoschaal (en in goede microscopen zelfs van atomen). In de elektronenmicroscoop wordt een dun object in een elektronenbundel geplaatst. De elektronen verstrooien aan atomen met een zware kern, waardoor de doorgaande bundel een 'schaduw' laat zien op de plek van dit atoom. Het op deze manier gegenereerde beeld wordt vervolgens met een digitale camera opgenomen.

De elektronentransmissie afbeeldingen bevatten echter slechts een tweedimensionaal beeld van een driedimensionaal object. Om toch een driedimensionaal beeld te krijgen maken we gebruik van tomografie. Hierbij wordt onder verschillende hoeken een elektronentransmissie opname gemaakt van het object. Vervolgens kan een driedimensionale reconstructie van het object gemaakt worden door de verschillende opnames op de juiste manier samen te voegen. De kwaliteit van deze reconstructie is afhankelijk van het aantal elektronentransmissie opnames en de reikwijdte van de hoeken waaronder ze zijn opgenomen.

Conclusie

Na een beschrijving van wat er nu zo bijzonder is aan structuren met een honingraaggeometrie en een beschrijving van de apparatuur die ik gebruikt heb om deze structuren te onderzoeken, rest de vraag welke resultaten er uit dit onderzoek zijn gekomen. Kort samenvattend zijn er twee grote resultaten behaald:

(1) Fundamenteel begrip van de manier waarop de atoomkrachtmicroscoop afbeeldingen maakt van grafeen. Dit fundamentele begrip opent nieuwe mogelijkheden om de structuur van grafeen te correleren aan de elektronische eigenschappen. Denk daarbij aan het bestuderen van defecten (ontbrekende atomen in het grafeenrooster), randen en grafeen nanostructuren. Met dit laatste hebben we al een begin gemaakt, zoals beschreven in Hoofdstuk 5.

(2) Kennis van de atomaire structuur van artificiele honingraatstructuren gemaakt van nanokristallen. Deze kennis maakt het mogelijk voorspellingen te doen over de elektronische eigenschappen van de structuur. Ook

biedt deze kennis de mogelijkheid om een mechanisme te bedenken waarmee deze structuren gevormd worden, en daarmee mogelijkheden om ze meer naar onze wens aan te passen.

Het eerste van deze resultaten zal zich vooral op de lange termijn moeten bewijzen, door toepassing in andermans onderzoek. Het tweede biedt echter al op de korte termijn perspectieven voor het onstaan van een nieuwe klasse materialen met allerlei mogelijke toepassingen. Hieronder volgt ten slotte een wat meer gedetailleerde samenvatting per hoofdstuk.

Samenvatting per hoofdstuk

Hoofdstuk 1 beschrijft de reikwijdte en de indeling van dit proefschrift. Hierna volgt een korte introductie in het materiaal grafeen. De interesse voor grafeen wordt gemotiveerd door de bandenstructuur hiervan af te leiden door middel van een simpel naaste buren 'tight-binding' model. Ook wordt de synthese van grafeen door middel van chemisch opdampen behandeld. Dan wordt het concept kwantumopsluiting behandeld voor verschillende opsluitingsgeometrieën. Voor elke geometrie wordt de bijbehorende toestandsdichtheid gepresenteerd. Vervolgens worden het concept kwantumtunneling en de rastertunnelmicroscoop geïntroduceerd. Daarna worden de verschillende krachten die een rol spelen op de atomaire schaal behandeld en wordt de atoomkrachtmicroscoop geïntroduceerd. De elektronenmicroscoop wordt behandeld voor zowel transmissie als donkerveld toepassingen en de theorie achter elektronentomografie wordt kort aangehaald. Ten slotte wordt lage energie elektronendiffractie geïntroduceerd als een methode om oppervlakken in de reciproke ruimte te bestuderen.

Hoofdstuk 2 beschrijft hoe het contrast in afbeeldingen van grafeen verkregen met een atoomkrachtmicroscoop afhangt van de reactiviteit van de naald van de atoomkrachtmicroscoop en van de afstand tussen naald en oppervlak. Experimenten met een metallische naald laten bij grote afstand tussen naald en oppervlak alleen Van der Waals attractie zien met een periodiciteit van het moiré patroon. Wanneer de naald dichter bij het oppervlak komt wordt een honingraatrooster van attractieve interactie zichtbaar. Dit wordt toegeschreven aan de formatie van een chemische binding tussen het uiterste metaalatoom van de naald en de koolstofatomen van het grafeen. Als we de afstand tussen naald en oppervlak nog verder verkleinen draait het contrast om naar een honingraatrooster van repulsieve interactie. Dit wordt toegeschreven aan een snellere toename van de Pauli repulsie boven de koolstofatomen dan boven de holle ruimtes tussen de koolstofatomen.

Identieke experimenten met een chemisch inerte naald met geadsorbeerd koolmonoxide (CO) molecuul laten geen attractieve interactie op de atomaire schaal zien. Wel wordt bij kortere afstand tussen naald en oppervlak de aanzet van repulsie in de vorm van het honingraatrooster van grafeen geobserveerd. Dit wordt opnieuw toegeschreven aan een snellere toename van Pauli repulsie boven de koolstofatomen dan boven de holle ruimtes tussen de koolstofatomen. Vervolgens worden de krachten geassocieerd met de formatie van de chemische binding en de Pauli repulsie gekwantificeerd. De grootte van deze krachten blijken goed te passen tussen waarden uit de literatuur. Ten slotte wordt met behulp van een met CO gemodificeerde naald een atomair opgeloste afbeelding gemaakt van de rand van een grafeen eiland.

Hoofdstuk 3 behandelt het oplossen van de moiré superstructuur die grafeen bovenop een Ir(111) kristal vormt. Deze moiré structuur wordt atomair opgelost met behulp van lage energie elektronendiffractie (LEED) en blijkt overeen te komen met voorspellingen in de literatuur op basis van Van der Waals gecorrigeerde dichtheidsfunctionaaltheorie (DFT) en staande-golf röntgen metingen. De atoomkrachtmicroscoop met een CO gemodificeerde naald is gebruikt als complementaire techniek om plaatselijke variaties in het moiré patroon te onderzoeken. Hieruit bleek dat willekeurige top posities binnen het moiré patroon plotseling veel hoger (10 pm) waren dan omliggende top sites in hetzelfde gebied. Ook werd er een geleidelijke variatie (tot 5 pm) in de golving van het moiré patroon geobserveerd. Deze variatie strekte zich uit over verschillende eenheidscellen in een groot eiland en resulteerde in een spreiding in de resultaten verkregen op verschillende kleine eilanden. Zowel de geleidelijke variatie als de willekeurige uitschieters konden niet worden gerelateerd aan eilandgrootte of aan het groeien over, of vanuit, stappen in het onderliggende iridiumkristal. Aan het eind van het hoofdstuk worden de formatie van een tweede-orde moiré patroon en het lokaal opheffen van spanning bediscussieerd als mogelijke oorzaken van deze plaatselijke variaties in de moiré golving.

Hoofdstuk 4 gaat over de fundamentele limieten van het gebruik van CO gemodificeerde naalden in de atoomkrachtmicroscoop. Aan het begin van het hoofdstuk wordt gedemonstreerd hoe afbeeldingen van grafeen op Ir(111) met een dergelijke naald veel kleinere zeshoeken laat zien op de top sites van het moiré patroon dan daar tussen. De geobserveerde verschillen in oppervlak zouden leiden tot fysisch onrealistische verschillen in bindingslengte binnen het sample. Met behulp van moleculaire mechanica simulaties op het molecuul pentaceen als simpel

model systeem konden we deze variaties in bindingslengte toeschrijven aan het buigen van het CO molecuul aan het uiteinde van de AFM naald als gevolg van een niet-lineair achtergrondsignaal van de omliggende atomen. De experimentele observaties op het grafeen/Ir(111) systeem konden met behulp van het model gereproduceerd worden bij gebruikmaking van fysisch realistische parameters. Ten slotte is het effect van achtergrondcorrectie door middel van filtering getest en een bruikbare filtermethode voorgesteld als manier om de geobserveerde contrastpatronen dichter bij de werkelijke posities van de atomen te brengen.

Hoofdstuk 5 rapporteert over kwantumopsluiting in kleine grafeen eilanden. De kwantumopsluiting resulteert in staande-golf patronen overeenkomend met het deeltje in een tweedimensionaal doosje probleem. Deze patronen konden worden gereproduceerd met behulp van 'tight binding' modellering en door de Klein–Gordon vergelijking op te lossen. Voor dit laatste is de vorm en grootte van het eiland geobserveerd in het experiment gebruikt als input. De relatie tussen de energie van de energetisch laagste opgesloten toestand (de S toestand) en het oppervlak van het eiland is bestudeerd om een beeld van de aard van de ladingsdragers in de grafeen eilanden te krijgen. Het resultaat was dat de energie van deze S toestand afhankelijk bleek van het oppervlak met $1/\sqrt{A}$, duidend op het gedrag van massaloze Dirac fermionen en een lineaire $E(\boldsymbol{k})$ dispersierelatie. De corresponderende Fermi snelheid bleek net iets lager te zijn dan eerdere resultaten behaald met ARPES.

Hoofdstuk 6 toont de potentie van elektronentomografie als analysemethode voor nanodeeltjes door een nieuwe kristalstructuur gemaakt van PbSe en CdSe nanokristallen te analyseren. Allereerst beschrijft het hoofdstuk hoe de formatie van binaire superroosters van nanokristallen tot dusver gerapporteerd, begrepen kon worden aan de hand van het harde-bollen model. Dan beschrijft het hoe verschillende binaire superroosters zijn gemaakt van nanokristallen met een grootteverhouding die, volgens de harde-bollen theorie, niet tot de formatie van een superrooster had mogen leiden. De kristalstructuur van deze superroosters was niet af te leiden uit de elektronenmicroscopie opnamen ervan. Echter, door het gebruik van elektronentomografie kon de kristalstructuur van drie verschillende superroosters opgelost worden. De eerste hiervan bleek te bestaan uit een gelaagde structuur van PbSe en CdSe nanokristallen die samen een kagome structuur (zeshoeken verbonden door driehoeken) vormen, met CdSe nanokristallen tussen deze lagen in. De kristalstructuur had een stoicheometrie van $[PbSe]_6[CdSe]_{19}$. Hoewel de structuur enigszins lijkt op die van mineralen uit de $EuMg_{5.2}$ familie kon

er geen atomaire tegenhanger van deze kristalstructuur gevonden worden. Het is niet gelukt om de stabiliteit van de kristalstructuur te verklaren met behulp van Monte Carlo simulaties. Deze simulaties hadden echter te lijden onder de grote en complexe eenheidscel van de kristalstructuur. Elektronentomografie opnamen van het tweede superrooster toonde aan dat dit in feite ook de $[PbSe]_6[CdSe]_{19}$ kristalstructuur had. Echter, door een kristallografisch defect was de bovenste helft van het superrooster verschoven ten opzichte van de onderste helft. Dit resulteerde in complexe elektronenmicroscopie opnamen die erg verschillend waren van die die waren opgenomen van het eerste superrooster. Het derde superrooster bleek ook de $[PbSe]_6[CdSe]_{19}$ kristalstructuur te hebben. Echter, in dit geval was de structuur gegroeid onder een andere hoek ten opzichte van het substraat en hadden droogkrachten de eenheidscel vervormd.

Hoofdstuk 7 beschrijft een grondige analyse op atomair en nanometer niveau van atomair coherente honingraatroosters gemaakt door georiënteerde aaneenhechting van nanokristallen. Allereerst behandelt het de synthese van PbSe nanokristallen en honingraatroosters daarvan, terwijl het ook een HAADF-STEM analyse geeft van de initiële vorm van de PbSe nanokristallen. In het regime van relevante groottes blijkt dat de PbSe nanokristallen de vorm hebben van een tweevoudig afgeknotte kubus. Deze vorm stelt drie verschillende kristalfacetten bloot, wat drie verschillende aaneenhechtingen mogelijk maakt die elk in een verschillende honingraatstructuur eindigen. Van deze drie modellen kan het vlakke, trigonale model snel ter zijde worden geschoven omdat de oriëntatie van de atomaire kristalstructuur ten opzichte van de honingraatstructuur niet overeenkomt met het resultaat van HAADF-STEM en elektronendiffractie experimenten. De andere twee modellen, met tetraëdrische en octaëdrische symmetrie laten beiden een golving van de honingraatstructuur zien. Deze golving is vervolgens ook geobserveerd in rastertunnelmicroscopie experimenten. Experimentele begrenzingen stonden echter niet toe om de mate van golving te kwantificeren, waardoor het niet mogelijk is op basis van deze experimenten onderscheid te maken tussen de twee verschillende structuren. Een GISAXS analyse wees uit dat de honingraatstructuur waarschijnlijk een octaëdrische symmetrie heeft. Dit kon uiteindelijk ook sluitend bewezen worden uit de resultaten van elektronentomografie met behulp van computergestuurde beeldanalyse. De op-één-na naaste buren (NNN) afstanden geobserveerd in STM, GISAXS en TEM, in combinatie met het octaëdrische model, impliceren dat de bindingen tussen de nanokristallen in de honingraatstructuur langer is dan de oorspronkelijke nanokristal diameter. Dit resultaat wordt ondersteund door

de metingen aan de data van de elektronentomografie analyse. Deze toename in bindingslengte valt uit te leggen met een model van georiënteerde aaneenhechting door middel van zelfassemblage, gevolgd door nekformatie voordat robuuste aaneenhechting plaatsvindt. Om de veelzijdigheid van de honingraatstructuren te demonstreren is kation uitwisseling gebruikt om de PbSe honingraatroosters om te zetten in CdSe. Analyse met behulp van elektronendiffractie, HAADF-STEM en elektronentomografie toont aan dat de atomaire structuur wordt omgezet in zinkblende, terwijl de nanogeometrie en de oriëntatie van het atomaire rooster ten opzichte van het honingraatrooster behouden blijft. Ten slotte worden de eerste resultaten verkregen met PbS nanokristallen gepresenteerd als een laatste demonstratie van de veelzijdigheid van deze methode om honingraatroosters met nanogeometrie te maken uit conventionele halfgeleiders.

Hoofdstuk 8 presenteert ten slotte een vooruitzicht op het hier beschreven onderzoek. Het hoofdstuk speculeert over de rol die de verkregen kennis over AFM met CO gemodificeerde naalden kan spelen in het veld van atomaire honingraatstructuren. Dan laat het zien hoe de gebruikte beeldanalyse methode toegepast kan worden op verschillende problemen. Ook worden mogelijke toepassingen van de op nanokristallen gebaseerde honingraatstructuren bediscussieerd en zaken die nog aandacht behoeven benoemd. In het bijzonder wordt er al aandacht besteed aan mogelijke problemen door wanorde en wordt een eerste analyse van wanorde op de nanometerschaal gepresenteerd.

Acknowledgements

If you are reading this: thank you! Because it is very likely that you are one of the many, many people that have in one way or another contributed to this thesis. Please know that I am ever so grateful to you.

First and foremost I would like to thank my promotor Daniël Vanmaekelbergh and my copromotors Peter Liljeroth and Ingmar Swart. Daniël, even after being one of your students for 7 years now (BSc, Msc, and PhD) I still think that there are many things you can teach me. Thank you for giving me the opportunity to be part of your group. I have very fond memories of our discussions on science, classical music, religion, politics, and science again. It was great to see how enthusiastic you could always be with the results from what I considered to be a failed or hopeless experiment, and then turn it into either a new research question or even a paper. Thank you for the freedom you gave me in pursuing what I thought was interesting. Peter, I think we had a fantastic start that paved the way for some later very fruitful collaborations. I will remember your visits from Finland as an energy boost in the lab and my work, always ending in a pleasant dinner at the Thaj Mahal with an endless discussion about the situation in the middle-east over coffee. Ingmar, you truly came at a turn of the tide. The 'baby' was not performing up to specs after having been down for over a year, and I had a hard time trying to do research with the one hand and repairs with the other. But you calmly took over most of the maintenance and got the machine operating better than ever, while also upgrading the lab quite a bit. And yes, we did some very nice research in between as well. Thank you for involving me in everything, and for securing a future for SPM in Utrecht.

Secondly, I would like to thank my students and collaborators: without your contribution this thesis would not have been possible. Zhixiang, when I started my research without any hands-on knowledge of UHV or SPM, you taught me

everything you knew, thank you. Wiel, your skills in the lab are simply amazing. The fascinating structures that you prepared sparked the research of the complete second half of this thesis. And without any problems you kept on preparing the ridiculous amount of samples for all the analysis techniques I asked you for. Sampsa, although separated in space by almost 2000 km, we had some bonding overlap in wave function that resulted in a very productive and pleasant collaboration with many shared papers. Joost, I think we had a fantastic run together. You had the wonderful talent of 'scavenging' old material to prepare the workaround we were looking for. This, combined with the fact that you are much more a chemist then I am (I confess, I have gone down the slippery slope of becoming a physicist) made you an invaluable addition to the group. It was good, and fun, to work with you. Rogier, you were my first master student. I am glad that all the setbacks we had during your stay at CMI did not ruin your appetite for SPM. I admire your perseverance when things get tough. When it was clear that experiments were not an option anymore, you did some high quality theoretical work, giving a valuable addition to our understanding of the self-assembly of nanorods. Jaco, you also had a hard start with the machine not performing as it should. Luckily, you also got to see the brighter days. Your contributions to the work on the honeycombs resulted not only in a very nice chapter in this thesis, but also in you creating your own PhD position. I have all confidence that you will drive this exciting research field forward by a great deal. Freddy, Jan, and Andrei, thanks for your help if I got stuck in k-space, and for the good time in Grenoble. Ben, you did very nice work on the theory of doping of nanocrystals. Maybe it did not find its way into this thesis, but I am sure it will find an application in our group sooner or later. Peter J., although you were officially not a student of mine, we did some nice work together on the moiré structure of graphene. It was always fun teasing you with your Groninger heritage. A special thanks also to the Finnish theory squad, in particular to Mari and Ari.

Furthermore, a special thanks goes out to those who brought me to this point by sharing their knowledge in teaching or supporting my research practically. Hans Ligthart, thanks for your endless support in keeping the 'baby' alive. Stephan, without your help many of the computer work would not have been possible. Hans Meeldijk, thank you for sharing your time and expertise on the TEM. Heiner, thank you for including me in your tomography work when I was still a master student. The things I learned from you at that time have proven invaluable for the last two chapters of this thesis. Laura, Weikai, and Marjolein, thank you for all the

efforts on the Monte Carlo front. Some teachers that deserve a special thanks include Paul Peijzel, Onno Gijzeman, Harold de Wijn, Andries Meijerink, John Kelly, and the people from the Guido de Brès, in particular Dr. Van der Scheer, Messrs. Jonkers and Van de Kamp, and Ms. Oldenhuis (who probably does not remember that she used a baseball bat to get me into the VWO).

Finally, I would like to thank everyone who helped me in a non-scientific way. The entire CMI group for a very pleasant stay, and in particular my roommates Zachar and Relinde for putting up with my taste for classical music. My (grand)parents, brothers, sister, in-laws, and friends for their interest in my work. And above all many thanks to Arjanne for her unending love, patience, support, help (feeding the 'baby' liquid helium and nitrogen), and ability to help me see what is really important in life. Of this Jesse is proof.

Soli Deo gloria

Publication list

This thesis is based on the following publications:

- M.P. Boneschanscher, J. van der Lit, Z. Sun, I. Swart, and D. Vanmaekelbergh, *Quantitative atomic resolution force imaging on epitaxial graphene with reactive and nonreactive AFM probes.*
  ACS Nano **6**, 10216–10221 (2012).
- S.K. Hämäläinen, M.P. Boneschanscher, P.H. Jacobse, I. Swart, K. Pussi, W. Moritz, J. Lahtinen, P. Liljeroth, and J. Sainio, *Structure and local variations of the graphene moiré on Ir(111).*
  Physical Review B, Rapid Communications **88**, 201406(R) (2013).
- M.P. Boneschanscher, S.K. Hämäläinen, P. Liljeroth, and I. Swart, *Sample corrugation affects the apparent bond lengths in atomic force microscopy.*
  ACS Nano **8**, 3006–3014 (2014).
- S.K. Hämäläinen, Z. Sun, M.P. Boneschanscher, A. Uppstu, M. Ijäs, D. Vanmaekelbergh, and P. Liljeroth, *Quantum-confined electronic states in atomically well-defined graphene nanostructures.*
  Physical Review Letters **107** (23), 236803 (2011).
- M.P. Boneschanscher, W.H. Evers, W. Qi, J.D. Meeldijk, M. Dijkstra, and D. Vanmaekelbergh, *Electron tomography resolves a novel crystal structure in a binary nanocrystal superlattice.*
  Nano Letters **13** (3), 1312–1316 (2013).

- M.P. Boneschanscher, W.H. Evers, J.J. Geuchies, T. Altantzis, B. Goris, F.T. Rabouw, S.A.P. van Rossum, H.S.J. van der Zant, L.D.A. Siebbeles, G. van Tendeloo, I. Swart, J. Hilhorst, A. Pethukov, S. Bals, and D. Vanmaekelbergh, *Long-range orientation and atomic attachment of nanocrystals in 2-D honeycomb superlattices.*
  Submitted.

Other relevant publications of the author:

- J. van der Lit, M.P. Boneschanscher, D. Vanmaekelbergh, M. Ijäs, A. Uppstu, M. Ervasti, A. Harju, P. Liljeroth, and I. Swart, *Contacting atomically well-defined graphene nanoribbons with atomic scale precision.* Nature Communications **4**, 2023 (2013).
- Z. Sun, M.P. Boneschanscher, I. Swart, D. Vanmaekelbergh, and P. Liljeroth, *Quantitative atomic force microscopy with carbon monoxide terminated tips.*
  Physical Review Letters **106**, 046104 (2011).
- H. Friedrich, C. Gommes, K. Overgaag, J.D. Meeldijk, W.H. Evers, B. de Nijs, M.P. Boneschanscher, P. de Jongh, A. Verkleij, K. de Jong, A. van Blaaderen, and D. Vanmaekelbergh, *Quantitative structural analysis of binary nanocrystal superlattices by electron tomography.*
  Nano Letters **9**, 2719–2724 (2009).

Oral presentations by the author:

- Physics@FOM Veldhoven 2012, 2013, *Veldhoven, NL*
- Functional Nanoparticle Solids Meeting, 2010–2013, *Utrecht/Delft, NL*
- Graphene Day 2012, *Groningen, NL*
- Int. Conference on Nanoscience + Technology (ICN+T) 2012, *Paris, FR*
- Int. Conference on non-contact Atomic Force Microscopy 2012, *Ceský Krumlov, CZ*
- Graphene Int. Conference 2012, *Brussels, BE*
- Invited speaker for the Debye lunch lecture 2012, *Utrecht, NL*
- European Conference on Surface Science (ECOSS) 2010, *Groningen, NL*

Poster presentations by the author:

- Graphene Day 2012, *Groningen, NL*
- Herodot Summerschool 2011, *Cargèse, Corsica, FR*
- Nederlandse Vereniging voor Microscopie (NVvM), 2011, *Eindhoven, NL*
- Dutch Scanning Probe Day 2011, *Nijmegen, NL*

Curriculum Vitae

Mark Pieter Boneschanscher was born on the 28^{th} of November 1985 in Amersfoort, The Netherlands. In 2004 he graduated from the Guido de Brès in Amersfoort, and started to study Chemistry at Utrecht University, with a minor in nanomaterials science. He obtained his bachelor's degree *cum laude* in 2007 after finishing his thesis 'Forces Involved in Nanocrystal Superlattice Formation' at the Condensed Matter and Interfaces group in Utrecht under supervision of Karin Overgaag and Daniël Vanmaekelbergh. He then followed the master's programme Nanomaterials: Chemistry and Physics, which he concluded with a 5 month internship at the European Patent Office, and the thesis 'Structural Analysis and Modeling of Nanocrystal Superlattices' supervised by Daniël Vanmaekelbergh. This thesis won the second prize in the KNCV golden master award 2009. He received his master's degree *cum laude* in 2009. During his bachelor's and master's studies he worked as a teaching assistant in the first years chemistry lab, the Junior College Utrecht, and the Science Shop Chemistry Utrecht. Also he participated in several education advisory committees.

In November 2009 he started as a PhD researcher in the Condensed Matter and Interfaces group under supervision of Daniël Vanmaekelbergh, Peter Liljeroth, and since 2012 Ingmar Swart. The project was funded by the FOM programme Control over Functional Nanoparticle Solids. The results of this project, presented in this thesis, were published in peer-reviewed journals and presented at international conferences. During his PhD, he supervised two master's students and one bachelor's student, and the quantum chemistry and analytical chemistry course for first year students. From the beginning of 2010 until the end of 2012 he participated in the Central Works Council of FOM, the last year as chairman.

Next to spending time with his family and friends, Mark enjoys playing the viola and reading a good book.